The Influence Of Rough Rolling Conditions On Austenite Evolution In Peritectic Microalloyed Plate Steels

by

Dannis Rorisang Nkarapa Maubane

Supervised by

Prof. C.W. Siyasiya

Prof. W.E. Stumpf

Submitted in partial fulfilment of the requirements of

Master of Engineering

(Metallurgical Engineering)

in the

Department of Materials Science and Metallurgical Engineering

Faculty of Engineering, Built Environment & Information Technology

UNIVERSITEIT VAN PRETORIA
UNIVERSITY OF PRETORIA
YUNIBESITHI YA PRETORIA

Abstract

The thermo-mechanical processing of microalloyed steels has been studied widely. However most of the work has been focused on the finishing stages of hot rolling where pancaking of the austenite is desired for strength and toughness. During roughing, full recrystallization is desired for a uniform, through-thickness austenite microstructure.

In this work the influence of the strain sequence during roughing on the evolution of austenite in plain carbon, C-Mn-V, C-Mn-Nb-V and C-Mn-Nb-Ti-V steels, was investigated during conventional hot rolling. This was done because strain is one of the most controlling parameters of recrystallization during hot rolling which in turn controls the austenite microstructure.

Reheating and roughing simulations were conducted in a Bähr 805D deformation dilatometer using a constant austenitising temperature of 1220 °C. Different heating cycles were adopted in the reheating simulations to see the influence of heating rate and soaking time on the austenite grain size. Heating rate of 7.5 °C/min and constant soaking time of 30 minutes were used for roughing simulations as this closely simulated the slab's centre thermal profile. The roughing strain sequence was varied from small (0.07 ε/ pass), intermediate (0.1 ε / pass) to large (0.15 ε / pass) at a temperature range of 1150-1050 °C and strain rates of 0.3-2.9 s^{-1}. Application of a non-standard 0.4 strain in the last pass of each strain schedule was introduced to study its effect on the austenite grain size. Double stroke tests were used to quantify the austenite softening behaviour. The prior austenite grain size was measured from quenched specimens. A FEM study was commissioned to study the localized strain distribution in axisymmetric compression and flat plate rolling simulations.

Reheat austenite grain sizes increased with increasing soaking time and decreasing heating rate. The C-Mn-Nb-Ti-V steel had the finest reheat grain size and the C-Mn steel was the coarsest. This was attributed to the presence of the stable TiN in the former.

The austenite grain size after roughing simulations decreased with increasing strain per pass. The C-Mn had the coarsest austenite grain size after roughing followed by the C-

Mn-Nb-V and C-Mn-Nb-Ti-V the finest. However application of the 0.4 strain in the last pass led to similar grain sizes across the steels especially at high exit temperatures.

At strains of 0.1 the Nb-containing microalloyed steels had a lower volume recrystallized fraction magnitude in the partially recrystallized passes compared to the plain C-Mn and the C-Mn-V steels. This is considered to be due to the retardation of recrystallization by the solute drag of Nb. Pass strains of 0.15 promoted full recrystallization from the second pass onwards in all the studied steels and led to grain refinement of the austenite with a narrower grain size distribution. This was attributed to the increased driving force for recrystallization and increased interfacial area per unit volume which provides nucleation sites for the recrystallized grains at a strain of 0.15 compared to that of 0.07 and 0.1.

The extent of grain refinement was found to decrease with decreasing initial grain size and increasing strain. The C-Mn steel, with the coarsest reheat grain size showed the most grain refinement response as compared to the fine grained microalloyed steels. This indicated that a saturation point is reached where no further grain refinement occurs under the studied conditions. Grain refinement of the austenite was due to static recrystallization occurring in the inter-pass times for strains of 0.07 and 0.1. Strains of 0.15 are thresholds where both static and metadynamic recrystallization may be responsible for grain refinement. An optimum uniform austenite microstructure was found when pass strains were at least 0.15.

FEM showed that the equivalent plastic strain is concentrated at the centre of an axisymmetrical compressed sample and at the sub-surface of a flat hot-rolled plate [97]. A linear relationship between the applied strain and the equivalent plastic strain at various locations in both the axisymmetrical compressed sample and flat rolled plate was found.

Recrystallization models correlated poorly with the measured recrystallized volume fraction in this work at strains of 0.07 to 0.1. This is primarily due to the fact that the recrystallized grain size is exaggerated at small strains due to a division by a smaller number in the models and this therefore leads to an erroneous time for 50 %

recrystallization. The other factor can be that at small strains recrystallization may be occurring through the SIBM (Strain induced boundary migration) process and not the classical nucleation theory as illustrated by the models. In the case of microalloyed steels the account of recrystallization retardation by solute Nb in the models may have led to the discrepancy by over-compensating for this retardation.

Acknowledgements

First and foremost I would like to thank God almighty for His grace and power to complete this milestone, and guidance and blessings He brought along the journey.

I want to thank Dr. Kevin Banks, my colleague and mentor at the University of Pretoria, Materials Science and Metallurgical Engineering Department (IMMRI) for the initiation of this project and his immeasurable support and guidance throughout the duration of the project. I also want to express my gratitude for the faith he had in me and grooming me to be where I am today, I am forever indebted. To my supervisors Prof. Charles Siyasiya and Prof. Waldo Stumpf, thank you for your support, constructive criticisms, guidance and time spent on this project. I really appreciate it.

I would like also to express my sincere gratitude to Prof. Schalk Kok and his Ph.D student, Jaco Jansen Van Rensburg, for their great assistance with FEM modelling. Your time, patience and valuable inputs made this project a success and I will forever be grateful.

To all the IMMRI staff, you have been like family to me, thank you for your support and understanding, your motivation and advice really gave me the punch I needed to complete this project. A special thanks to Mrs Elsie Snyman-Ferreira for helping to organize the dissertation and making it look professional.

I would like to extend my gratitude to everyone who immeasurably added value to my life before embarking this journey and to pick a few, Mrs. Disebo Sathekge my Secondary school teacher, for her continual support to me and loving me just like her own son and Prof. Tom von Moltke for the mentorship he provided during my undergraduate days, his advice and constructive criticisms made me who I am today.

To my siblings, thank you for the motivation and support, even during tough times you continued to believe in me, you are the best. Thanks to my wife, Delina Maubane, who has been there from the start to the finish of this project, your love, patience and support kept me going strong.

This dissertation is dedicated to my late mom, Monica Maubane, my true heroine and friend who kept motivating and encouraging me to work hard in life especially in my academics. I know wherever you are you will be proud of me, may your soul rest in peace.

Table Of Contents

List of Figures

List of Tables

List of Symbols and Acronyms

Ar_3	Austenite to ferrite transformation start temperature
$avg\overline{L}$	average linear intercept grain size
b	barrelling factor
C_0	concentration in the matrix in equilibrium with a very large secondary phase particle at a given temperature
C_g	concentration of solute atoms at grain boundaries
C_C	equilibrium concentration of carbon
C_{Nb}	equilibrium concentration of niobium
C^e_C	instantaneous concentration of carbon
C^e_{Nb}	instantaneous concentration of niobium
CCR	conventional controlled rolling
d_0	initial diameter of a cylinder
d_m	maximum diameter of a cylinder
D_{diff}	diffusivity of the rate controlling solute in the matrix
D_{gb}	diffusion coefficient of the grain boundary
$D_{gs,0}$	initial grain size
D_{gs}	grain size after grain growth
D_{MDRX}	metadynamic recrystallized grain size
D_{rex}	recrystallized grain size
D_{SRX}	static recrystallized grain size
D_u	mean unrecrystallized grain size
DRV	dynamic recovery
DRX	dynamic recrystallization
DRCR	dynamic recrystallization controlled rolling
E	Young's modulus
E_1, E_2	energy of the deformed grains separated by a bulging boundary
EB	interfacial energy associated with the bulging region of the grain boundary
E_d	difference in the elastic distortion energy of solute atoms distributed within the grain boundaries
f	friction factor
F	friction force
F_P	pinning force by precipitates
F_V	volume fraction of the pinning particle
FEM	finite element modelling
h	exit height of a plate/cylinder
H	entry height of a plate/cylinder
h_n	height of plate at the neutral point of contact
k	Arrhenius constant
k_f	shear flow stress
k_s	super-saturation ratio
k_m	mean hot deformation resistance
L	length of a gridline
m	average friction factor
M	Taylor factor
MFS	mean flow stress
MFS'	plane mean flow stress
MDRX	metadynamic recrystallization
n	grain growth exponent
N	total number of gridlines

N_{gb}	number of intercepts on the grain boundaries	SRX	static recrystallization
		T	Temperature
P	roll force	t	time
P_r	radial force	$t_{0.05p}$	time for 5% precipitation
Q	load multiplication factor	$t_{0.05x}$	time for 5% recrystallization
Q_R	roll pressure function	$t^{MDRX}_{0.5}$	time for 50% metadynamic recrystallization
Q_{app}	apparent activation energy		
Q_{gb}	activation energy for diffusion down the grain boundaries	T_{NR}	nil-recrystallization temperature
		$t_{0.95x}$	time for 95% recrystallization
Q_{gg}	Activation energy for grain growth	T_s	solubility temperature of precipitates
Q_{MDRX}	Activation energy for metadynamic recrystallization	V	tangential velocity of the roll
		V_0	entry speed of the plate
		V_e	exit speed of the plate
Q_{SRX}	Activation energy for static recrystallization	V_m	molar volume of precipitates
R	universal gas constant	V_n	Speed of the plate at the neutral point of contact
R’	flattened roll radius		
R_0	initial radius of cylinder	w	width of the plate
R_{av}	average radius of cylinder	X	recrystallized volume fraction
R_B	spherical cap radius of the bulging grain boundary	X_f	recrystallized volume fraction after accounting for recovery
R_{crit}	critical radius of the bulging grain boundary	X_{MDRX}	metadynamic recrystallized volume fraction
R_{lim}	maximum grain radius of particle/precipitate	X_{SRX}	static recrystallized volume fraction
R_m	maximum radius of a cylinder	Z	Zener Hollomon parameter
R_{roll}	roll radius	Z_H	heterogeneity parameter
R_t	top radius of a cylinder	α	angle of bite
R(t)	mean particle/precipitate radius	β	shear modulus
		$\vec{b}$	Burger’s vector
RCR	recrystallization controlled rolling	ΔE	driving force for recrystallization trough the SIBM process
ROT	run-out table		
SD	standard deviation	ΔG(t)	driving force for recrystallization through the classical nucleation theory
SIBM	strain induced boundary migration		
SRCT	static recrystallization critical temperature	ΔG_{gc}	driving force for grain coarsening
SRV	static recovery	Δh	draft

ε	nominal true strain	φ	proportionality constant
ε_a	accumulated strain	Φ_n	neutral plane angle
ε_c	critical strain for DRX	θ	ratio of the real to the apparent area
ε_p	peak strain		
ε_r	redundant strain	τ	friction stress
ε_T	trainsition strain	σ	flow stress
γ_{gb}	grain boundary interfacial area	$\sigma_{m,i}$	maximum flow stress at pass i
γ_{ppt}	surface energy of the precipitate	$\sigma_{2\%,i}$	2% offset flow stress at pass i
$\bar{L}$	linear intercept grain size	$\sigma_{2\%,i+1}$	2% offset flow stress at pass i+1
$\bar{L}_i$	linear intercept grain size of gridline i	υ	Poisson's ratio
μ	coefficient of friction		
ρ	dislocation density		

Chapter 1. Introduction

1.1. Microalloyed Steels

Microalloyed or HSLA (High Strength Low Alloy) steels contain dilute combinations of Ti, V, and Nb for enhanced mechanical and microstructural properties. HSLA steels were developed in the 1960's and the combined microalloy additions with thermo-mechanical processing (TMP) are employed to achieve desirable mechanical properties through microstructural control [1,2,3,4]. These steels are also known for their outstanding mechanical properties, such as resistance to brittle fracture, cold formability and good weldability [5]. Small additions of Nb, Ti and V (≤0.1% each) can strengthen the standard C-Mn steels without interfering with subsequent processing and help control the austenite microstructure during hot working and further processing [6]. Nb is the most effective alloying element since it controls the austenite grain size through both the solute drag and strain induced precipitation effects [7,8]. The increased strength of these steels is due to a combination of ferrite grain refinement, solid solution strengthening, precipitation strengthening and dislocation strengthening [3,4,9,10]. Grain refinement is the major contributor, since it simultaneously improves the strength and toughness of the steel without altering the chemical composition [11]. Applications of micro-alloyed steels include oil and gas pipelines, heavy duty highway and off-road vehicles, construction and farm machinery, mine and rail cars [1,3,5,7,9,12,10]. This is due to the fact that no heat treatment is required after forming of the parts thus making them more economically viable (time and cost minimized) [13,14].

Microalloyed steels are classified into different categories namely, microalloyed pearlite-ferrite steels, weathering steels, acicular ferritic steels, low carbon bainitic steels and dual phase steels. Microalloyed pearlitic-ferritic steels contain small amounts, normally less than 0.1%, of strong carbide, nitride or carbonitride forming elements for precipitation hardening and grain refinement but these steels cannot readily exceed the yield strength of 400 MPa in reasonable section sizes [15]. Weathering steels contain small amounts of alloying elements such as copper and phosphorus for improved atmospheric corrosion resistance and solid solution hardening. Acicular ferritic steels contain low carbon (0.03%C) and high manganese contents of about 2% and they have

a fine lath-like ferritic grain structure with a high dislocation density. They have improved toughness since no precipitation occurs in-between the laths. Dual phase steels contain a polygonal ferritic matrix with a dispersion of about 15% martensite and retained austenite with a tensile strength of about 655 MPa [16].

Pearlitic-ferritic HSLA steels are strengthened through grain refinement, solid solution and precipitation hardening, strain ageing and dislocation hardening [16].

Figure 1.1 shows those factors affecting the yield strength and impact transition temperature of HSLA steels.

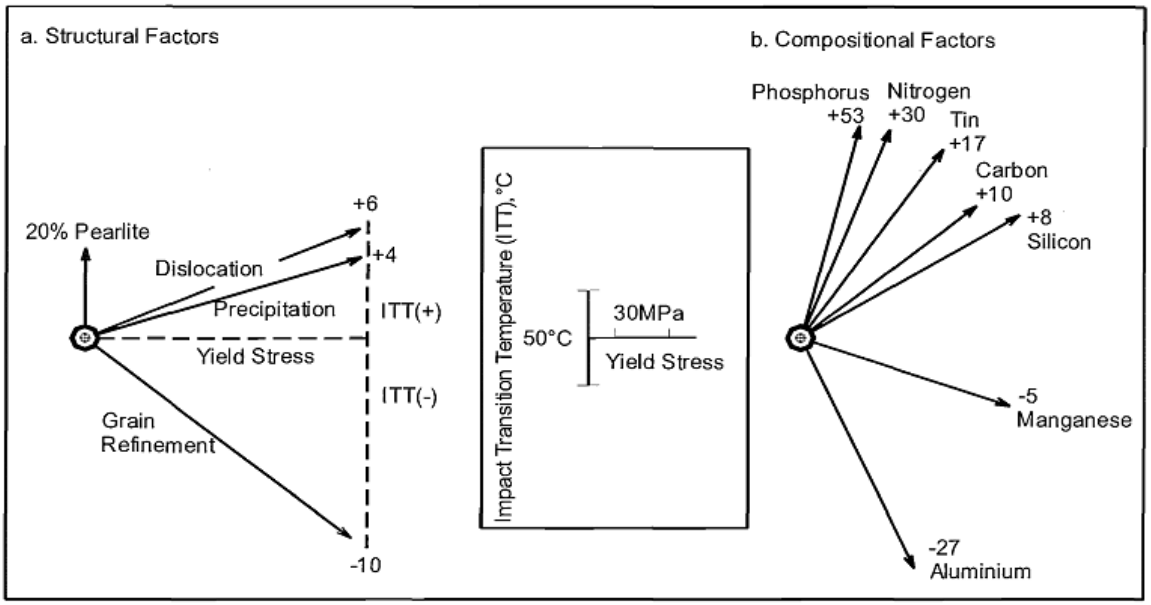

Figure 1.1: Structural and compositional factors affecting yield strength and impact transition temperature of HSLA steels [16]

Figure 1.1 shows that both precipitation and dislocation strengthening leads to a loss of toughness.

Mechanical properties of microalloyed steels are strongly influenced by their ferrite grain structure, where a fine and uniform ferrite grain size is desired in the final microstructure as it provides high strength and toughness. The final microstructure and the associated mechanical properties are influenced by the austenite microstructure after rolling which is influenced by the rolling schedule through the interaction between recrystallization,

grain growth and precipitation effects with the cooling conditions on the run-out table and coiling temperature [16,17,18] for strip steels.

After continuous casting of the slab or ingot casting, microalloyed steels undergo a primary reduction and are then hot rolled into sheet, strip, plate, bar or structural sections. Special hot rolling processes and treatments such as controlled rolling, accelerated cooling, quenching, normalizing and intercritical annealing may be employed to obtain the desired mechanical properties, such as high yield strength, low ductile to brittle transition temperature, formability and weldability [16].

Niobium (Nb), Titanium (Ti) and Vanadium (V) are strong carbide and nitride formers and these have a significant influence on the austenite recrystallization and grain growth kinetics. If the austenite recrystallization is suppressed during finishing, microalloying elements can act as ferrite grain refiners thus improving the toughness since they form precipitates such as VN, VC, NbN, NbC, Nb(C_x,N_x), TiN and TiC, some of which control the austenite grain growth through grain boundary pinning, provided they are not coarse. In Ti-containing microalloyed steels, a Ti/N ratio below the stoichiometric value of 3.42 yields good results in controlling the austenite grain size provided that the precipitates are fine, i.e. less than 30nm [19]. The austenite recrystallization is suppressed by the strain-induced carbonitrides which inhibit the movement of sub-grain boundaries and if microalloying elements are in solution, they retard the movement of sub- and grain boundaries through solute drag [20]. In addition to the chemical composition, the grain growth of the austenite prior to finishing will be influenced by parameters such as the reheating and roughing conditions (rough rolling temperature, strain, strain rate and inter-pass time), static (SRX), meta-dynamic (MDRX) and dynamic (DRX) recrystallization of austenite and cooling rate [17,21-25].

1.2. Peritectic Microalloyed Steels

Peritectic steels are steels with carbon content between 0.09 and 0.16 % which undergo the peritectic reaction. Peritectic reaction is known as a reaction of a liquid and a solid to form one solid product during cooling and reversible during heating in a binary system. In a Fe-C binary system this reaction is comprised of a transformation of δ-

ferrite and liquid to austenite during cooling [103,104]. These steels are associated with surface defects during continuous casting because the peritectic reaction takes place in the meniscus region when the shell is extremely thin. This reaction is associated with volume contraction with the δ-ferrite (BCC) transforming to austenite (FCC) and this leads to detachment of the solid shell from the mould causing a decrease in heat flux which increases risks of surface cracking and breakouts [104,105, 106].

1.3. Scope Of The Study

During conventional hot rolling of steels, the resultant microstructures are often non-uniform and coarse, especially at the centreline of the plate. This is due to incomplete recrystallization during inter-pass times and grain growth during air cooling after rolling. These unfavourable microstructures can be detrimental to both strength and toughness. To correct this, further heat treatments such as normalizing are employed but this incurs further production costs due to additional energy consumption, handling etc.

Figure 1.2 shows the final microstructures of an industrial conventionally hot rolled 16 mm Nb-Ti-V steel plate subjected to a 93 % reduction in 19 passes in the as hot rolled condition and after the normalizing heat treatment. The microstructure of the as hot rolled plate shows a mixture of coarse polygonal ferrite, coarse pearlite, acicular ferrite and pearlite banding. In the as normalized condition, an improved microstructure is obtained with the ferrite grains more refined although not uniform with pearlite banding still persisting.

The present study concerns the influence of roughing parameters on the evolution of austenite to produce a metallurgically sound (fine and uniform), through-thickness microstructure at the end of roughing without compromising mill constraints. Four peritectic steel types are studied: 1) C-Mn to serve as a benchmark, 2) C-Mn-V, 3) C-Mn-Nb-V and 4) C-Mn-Nb-Ti-V. The influence of light, medium and heavy pass reductions with typical industrial strain rates on the recrystallization behaviour and microstructural evolution will be investigated. The effect of localized strain in the roll gap on the austenite microstructure will be determined from finite element modelling (FEM) to establish localized strain distributions in the through-thickness of the slab.

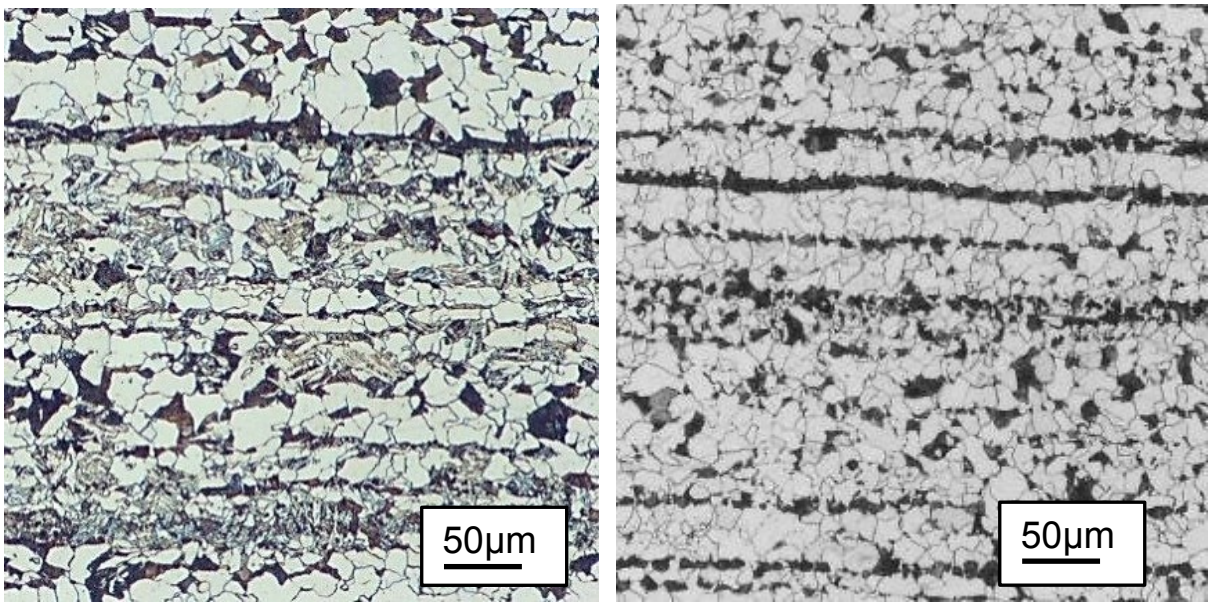

Figure 1.2.: Industrial conventionally hot rolled peritectic Nb-Ti-V 16 mm plate in the a) As hot rolled and b) as normalized conditions. As hot rolled condition shows a non-uniform and coarse microstructure whilst the as normalized condition shows a more refined structure although not uniform.

Chapter 2. Grain Growth

2.1. Introduction

Grain growth is the evolution of a microstructure due to the motion of grain boundaries driven by the reduction in total grain boundary interfacial energy per unit volume. Grain growth is characterized by the growth of larger grains at the expense of smaller ones, leading to an increase in average grain size [23,26]. Austenite grain growth is influenced by austenitising temperature and time, heating rate, alloy composition, hot rolling history, the alloy's grain boundary energy and initial grain size distribution [22-24,27-28].

Isothermal austenite grain growth kinetics can be described by the following equation:

$$D_{gs}^{n} - D_{gs,0}^{n} = Kexp(\frac{-Q_{gg}}{RT})t \quad \text{.....(2.1)}$$

where $D_{gs,0}$ and D_{gs} are the initial and final grain size respectively. The grain growth exponent n, the Arrhenius constant K, and the activation energy for grain growth Q_{gg}, have been previously determined for specific chemical compositions and processing conditions. Table 2.1 show these constants as reported by Priadi et al. [23]

Table 2.1.: Summary of empirical models describing austenite grain growth [23]

Steel	Austenite conditions	n	K (m/s)	Q (kJ/mol)
C-Mn	Statically recrystallized	10	3.87×10^{32} for T>1000°C	400 for T>1000°C
Low C-Mn	Statically recrystallized	2	4.27×10^{12}	66.6
C-MN and C-Mn-V	Statically or metadynamically recrystallized	7	1.45×10^{27}	400
C-Mn-Nb	Statically or metadynamically recrystallized	4.5	4.1×10^{23}	435

2.2. Normal And Abnormal Grain Growth

Normal grain growth is a process whereby the size distribution of the individual grains remains uniform and only the average grain size of the distribution increases. Abnormal grain growth is a process whereby the distribution of grains is non-uniform due to some grains growing rapidly at the expense of others [2,26,29,30]. Normal grain growth results from the interaction between the topological requirements of space-filling polyhedra and geometrical needs of surface tension equilibrium. The phenomenon of normal grain growth has the following theoretical features [26]:

- The grain sizes are distributed into a narrow size range;
- After sufficient time during grain growth, the grain size increases but the grain size distribution remains the same;
- The grain size distribution is more or less log normal;
- The final grain size distribution is more or less independent of the initial distribution; and
- During grain growth the average grain size (D_{gs}) increases as in equation 2.1.

Abnormal grain growth is also known as secondary recrystallization and can only occur when normal grain growth is inhibited, mostly by pinning particles. It occurs at elevated temperatures and when the particle dispersion becomes unstable. Abnormal grain growth may occur due to the presence of heterogeneities such as within a particle distribution and is accompanied by an increase in the heterogeneity parameter (Z_H)

which is the ratio of the size of the growing grain to the size of the neighbouring grains i.e.:

$$Z_H = \frac{D_{gs,max}}{D_{gs}} \quad (2.2)$$

When $Z_H \geq 2$ the distribution becomes unstable and secondary recrystallization sets in. Main factors leading to abnormal grain growth are localised effects of second-phase particles, texture and surface effects [30].

2.3. Grain Boundary Pinning

Grain boundary migration (*M*) is dependent on the temperature as shown in equation 2.1 and is expressed as [2,22,31]

$$M = K_0 exp^{(-\frac{Q}{RT})} \quad (2.3)$$

This boundary migration can also be affected by factors such as the segregation of solute elements to the grain boundaries and the presence of the second phase particles. The former introduces a frictional drag on the moving boundary whilst the latter decreases the grain boundary area and hence the overall boundary energy, therefore creating a boundary pinning effect. Austenite grain boundary pinning is effective and important for the toughness of steels [22].

Normal grain growth will be completely inhibited when the grain size reaches a critical maximum grain radius, R_{lim} which is described by the Smith-Zener equation as follows [2,22, 30, 22,]:

$$\mathrm{R_{lim}} = \frac{4\mathrm{r}}{3\mathrm{f_v}} \quad (2.4)$$

where *r* and f_v are the average radius and volume fraction of the pinning particles respectively.

The pinning force (F_p) exerted by a number of equally sized particles per unit area (N_s) is given by [19]:

$$F_p = \pi r \gamma_{gb} N_s \quad (2.5)$$

The average particle pinning force (F_p) is related to the limiting grain radius as follows [2]:

$$F_p = \gamma_{gb} \frac{3f_v}{4r} = \gamma_{gb} \frac{1}{R_{lim}} \quad (2.6)$$

where γ_{gb} is the grain boundary interfacial energy.

Equation 2.4 was derived by only considering an isolated spherical grain radius and neglecting the neighbouring grains. For a model which assumes space filling tetrakaidecahedra, the following equation was derived [22,30, 32]:

$$R_{lim} = \frac{\pi}{6}\left(\frac{3}{2} - \frac{2}{Z_H}\right) \quad (2.7)$$

where Z_H is the ratio of the growing grain's and matrix grain's radii and is commonly assumed as 1.5.

For abnormal grain growth, a correction factor, β, was added to the Smith-Zener equation and was derived as [30]:

$$R_{lim} = \frac{4r}{3f_v \beta} \quad (2.8)$$

where β = 0.125ln(40R/ř) and R the grain radius. Note, however, that these corrective additions only affect the constants and that the basic terms governing pinning of r/f_v remain, i.e. for effective pinning one needs small particles and large numbers of them.

Austenite grain growth in the presence of second phase particles obeys the following relation [34]:

$$\frac{dR}{dt} = M\left(\frac{1}{R} - \frac{3f_v}{4r}\right) \quad (2.9)$$

The driving force for grain coarsening (G_{gc}) is the reduction in surface energy associated with grain boundaries and is given by [35]:

$$\Delta G_{gc} = \frac{2\gamma_{gb}}{D_{gs}} \quad (2.10)$$

To have a fine grained structure there must both be small particles present and a high volume fraction of these fine precipitates i.e. a lower r/f_v ratio. This ratio remains fixed until subsequent reheating for hot rolling commences where it will now be controlled by either the rate of dissolution of the particles or by their rate of coarsening. Particle dissolution has the following effects a) a direct effect in reducing the f_v and b) an indirect effect of increasing the rate of particle coarsening by providing the higher solute concentration necessary for mass transport [32].

At elevated temperatures the particles start coarsening and the Lifshitz-Slyozov-Wagner (LSW) equation below describes the kinetics of particle coarsening controlled by matrix diffusion of the rate controlling solute [22, 27,33]:

$$r^3 - r_0^3 = \frac{8\gamma_{ppt}D_{diff}C_0V_m}{9RT}t \quad (2.11)$$

where r is the average particle radius after time t and r_0 is the initial particle radius, D_{diff} is the diffusivity of the rate controlling solute in the matrix, V_m is the particle molar volume, γ_{ppt} is the surface energy of the precipitate and C_0 is the concentration in the matrix in equilibrium with a very large secondary phase particle at temperature T.

An increase in nitrogen content in steels increases the resistance of carbonitride particles to coarsening and thus promotes their ability as grain boundary pinning agents [33]. The grain coarsening temperature, T_c increases with increasing nitrogen content and is lower than the complete dissolution temperature, T_s, of the carbonitrides [32, 36]. Figure 2.1 shows this effect on steels studied by Cuddy and Raley [32], where TiN is significantly more effective than any of the other second phases and is simply because of its higher thermodynamic stability ($-\Delta H_f$).

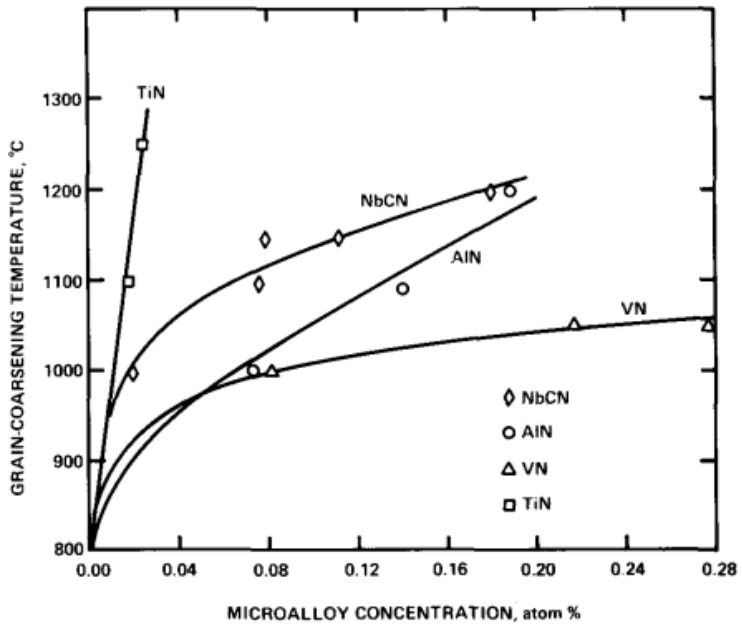

Figure 2.1.: Effect of microalloy particle concentration on the austenite grain-coarsening temperature [32]

Cuddy and Raley [32] derived an equation to predict the austenite grain-coarsening temperature (T_C) in low carbon microalloyed steels and is given by:

$$T_C = A + BT_s \quad (2.12)$$

where T_s is in degrees Celsius for the precipitate responsible for grain boundary pinning, A and B are grain coarsening constants that depend on the type of precipitate and are given in Table 2.2 below.

Table 2.2.: Grain-coarsening constant in microalloyed steels determined by Cuddy and Raley [32]

Precipitate	A (°C)	B
AlN	385	0.535
VN	616	0.376
TiN	-279	0.899
Nb(C,N)	460	0.569

2.4. Grain Growth in C-Mn Steels

During hot rolling of plain carbon steels the dominant process is austenite grain growth in both the reheating furnace and between the rolling stands. In Al-killed plain carbon steels the austenite grain growth kinetics are strongly influenced by the AlN precipitates [18]. Militzer *et al.* [18] showed that the austenite grain size of Al-killed plain carbon steels increases with time, temperature and decreasing heating rate, as in Figure 2.2 and Figure 2.3. EQAD is the equivalent area diameter in both figures.

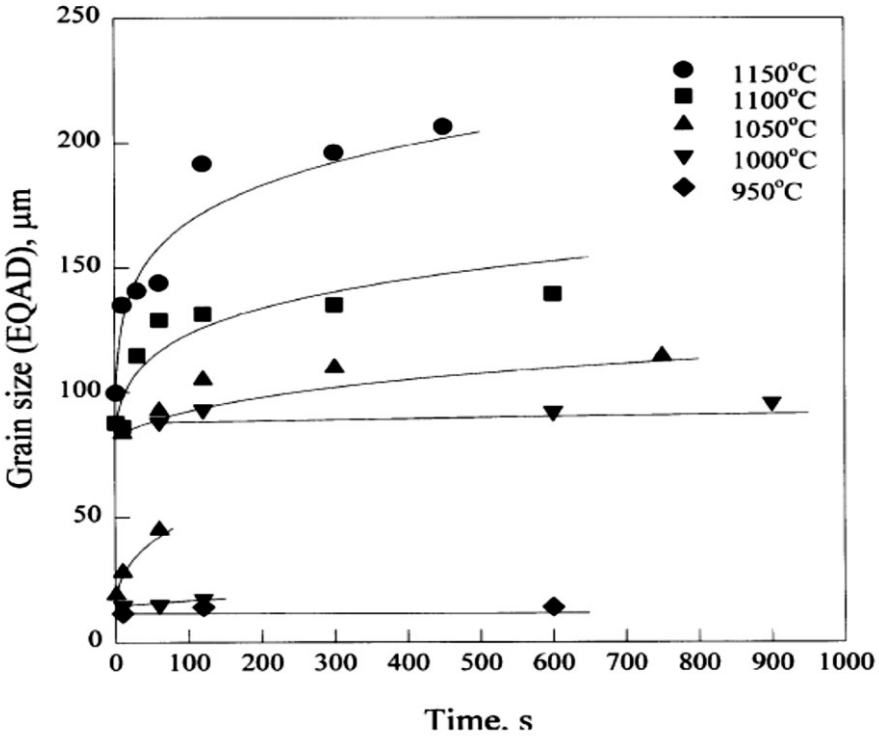

Figure 2.2.: Influence of temperature and time on the austenite grain size in Al-killed plain carbon steels after a heating rate of 5 ^{0}C/s from room temperature [18]. EQAD means Equivalent Area Diameter.

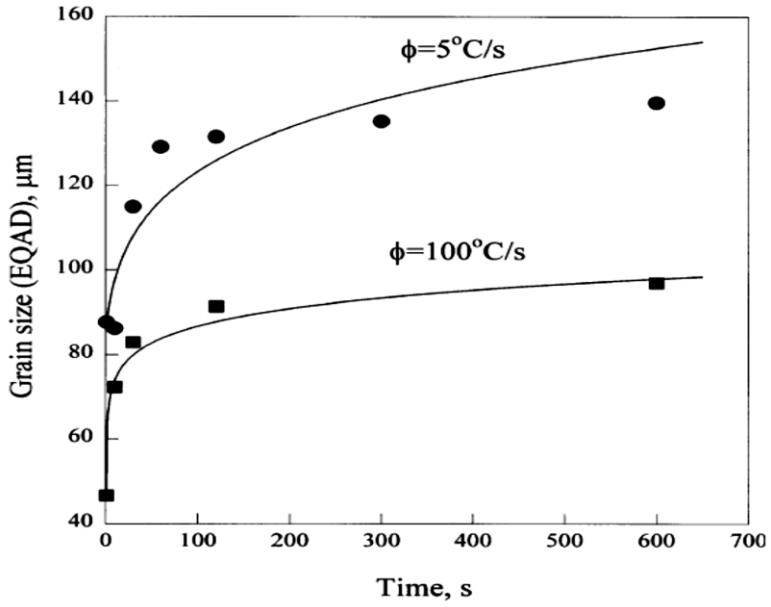

Figure 2.3.: Influence of heating rate from room temperature to the start temperature on the austenite grain size in Al-killed plain carbon steels. The 5 ^{0}C/s heating rate was from room temperature and increased to 100 ^{0}C/s from 900 ^{0}C [18].

The grain boundary mobility for plain C-Mn steels is given by [32]:

$$M_{C-Mn} = \frac{0.192}{T(t)} \exp\left(\frac{-20837.14}{T(t)}\right) \quad (2.13)$$

2.5. Grain Growth In Microalloyed Steels

It is common practice to control the austenite grain size of microalloyed steels by additions of Al, Nb, Ti and V since they have a strong affinity for N and C, except for Al that is only a nitride former. These elements form nitrides, carbonitrides and carbides which control the austenite grain growth through grain boundary pinning [16,17,22-25]. Grain refinement is the best option in these steels since it leads to a simultaneous improvement in both strength and toughness [37,38]

Additions of Nb, V and Al to titanium-containing steels decreases the austenite grain coarsening temperature due to the increased amounts of dissolved species which control the carbonitride's coarsening rate [22]. *Gao and Baker* [30] showed that the addition of Ti to Al-V-N steels refines the austenite grain size and increases the grain coarsening temperature whereas in the Al-V-N steels a distinct two stage grain growth was observed showing that above a critical temperature these steels undergo accelerated grain coarsening (Figure 2.4).

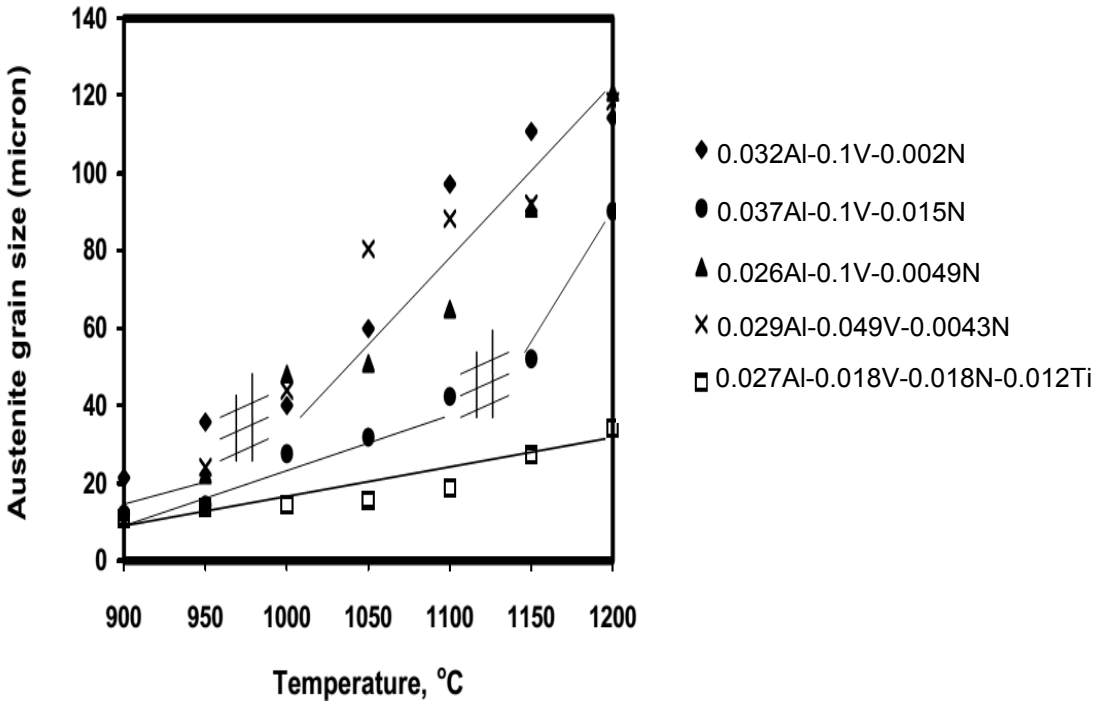

Figure 2.4.: Influence of temperature on austenite grain size on Al-V-N and Al-V-N-Ti steels [30]

Siwecki and Engberg [37] showed that in Ti-V-N HSLA steels, TiN is a better austenite grain growth inhibitor whereas VN alone is not effective (see Figure 2.5), most likely due to the fact that VN tends to form at lower temperatures where grain growth is effectively slowed down in any case.

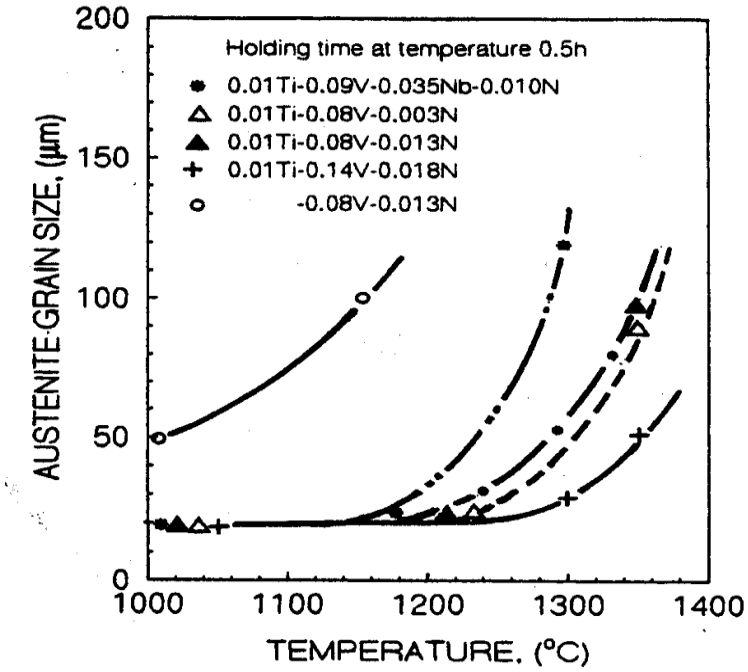

Figure 2.5.: Austenite grain growth in as-cast Ti-V-(Nb)-N steels as a function of temperature [37].

Zhao *et al.* [27] showed that for a medium carbon Nb-steel the austenite grain size increases with time and temperature and that the grain coarsening temperature in this steel is 1100 °C, Figure 2.6. This is in agreement with the work by Cuddy and Raley [32] who showed that the grain coarsening of Nb-containing steel was 1150 °C and for vanadium steel was 1000 °C. Work by Maalekian et al. [39] showed that in a Nb-Ti steel which was soaked at 1150 °C for a minute, abnormal grain growth was observed until it was overshadowed by the precipitation of TiN after soaking for 6 minutes, which lead to normal grain growth thereafter. At this point, the Nb was still in solid solution.

Yu *et al.* [40] found the grain coarsening temperature for a 0.041%C steel with 0.015%Nb, to be 1240 °C but the grain mobility was retarded by solute drag of Nb atoms at grain boundaries and not by precipitates. Grain coarsening temperatures for V-Ti-N steels were found to be in the range of 1200 to 1265 °C by Zajac and co-workers [41]. The coarsening temperature increased with an increase in the N content. The N combined with Ti to form fine and stable TiN particles which were effective in pinning the austenite grains at high temperatures. Alogab et al. [42] showed that additions of Nb to a Ti-stabilised SAE 8620 Ni-Cr-Mo steel inhibited grain coarsening and increased the grain coarsening temperature.

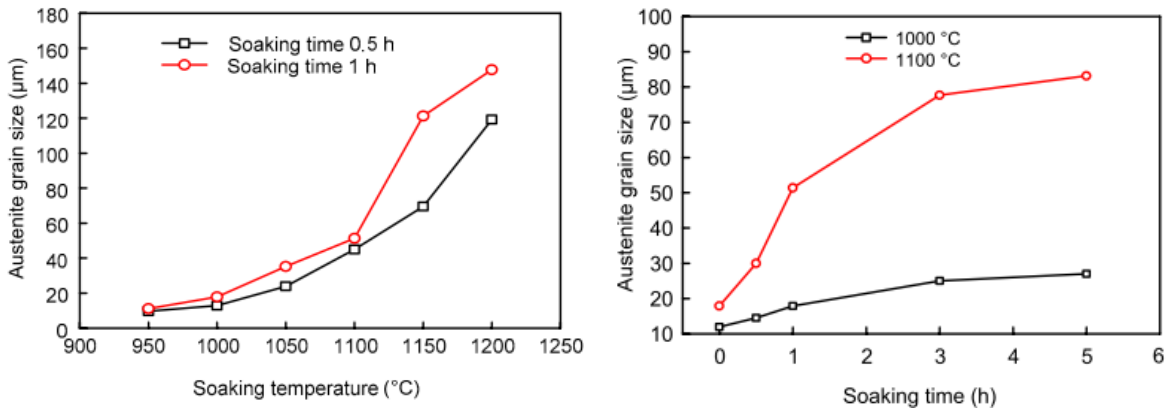

Figure 2.6.: The influence of soaking time and temperature on the austenite grain size of a medium carbon Nb-microalloyed steel [27].

The commercial reheating temperatures for microalloyed steels before hot rolling are between 1150 and 1250 ^{0}C. Davis and Strangwood et al [17,18,2,1] found that reheating between 1150 and 1225 ^{0}C led to a bimodal grain structure whereas reheating at ≥1225 ^{0}C led to a unimodal coarse austenite grain structure which is an indication of complete dissolution of precipitates at and above this temperature.

A study on non-isothermal austenite grain growth in a Nb-Ti-Mo microalloyed X80 linepipe steel by Banejere *et al.* [31] showed that rapid dissolution of Nb-rich particles enables grain growth above the dissolution temperature and that for heating rates greater than 100 ºC/s the austenite grain size is independent of the heating rate and is only a function of the soaking temperature.

Adrian and Pickering [22] showed that in a Nb-Ti-containing steel, at soaking temperatures greater than 1050 ºC the austenite grain size decreases and the grain coarsening temperature increases with increasing (Nb+Ti) content. This is accounted for by the fact that Nb optimizes the TiN's ability to decrease the austenite grain size by producing smaller overall particle sizes since Nb prevents precipitation of carbonitrides during solidification.

The particles that precipitate in the solid state below the solidus temperature during solidification are more effective than those which precipitate above the solidus and these particles should be less than 0.1 µm in diameter to be effective [22]. Nb which is

the most effective grain refiner in hot rolling, segregates strongly to the interdendritic regions along with C and N during solidification and leads to a substantial difference in pinning force between the dendritic and interdendritic regions [17].

The effect of Nb solute elements on the mobility of grain boundaries M(t) in Nb-containing microalloyed steels is given by [43,44]:

$$\mathrm{M(t)} = (\frac{1}{\mathrm{M_{pure}}} + \alpha \mathrm{C_{Nb}})^{-1} \quad (2.14)$$

where C_{Nb} is the concentration of Nb in solution, and constants α and M_{pure}, which is the intrinsic grain boundary mobility, are given by the following equations:

$$\alpha = \frac{\delta N_v (kT)^2}{E_b D} \left(\sinh\left(\frac{E_b}{kT}\right) - \frac{E_b}{kT}\right) \quad (2.15)$$

$$M_{pure} = \frac{1 \delta D_{diff_{gb}} V_m}{10 b^2 RT} \quad (2.16)$$

where δ is the width of the grain boundary, N_v is the number of atoms per unit volume, E_b is the solute boundary binding energy, D_{gb} is the grain boundary self-diffusion coefficient, V_m is the molar volume of austenite and b is the burgers vector. D_{diff} is the average value of the diffusion coefficient in the vicinity of the grain boundary [43,44] and is twice the bulk diffusion coefficient of Nb in austenite [35] and is given by:

$$D_{diff} = 2[8.3 \times 10^{-5} \exp\left(\frac{-266500}{RT}\right)] \quad (2.17)$$

Some authors replace M_{pure} with the grain boundary mobility of plain C-Mn steel, i.e. $M_{C\text{-}Mn}$ which was discussed above in section 2.3 [35].

2.6. Solubility Models For Microalloyed Steels

There are many equations to predict the dissolution temperatures of carbide and nitride precipitates of Nb, Ti, V and Al which are based on different solubility products. Before using them, it should however be noted that these equations are a) designed and

applicable under equilibrium conditions that are most unlikely to exist in industrial hot rolling practice, b) the solubility product can be reformed by the presence of other solutes and c) the solubility product can be changed by the Gibbs-Thomson surface solubility or capillary effect that accounts for the influence of particle curvature on solubility [15]. Table 2.3 shows the solubility products of NbC, NbN, and Nb(C,N) compiled by DeArdo [15]. The methods used to determine these solubility products are also included in Table 2.3 and are as follows [2,15]:

A: thermodynamic calculations;

B: chemical separation and isolation of precipitates;

C: equilibrating a series of steels with different Nb contents within a H_2-CH_4 atmosphere at different temperatures after which the carbon contents were analysed;

D: hardness measurements;

E: statistical treatment of previous solubility products and;

F: atomic absorption spectroscopy.

Table 2.3.: Solubility products for NbC, NbN, and Nb(C,N) systems in austenite [15].

Solubility product	Temperature range (°C)*	Method#	Ref.‡
NbC system			
Log[Nb][C]=2.9-7500/T	900-1200	D	
Log[Nb][C]= 3.04-7290/T	900-1300	B	
Log[Nb][C]= 3.7-9100/T	1000-1300	C	
Log[Nb][C]= 3.42-7900/T	800-1300	B	
Log[Nb][C]= 4.37-9290/T	-	C	
$Log[Nb][C]^{0.87}$= 3.18-7700/T	1000-1300	B	
$Log[Nb][C]^{0.87}$= 3.11-7520/T	-	E	
Log[Nb][C]= 2.96-7510/T	-	E	
$Log[Nb][C]^{0.87}$= 3.4-7200/T	-	A	
Log[Nb][C]= 3.31-7970/T+α		B	
$Log[Nb][C]^{0.87}$= 2.81-7019.5/T	-	A	
Log[Nb][C]= 1.18-4880/T	-	-	
Log[Nb][C]= 3.89-8030/T	-	-	
Log[Nb][C]= 4.04-10230/T	-	C	
Log[Nb][C]= 3.79-10150/T	-	B	
Log[Nb][C]= 3.36-7167/T	-	A	

Solubility product	Temperature range (°C)*	Method[#]	Ref.[ŧ]
Log[Nb][C]= 2.26-6770/T	-		[22]
Log[Nb][C]= 2.06-6700/T	-	-	[45]
NbN system			
Log[Nb][N]= 2.8-8500/T	-	B	
Log[Nb][N]= 3.7-10800/T	-	B	
$Log[Nb][N]^{0.87}$= 2.86-7927/T	-	A	
Log[Nb][N]= 4.2-10000/T	-	-	
Log[Nb][N] =4.04 -10230/T	-	-	[22]
NbCN system			
$Log[Nb][C]^{0.24}[N]^{0.65}$= 4.09-10500/T	900-1300	B	
Log[Nb][C+12/14N]= 3.96-8800/T	-	C	
Log[Nb][C+N]= 1.54-5860/T	900-1200	B	
$Log[Nb][C]^{0.83}[N]^{0.14}$= 4.46-9800/T	950-1225	B	
Log[Nb][C+12/14N]= 2.26-6770/T	900-1300	C	
Log[Nb][CN]=1.33-6670/T	-	-	[31]
Log[Nb][CN]=2.26-6770/T			[32

$\alpha=[Mn](1371/T-0.9)-[Mn]^2(75/T-0.0504)$
*** found from compiled data in the research work by Lechuck [2].**
[#][ŧ] not quoted by DeArdo [15].

The solubility products of TiC and TiN compiled by Lechuck [2] are portrayed in Table 2.4.

Table 2.4.: Solubility products of TiC and TiN systems in austenite [2].

Solubility product	Temperature range (°C)	Method	Ref.[ŧ]
TiN system			
Log[Ti][N]=0.32-8000/T	1150-1430	F	
Log[Ti][N]=5.19-15490/T	1100-1350	C	
Log[Ti][N]=4.94-14400/T	1000-1290	C	
Log[Ti][N]=5.0-14400/T		A	
Log[Ti][N]=3.82-15020/T			[32]
TiC system			
Log[Ti][C]=2.75-7000/T	950-1350	B	
Log[Ti][C]=4.1-9070/T	1000-1200	C	
Log[Ti][C]=5.33-10475/T	900-1300	B	
Log[Ti][C]=3.23-7430/T	-	-	

[ŧ]not quoted by Lechuck [2].

The solubility products of VN and VC are shown in Table 2.5.

Table 2.5.: Solubility products of VN and VC systems in austenite.

Solubility product	Temperature range (°C)	Method	Ref.
VN system			
log [V][N] = 3.02 - 7840/T			[22]
log [V][N] = 3.63 - 8700/T			[32]
log [V][N] = 3.4 - 8330/T			[14]
VC system			
log [V][C] = 6.72 - 9500/T			[22]

As discussed earlier, Al has affinity for nitrogen only, and forms AlN precipitates. The solubility products for AlN are shown in Table 2.6.

Table 2.6.: Solubility products of AlN in austenite.

Solubility product	Ref.
log [Al][N] = 1.03 - 6770/T	[32]
log [Al][N] = 1.55 - 7261/T	[18]
log [Al][N] = 1.80 - 7750/T	[30]

2.7. Solute Drag Effects

The austenite grain size is also controlled by solute drag effects which reduce the grain boundary migration rate (*M*), which is given by [40]:

$$M = \frac{D_{gb}}{RT} \quad (2.18)$$

where D_{gb} is the diffusion coefficient of the grain boundary and is given by:

$$D_{gb} = D_{diff,0}\exp(-\frac{Q_{gb}}{RT}) \quad (2.19)$$

where $D_{diff,0}$ is the diffusion constant for grain boundary diffusion and Q_{gb} is the activation energy of diffusion along grain boundaries.

The concentration of the solute atoms at the grain boundaries (c_g) is given by [40]:

$$c_g = c_{0,bulk}\exp(\frac{E_d}{RT}) \quad (2.20)$$

where $c_{0,bulk}$ is the concentration of the solute atoms in the bulk and E_d is the difference in the elastic distortion energy of neighbouring solute atoms distributed within the grain boundaries.

The austenite grain growth rate (v) is given by [40]:

$$v = f_V F_{net} \quad (2.21)$$

where F_{net} is the net driving force and is given by:

$$F_{net} = \frac{\Delta\beta}{\delta} \quad (2.22)$$

where $\Delta\beta$ is the chemical potential difference across the two sides of the grain boundary and δ is the grain boundary width.

Chapter 3. Thermomechanical Processing Of Microalloyed Steels

3.1. Hot Rolling

Hot rolling is a process of plastically deforming cast slabs, billets, or blooms between working rolls into plates, sheets, rolls, bars or rails. Figure 3.1 shows the hot rolling process of slab, billet and bloom and downstream processing after hot rolling of these cast materials respectively. During hot rolling there are three process steps which include reheating, rolling and cooling. In reheating the metallurgical phenomena taking place are ferrite to austenite transformation, grain growth and dissolution of precipitates in HSLA steels. Rolling consists of work hardening, recovery/recrystallization, austenite grain growth and precipitation. Figure 3.2 shows these phenomena during hot rolling. Cooling includes austenite-to-ferrite transformation and precipitation [3]. The main purpose of hot rolling in steels is to produce a fine grained uniform microstructure resulting from phase transformation [46].

Initial passes during hot rolling known as roughing, are carried out at high temperatures just below slab reheating temperatures and at these high temperatures the deformed austenite may undergo static or metadynamic/dynamic recrystallization [16]. Static recrystallization is recrystallization that takes place after deformation whereas dynamic recrystallization occurs during deformation. Metadynamic recrystallization is known as the growth of the dynamically recrystallized nuclei that occurs after deformation [5]. Figure 3.3 shows a stress-strain curve depicting the characteristic effects that dynamic recrystallization, dynamic recovery and work hardening have on this curve. Dynamic recovery is the annihilation and rearranging of dislocations during deformation with formation of new sub-grains whereas work hardening is the pile up of dislocations due to the dislocations meeting obstacles and other dislocations of the same sign [5]. If no restoration occurs the dislocation pile-up will cause an increase in stress as shown on the work hardening curve in Figure 3.3. If recovery is the only form of restoration the flow stress will reach a plateau in the stress-strain curve and become steady-state [5].

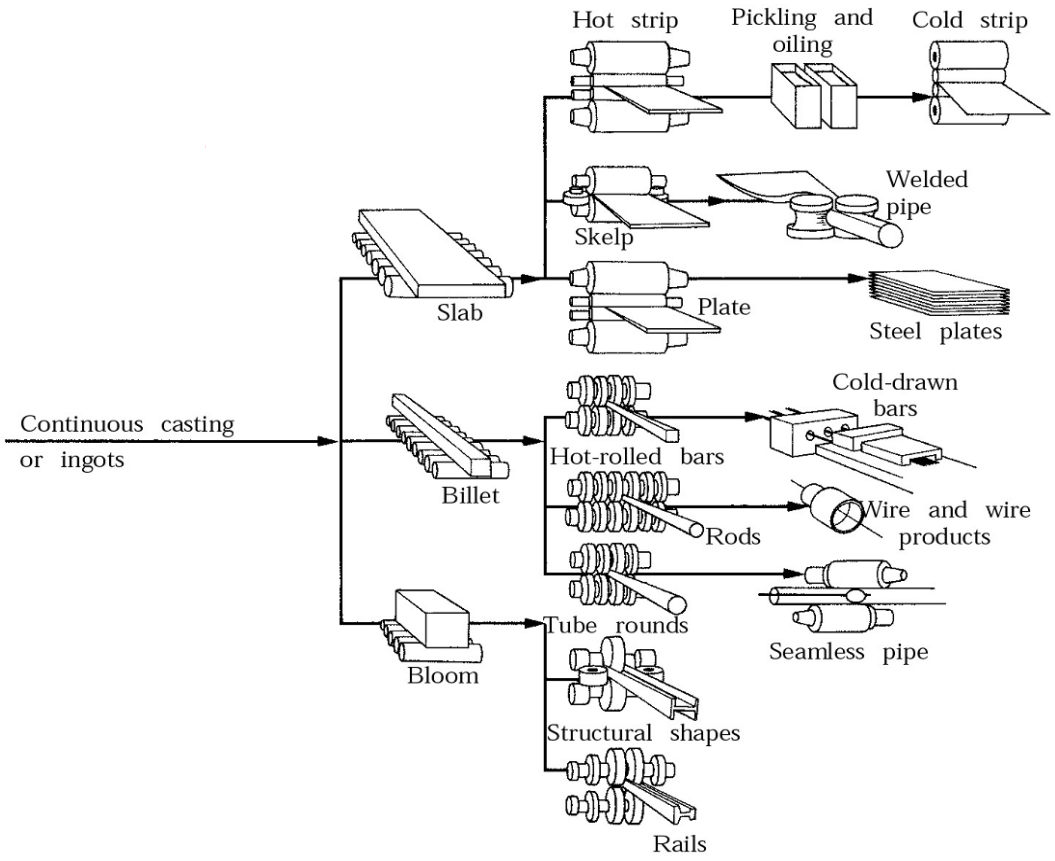

Figure 3.1.: Rolling process of slabs, billets and blooms

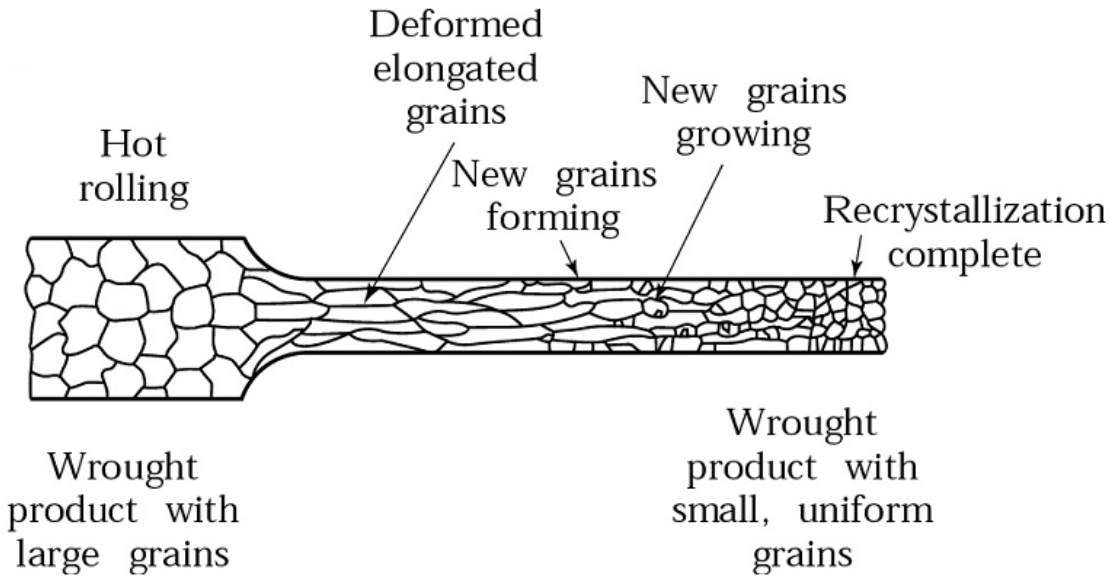

Figure 3.2.: Metallurgical phenomena during hot rolling of metal

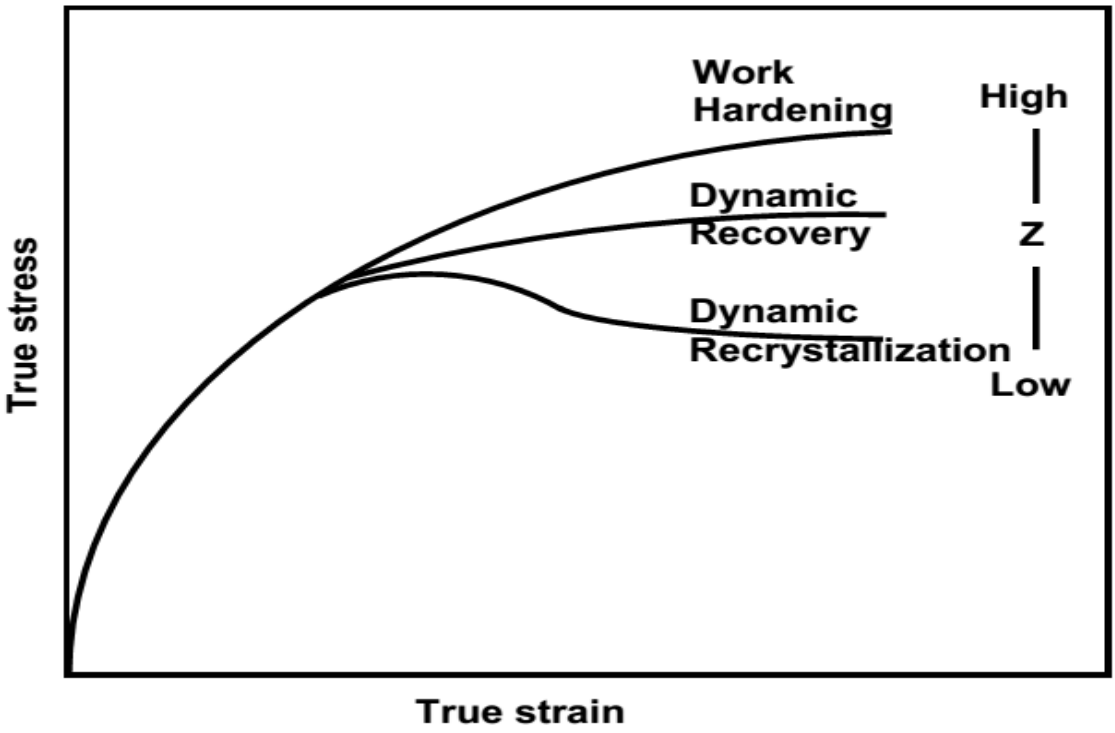

Figure 3.3.: A schematic representation of the characteristic effect of work hardening, dynamic recovery and dynamic recrystallization on the stress-strain curve [5]. Z is the Zener-Hollomon parameter which is a function of strain rate and hot rolling temperature.

3.2. Thermomechanical Processing (TMP)

Thermomechanical processing is designed not only to produce the required external steel shape but often to also to improve the mechanical properties such as strength, fracture toughness and weldability [5,47,48, 49] through grain refinement of austenite [50]. During multi-pass rolling of HSLA steels, the toughness can be impaired through mixed grain formation that occurs in the process [38]. Non-uniform austenite microstructures during hot rolling will lead to a non-uniform ferrite structure and thus normalizing after hot rolling has been employed to achieve a fine ferrite grain size in HSLA linepipe steel production, offshore platform steels and hot rolled plates, but this process adds costs and is generally limited to a minimum grain size of about 10 μm [16]. In microalloyed steels grain refinement is attained by controlling the interaction of recrystallization and precipitation during hot rolling [11]. In thermomechanical

processing, the combination of alloy additions, slab reheating, controlled hot rolling, controlled cooling and quenching technologies may be used to achieve the desired mechanical properties, thus saving energy by minimizing heat treatment after hot working [5, 11]. The success of TMP is largely dependent on the control of the softening and hardening processes, which are static recovery, static recrystallization, dynamic recovery, dynamic recrystallization and metadynamic recrystallization [4]. There are various types of thermo-mechanical processes namely; conventional hot rolling, conventional controlled rolling (also known as low temperature controlled rolling), dynamic recrystallization controlled rolling and recrystallization controlled rolling [5]. Conventional hot rolling is aimed at changing the shape of the work-piece to the required dimensions through multi-pass deformation while the others aim not only to control the shape but also to control the microstructural evolution and are discussed in detail below [11]. Figure 3.4 shows the differences between recrystallization controlled rolling and low temperature controlled rolling:

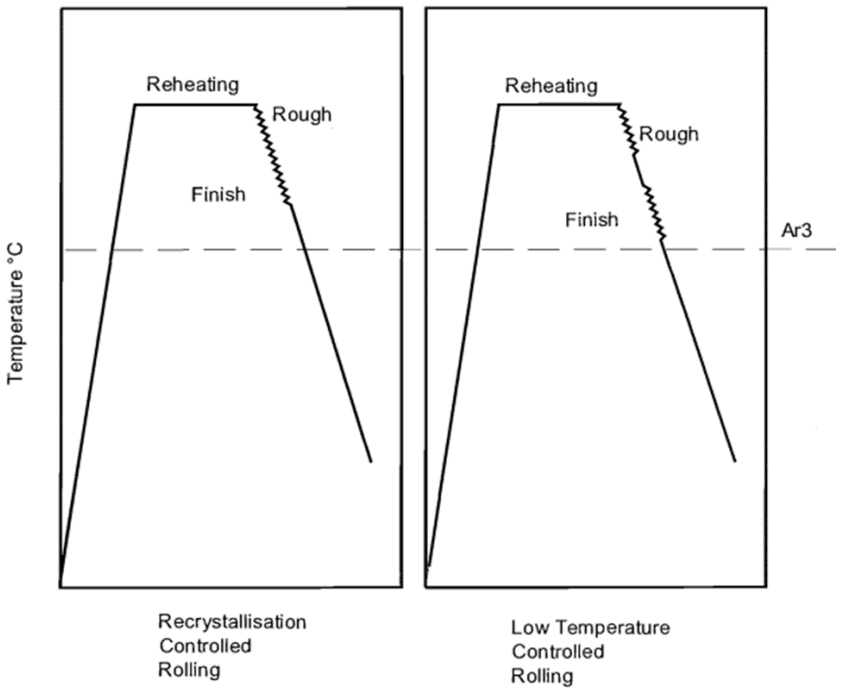

Figure 3.4.: Rolling schedules for different types of thermomechanical processing [16]

3.2.1. Types Of TMP

3.2.1.1. Conventional Controlled Rolling (CCR)

Conventional controlled rolling is a combination of heat treatment and thermo-mechanical processing. The objectives during CCR are grain refinement, precipitation hardening, homogeneous properties and geometry, reduced mill loads and limited roll wear [51]. CCR comprises the control of all four stages of hot rolling namely, reheating, roughing, finishing and cooling [4]. Figure 3.5 is an example of a conventional controlled strip rolling of Nb-containing linepipe steels [16].

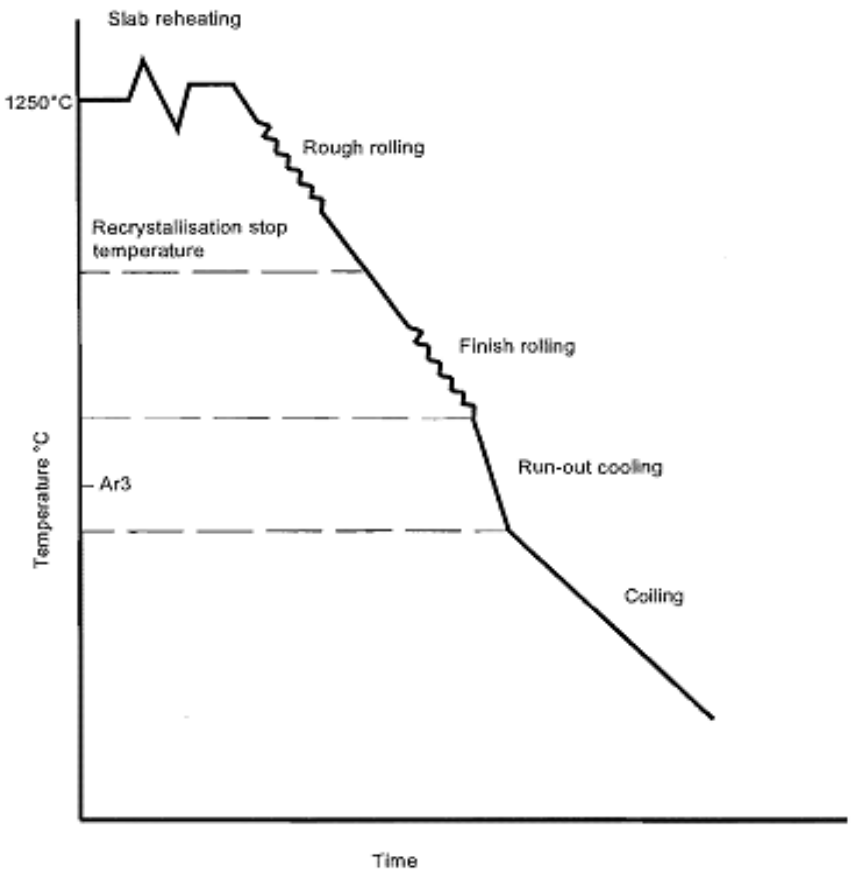

Figure 3.5.: Schematic representation of hot rolled strip process for linepipe steels [16]

In Figure 3.5, the slab reheating temperature is generally about 1250 ºC in order to take most of the microalloys, but particularly the NbC, into solid solution in the austenite. The rough rolling process is completed above the nil-recrystallization temperature (T_{NR}) where dynamic and static recrystallization will cease, to achieve the finest recrystallized austenite grain as possible proceeding to the finish rolling mill, by repeated deformation

and static recrystallization. The cooling rate of the plate between the end of roughing and start of finishing is fast. The finish rolling is commenced below the T_{NR} to achieve thin, elongated, non-recrystallized (pancaked) austenite, which increase the average grain boundary area per unit volume, thus increasing the number of potential nucleation sites, so that fine ferrite grains nucleate on the austenite grain boundaries, induced deformation bands and annealing twins that had been deformed and extended by a heavy rolling reduction [52,47,5,53,51,4,36]. For effective pancaking of the austenite, 50-80% of the reduction in the finishing mill should be below the T_{NR} [47]. The fine ferrite grains formed in this process lead to a combination of good strength and toughness [51,4]. In conventional controlled rolling the occurrence of recrystallization is retarded or prevented by particle pinning resulting from Nb(C,N) precipitation [52]. Figure 3.6 shows the CCR practice and how the austenite microstructure evolves during hot rolling. The advantages of CCR is that, if finishing is undertaken below the T_{nr} in the absence of precipitation, strain accumulation takes place which can lead to softening between passes through metadynamic recrystallization (MDRX) and static recrystallization (SRX) [52]. Fast cooling after finish rolling can lower the austenite-to-ferrite transformation temperature Ar_3, preventing the recrystallization of the austenite, and limiting the extent of carbonitride precipitation in the austenite. This will lead to a more refined ferrite grain size since the ferrite grain growth will be limited due to the suppressed Ar_3 temperature and the copious amount of microalloys available for precipitation in the ferrite phase, which hence produces improved properties [4].

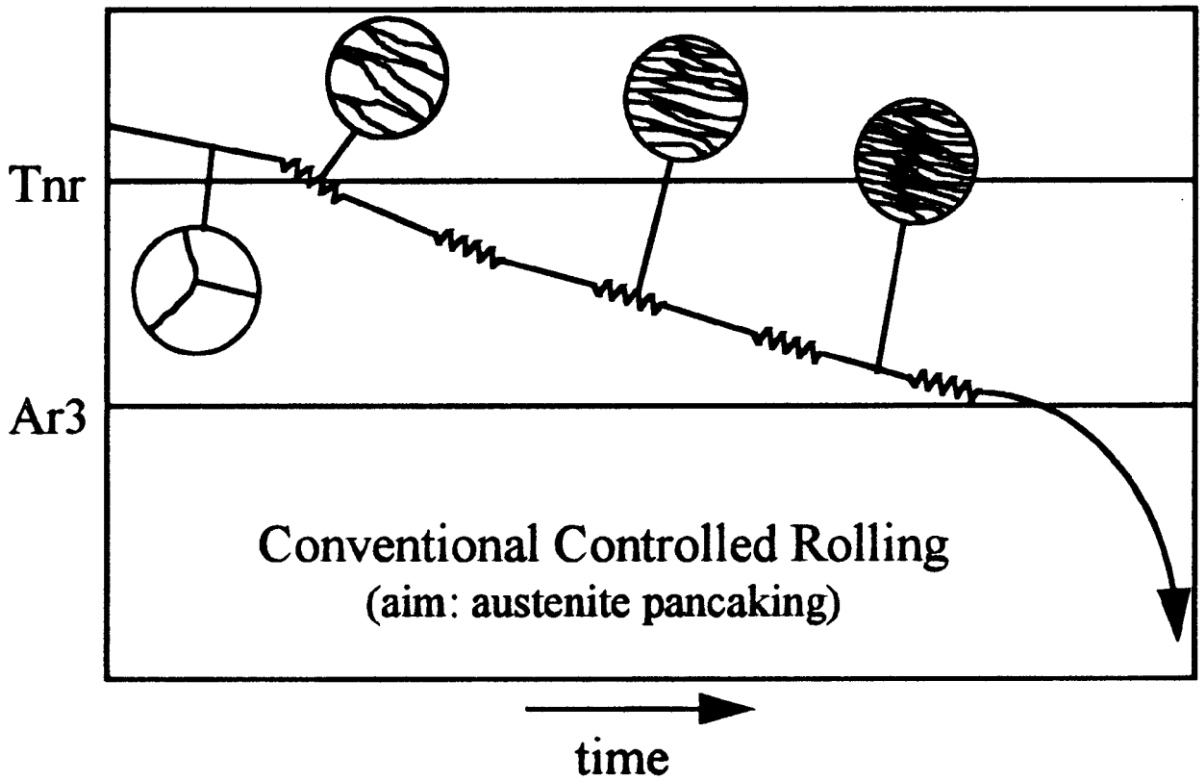

Figure 3.6.: CCR processing and microstructural evolution per pass during finish rolling[52]

Low temperature finish rolling was found to be more effective in niobium containing steels than in plain C-Mn steels [5]. The disadvantage of CCR is that it decreases the production rate due to delays while cooling to the finish rolling entry temperature and requires structurally powerful mills due to high deformation resistance at lower temperatures [41].

3.2.1.2. Recrystallization Controlled Rolling (RCR)

Recrystallization controlled rolling is a process designed for the production of heavy plates and thick-walled seamless tubes which cannot be finish rolled at lower temperatures due to increased roll forces. Thus it leads to a required fine microstructure by controlling the austenite recrystallization such that it occurs even during finish rolling at temperatures ≥ 900 ºC [4]. Owing to the high finish rolling temperatures in RCR, it is attractive for Ti-V-N-microalloyed steels, due to stable TiN precipitates that can hinder grain growth and VN precipitates that can strengthen the ferrite thus eliminating the normalizing step during production of steel plates for

moderate to high toughness specifications [16,54]. RCR followed by accelerated cooling aims to achieve hot rolled steels having high strength and toughness and good weldability. This is achieved by making use of grain refinement by repeated recrystallization of austenite through good manipulation of the design of deformation temperature schedules to retain the fine austenite microstructure during inter-pass and during cooling down to the Ar_3 temperature by suitable dispersion of second phase particles [37].

For a successful RCR process, the following conditions should be met; a) recrystallization must be quick, i.e. take less time and b) grain growth must be inhibited during inter-pass times. Condition a) is achieved by employing V-microalloyed steels to avoid the solute drag effect on hindrance of recrystallization kinetics, and b) by Ti additions to form stable TiN fine particles which can prevent grain growth during the inter-pass times [4,54,41]. For optimum ferrite grain refinement, it is important to maximize the austenite grain boundary area per unit volume at the beginning of the phase transformation to ferrite through low temperature controlled rolling or recrystallized controlled rolling and ensuring that no partial recrystallization takes place during the inter-pass times [37,38]. Figure 3.7 shows various thermomechanical controlled processes, where T_{reh} is the reheating temperature; RST (or T_{NR}) is the recrystallization stop temperature, Ar_3 is the austenite to ferrite transformation end temperature, RS the roughing start temperature, ACC the accelerated cooling, FRT is the finish rolling temperature, and FCT is the finish cooling temperature.

RCR takes place above the temperature of no recrystallization (T_{NR}) [52,53], hence SRX (static recrystallization) is considered to take place in-between rolling passes and aims to achieve full recrystallization, see Figure 3.8 [52]. RCR makes use of grain refinement from static recrystallization of the austenite at temperatures greater than the T_{NR} and to retain the refined microstructure during inter-pass delays and cooling through a dispersion of second phase particles [37].

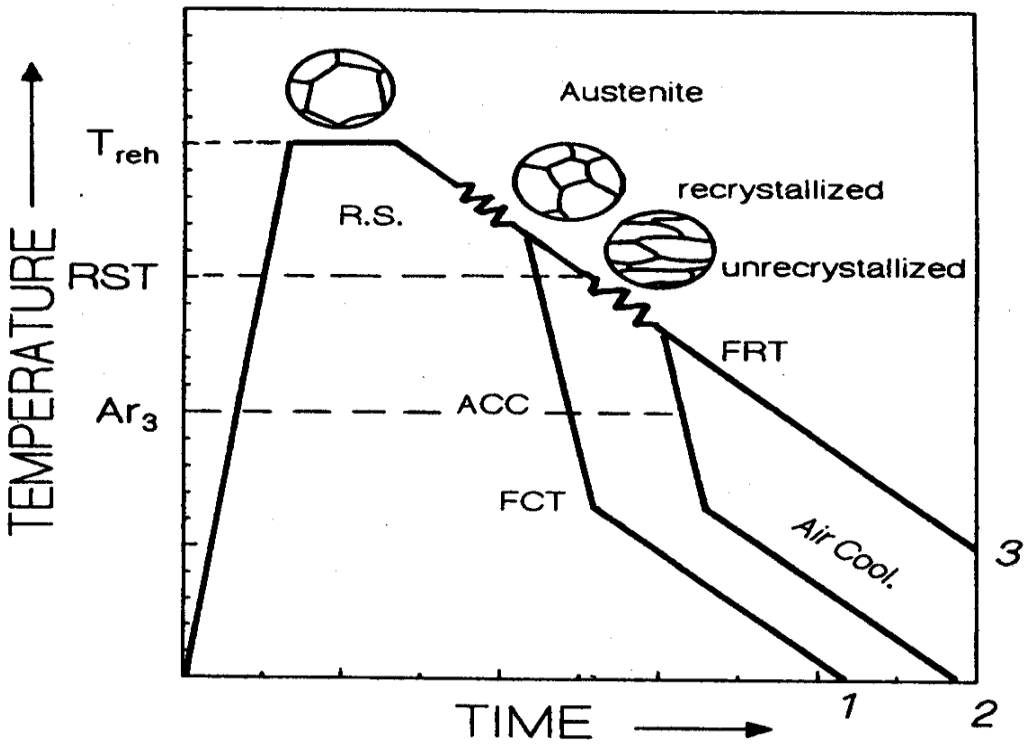

Figure 3.7.: Thermomechanical controlled processes. 1. RCR and accelerated cooling, 2. Controlled rolling and accelerated cooling, 3. RCR or controlled rolling with air cooling [37].

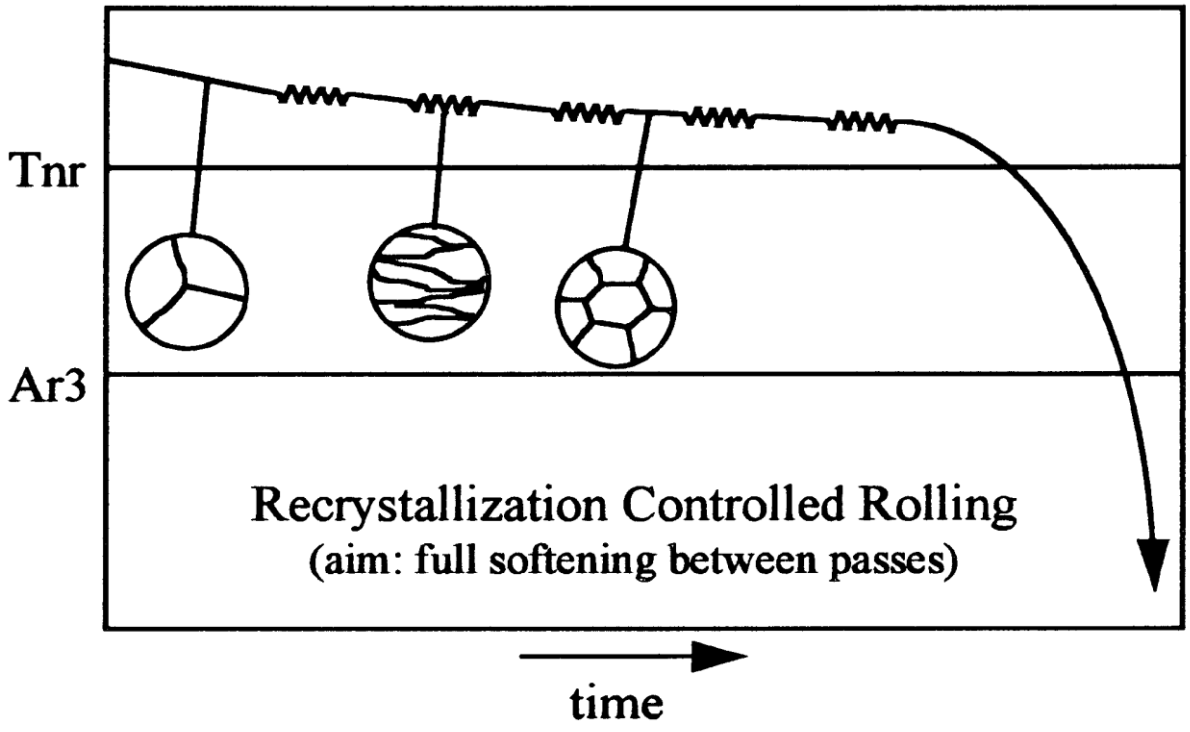

Figure 3.8.: RCR processing and microstructural evolution per pass [53]

3.2.1.3. Dynamic Recrystallization Controlled Rolling (DRCR)

Dynamic recrystallization rolling is adopted more for hot rolling of rod, bar and hot strip where there is insufficient time for static recrystallization and carbonitride precipitation to take place during the inter-pass times [4]. DRCR includes DRX in one or more passes during the rolling schedule by applying large single strains or through strain accumulation or strain induced phase transformation in austenite which helps to achieve intense grain refinement through DRX [52,38,53,4], Figure 3.9. This type of TMP is the most effective process for grain refinement [55] and leads to lower rolling loads [51] than CCR and RCR processes.

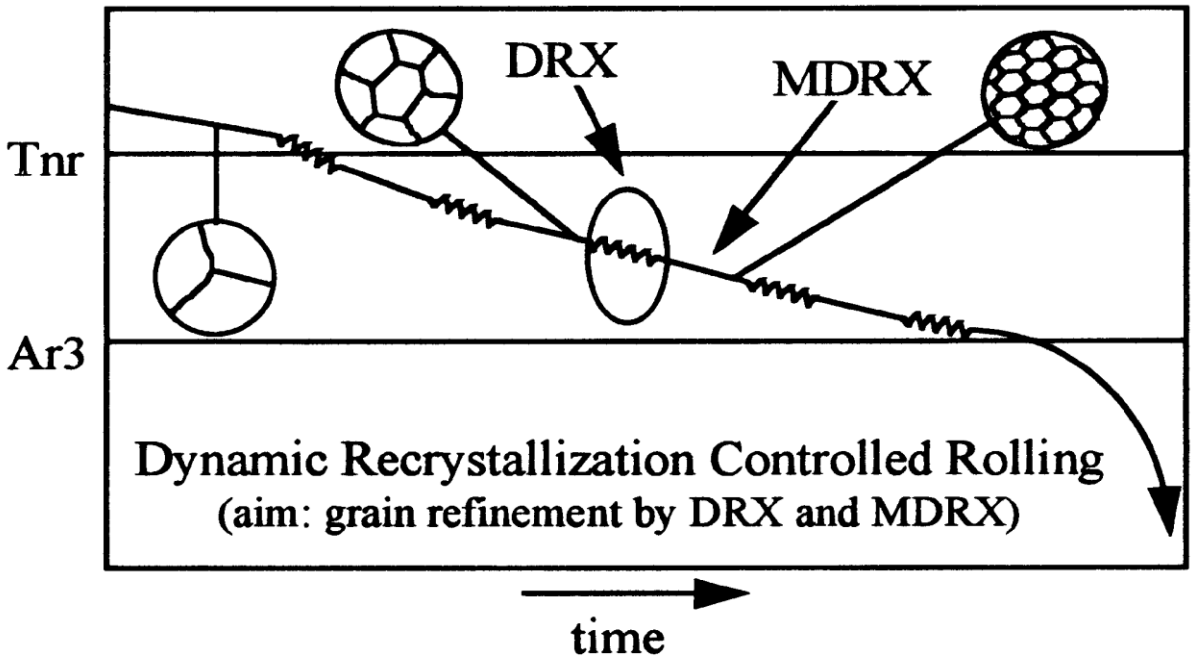

Figure 3.9.: DRCR processing and microstructural evolution per pass [52]

3.2.2. T_{NR} Equations

T_{NR} temperatures that have been modelled allow them to be used online in the plant during hot rolling of microalloyed steels and some of the equations are shown below [55,56]

$$T_{NR} = 849 - 349C + 676\sqrt{Nb} + 337V \quad (3.1)$$

$$T_{NR} = 174\log\left[Nb\left(C + \frac{12}{14}N\right)\right] + 1444 \quad (3.2)$$

$$T_{NR} = 203 - 310C - 149\sqrt{V} + 657\sqrt{Nb} + 683e^{-0.36\varepsilon} \quad (3.3)$$

Total alloy content is used in the above equations except eqn. 3.3 where *N* is the remaining nitrogen content after combining with TiN. Eqn. 3.3 includes the applied strain, ε.

3.3. Mathematical Modelling Of The Hot Rolling Of Metal

Figure 3.10 and Figure 3.11 show the geometry between the work rolls and the plate or strip during rolling and the neutral point geometry where the strip speed is equal to the peripheral speed of the roll. In both Figure 3.10 and Figure 3.11, R' is the flattened roll radius, H and h are the entry and exit plate/strip thicknesses respectively, α is the angle of bite, ϕ_n is the neutral plane angle, V is the tangential velocity of the roll, V_0 and V_e are the entry and exit plate/strip velocity respectively, h_n and V_n are the thickness and velocity of the plate or strip at the neutral point of contact respectively. F is the frictional force responsible for drawing the plate/strip into the roll gap.

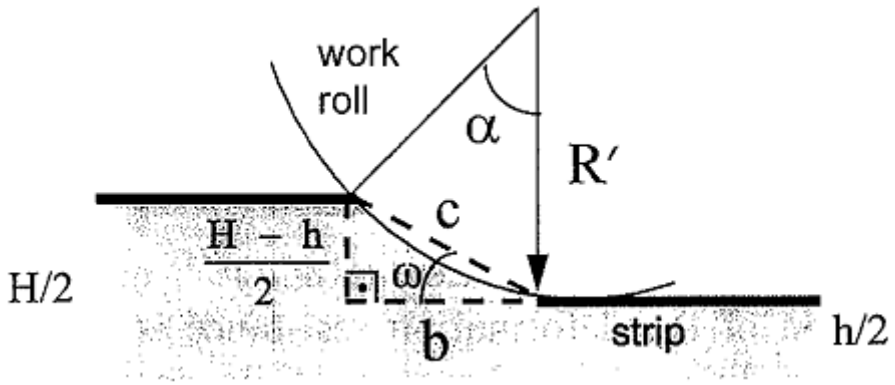

Figure 3.10.: The geometry of work roll and strip contact [64].

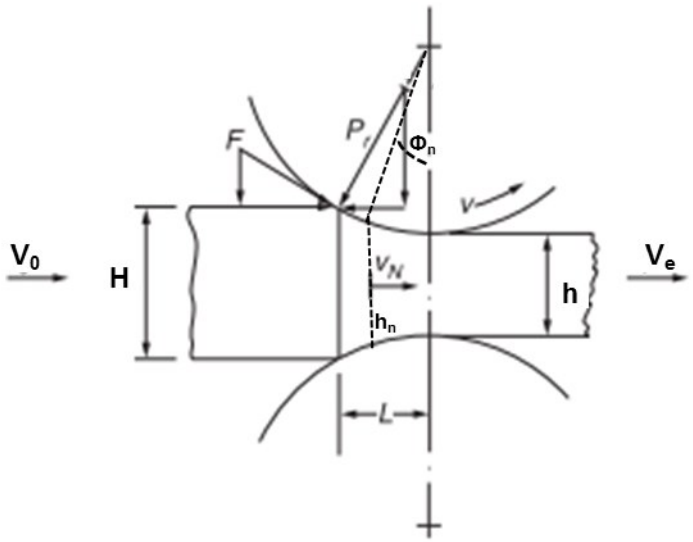

Figure 3.11.: The geometry at the neutral point of contact [109].

Friction is responsible for drawing the work-piece into the roll gap to initiate rolling. This is reached when the horizontal component of the frictional force, *F* is equal to the horizontal component of the radial force P_r. i.e.

$$\frac{F}{P_r} > tan\alpha \quad (3.4)$$

The maximum possible draft in a pass is:

$$\Delta h_{max} = \mu^2 R \quad (3.5)$$

where R is the roll radius and μ is the friction of coefficient given by F/P_r, thus:

$$\mu = tan\alpha \quad (3.6)$$

3.3.1. Flattened Work Roll Radius

The flattened work roll radius is given by the Hitchcock's equation [64,65,66]:

$$R' = R_{roll}(1 + {}^{CP}/_{w\Delta h}) \quad (3.7)$$

where *R* is the nominal roll radius, *Δh* is the reduction (H-h), *P* is the rolling load, *w* is the width of the rolled material and *C* is given by:

$$C = \frac{16(1-\upsilon^2)}{\pi E} \quad (3.8)$$

υ is the Poisson's ratio and E is the Young's modulus for the work roll material.

3.3.2. Redundant Strain

Redundant strain is the additional shear strain to the applied nominal strain on and below the surface of a plate/strip due to friction during hot rolling and is dependent on the geometry of the work-piece and the rolls [109]. The expression of the redundant strain during hot rolling is given by [64]:

$$\varepsilon_r = \frac{H-h}{4\sqrt{4R'^2\sin^2({}^{\alpha}/_{2}) - \frac{(H-h)^2}{4}}} \quad (3.9)$$

α the angle of bite is given by:

$$\alpha = \arccos\left(1 - \frac{H-h}{2R'}\right) \quad (3.10)$$

Stumpf [67] found that ε_r lies between 0.05 and 0.07 in the roughing stage and 0.01 to 0.04 in the finishing stages of a CSP strip hot rolling process and Siciliano et al. [64] found that it falls between 0.07-0.16 times the nominal strain in each pass during strip hot rolling.

3.3.3. Forward Slip Ratio

The linear strip speed is slower than the work roll's tangential velocity, V_r, between the entrance and the neutral axis while after the neutral axis the strip speed is again faster

[64]. The exit strip speed V_e corrected for forward slip which is a function of ϕ_n is given by the expression:

$$V_e = \mathrm{V}[1 + \left(\frac{2R'}{h} cos\phi_n - 1\right)(1 - cos\phi_n)] \quad (3.11)$$

Φ_n is given by:

$$\phi_n = (\frac{h}{R'})^2 \tan[\frac{\pi}{8}(\frac{h}{R'})^{1/2} \ln(1-r) + \frac{1}{2} tan^{-1}\left(\frac{r}{r-1}\right)^{1/2}] \quad (3.12)$$

where $r = \Delta h/H$

3.4. Through-Thickness Inhomogeneity Due To Friction

Friction plays a major role in determining the tool/working roll life, the formability of the work material and the final product properties i.e. surface finish, internal structure and mechanical properties. Excessive friction leads to heat generation wear, pick-up and galling of the tool surface leading to premature failure of the tools. Friction increases the inhomogeneity of deformation. Lubricants are often used to reduce the coefficient of friction during hot working processes but these lubricants are not always effective as they cannot withstand high temperatures [107,110]. Friction is however a necessity for hot rolling process since it is responsible for pulling the work-piece in the roll gap [109]. During conform extrusion and extrusion forging, beneficial effects of friction are favourable to achieve the end product [110]. This section will look into the effects of friction in both hot rolling and axisymmetric compression.

3.4.1. Strip/Plate Hot Rolling

Strain inhomogeneity in the cross section of the cast slab is one of the main features to be controlled during strip/plate rolling. Properties of steel are moulded through the deformation applied per pass which is then inherited in successive passes which lastly determines the mechanical properties of the final product. For this reason it is important that the strain distribution within the slab is known during substantial slab multi-pass rolling [57]. To avoid strain inhomogeneity, a '*critical reduction at a critical thickness*'

approach should be taken [58]. This is an approach whereby an optimized pass reduction is applied at a metallurgical key thickness to condition the austenite to a homogeneous through-thickness grain size which the ferrite will inherit for optimized properties [58].

The equivalent strain of the slab under plane strain conditions is given by the Von Mises equation [57]:

$$\varepsilon_e = \frac{2}{\sqrt{3}}\sqrt{\varepsilon_x^2 + \frac{1}{4}\gamma_{xy}^2} \quad (3.13)$$

where ε_x=-ε_y is the linear tensile and compressive strain along the corresponding axes, and γ_{xy} is the shear strain.

The accumulated equivalent strain is given by the expression below [20]:

$$\varepsilon_\Sigma = \int_0^{t_n} \frac{d\varepsilon_e}{dt} dt \quad (3.14)$$

where t_n is the total time of deformation.

During hot rolling of steel most of the strain is concentrated at the surface and this is because of the additional friction-caused redundant strain which is discussed in section 3.3.2. FEM (Finite Element modelling) by Muntin and Zinyagin [57] showed that most of the strain is sited just under the surface after applying a single 10 % reduction pass while the centre has the least deformation, Figure 3.12.

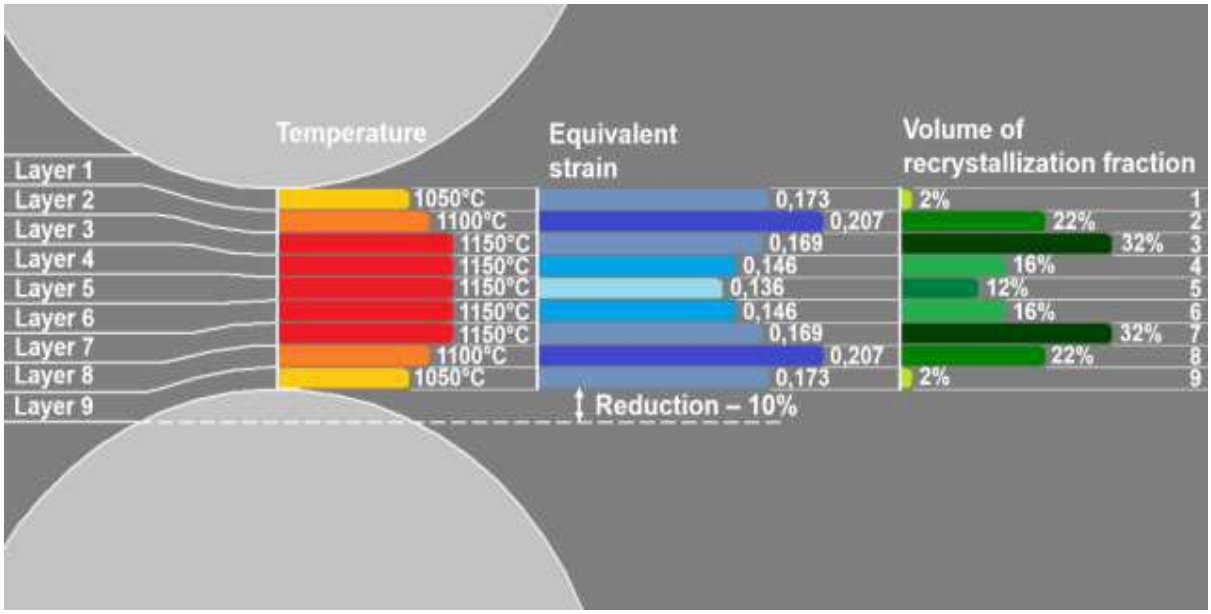

Figure 3.12.: Through-strain distribution on a 300mm thick slab after a FEM simulated 10% reduction at 1150°C [57].

Pereda *et al.* [58] showed that using the concept of *'critical reduction at a critical thickness',* can improve the amount of strain situated at the centre of the slab to promote grain refinement. Two different rolling strategies are compared in Figure 3.13 showing the variation of plastic strain from the surface to the centre of the 45 mm thick plate.

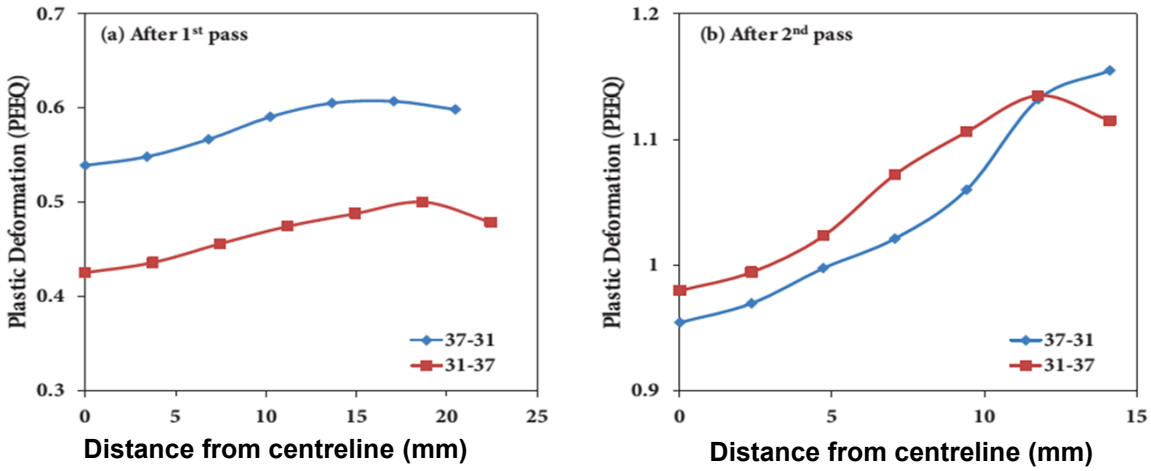

Figure 3.13.: Through-thickness equivalent plastic strain (PEEQ) for two different reduction strategies 37-31 and 31-37. a) After the first rolling pass and b) after the second rolling pass [58].

Through-thickness inhomogeneity causes variations in final properties of the strip or plate and one of them is hardness. The inhomogeneity factor can be measured as the percentage difference between the hardness at the centre and surface of the plate plotted as a function of percentage reductions [109]. Figure 3.14 depicts the influence of lubrication on the inhomogeneity factor as a function of reduction [109].

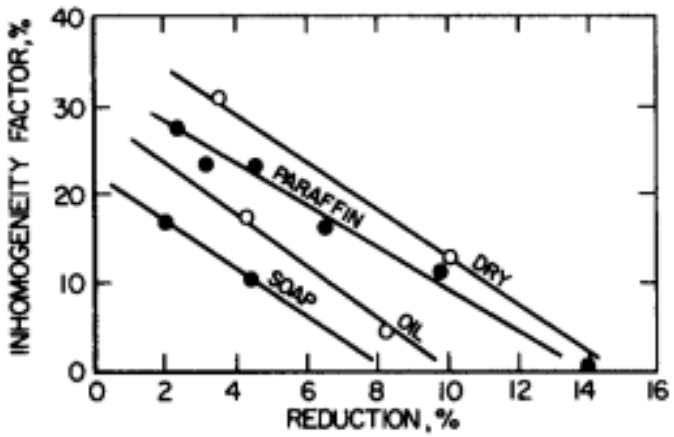

Figure 3.14.: Effect of lubrication on the inhomogeneity of deformation [109]

During hot rolling there is occurrence of a so called friction hill which arises from friction and it is the pressure distribution between the rolls and the section of the contact arc [109]. Figure 3.15 is a schematic representation of the friction hill and its shape during strip hot rolling. The peak of the friction hill occurs at the neutral point and its shape depends on the magnitude of the friction [109].

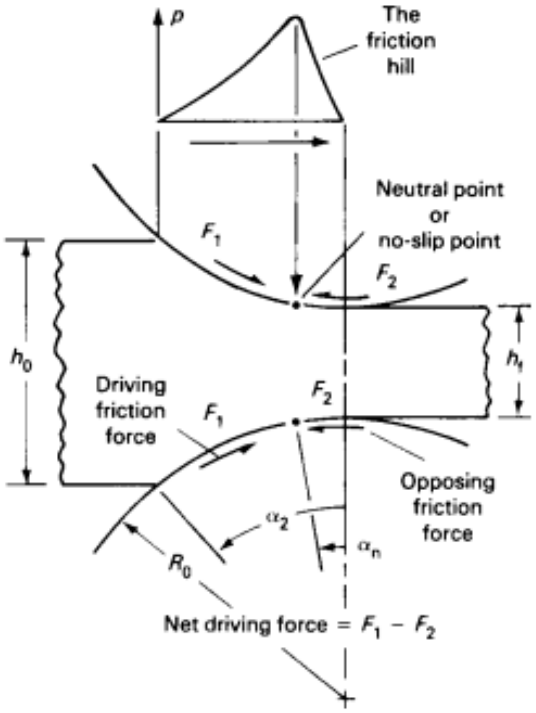

Figure 3.15.: The influence of positive and negative frictional forces on the occurrence of the friction hill during strip hot rolling [109].

As discussed earlier friction affects the tool life, in hot rolling the tool is the work rolls. Typical friction values are between 0.3-0.4 during hot rolling of steel [109]. The wear mechanism on the rolls associated with hot rolling is mainly abrasive and thermal fatigue. Lubrication is used to increase the tool life and for thermal control typical lubrications are water or oil based [109].

3.4.2. Axisymmetric Compression

Plastic strain inhomogeneity is not only prevalent during industrial hot rolling of steel, but also during laboratory simulated hot rolling by compression. During axisymmetric hot compression tests, the friction between the specimen and the platens at their surfaces of contact causes heterogeneous deformation which in turn leads to barrelling of the test specimen [108]. Friction at the faces of contact retards the plastic flow of material on the surface and in its surrounding area whilst a conical wedge of a relatively undeformed material is formed directly below it and the rest of the material suffers high strain-hardening or strain softening depending on the temperature and strain rate and

bulges out in the form of a barrel [108]. Figure 3.16shows the expected deformation zones on an axisymmetric compressed sample.

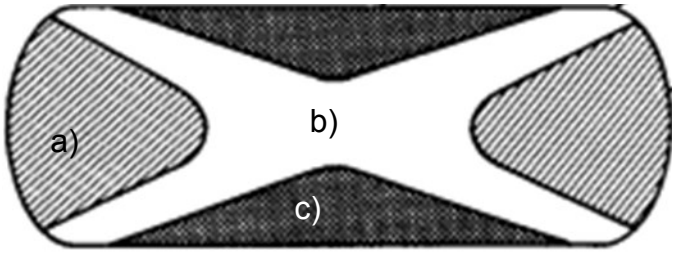

Figure 3.16.: A schematic cross-section of a compressed sample showing different deformation zones a) moderate deformation b) high deformation c) dead zone [109].

Lubrication at the interface between the platen and the cylinder is important in achieving uniform deformation, however just as in high temperature hot working processes this can be difficult. Typical lubricants are graphite sheet, water-base graphite, boron nitride solutions, molybdenum disulphide and low melting glasses [109].

The barrelling factor is given by the following expression [109]

$$b = \frac{d_m^2}{d_0^2} \cdot \frac{H}{h} \quad \text{.....(3.15)}$$

where d_m is the maximum diameter of a cylinder deformed to height h, d_o and H are the initial diameter and height respectively.

Ebrahimi and Najafizadeh [110] modified the barrelling factor to be a function of the difference between the maximum radius R_m and top radius R_t after deformation, ΔR.

$$b = 4\frac{\Delta R}{R_{av}} \cdot \frac{H}{\Delta h} \quad \text{.....(3.16)}$$

where Δh is the height reduction and R_{av} is the average radius and is given by [110]

$$R_{av} = R_0\sqrt{\frac{H}{h}} \quad \text{.....(3.17)}$$

R_0 is the initial radius of the cylinder.

Measuring the top radius of the cylinder after deformation is difficult in practice and can be approximated as follows [110]

$$R_t = \sqrt{3\frac{H}{h}R_0^2 - 2R_m^2} \quad (3.18)$$

If the barrelling factor is less than zero, the effect of the barrelling can be neglected on the analysis of the results.

The average friction factor, *m*, for hot compression testing can be determined by measuring the degree of barrelling as follows [107]

$$m = \frac{\frac{Rav}{h}.b}{\frac{4}{\sqrt{3}} - \frac{2b}{3\sqrt{3}}} \quad (3.19)$$

m lies between 0, which is the conditions for perfect sliding and 1 which illustrates sticking friction conditions.

Common friction models used in bulk metal forming are as follows [111]

1. Coulomb friction model $\tau = \mu p$
2. The constant friction model $\tau = mk_f$
3. The general friction model $\tau = f\theta k_f$

where τ is the friction stress, μ is the Coulomb coefficient of friction, k_f the shear flow stress, *f* is the friction factor expressing the friction in the real contact area ($0 \leq f \leq 1$) and θ is the ratio of the real to the apparent contact area. The friction factor *m* and Coulomb coefficient of friction have the following relationship [109]:

$$m = \sqrt{3}\mu \quad (3.20)$$

Based on this relationship μ lies between 0 (perfect sliding) and 0.58 (sticking friction) during axisymmetric compression.

Other authors [59,60,61,62] have studied the strain distribution on lab simulated axisymmetric compression and plane strain compression and this was done to validate flow stress models derived from lab simulations. Szeliga *et al.* [59] showed that there is a strong inhomogeneity of strains on an axially compressed sample with a 4 mm diameter, Figure 3.17. Localized strains were calculated by FEM after measuring the grain size at various locations at the cross-section of the sample.

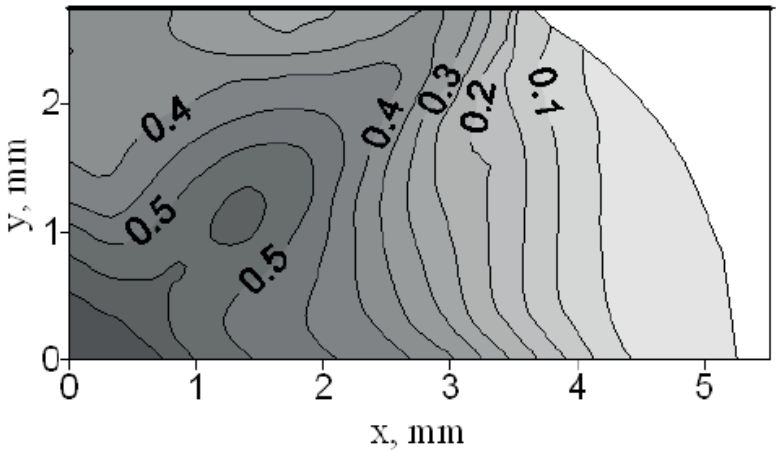

Figure 3.17.: FEM calculated effective strain distribution at the cross section of an axisymmetric compressed sample after subjected with a 4 mm diameter [59].

Lin *et al.* [63] also showed that most of the strain is at the centre of an axisymmetrical sample during hot upsetting of a 42CrMo steel (AISI 4140) and showed the effect of roll-over where the strains are higher on the deformed face edges of the diameter where the sample is in contact with the punches, Figure 3.18.

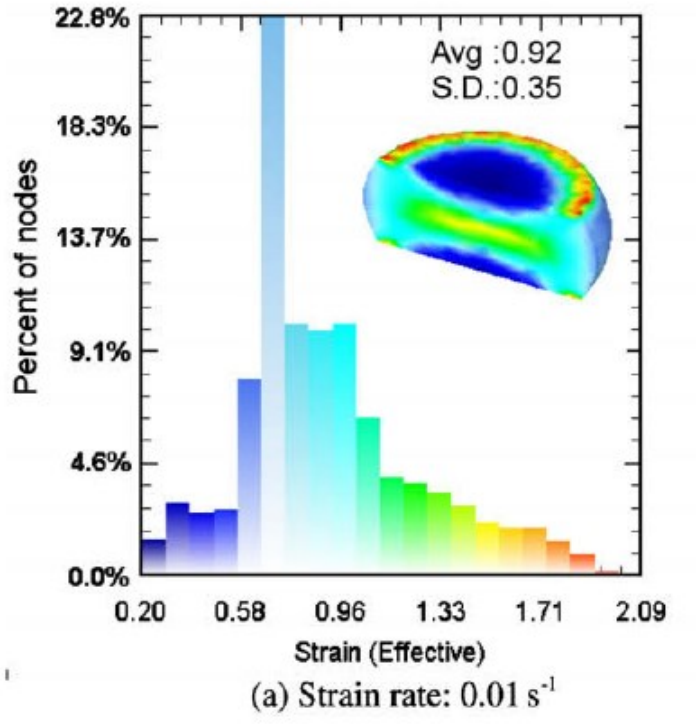

Figure 3.18.: A schematic showing strain distribution on an axisymmetric hot compressed 42CrMo steel AISI 4140 [63]

3.5. Mill Loads During Hot Rolling Of Steel

The rolling load, torque and motor power are important process outputs which are influenced by *inter alia* the shape and size of the roll gap [65]. The rolling load is given by the Sims equation:

$$P = MFS'Qw\sqrt{R'\Delta h} \quad \text{.....(3.21)}$$

where *MFS'* is the plane strain mean flow stress, $\sqrt{R'\Delta h}$ is the projected arc of contact and *Q* is the load multiplication factor which is a function of the flattened roll radius R′, the final thickness of the rolled material h and reduction per pass ∆h [65-66]. The expression for *Q* is given by [67]:

$$Q = (\frac{1}{2})(\frac{1-r}{r})^{1/2}(K_3 - K_4) - \pi/4 \quad \text{.....(3.22)}$$

where

$K_3 = 2\pi K2$

$$K_2 = \frac{1}{2}\tan^{-1}\left(\frac{r}{1-r}\right)^{1/2}$$

$$K_4 = \left(\frac{R'}{h}\right)^{1/2}\ln\left[\left(\frac{Y}{h}\right)^2(1-r)\right]$$

$$Y = 2R'(1-cos\phi)+h$$

$$\phi = \left(\frac{h}{R'}\right)^{1/2}\tan(K_1+K_2)$$

$$K_1 = \frac{\pi}{8}\left(\frac{h}{R'}\right)^{1/2}\ln(1-r)$$

For lab simulated hot rolling, the mean flow stress (MFS) of a material is determined by the area under the stress-strain curve and dividing by the pass strain range and is expressed as [47,68,65,66]:

$$MFS = \frac{1}{\varepsilon_2-\varepsilon_1}\int_{\varepsilon_1}^{\varepsilon_2}\sigma d\varepsilon = \frac{1}{\varepsilon_2-\varepsilon_1}\sum_{\varepsilon_1}^{\varepsilon_2}\sigma_{ave}\,\Delta\varepsilon \quad \text{.....(3.23)}$$

The mean flow stress is multiplied by $2/\sqrt{3}$ to convert to von Mises plane strain conditions for flat rolling [66].

$$MFS' = \frac{2}{\sqrt{3}}MFS \quad \text{.....(3.24)}$$

MFS models are employed to predict the rolling loads during hot rolling. These models take into account the chemistry and the rolling parameters. Misaka's equation [52,64] is the model used to predict MFS in (kgf/mm^2) for plain C-Mn steel during hot strip rolling and needs to be multiplied by a factor of 9.81 to convert to MPa, T is in Kelvin and C is the total alloy content in mass %:

$$MFS_{Misaka} = \exp\left(0.126-1.75C+0.594C^2+\frac{2851+2968C-1120C^2}{T}\right)\varepsilon^{0.21}\dot{\varepsilon}^{0.13} \quad \text{...(3.25)}$$

Siciliano *et al.* [64] modified the original Misaka equation to correct for the Mn strengthening effect and has the form:

$$MFS_{Siciliano} = MFS_{Misaka}\,(0.78 + 0.137Mn) \quad \text{.....(3.26)}$$

The Misaka equation was then modified to incorporate the strengthening mechanisms of Nb, Mn and Ti by Miniami *et al.* [68]:

$$MFS_{Miniami} = MFS_{Misaka}(0.768\ + 0.51Nb + 0.137Mn + 4.217Ti) \quad \text{.....(3.27)}$$

Siciliano *et al.* [69] modified the original Misaka equation to incorporate the effects of Mn and Nb in the exponential term as the C in the Misaka's equation and not as a multiplying factor for a 0.06%C-Nb steel produced via the CSP (Compact Strip Processing) route.

$$MFS_{Siciliano\&Leduc} = 9.81\exp\left(\frac{2704+3345Nb+220Mn}{T}\right)\varepsilon^{0.21}\dot{\varepsilon}^{0.13} \quad \text{.....(3.28)}$$

The above equation shadowed the one derived by Siciliano and Bruna [69,70] who also incorporated the Nb, Mn and Mo contents in the exponential term as shown:

$$MFS_{Siciliano\&Bruna} = 9.81\exp\left(\frac{3126+68C+2117Nb+54Mn+152Mo}{T}\right) \quad \text{.....(3.29)}$$

Other modified MFS models having the same expression of incorporating different alloy contents as a multiplication factor are shown below [69]:

$$MFS_{Poliak} = \sigma_m(1.09 + 0.056Mn + 4.54Nb + 1.21Ti\ + 0.056Al + 0.1Mo) \quad \text{.....(3.30)}$$

$$MFS_{Misaka\ et\ al.} = \sigma_m(0.916 + 0.137Mn + 0.389V + 0.191Mo + 0.004Ni) \quad \text{.....(3.31)}$$

$$MFS_{Kirihata} = \sigma_m\,(0.835 + 0.098Mn + 0.51Nb + 0.175V + 0.144Mo + 0.01Ni + 0.128Cr) \quad \text{.....(3.32)}$$

$$MFS_{kang} = \sigma_m(0.68 + 0.161Mn + 2.74Nb + 4.03Ti + 0.86V + 0.29Mo + 0.128Cr) \quad \text{.....(3.33)}$$

$$MFS_{Bruna} = \sigma_m(1.02 + 0.097Mn + 2.13Nb + 0.53V + 1.01Ti + 0.3Cu) \quad \text{.....(3.34)}$$

where σ_m is the MFS of Misaka's original equation.

3.6. Microstructural Evolution During Hot Rolling

As discussed in section 3.1, during hot rolling the metallurgical phenomena taking place are recovery (static and dynamic), recrystallization (SRX and DRX/MDRX), grain growth and precipitation. In this section these phenomena and how they affect the microstructural evolution during hot rolling of microalloyed steels will be discussed in more detail. During hot rolling most of the energy put into the steel turns to heat whilst only about ~3-5% is converted to stored energy [109]. The stored energy is increased by accumulation of dislocations due to tangling of existing and forming of new dislocations. This stored energy is the driving force for recovery and recrystallization [5]. Recovery and recrystallization are important in the design of pass schedules for controlled rolling since they have a significant effect on the final microstructure and properties of the hot rolled steel [59,71].

3.6.1. Dislocation Recovery

3.6.1.1. Static Recovery (SRV)

After plastic deformation the stored energy in the deformed material is released by the annihilation and rearrangement of dislocations and this type of recovery precedes static recrystallization in steels [4,5]. It involves dislocation climb and cross-slip and movement of vacancies but no movement of high angle grain boundaries occur [46,4,20] .When a strain of less than 10% is applied, only recovery will occur with no recrystallization taking place [72] according to the classical nucleation theory but it is known that recrystallization is favoured at low strains through the strain induced boundary migration (SIBM) phenomenon [112] which will be discussed later. The recovery rate is influenced by temperature, strain, strain rate and the presence of the alloying elements. An increase in the former two leads to an increase in the recovery rate due to enhanced thermal activation and more stored energy that arises from an increased dislocation density [4]. Recovery decreases the driving force for recrystallization [43]. There is an interaction between recovery and precipitation and may occur in three different ways; a) recovery may delay the onset of precipitation by decreasing the amount of nucleation sites, b) recovery may be retarded by the presence of fine precipitates that pin segments of the dislocation network, c) the amount of solute

content of microalloys can retard the progress of recovery by solute drag effects on dislocation mobility [43].

Recovery consists of formation of cells, annihilation of dislocations within cells by moving to the cell walls, formation of low-angle sub-grains and sub-grain growth [5] as shown in Figure 3.19.

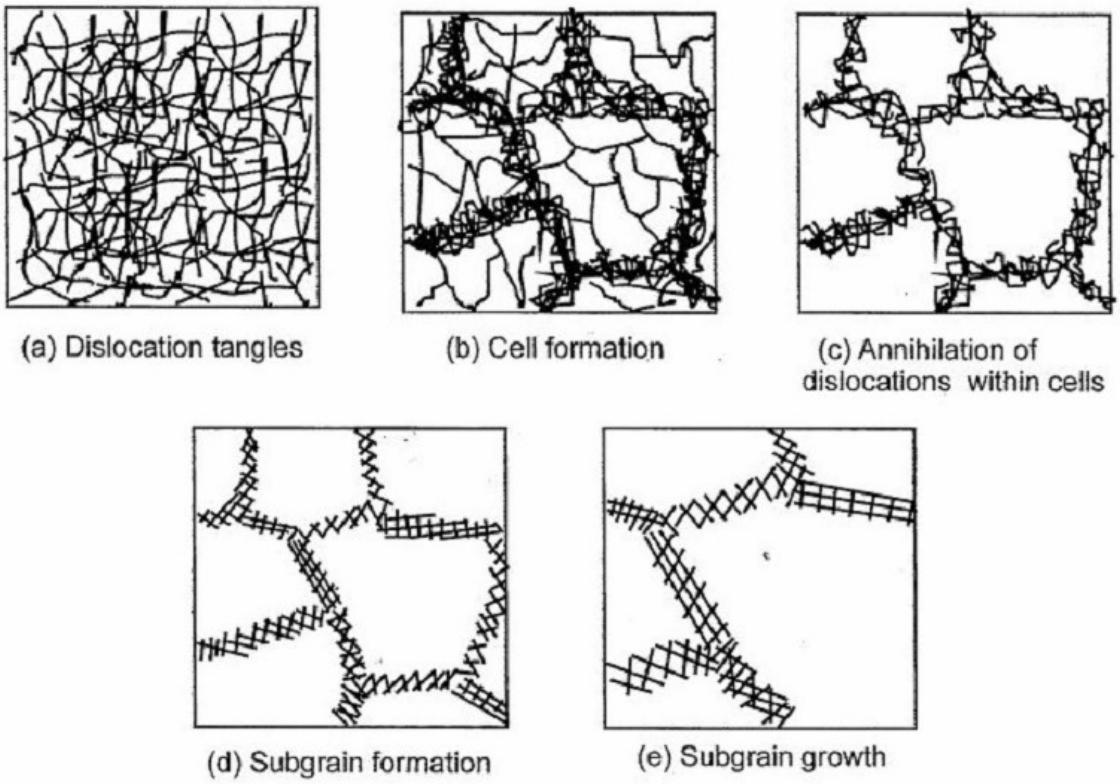

Figure 3.19.: Steps that occur during recovery [5].

Sub-grains formed during recovery act as nucleation sites for recrystallization during the recrystallization process [5] but with the SIBM mechanism high angle grain boundaries act as starting sites for recrystallization [112].

The flow stress during deformation is a function of dislocation density ρ and is given by:

$$\sigma = \sigma_0 + M\varphi\vec{b}\sqrt{\rho} \quad \text{.....(3.35)}$$

σ_0 is the flow strength of a well annealed metal, M is the Taylor factor which is an orientation function of the particular grain being deformed, φ is the proportionality constant (~0.5), β is the shear modulus and $\vec{b}$ is the burgers vector [5]

3.6.1.2. Dynamic Recovery (DRV)

Similar to SRV, dynamic recovery precedes dynamic recrystallization and takes place during plastic deformation unlike the former that occurs after deformation. During the early stages of deformation, the dislocation density increases with increasing strain (work hardening) and this leads to rearrangement and annihilation of dislocations (DRV). When the rate of work hardening and the rate of DRV is equal, a steady state regime is reached. The stress-strain curve is thereafter characterised by a steady stress and this is known as a DRV curve (see section 3.1). Dynamic recrystallization (DRX) only occurs when the dislocation density reaches a critical value [4].

3.6.2. Recrystallization By The Classical Nucleation Theory

Recrystallization is a process whereby formation of strain-free grains occurs at an expense of former deformed grains by the formation and migration of high angle grain boundaries which are driven by the stored energy of deformation, leaving a new structure with low dislocation density [5,43]. The driving force for recrystallization, ΔG_{rex} which is given by the stored energy per unit volume, is given by [37,43]:

$$\Delta G(t) = \frac{1}{2}\rho\beta\vec{b}^2 \quad \text{.....(3.36)}$$

where ρ is the dislocation density, β is the shear modulus of the matrix and $\vec{b}$ is the Burgers vector. The dislocation density increases with increasing applied strain and the critical radius for recrystallization decreases, thus decreasing the incubation time for static recrystallization nucleation [35].

The recrystallization process consists of nucleation of new grains and growth of these grains. Nucleation involves the formation of a small volume of relatively perfect material which is at least partly bounded by a high angle grain boundary within the deformed

material. This small volume of material must be of a critical size to be able to grow into the deformed material so that it acts as a viable nucleus [113]. The growth stage involves movement of the high angle grain boundary into the deformed or recovered material. The growth rate is dependent on the boundary mobility and the driving force [113].

For recrystallization to occur a critical sub-grain size needs to be reached such that this sub-grain can grow and not shrink and the misorientation should be high enough (High angle grain boundaries). This critical sub-grain size is larger than the mean sub-grain size suggesting that abnormal growth should occur to reach this size. Grain boundaries are the preferred nucleation sites for recrystallization but when the grains are large intragranular nucleation occurs [23]. When the grains are fine, the high grain boundary area per unit volume will increase the nucleation rate on the grain boundaries [72].

Figure 3.20 depicts the development of recrystallizing grains. As deformation takes place nucleation sites for recrystallization are increased since the recrystallized grain size is reduced and introduces smaller sub-grains. However this phenomenon is minimized with increasing strains and there is a critical strain where this is completely inhibited [5].

The recrystallized grain size is a strong function of temperature and thus at lower temperatures it is fine and the grain growth rate is slow, this promotes more nucleation for recrystallization which in turn leads to a finer recrystallized grain size. Increasing the strain rate will increase the driving force for recrystallization and the recrystallization kinetics will be faster. This is due to less time available for dynamic recovery and the decrease in the sub-grain size which lead to an increase in the stored energy [72].

Nucleation and growth of recrystallized grains show a sigmoidal shape of a recrystallized volume fraction versus log time as shown in Figure 3.21. The dependence of recrystallization fraction on time can be modelled using the Johnson-Mehl-Avrami-Kolmogorov (JMAK) equation [16,46]:

$$X = 1 - \exp(kt^n) \quad \text{.....(3.37)}$$

where n is the Avrami constant and is a material parameter whereas k is dependent on other parameters such as temperature, prior strain and grain size [16].

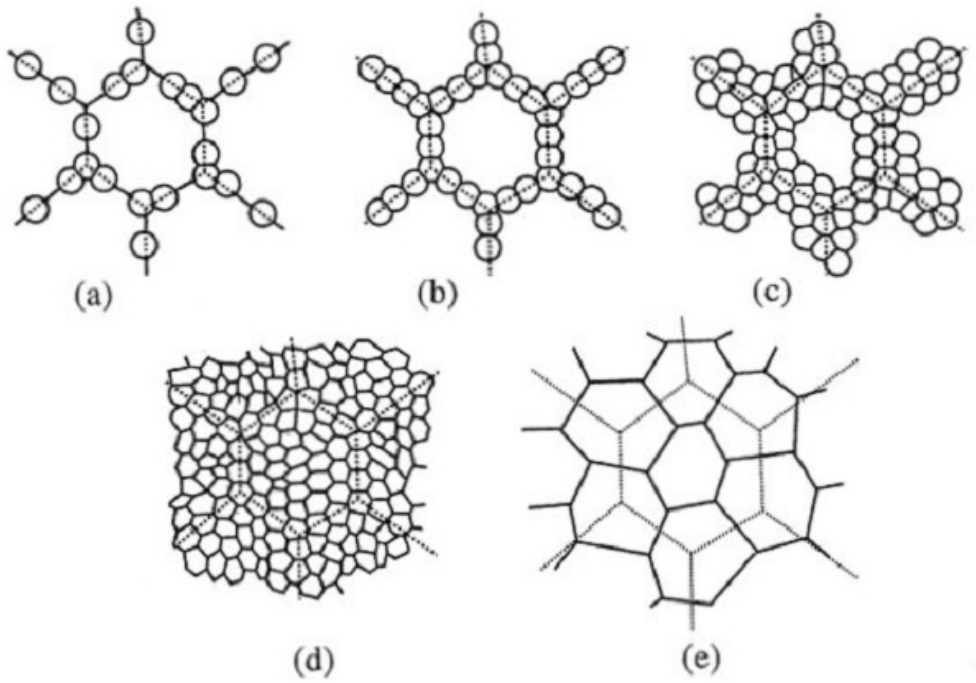

Figure 3.20.: Schematic illustration of the development of recrystallizing grains [5].

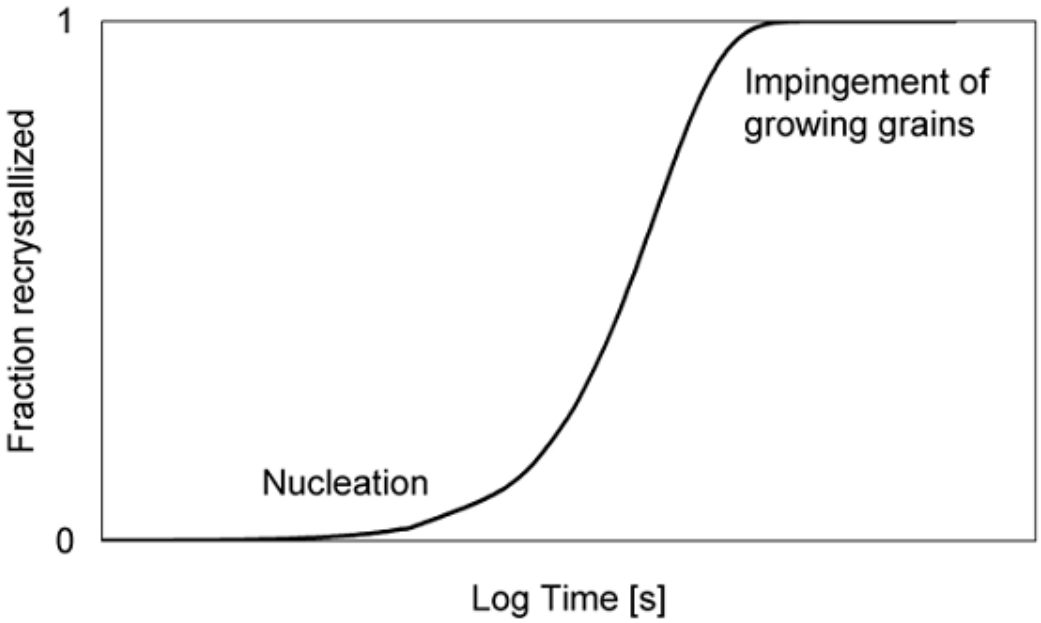

Figure 3.21.: Schematic diagram of isothermal recrystallized volume fraction versus log time curve [5]

There are three types of recrystallization that may occur during high temperature deformation namely static recrystallization (SRX), dynamic recrystallization (DRX), and meta-dynamic recrystallization (MDRX). Figure 3.22 shows the dependence of static and metadynamic softening mechanisms on the applied strain [27].

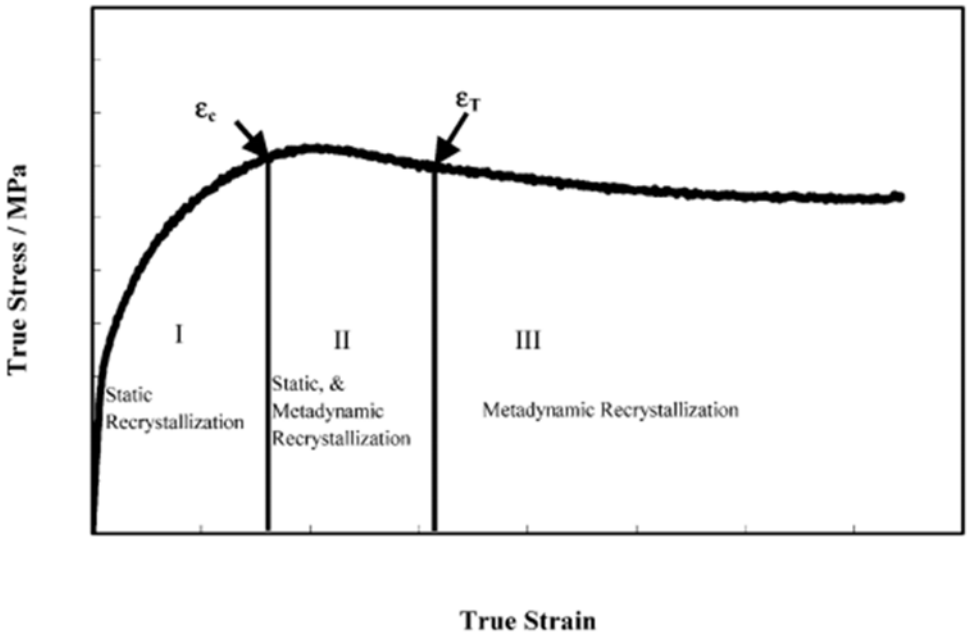

Figure 3.22.: The effect of applied strain on the softening mechanisms during inter-pass intervals [27].

When $\varepsilon<\varepsilon_c$ (critical strain for initiation of DRX), softening in the inter-pass time is due to static recrystallization (SRX), which is discussed in detail in *section 3.6.2.1*. If hot working takes place at $\varepsilon>\varepsilon_T$ (transition strain) only metadynamic recrystallization (MDRX) takes place in the inter-pass time (*section 3.6.2.2*). If hot working occurs at $\varepsilon_c<\varepsilon<\varepsilon_T$ both static and metadynamic recrystallization occur in the inter-pass times [72,73] :

3.6.2.1. Static Recrystallization (SRX) ($\varepsilon<\varepsilon_c$)

SRX is a type of recrystallization that takes place during inter-pass times between deformation passes. SRX occurs below a critical strain ε_c needed for initiation of DRX and requires an incubation time during which the nuclei form [5]. Mostly SRV leads to 25% softening and SRX to about 75% and thus the latter is a significant softening mechanism in hot rolling [4].

The equation for the fraction static recrystallized (X_{SRX}) is expressed as follows:

$$X_{SRX} = 1 - \exp[-0.693(t/t_{0.5}^{SRX})^n] \quad (3.38)$$

where t is the inter-pass time, and $t_{0.5}^{SRX}$ is the time for 50% static recrystallization which is a function of applied strain (ε), strain rate ($\dot{\varepsilon}$) and the initial austenite grain size ($D_{gs,0}$) and is given by [3,46]:

$$t_{0.5}^{SRX} = A D_{gs,0}{}^{p} \varepsilon^{q} \dot{\varepsilon}^{r} \exp\left(\frac{Q_{SRX}}{RT}\right) \quad (3.39)$$

where Q_{SRX} is the driving force for static recrystallization, R the gas constant (8.314J/mol.K) and T the deformation temperature in Kelvin. Constants p, q, r, are considered to be material constants. The rate of static recrystallization is increased by higher temperatures, higher strains, lower strain rates and smaller austenite grain sizes [4].

The static recrystallized grain size (D_{SRX}) during deformation is a strong function of the applied strain and the initial austenite grain size while the deformation temperature has little influence [16]:

$$D_{SRX} = \delta D_{gs,0}{}^{s} \varepsilon^{u} \exp\left(\frac{-Q_{gx}}{RT}\right) \quad (3.40)$$

Some expressions of D_{SRX} have the form that excludes the Arrhenius term ($exp(-Q/RT)$) and are simply given as [52]:

$$D_{SRX} = \delta d D_{gs,0}{}^{s} \varepsilon^{u} \quad (3.41)$$

Siwecki [54] derived the D_{SRX} for Ti-V-Nb-N as follows:

$$D_{SRX} = 1.25 + 24.4\,(V + Nb)^{-0.2} N^{-0.04} D_{gs,0}^{0.25} \left[\exp\left(\frac{350000}{RT}\right)\right]^{-0.07} \quad (3.42)$$

The constants are summarized in Appendix A, Table 11.1, in terms of chemistry and processing parameters.

3.6.2.2. Dynamic Recrystallization (DRX) ($\varepsilon > \varepsilon_T$)

Dynamic recrystallization (DRX) is a softening mechanism that takes place during the actual deformation and a critical strain ε_c must be reached for this mechanism to occur. It can be initiated by a single pass or by strain accumulation from one pass to the other [4,72,78]. The preferred nucleation sites for dynamic recrystallization are grain boundaries with high dislocation density and deformation bands within the grains and subgrains [4]. The DRX occurring at the austenite grain boundaries is propagated into the grain interiors by a necklacing phenomenon, which progresses with continuing deformation until the deformed austenite is entirely replaced by a fine grain size [4].

When dynamic recrystallization occurs, the flow stress of a stress strain curve lowers to a steady-state stress after reaching a peak stress as shown in Figure 3.3 above [5]. Softening that occurs after DRX does not provide complete softening of the material since there are already new lightly deformed portions in the dynamically recrystallized structure.

The ratio of the critical strain (ε_c) to the peak strain (ε_p) during dynamic recrystallization lies in the range of 0.67-0.86 [52]. Sellars [75,76] approximated ε_c for C-Mn steels as 80% of the peak strain, ε_p which is expressed as:

$$\varepsilon_p = 6.97 \times 10^{-4} {D_{gs,0}}^{0.3} Z^{0.17} \quad (3.43)$$

Multiplying this expression by 0.8 results in an expression for ε_c as follows [64]:

$$\varepsilon_c = 5.6 \times 10^{-4} {D_{gs,0}}^{0.3} Z^{0.17} \quad (3.44)$$

where Z is the Zener-Hollomon parameter and is given by:

$$Z = \dot{\varepsilon} \exp\left(\frac{Q_{def}}{RT}\right) \quad (3.45)$$

where Q_{def} is the activation energy for the internal restoration during deformation.

The critical strain for Nb-containing microalloyed steels has been proposed as [52,68]:

$$\varepsilon_c = \left(0.8 - 13Nb_{eff} + 112Nb_{eff}^2\right) \times \varepsilon_p \quad (3.46)$$

where Nb_{eff} wes defined as:

$$Nb_{eff} = Nb - \frac{Mn}{120} + \frac{Si}{94} \quad (3.47)$$

and ε_p was found as:

$$\varepsilon_p = \left(\frac{1+20Nb}{1.78}\right) \times 2.8 \times 10^{-4} {D_{gs,0}}^{0.5} Z^{0.17} \quad (3.48)$$

The expression for ε_p for Nb-Ti steels was found as [73,80,82]:

$$\varepsilon_p = \left(\frac{1+20[Nb]+0.02[Ti]}{1.78}\right) \times 3.7 \times 10^{-3} {D_{gs,0}}^{0.147} Z^{0.155} \quad (3.49)$$

and the critical strain, ε_c and the transition strain, ε_T relate to ε_p as follows [73,82]:

$$\varepsilon_c = 0.77\varepsilon_p \quad (3.50)$$

$$\varepsilon_T = 2.2\varepsilon_c \quad (3.51)$$

The dynamic recrystallization volume fraction (X_{DRX}) was given by [68]:

$$X_{DRX} = 1 - \exp\left[-0.693\left(\frac{\varepsilon-\varepsilon_c}{\varepsilon_{0.5}}\right)^2\right] \quad (3.52)$$

where $\varepsilon_{0.5}$ is the strain for 50% recrystallization and is given by [68]:

$$\varepsilon_{0.5} = 1.144 \times 10^{-3} {D_{gs,0}}^{0.25} \dot{\varepsilon}^{0.05} \exp\left(\frac{6420}{T}\right) \quad (3.53)$$

3.6.2.3. Meta-Dynamic Recrystallization (MDRX) ($\varepsilon > \varepsilon_T$)

Meta-dynamic recrystallization MDRX does not need an incubation time since the nuclei are already formed from DRX, thus it proceeds rapidly at the end of deformation passes [5,72,4]. MDRX occurs between deformation passes but only if ε_c had been reached, and is defined as the growth of the dynamically recrystallized nuclei [5,4].

The kinetics of MDRX are a strong function of strain rate and are very weakly dependant on deformation or the holding temperature [78,77].

Since DRX does not provide complete softening, MDRX only contributes about 15% of softening and is followed by static recovery which provides an additional 10% softening. Recovery provides the recrystallization nuclei followed by SRX which contributes a further 55% softening [5].

The meta-dynamic recrystallization volume fraction (X_{MDRX}) was given by [72]:

$$X_{MDRX} = 1 - \exp[-0.693(t/t_{0.5}^{MDRX})^n] \quad \text{.....(3.54)}$$

whereby the time for 50% metadynamic recrystallization $t_{0.5}^{MDRX}$ was given by the following expression [64,75,59]:

$$t_{0.5} = AZ^a \exp\left(\frac{Q_{MDRX}}{RT}\right) \quad \text{.....(3.55)}$$

where Q_{MDRX} is the activation energy for MDRX.

The expression for $t_{0.5}$ by Elwazri *et al.* [72] was derived as:

$$t_{0.5} = A\dot{\varepsilon}^b \exp\left(\frac{Q_{app}}{RT}\right) \quad \text{.....(3.56)}$$

where Q_{app} is the apparent activation energy which is a function of the activation energy for recrystallization for MDRX (Q_{MDRX}) and the activation energy for deformation (Q_{def}) and is given by:

$$Q_{app} = Q_{MDRX} - 0.6Q_{def} \quad (3.57)$$

The apparent activation energy (Q_{app}) was reported as 170 kJ/mol for C-Mn-V steel [72]. The expression by Kim *et al.* [74] was given as follows:

$$t_{0.5} = AD_{gs,0}{}^{c}\dot{\varepsilon}^{e}\exp\left(\frac{Q_{MDRX}}{RT}\right) \quad (3.58)$$

The recrystallized grain size was given by [52]:

$$D_{MDRX} = \delta Z^{f} \quad (3.59)$$

where δ and f are constants. For Nb containing steels, the expression for the meta-dynamically recrystallized grain size is in the form [52,83]:

$$D_{MDRX} = 1370 \times \varepsilon^{-0.13}\exp\left(-\frac{45000}{RT}\right) \quad (3.60)$$

The constants in terms of chemistry and processing parameters are summarized in Table 11.2 in Appendix A

3.6.2.4. Static Recrystallization (SRX) + Meta-Dynamic Recrystallization (MDRX) ($\varepsilon_c<\varepsilon<\varepsilon_T$)

When both static and meta-dynamic recrystallization take place during the inter-pass times, the total fraction of softening is given by the sum of the individual components:

$$X = X_{SRX} + X_{MDRX} \quad (3.61)$$

When static softening is completed, the final contribution of static recrystallization ($X_{f,}^{SRX}$) and the final contribution of meta-dynamic recrystallization (X_f^{MDRX}) are equal to 1 [72,73,80]. At strains close to ε_c, SRX will be the main contributor and as the strains approach ε_T, MDRX will be the major contributor in softening [80]. The contributions of the individual mechanisms are given by the expressions below:

$$X_f^{MDRX} = \frac{\varepsilon - \varepsilon_c}{\varepsilon_T - \varepsilon_C} \quad (3.62)$$

$$X_f^{SRX} = 1 - X_f^{MDRX} \quad (3.63)$$

Thus the individual components are given by [72,73,80]:

$$X_{SRX} = X_f^{SRX}[1 - \exp(-0.693(\frac{t}{t_{0.5}^{SRX}})^n] \quad (3.64)$$

$$X_{MDRX} = X_f^{MDRX}[1 - \exp(-0.693(\frac{t}{t_{0.5}^{MDRX}})^n] \quad (3.65)$$

The mean recrystallizing grain size D_r is given by [73]:

$$D_r = D_{r,SRX}X_{SRX} + D_{r,MDRX}X_{MDRX} \quad (3.66)$$

where $D_{r,SRX/MDRX}$ is given by:

$$D_{r,SRX/MDRX} = D_{SRX/MDRX}X_{SRX/MDRX}^{\frac{1}{3}} \quad (3.67)$$

and the mean unrecrystallized grain size, D_u, is given by [73]:

$$D_u = 1.06D_{gs,0}\exp(-\varepsilon)(1 - X)^{1/3} \quad (3.68)$$

When partial recrystallization has taken place, the initial grain size for the next pass ($D_{gs,0i+1}$) is given by the following relationship [52,68]:

$$D_{gs,0_{i+1}} = D_{rex_i} \times X_i^{4/3} + D_{gs,0_i}(1 - X_i)^2 \quad (3.69)$$

where X_i is the volume recrystallized fraction at pass i, D_{rexi} and $D_{gs,0i}$ are the recrystallized (SRX/MDRX) and initial grain sizes of pass i respectively.

This partial recrystallization leads to retained strain which is accumulated to the next deformation pass. The accumulated strain (ε_a) is given by the following expression [52,68,78]:

$$\varepsilon_{ai+1} = \varepsilon_{i+1} + j(1 - X_i)\varepsilon_i \quad \text{.....(3.70)}$$

where *j* is a constant that lies between 0.5 and 1 and is related to the rate of recovery. It is assumed as 1 for C-Mn and microalloyed steels.

To determine whether MDRX occurs during interpass times, a limiting Zener-Hollomon parameter (Z_{lim} has been employed which separates flow curves with a peak from those without a peak [3] and is given by the form:

$$Z_{lim} = \eta \exp(-\chi D_{gs,0}) + Z_0 \quad \text{.....(3.71)}$$

The magnitude of the constants in terms of chemistry are summarized in Table 3.1. If Z is less than Z_{lim}, then meta-dynamic recrystallization will occur provided that the applied strain is larger than the critical strain ε_c [3].

Table 3.1.: Parameters describing the boundary that separates static and metadynamic recrystallization for various steel grades [3].

Steel type	η (s^{-1})	χ (μm^{-1})	Z_0 (s^{-1})
C-Mn	$5x10^{15}$	0.129	0
C-Mn-V	$5x10^{15}$	0.129	0
C-Mn-Nb-Ti	$3.76x10^{19}$	0.0116	0

3.6.3. Recrystallization By The SIBM Mechanism

SIBM involves the bulging of part of a pre-existing grain boundary, leaving a region behind the migrating boundary with a lower dislocation content [112]. The SIBM mechanism also known as boundary migration [116] has a characteristic feature that the new grains have similar orientations to the old grains out of which they are formed [112].

Recrystallization is assumed to primarily occur by SIBM where the strains are relatively small (0.1-0.4) [114] and this applies therefore especially in rough rolling. Bellier and Doherty confirmed that SIBM was the dominant recrystallization mechanism in reductions of less than 20 % in rolled aluminium [quoted by 112] and is of significant importance for reductions of less and up to 40 % in most metals [115]. This mechanism is believed to be more dominant than the classical nucleation theory because of the low driving force associated with the latter hence the nuclei which gives rise to the new recrystallized grains are not formed during annealing or inter-pass times but are already present in the deformed state [115,116]. The driving force for SIBM arises from the difference in dislocation content on the opposite sides of the grain boundary [112]. Figure 3.23 is a schematic illustration of the SIBM mechanism process [112].

The bulge of the grain boundary will grow when its spherical cap of radius, R_B reaches a critical radius R_{crit} [112]:

$$\mathrm{R_B} = \mathrm{R_{crit}} > \frac{2\gamma_{gb}}{\Delta E} \quad \text{.....(3.72)}$$

where ΔE is the driving force for recrystallization through the SIBM process given by the energy difference between the two deformed grains separated by the bulging boundary [112]. The ΔE is given by: [114]

$$\Delta \mathrm{E} = \mathrm{E_2} - \mathrm{E_1} = \frac{1}{2}\Delta\rho\beta\vec{\mathrm{b}}^2 \quad \text{.....(3.73)}$$

where $\Delta\rho$ is the dislocation density difference between the two sides of the boundary.

The interfacial energy associated with the bulging region of the boundary is given by [112]:

$$E_B = 4\pi R_B^2 \gamma_{gb} \quad \text{.....(3.74)}$$

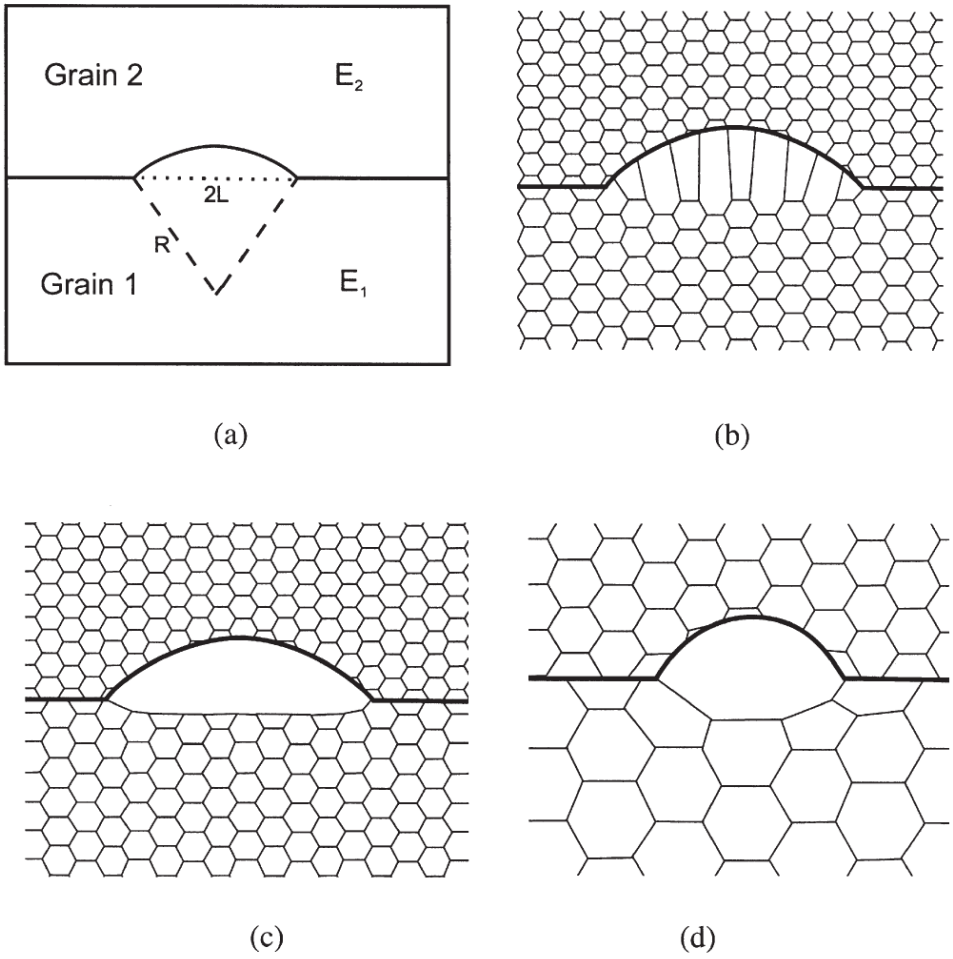

Figure 3.23.: Schematic illustration of the SIBM process a) SIBM of a grain boundary separating a grain of low stored energy (E1) from one of higher energy (E2) b) dragging of the dislocation structure behind the migrating boundary c) the migrating boundary is free from the dislocation structure and d) SIBM originating at a single large subgrain [112].

In the SIBM mechanism the following conditions hold; i) the orientation of the nucleus is present in the deformed structure, ii) nucleation occurs by the growth of the subgrains and iii) an orientation gradient must be present for a high angle grain boundary to be produced by the SIBM mechanism [112].

3.6.4. Interaction Of Precipitation With Recrystallization

In HSLA steels, microalloying elements Nb, Ti and V, dissolved as a solid solution raise the recrystallization temperature of the deformed austenite due to the segregation on

dislocations and grain boundaries, leading to a decrease in recovery rate and grain boundary mobility. While precipitation of these microalloying elements as MX (M = metal, X = metalloid) phases on the dislocations, retard both dynamic recovery and dynamic recrystallization during plastic deformation, they decrease the rate of thermal recovery and static or meta-dynamic recrystallization. As a result, this limits the grain growth of the recrystallized austenite during inter-pass times [77,44,36]. Nb is known to be more effective in retarding the recrystallization in austenite than V [84]. Andrade *et al.* [71] found that the addition of Nb, V and Mo to a 0.05% C-Mn steel increased the recovery and recrystallization time after hot working at 1000 °C at a strain rate of 2 s^{-1} through solute drag, Figure 3.24. It was also found that Nb is the most effective in retarding static recovery and recrystallization followed by Mo, and V having the least retardation effect. This is consistent with work done by Maruyama *et al.* [20] on Nb, Ti and V microalloyed steels who found that Nb is the most effective alloying element in retarding SRV and SRX followed by Ti and then lastly V.

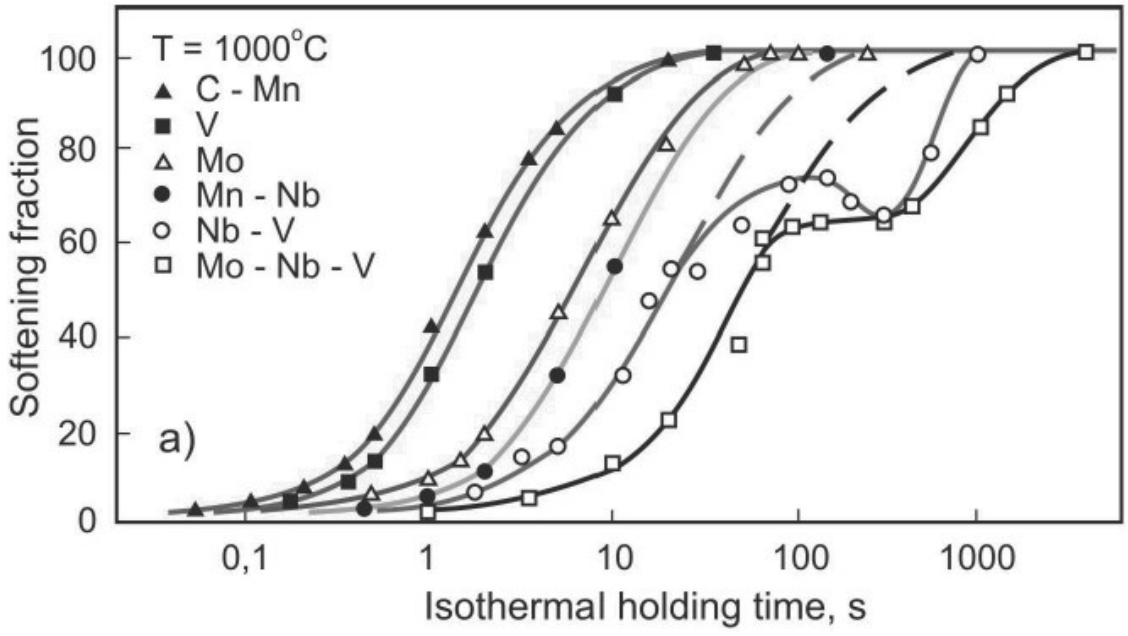

Figure 3.24.: Influence of Mo, Nb and V content on the recovery and recrystallization of a 0.05% C-Mn steel after hot working at 1000°C at a strain rate of 0.2s-1 [77,71]

The interaction between recrystallization and strain induced precipitation in microalloyed steels may occur in three different ways;

- recrystallization can retard the onset of strain-induced precipitation by decreasing the number of dislocations thus decreasing the number of nucleation sites;
- a dispersion of precipitates provides a pinning force on the grain boundaries and thus can hinder the progress of recrystallization;
- as precipitation takes place it decreases the matrix solute content which strongly affects the mobility of grain boundaries thus affecting the progress of recrystallization [43].

Extensive work on the interaction of strain induced precipitation and recrystallization has been done where the recrystallization-precipitation-time-temperature curves were developed for steels microalloyed with Nb, Ti, V in varying combinations [85,86,87]. The driving force for recrystallization as precipitation takes place and dislocation density is decreased by the recovery process, is time-dependant and is given by:

$$G(t) = \frac{1}{2}\rho\beta\vec{b}^2 - \frac{3\gamma_{gb}F_v(t)}{R(t)} \quad \text{.....(3.75)}$$

The second term of the equation is the Zener pressure exerted by the precipitates and γ_{gb} is the austenite grain boundary energy, $F_v(t)$ is the precipitate volume fraction and $R(t)$ is the mean precipitate radius [43].

3.6.5. Grain Growth

After complete recrystallization has taken place the recrystallized austenite grains are coarsened due to grain growth which is driven by the decrease in the free energy associated with the grain boundaries [74,59]. Grain growth modelling after recrystallization is based on the isothermal grain growth equation ($D_{gs}^n - D_{gs,0}^n = Kexp(\frac{-Q}{RT})$ *eqn. 2.1*).

For C-Mn steels the grain growth is described by the following equations [64,59]:

For interpass time t, greater than 1s the grain growth model is described by:

$$D_{gs}^{7} = \mathrm{D}_{\mathrm{SRX}}^{7} + 1.5 \times 10^{27}(\mathrm{t} - 4.32\mathrm{t}_{0.5})\exp\left(-\frac{400\,000}{\mathrm{RT}}\right) \text{ for SRX} \quad (3.76)$$

$$D_{gs}^{7} = \mathrm{D}_{\mathrm{MDRX}}^{7} + 8.2 \times 10^{25}(\mathrm{t} - 2.65\mathrm{t}_{0.5})\exp\left(-\frac{400\,000}{\mathrm{RT}}\right) \text{ for MDRX} \quad (3.77)$$

For inter-pass times less than 1s, the grain growth model is described as:

$$D_{gs}^{2} = \mathrm{D}_{\mathrm{SRX}}^{2} + 4 \times 10^{7}(\mathrm{t} - 4.32\mathrm{t}_{0.5})\exp\left(-\frac{113\,000}{\mathrm{RT}}\right) \text{ for SRX} \quad (3.78)$$

$$D_{gs}^{2} = \mathrm{D}_{\mathrm{MDRX}}^{2} + 1.2 \times 10^{7}(\mathrm{t} - 2.65\mathrm{t}_{0.5})\exp\left(-\frac{113\,000}{\mathrm{RT}}\right) \text{ for MDRX} \quad (3.79)$$

The grain growth models describing medium C-Mn-V-Ti steel are as follows [74]:

$$D_{gs}^{7}{}^{7} = \mathrm{D}_{\mathrm{SRX}}^{7} + 1.31 \times 10^{18}\mathrm{texp}\left(-\frac{172\,000}{\mathrm{RT}}\right) \text{ for SRX} \quad (3.80)$$

$$D_{gs}^{7} = \mathrm{D}_{\mathrm{MDRX}}^{7} + 4.32 \times 10^{19}\mathrm{texp}\left(-\frac{217\,000}{\mathrm{RT}}\right) \text{ for MDRX} \quad (3.81)$$

For Nb containing steels (C-Mn-Nb-Ti & C-Mn-Nb-Ti-V) the grain growth model is described as for both SRX and MDRX [52,68,73]:

$$D_{gs}^{4.5} = \mathrm{D}_{\mathrm{SRX/MDRX}}^{4.5} + 4.1 \times 10^{23}\mathrm{texp}\left(-\frac{435\,000}{\mathrm{RT}}\right) \text{ or} \quad (3.82)$$

$$D_{gs}^{4.5} = \mathrm{D}_{\mathrm{SRX/MDRX}}^{4.5} + 4.1 \times 10^{23}(\mathrm{t} - 4.32 \times \mathrm{t}_{0.5})\exp\left(-\frac{435\,000}{\mathrm{RT}}\right) \quad (3.83)$$

Grain growth requires no nucleation process and therefore requires no incubation time and will, therefore proceed simultaneously with SRX, DRV, DRX and MDRX.

3.6.6. Precipitation

Precipitation can occur during the reheating stage, the hot rolling stage, during cooling on the run-out table (ROT) and during coiling [88]. Precipitates formed at high temperatures are generally incoherent with the final metallic matrix and the ones formed at lower temperatures after the transformation, are generally coherent with the parent matrix which leads to lower coarsening rates and therefore leads to higher precipitation strengthening [89].

Niobium, Titanium and Vanadium have a high affinity for both carbon and nitrogen when added to steels. Nb forms niobium nitride (NbN) and niobium carbide (NbC) that both have a cubic-type crystal structure. These precipitates do not always occur individually and niobium can form a carbonitride precipitate with C and N as Nb(C,N) [2]. Ti on the other hand is preferentially bound to nitrogen rather than to carbon. It forms a cubic crystal structure of TiN at elevated temperatures. This TiN is very stable and less soluble in austenite [2].

In microalloyed steels, Nb-microalloyed steels are the most preferred since they have relatively smaller strain-induced precipitates and have a higher strain-induced precipitation start temperature, thus a wider temperature range is available for pancaking the austenite in the finishing stages than with V and Ti microalloyed steels, thereby leading to improved combination of strength and toughness [85]. This is because in Ti-microalloyed steels the TiN and TiC form at too high temperatures and cannot be dissolved at practical temperatures and on the other hand VN forms at too low temperatures to give a T_{NR} that is useful for effective pancaking of the austenite. Hansen *et al*. [10] found that strain-induced precipitation of Nb(C,N) from hot rolled austenite occurs in two stages; firstly, initial precipitation at prior austenite grain boundaries and deformation bands and secondly, general matrix precipitation on the substructure of the unrecrystallized austenite with the latter stage being slower if recrystallization occurs before precipitation.

In Nb microalloyed steels the time for 5% precipitation ($t_{0.05p}$) and time for 5% recrystallization ($t_{0.05x}$) during hot rolling were given by the following equations [52,90,91,8]

$$t_{0.05p} = 3 \times 10^{-6}[Nb]\varepsilon^{-1}Z^{-0.5}\exp\left(\frac{270000}{RT}\right)\exp\left(\frac{2.5\times10^{10}}{T^3 \ln k_s^2}\right) \quad \text{(3.84)}$$

$$t_{0.05X} = 6.75 \times 10^{-20}D_{gs,0}^{2}\varepsilon^{-4}\exp\left(\frac{300000}{RT}\right)\exp\left\{\left(\frac{2.75\times10^{5}}{T} - 185\right)[Nb]\right\} \quad \text{(3.85)}$$

where k_s is the super-saturation ratio and is given by:

$$k_s = \frac{[Nb][C+\frac{12}{14}N]}{10^{2.26-6770/T}} \quad \text{(3.86)}$$

For $t_{0.05x}<t_{0.05p}<t_{0.95X}$ recrystallization is retarded by precipitation and for $t_{0.05x}> t_{0.05p}$ recrystallization does not take place at all [90].

Although the equation for $t_{0.05p}$ does not include the influence of grain size, Medina *et al*. [86] showed that increasing the austenite grain size increases the static recrystallization critical temperature (SRCT). This is the temperature at which the strain-induced precipitation starts under isothermal conditions. The SRCT for V-microalloyed steel in Kelvin is given by [92]:

$$\mathrm{SRCT} = \mathrm{T_s} - 708.2[1000(\%\mathrm{V})(\%\mathrm{N})]^{0.38}\varepsilon^{0.3}\dot{\varepsilon}^{0.16}\mathrm{D}_{\mathrm{gs},0}^{-0.34} \quad \text{.....(3.87)}$$

where, T_s is the solubility temperature of VN (in K).
The driving force for precipitation in Nb-microalloyed steels is given by [36]:

$$\Delta\mathrm{G_v} = -\frac{\mathrm{RT}}{\mathrm{V_m}}\ln\left(\frac{\mathrm{C_{Nb}C_C}}{\mathrm{C_{Nb}^e C_C^e}}\right) \quad \text{.....(3.88)}$$

where R is the universal gas constant, T is the isothermal soaking temperature, V_m is the molar volume of the precipitates, C_{Nb} and C_C are the instantaneous concentrations of Nb and C respectively, C_{Nb}^e and C_C^e are the equilibrium concentrations of Nb and C at the soaking temperature.

Chapter 4. Experimental Procedure

4.1. Experimental Steels

Four peritectic industrial steels in the as-cast condition were studied namely a plain C-Mn steel which served as a benchmark, V-only, V-Nb and Nb-Ti-V steel. No homogenization heat treatment was conducted on steels prior to the experiments. Table 4.1 shows the chemistry of the steels used in this study in mass %, the spectrographic analysis was conducted on the same location where the specimens were sampled.

Table 4.1.: Chemical composition in mass % of the steels

Steel	Type	C	Mn	Si	Nb	Ti	V	Al	N (ppm)	S (ppm)
A	C-Mn	0.161	1.13	0.24	0.000	0.002	0.001	0.035	58	40
B	C-Mn-V	0.133	1.54	0.4	0.001	0.002	0.061	0.033	90	22
C	C-Mn-V-Nb	0.156	1.61	0.53	0.011	0.004	0.064	0.058	127	19
D	C-Mn-Nb-Ti-V	0.134	1.50	0.38	0.040	0.025	0.028	0.049	55	41

4.2. Initial Austenite Grain Size Determination

The starting grain size entering the roughing mill influences a number of subsequent metallurgical phenomena such as austenite recovery and recrystallization, grain growth and precipitation of various species of the steel. The initial grain size is controlled by the chemistry and reheating conditions i.e. heating rate, soaking temperature and duration. In this study, the desired initial austenite grain size was that typical of an industrial grain size and representative of the centre of a 240 mm thick slab.

A typical [17] furnace reheating temperature of 1220 ºC for microalloyed steels was chosen. To produce industrially relevant initial austenite grain sizes, the samples were heated to 1220ºC at a rate of 81 ºC/min in a Bähr dilatometer 805D and soaked for 30, 60 and 120 minutes followed by quenching at a rate of 600 ºC/s using helium gas to form martensite thereby revealing the prior austenite grains, Figure 4.1.

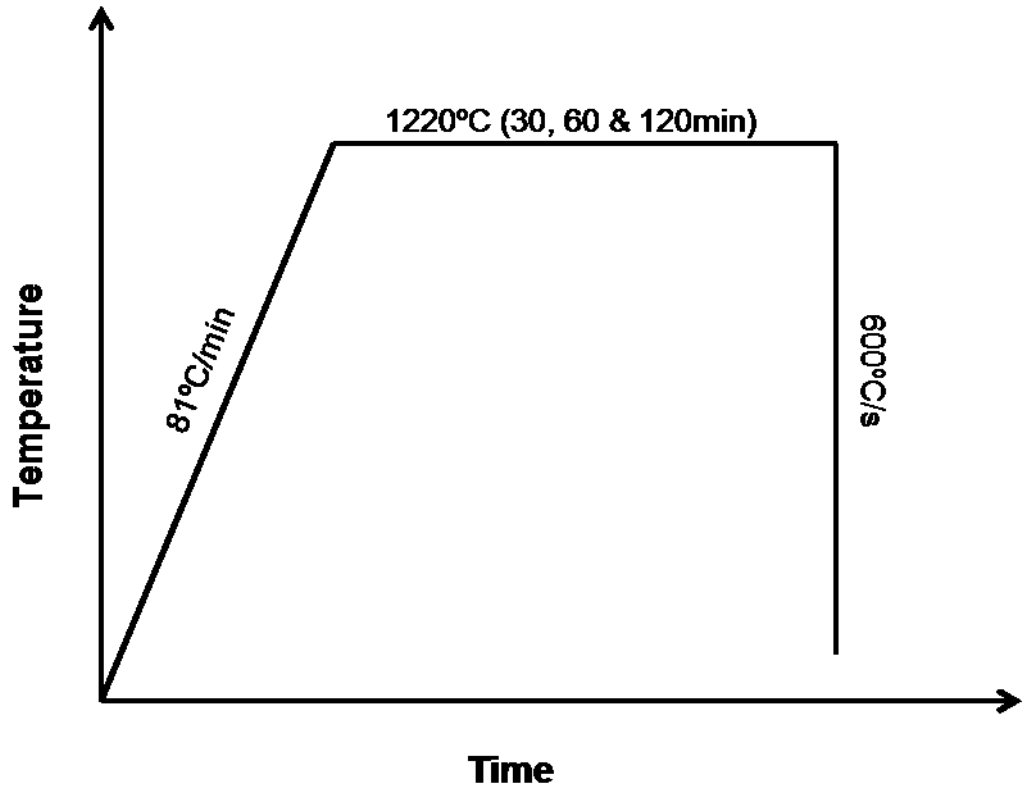

Figure 4.1.: Schematic diagram depicting the reheat schedule to determine the initial austenite grain size

The maximum grain size after initial tests on the plain C-Mn steel was smaller (233 µm) after 120 min soaking time than reported by Yoshie [93] (≥500 µm) for a similar steel at the same temperature but with a heating rate of 7.5ºC/min. FEM work [94] has shown that heating a 240 mm thick slab takes about 5 hours for the centre of the slab to reach 1200ºC, Figure 4.2.

Following this result, the reheating profile was adjusted to promote further grain growth leading to grain sizes similar to that of the centre of the slab since this work focused on

charaterizing the microstructure at the centre of the plate. In addition to the heating rate of 81 ºC/min (HT1), the samples were heated rapidly to 690 ºC at 10 ºC/s, then heated slowly to 1220 ºC at 7.5 ºC/min (HT2). All other specimens were heated from room temperature to 1220 ºC at a rate of 7.5 ºC/min (HT3), Figure 4.3.

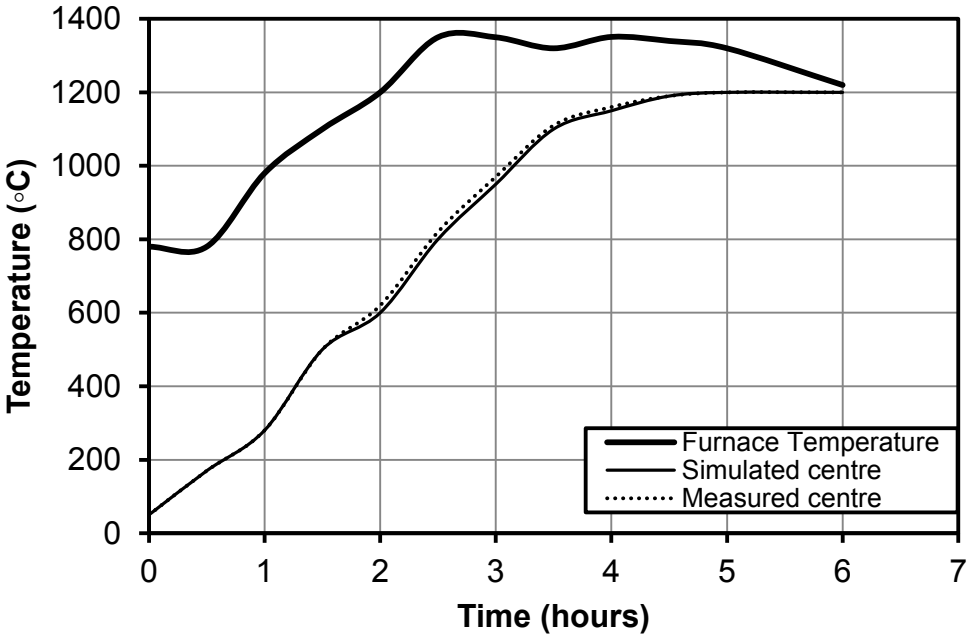

Figure 4.2.: A FEM temperature model showing the time to heat a 240mm thick slab at the centre [94].

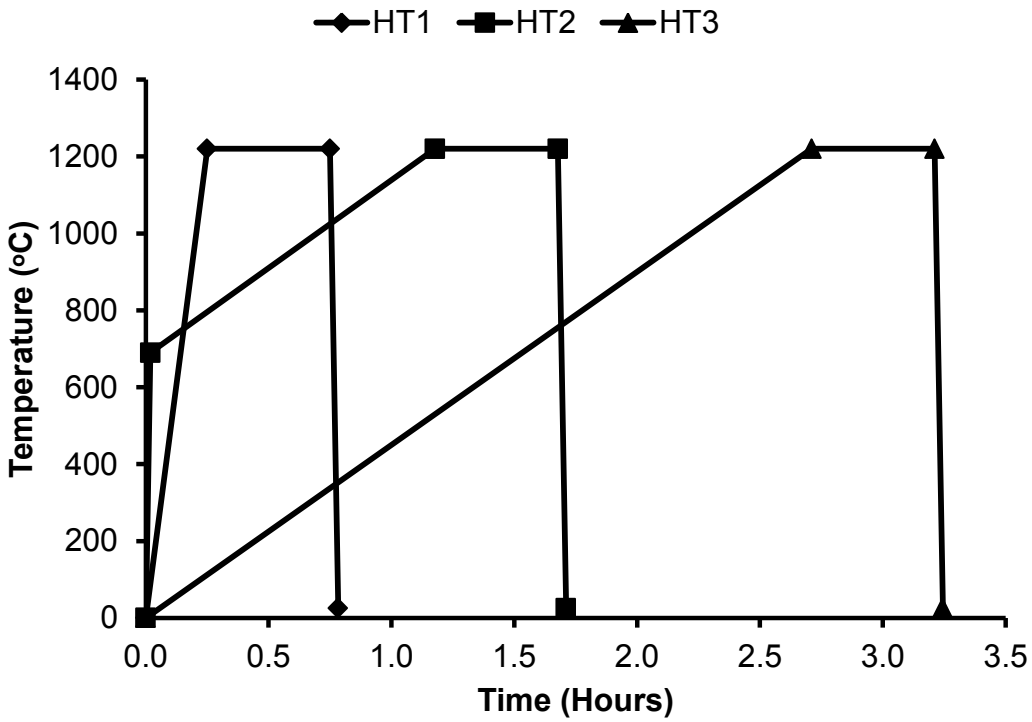

Figure 4.3.: Temperature profiles for determining the austenite grain size at different heating rates with soaking for 30 minutes at 1220ºC.

4.3. Hot Rolling Simulations

Axisymmetric compression samples were machined to a standard 5 mm diameter and 10 mm length size for testing in a Bähr 805D deformation dilatometer. The HT3 thermal profile was followed for the compression tests since it simulated the industrial process more closely. After soaking at 1220 ºC for 30 minutes the samples were cooled at 2 ºC/s to 1150 ºC, the hot rolling roughing entry deformation temperature. Compression tests consisting of various strain sequences were performed, where small (Schedule I), intermediate (Schedule II) and large (Schedule III) strains were studied. Schedules IV, V and VI are manipulations of schedules I-III respectively which include a non-standard large applied strain of 0.4 in the final pass to observe its influence on the microstructural evolution. Two sets of simulations were performed for schedule II and IV; tests that included a high exit roughing temperature (T ≥ 1105 °C) and tests employing a low exit roughing temperatures (T < 1100 °C). Table 4.2 shows the parameters for the high exit temperature hot rolling simulations. The strain rate increases after each pass and the

inter-pass time was fixed at 9 s. After the last pass, the samples were quenched at 600 ºC/s using helium to form martensite so as to reveal the prior austenite grains.

Table 4.2.: High exit temperature simulated hot rolling simulations.

Pass	R1	R2	R3	R4	R5	R6	R7	R8	R9	R10	R11	R12	R13	R14
ε̇ (s^{-1})	**0.3**	**0.5**	**0.7**	**0.9**	**1.1**	**1.3**	**1.5**	**1.7**	**1.9**	**2.1**	**2.3**	**2.5**	**2.7**	**2.9**
T (°C)	**1150**	**1145**	**1140**	**1135**	**1130**	**1125**	**1120**	**1115**	**1110**	**1105**	**1100**	**1095**	**1090**	**1085**
Schedule	**Nominal true strain**													
I	0.07	0.07	0.07	0.07	0.07	0.07	0.07	0.07	0.07	0.07	0.07	0.07	0.07	0.07
II	0.10	0.10	0.10	0.10	0.10	0.10	0.10	0.10	0.10	0.10				
III	0.15	0.15	0.15	0.15	0.15	0.15								
IV	0.07	0.07	0.07	0.07	0.07	0.07	0.07	0.07	0.40					
V	0.1	0.1	0.1	0.1	0.1	0.1	0.40							
VI	0.15	0.15	0.15	0.15	0.40									

Table 4.3 shows the low exit temperature hot rolling simulations of the intermediate strain sequence. Schedule VII and VIII are the low exit roughing temperatures of schedule II (0.1ε/pass), and schedule V (0.1ε/pass + 0.4ε) in Table 4.2 respectively. In order to exit at low roughing temperatures (T < 1105 °C) the cooling rate was doubled from 0.6 to 1.1 °C/s between passes, and inter-pass times were kept constant at 9 s. Schedule IX is a modification of schedule VIII where the non-standard last pass of 0.4 was delayed by 36 s so that the exit temperature can be similar to the one of schedule VII.

Table 4.3.: Low exit temperature of intermediate strain sequence hot rolling simulations.

Pass	R 1	R 2	R 3	R 4	R 5	R 6	R 7	R 8	R 9	R 10
έ (1/s)	**0.3**	**0.5**	**0.7**	**0.9**	**1.1**	**1.3**	**1.5**	**1.7**	**1.9**	**2.1**
T (^{0}C)	**1150**	**1140**	**1130**	**1120**	**1110**	**1100**	**1090**	**1080**	**1070**	**1060**
Schedules	**Nominal true strain**									
VII	0.1	0.1	0.1	0.1	0.1	0.1	0.1	0.1	0.1	0.1
VIII	0.1	0.1	0.1	0.1	0.1	0.1	0.4			
IX	0.1	0.1	0.1	0.1	0.1	0.1				0.4

Table 4.4 shows the low exit temperature hot rolling simulations of the large strain sequence. Schedule X and XII are the low exit roughing temperatures of schedule III (0.15ε/pass), and schedule VI (0.15ε/pass + 0.4ε) respectively in Table 4.2. Due to the deformation constraints of axisymmetric compression, the total strain was limited. Thus, for the low exit temperature for the large strain sequence hot rolling simulation, the inter-pass time was doubled to 18 s and the cooling rate kept the same as the simulations in Table 4.3 at 1.1 °C/s to ensure that the last pass was lower than 1100°C. Schedule XII is a modification of schedule XI where the non-standard last pass of 0.4 was delayed by 36 s so that the exit temperature can be similar to the one of schedule X.

Table 4.4.: Low exit temperature of large strain sequence hot rolling simulations.

Pass	R1	R2	R3	R4	R5	R6
ε̇ (1/s)	0.3	0.5	0.7	0.9	1.1	1.3
T (^{0}C)	1150	1130	1110	1090	1070	1050
Schedule	Nominal true strain					
X	0.15	0.15	0.15	0.15	0.15	0.15
XI	0.15	0.15	0.15	0.15	0.40	
XII	0.15	0.15	0.15	0.15		0.4

4.4. Microstructural Analysis

This research is focused mainly on the initial austenite microstructure entering the roughing mill, and the evolution thereof during the roughing process, thus the microstructure before and after the deformation stage is of great importance in this work.

To determine the austenite grain size, samples were mounted using a thermoplastic transparent mounting powder, ground and polished to a 3 μm finish. The samples were etched using saturated picric acid, with a combination of a wetting agent and a few drops of HCl. The solution was heated to 60-80ºC on a hotplate and the samples immersed in the solution to reveal the prior austenite grain boundaries. The etched samples were observed under an *Olympus BX51M* optical microscope.

The austenite grain size was quantified by using the mean linear intercept method with the aid of the *Image J*® software that randomly places gridlines of known length vertically and horizontally on the micrographs. These gridlines were calibrated based on the used magnification. The number of times each gridline intercepts the austenite grain boundaries, was recorded and the grain size measured using equation 4.1:

$$\overline{L} = \frac{L}{N_{gb}} \quad (4.1)$$

where $\overline{L}$ is the linear intercept grain size, L the known length of the gridline, and N_{gb} the number of times this gridline intercepts the austenite grain boundaries. The average of $\overline{L}$ ($avg\overline{L}$) was taken for all the gridlines and the standard deviation (SD) was estimated using the following expression:

$$SD = \sqrt{\frac{1}{N}\sum_{i=1}^{N}(\overline{L_i} - avg\overline{L})^2} \quad (4.2)$$

where N is the total number of gridlines, $\overline{L_i}$ is the linear intercept grain size of each gridline.

4.5. Determination of the Recrystallized Volume Fraction

The amount of recrystallization during the rolling process controls the microstructural evolution. To quantify the recrystallized volume fraction in this work, the double stroke approach was used [47]. The 2 % offset method was adopted, as shown in equation 4.3, where $\sigma_{m,i}$ is the maximum stress at pass i and $\sigma_{2\%,i}$ and $\sigma_{2\%,i+1}$ are the 2 % stresses of passes i and i+1 respectively.

$$X = \frac{\sigma_{m,i} - \sigma_{2\%,i+1}}{\sigma_{m,i} - \sigma_{2\%,i}} \quad (4.3)$$

A value of 15% was accounted for recovery [25], then the final recrystallized volume fraction X_f was calculated using equation 4.4.

$$X_f = \frac{X - 15\%}{85\%} \quad (4.4)$$

Models by Sellars [75,76], Siciliano and Jonas [52,64], Militzer [3] and Uranga [78,80] to calculate the recrystallized volume fraction discussed in section 3.6, were used to compare with the measured one. In the use of these models, the accumulated strain (ε_a) was taken into account and was calculated using eqn. 3.70.

4.6. Mean Flow Stress Calculations

In this work, the mean flow stress was calculated as discussed in section 3.5, and most of the results are portrayed in this manner. Only when the laboratory results are compared to models from literature, the MFS was then converted to Von Mises plane strain stresses. Due to different strains and strain rates between the laboratory and the mill, the mean flow stress was corrected for a constant strain of 0.4 and a constant strain rate of 5 s^{-1} using the Minami *et al.* approach [68]:

$$MFS_{Corr\varepsilon/\dot{\varepsilon}} = MFS_{Sims}\left(\frac{0.4}{\varepsilon_{pass}}\right)^{0.21}\left(\frac{5}{\dot{\varepsilon}_{pass}}\right)^{0.13} \quad (4.5)$$

4.7. Critical Strain (ε_c) Determination

Single hit deformation tests were performed to determine the critical strain for initiation of DRX. These tests were performed between 1050-1150 °C, the hot rolling simulation temperature range, at a strain rate of 0.1 and 1 s^{-1} and a true strain of 0.8.

The procedure followed to determine the critical stress and strain for initiation of DRX is shown in Figure 4.4 [117]. The procedure is as follows a) the true stress-strain curve is differentiated from the 2% offset to the peak stress to determine the work hardening rate, b) then the work hardening rate is differentiated with respect to stress, c) and finally the second derivative of the work hardening with respect to stress is determined, and where this is equal to zero, that's the critical stress for DRX, d) then using the critical stress the critical strain is read off the original true stress-strain curve.

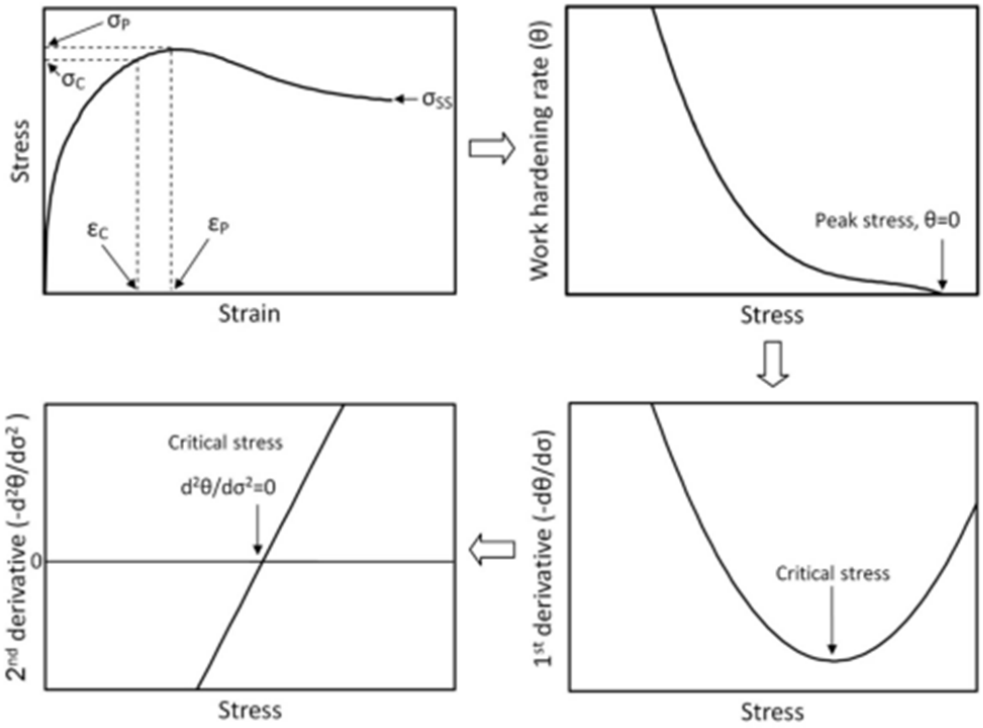

Figure 4.4.: Procedure for determining the critical stress and strain for the initiation of DRX [117].

4.8. Thermo-Calc ®

Thermo-Calc is a computer software data base which performs thermodynamic predictions of equilibrium phase transformations given different alloy compositions and temperatures. It shows the influence of elements on phase stabilities, solubility of different elements, the composition of precipitates and their amounts as a function of temperature. Thermo-Calc can also predict nucleation driving forces, equilibrium and non-equilibrium solidifications [96].

To understand the precipitation behaviour of the studied steels Themo-Calc ® software was used to determine the amount of microalloying elements in solution at different temperatures and the type of precipitates formed. Although these were strictly for equilibrium conditions, it gives an idea of what to expect in terms of precipitation behaviour in these steels. This would help explain the behaviour of the studied steels during the reheating and hot rolling stages.

4.9. Finite Element Modelling (FEM)

In a metallurgical approach, often the bulk and total strains are used in constitutive and empirical equations that describe the behaviour of steel during hot rolling. FEM is a powerful tool that helps to describe the localized strain and strain distribution in the plate which helps to understand the microstructural distribution and evolution during the hot rolling of steel.

The main objective of the study is to achieve a homogeneous through-thickness microstructure after roughing for entering into the finishing mill. For a homogeneous microstructure, complete recrystallization is of importance in the roughing stages [71,35]. One of the controlling variables together with the temperature, strain rate and grain size, is the amount of strain applied. Since compression tests consist of strong inhomogeneities of strains, stresses and temperature [59], a FEM study was commissioned [97] to model the localized strains during the compression of an axi-symmetrical Bähr sample (5 mm diameter and 10 mm long) and the actual hot rolling of a 240 mm thick slab using a 950 mm roll diameter.

The FEM simulations were carried out using the Abaqus 6.11 computer software. Single pass simulations with different reductions were carried out at a constant temperature of 1100°C and a strain rate of $1.5s^{-1}$ for the axi-symmetrical deformation simulation and a roll peripheral speed of 1.5 ms^{-1} for the flat rolling simulation.

Chapter 5. Experimental Results

This chapter focuses on all the experimental results, the initial microstructures pertaining to the different heating cycles and soaking times. The stress-strain curves associated with all of the different roughing schedules, also the mean flow stresses associated with these stress-strain curves have been addressed. The volume recrystallized fraction results are also portrayed along with the post deformation austenite microstructures. FEM simulation results are used to explain the through-thickness strain distribution during deformation for both the axisymmetrical and flat rolling results. Thermo-Calc results are used to explain the behaviour of the steels during reheating in terms of the austenite grain size evolution and the stress-strain behaviour in the deformation stages.

5.1. Thermo-Calc®

Figure 5.1 depicts the amount of the microalloying elements in solution with respect to temperature while Figure 5.2 shows the type of precipitates expected in these steels. The faint dotted line in the figures depicts the reheating temperature of 1220°C and the bold dotted lines depict the deformation temperature range studied in this work of 1050-1150°C.

As may be seen in Figure 5.1 and Figure 5.2, the Al, Nb and V are fully dissolved at a reheating temperature of 1220ºC with the exception of Ti, i.e. only about 15% of Ti was in solution for the C-Mn-Nb-Ti -V steel, and most of which was as a stable Ti(C,N) precipitate. Thus grain boundary pinning was not expected for C-Mn, C-Mn-Nb-V and C-Mn-V steels during the reheating stages. At the deformation temperature range of 1050-1150ºC, precipitation of Nb(C,N) and Ti,(C,N) was expected to occur for the C-Mn-Nb-Ti-V steel., but to a lesser extent than the ones predicted since cooling during hot rolling will restrict precipitation. No precipitation of V,(C,N) was expected in the studied deformation range, see Figure 5.2.

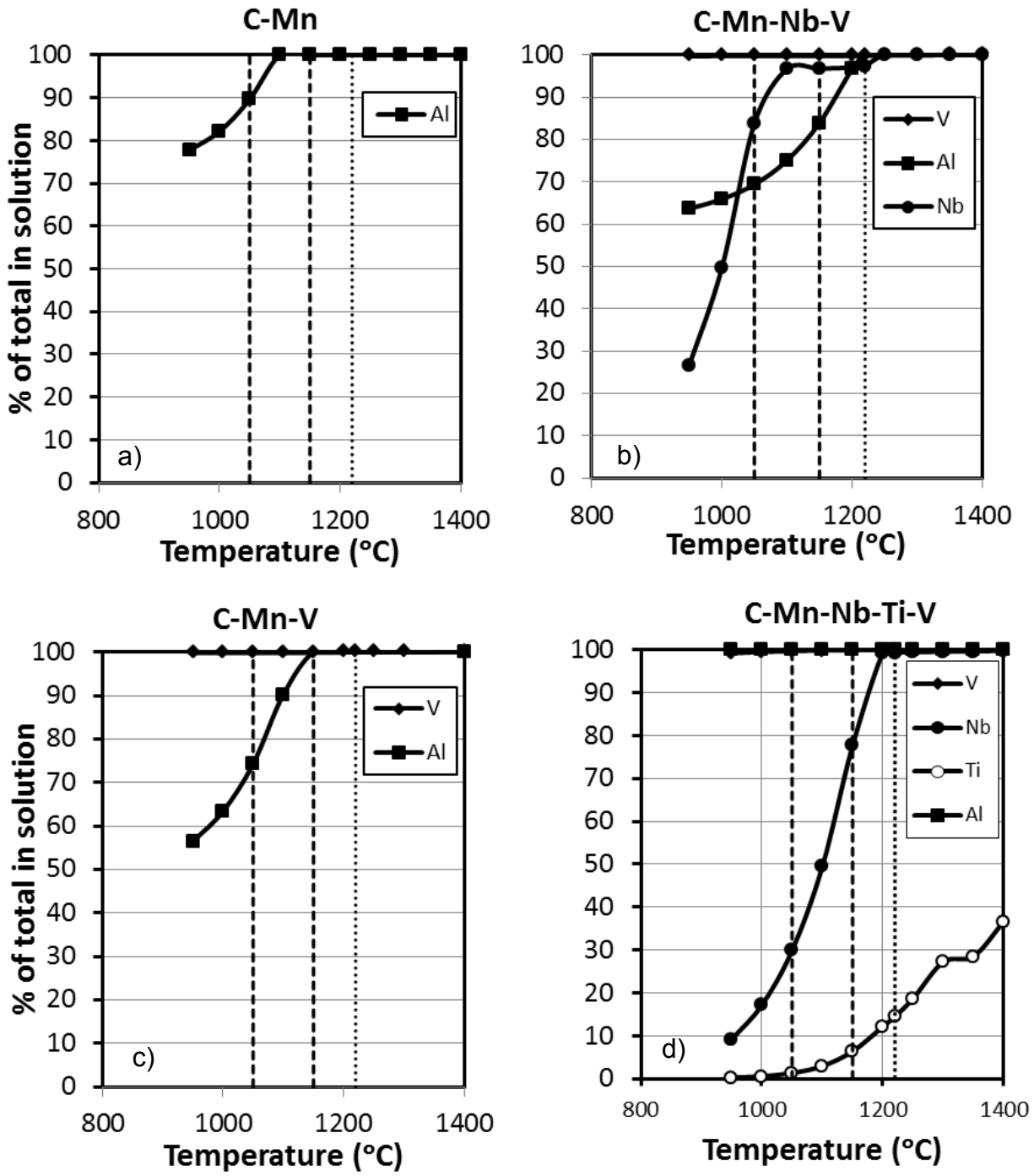

Figure 5.1.: Thermo-Calc ® results depicting the dissolution thermodynamics of the studied steels a) C-Mn b) C-Mn-Nb-V, c) C-Mn-V and d) C-Mn-Nb-Ti-V. The faint dotted line shows the reheating temperature and the bold dotted lines the deformation temperature range. At 1220ºC, 100% of Al, V, Nb precipitates are in solution for all the studied steels except C-Mn-Nb-Ti-V, where only 15% of Ti precipitates are soluble.

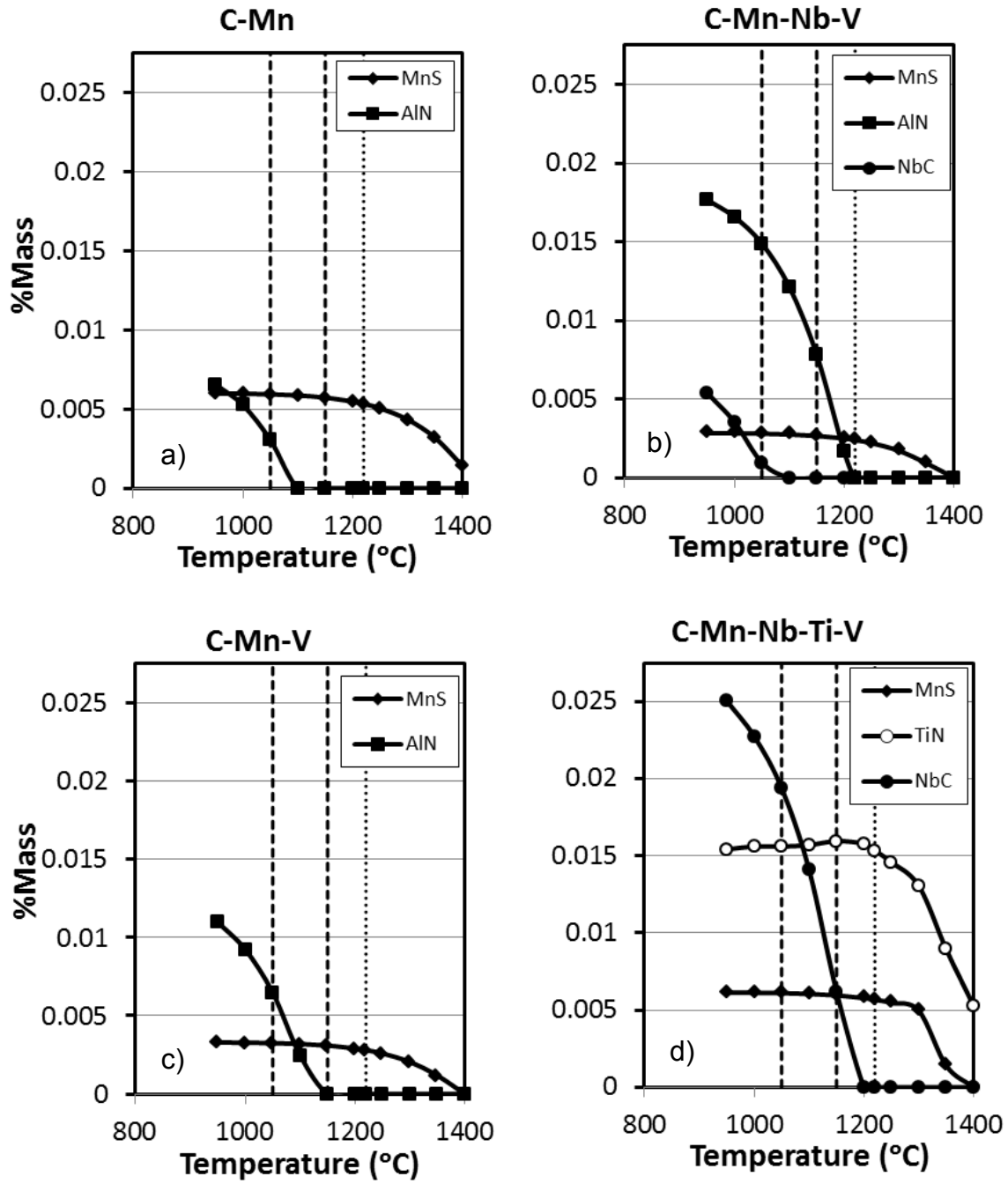

Figure 5.2.: Thermo-Calc ® results depicting the expected precipitates in the studied microalloyed steels a) C-Mn b) C-Mn-Nb-V, c) C-Mn-V and d) C-Mn-Nb-Ti-V.

5.2. T_{NR} Of The Studied Steels

Table 5.1 shows the T_{NR} for the studied steels predicted from models in literature as discussed in section 3.2.2 eqns.3.1 to 3.3 were used. The predictions show that the roughing simulations were undertaken above the T_{NR} for all the studied steels.

Table 5.1. Predicted T_{NR} for the steels from models in the literature [56]

	Predicted T_{NR}	
Steel	Eqn. 3.1	Eqn. 3.2
C-Mn	800	612
C-Mn-V	845	774
C-Mn-Nb-V	887	887
C-Mn-Nb-Ti-V	947	1051

5.3. Initial Microstructures

In this section the initial austenite microstructures are portrayed, quantified and compared. The influence of different soaking times, heating cycles and chemistries on the initial austenite grain size will be shown.

5.3.1. Influence of Soaking Time (HT1 Thermal Cycle (81°c/Min))

Figure 5.3 shows the typical initial austenitic microstructures of the studied steels after the HT1 thermal cycle, after soaking for 120 minutes at 1220 °C. The austenite grain sizes were quantified using the mean linear intercept method as discussed in section 4.4. The measured grain sizes are summarized in Table 5.2 and graphically shown in Figure 5.4. As expected, the austenite grain size increased with increasing soaking times for all of the studied steels. The C-Mn-Nb-Ti-V exhibited the finest austenite grain size at all soaking times with the plain C-Mn being the coarsest. Selected micrographs are shown in Appendix B: Reheat austenite microstructures.

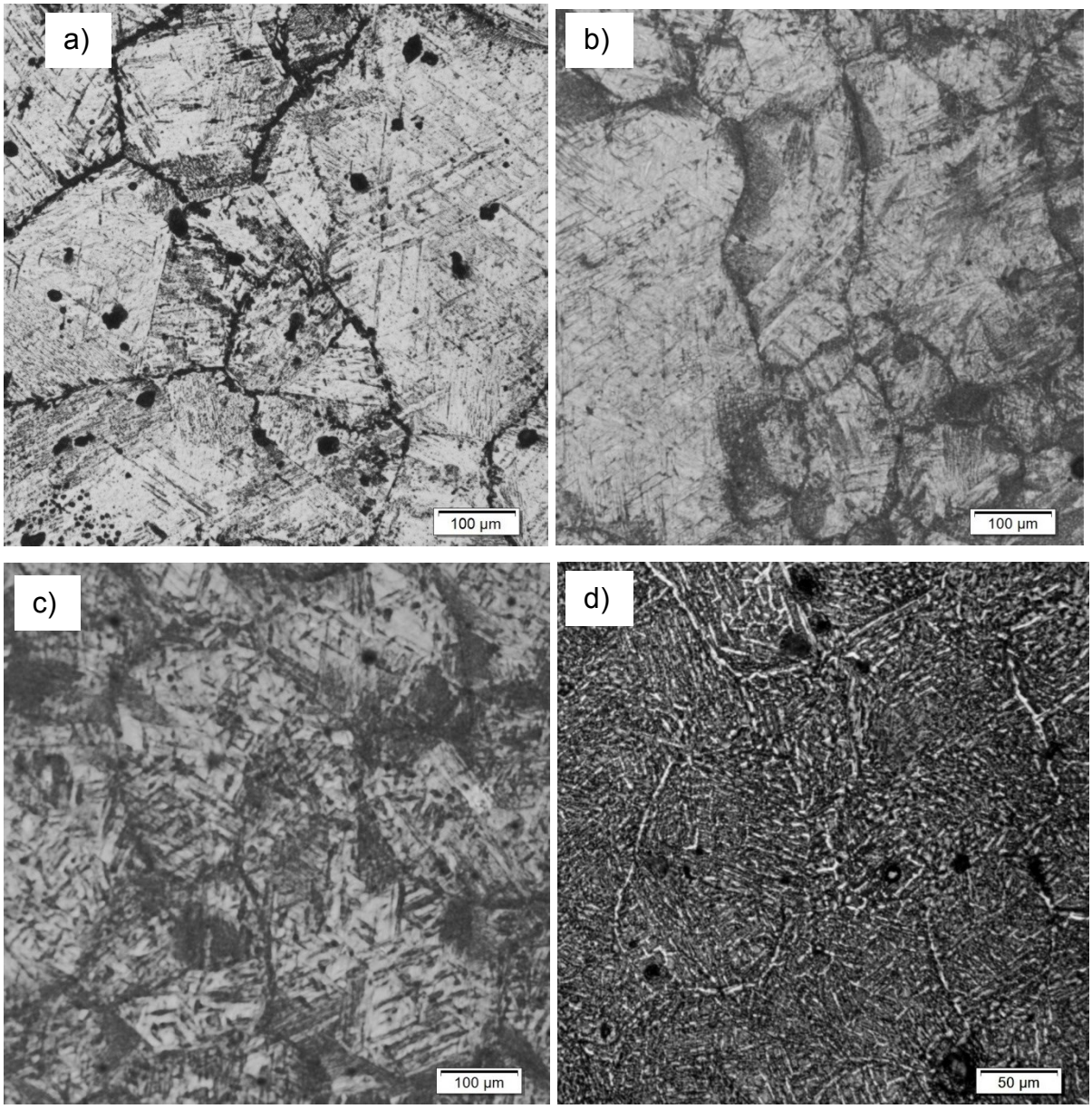

Figure 5.3.: .The austenite microstructure of a) C-Mn steel, b) C-Mn-Nb-V, C) C-Mn-V and d) C-Mn-Nb-Ti-V for the relatively fast heating rate of 81 ^{o}C/s, HT1, thermal cycle after soaking for 120 min at 1220ºC.

Table 5.2.: Measured austenite grain sizes for the studied steels for different soaking times.

	Austenite grain size (µm)			
Soaking time (Minutes)	**C-Mn**	**C-Mn-V**	**C-Mn-Nb-V**	**C-Mn-Nb-Ti-V**
30	126	-	84	44
60	130	80	79	-
120	233	147	119	76

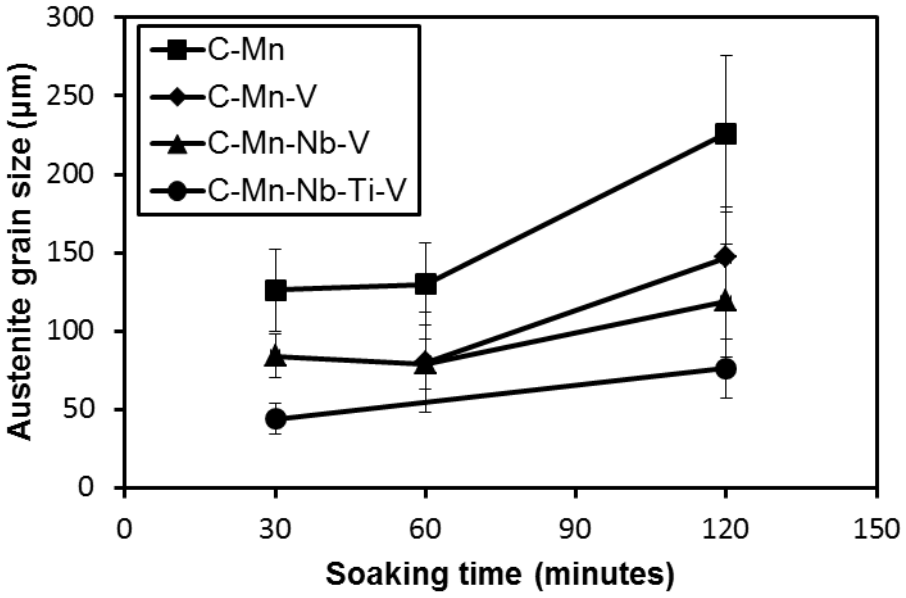

Figure 5.4.: Average austenite grain size of the studied steels as a function of soaking time at 1220 °C.

5.3.2. Influence Of Heating Rate

Figure 5.5 shows the initial austenite microstructures of the studied steels following the slowest heating rate of 7.5 ^{o}C/s, (HT3, thermal cycle), for a soaking time of 30 minutes. The austenite microstructures after the HT2 thermal cycles are shown in Appendix B: Reheat austenite microstructures. The measured grain sizes are summarized in Table 5.3 and graphically shown in Figure 5.6. The longer the heating time the coarser the austenite grain size became for all the studied steels. The heating rate of 7.5 °C/min (HT3) from room temperature led to the coarsest austenite microstructure for the C-Mn steel (353 µm). An insignificant increase in grain size was observed in the C-Mn-Nb-V

and C-Mn-Nb-Ti-V steels for the different heating cycles. This is attributed to the stable and fine TiN in the latter and solute drag of Nb in the former. The HT3 reheating cycle was adopted for the hot rolling simulation tests because it closely mimicked industrial slab reheating conditions at the centre of a 240 mm slab before hot rolling.

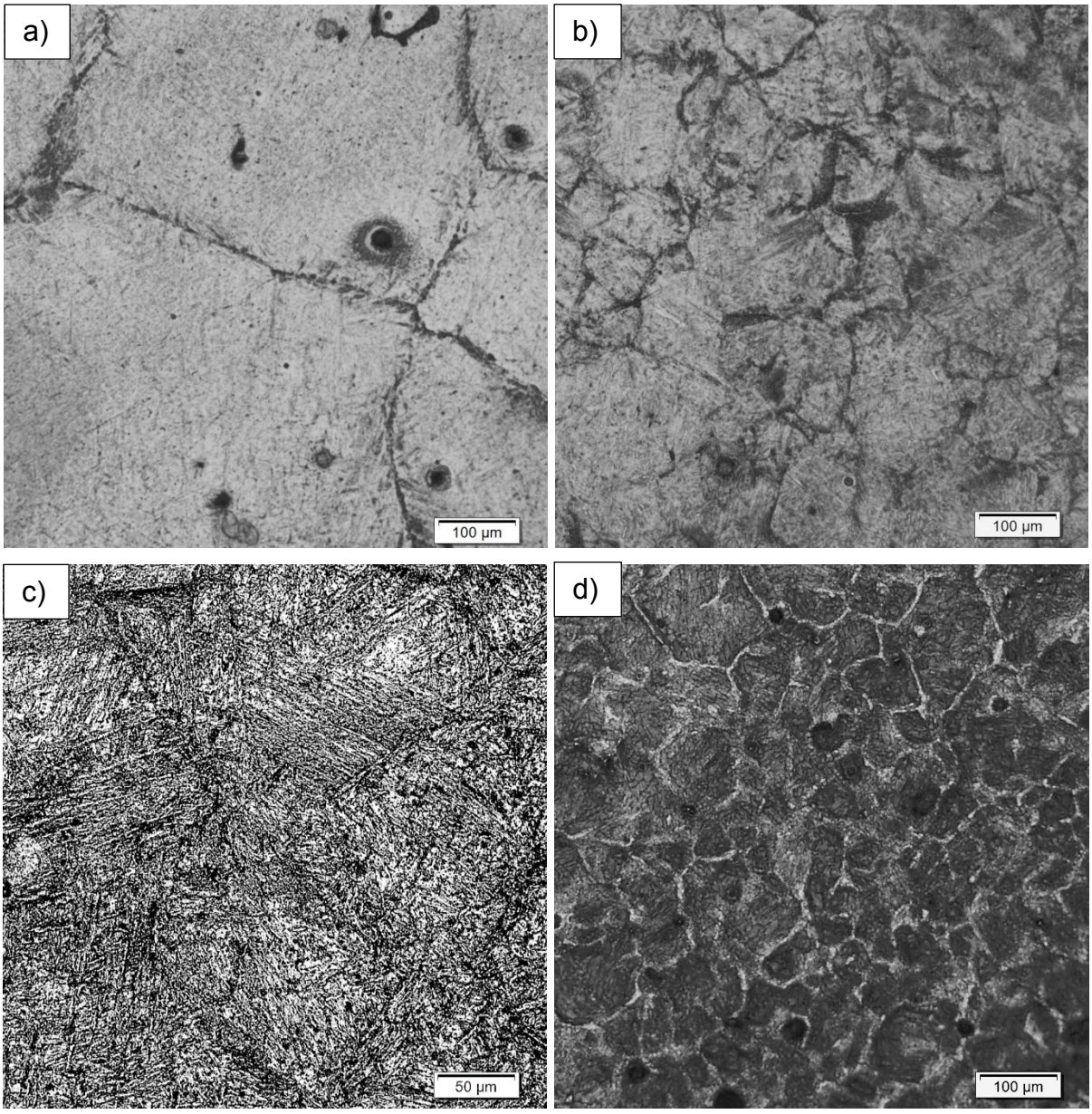

Figure 5.5.: The austenite microstructure of a) C-Mn, b) C-Mn-Nb-V, c) C-Mn- V and d) C-Mn-Nb-Ti-V after soaking for 30 minutes for the HT3 heating profiles to 1220ºC.

Table 5.3.: Measured austenite grain sizes for the studied steels for different heating cycles after soaking for 30 minutes.

	Austenite grain size (µm)			
Heating cycle	**C-Mn**	**C-Mn-V**	**C-Mn-Nb-V**	**C-Mn-Nb-Ti-V**
HT1	126		84	44
HT2	189		91	72
HT3	353	111	94	78

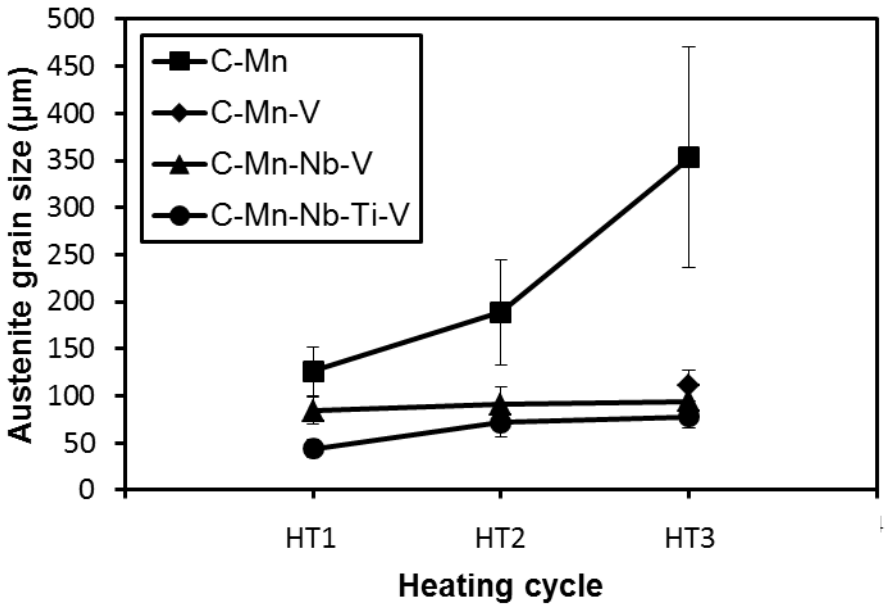

Figure 5.6.: The average austenite grain size as a function of heating cycle after soaking for 30 minutes at 1220 ºC.

5.4. Hot Rolling Simulation Results

In this section the stress-strain curves of the axisymmetric compression tests will be presented. The results are presented according to the different simulated multi-pass rolling schedules. Figure 5.7 to Figure 5.12 are the stress strain curves of high exit roughing temperatures while Figure 5.13 to Figure 5.16 are for the low exit roughing temperature schedules. The curves are super-imposed for comparison and demonstrate the influence of chemical composition, if any.

5.4.1. High Exit Roughing Temperatures

Figure 5.7 to Figure 5.12 show the true stress-strain curves for small (I & IV), intermediate (II & V) and large (III & VI) strain sequence schedules along with their corresponding MFS vs 1000/T plots respectively.

In Figure 5.7a) the true stress-strain curves show no softening between R1 and R2 for all steels and this is supported by the significant increase in the MFS from R1 to R2, Figure 5.7b) indicating strain accumulation. Softening occurs in all other roughing passes and the oscillation of the MFS with decrease in temperature may be due to the partial recrystallization taking place in this schedule and thus the retained strain from the previous partial recrystallized pass is caried to the next pass and hence did lead to a slight increase in the MFS.

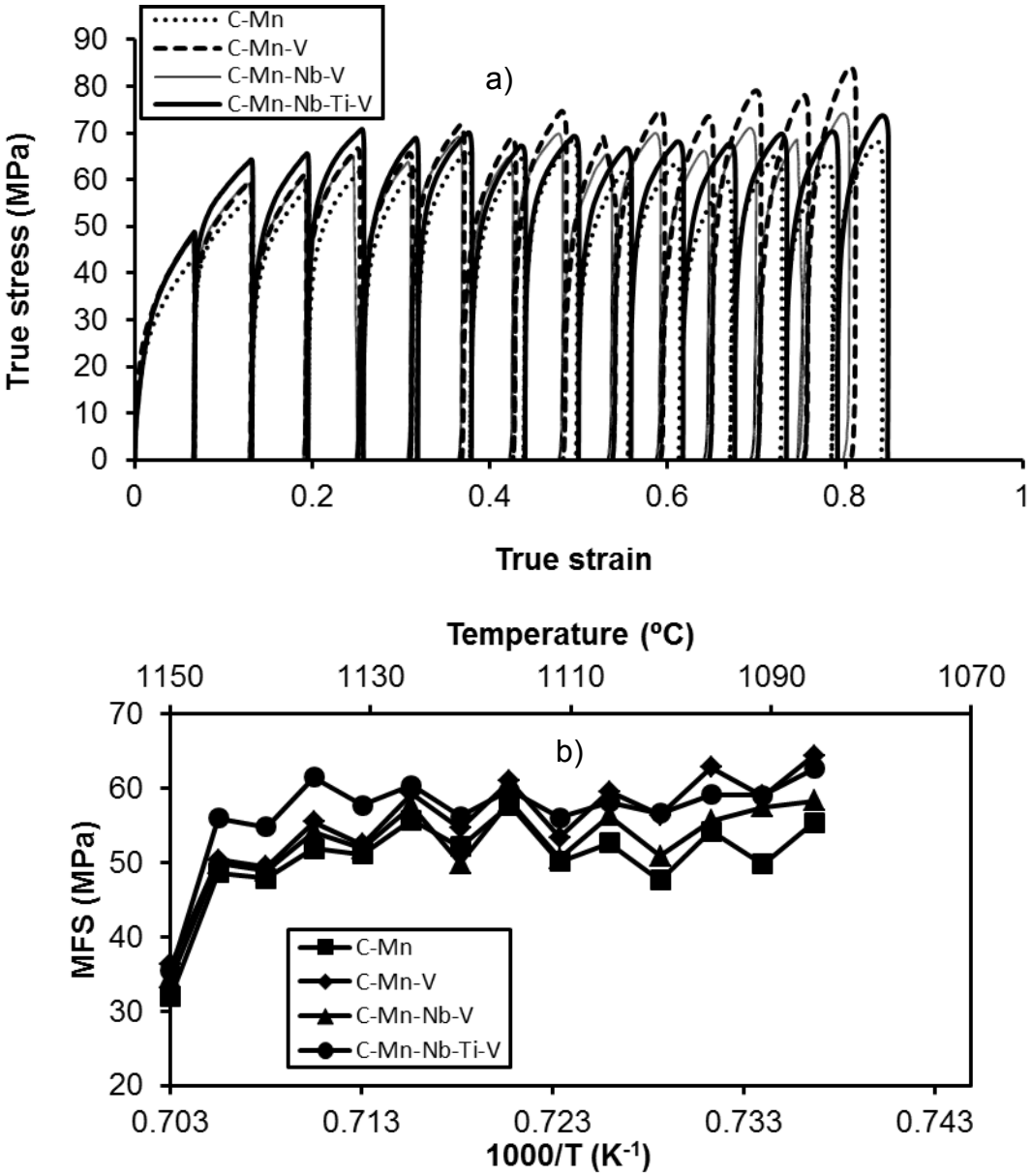

Figure 5.7.: a) True stress-strain curves for the small strain sequence simulations for schedule I_0.07 ε/pass 1085 ºC exit temperature and b) the corresponding MFS for all the studied steels.

The same characteristics with that of schedule I are observed, with no softening taking place between R1 and R2, Figure 5.8a) and b). Application of the 0.4 strain in the last pass increased the stress for all steels and led to a work hardening curve for the C-Mn-Nb-Ti-V steels and a DRV curve for all the other steels.

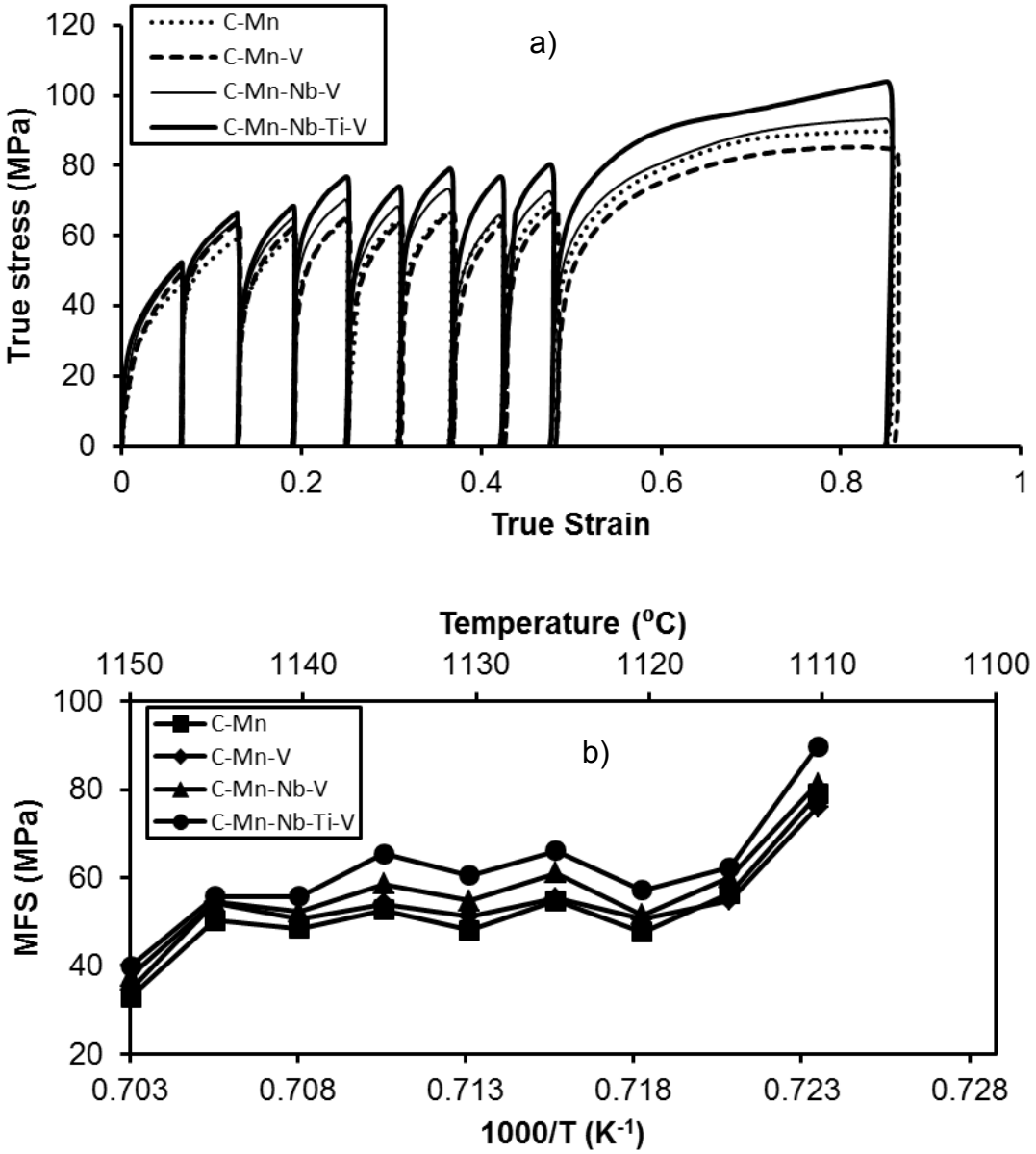

Figure 5.8.: a) True stress-strain curves for the small strain sequence simulations for schedule IV _0.07 ε/pass + 0.4 ε last pass 1110 ºC exit temperature and b) the corresponding MFS for all the studied steels.

Figure 5.9a) and b show a significant decrease in stress in schedule III for the C-Mn, C-Mn-Nb-V (both starting from R6) and C-Mn-Nb-Ti-V (starting from R7) steels. This decrease in stress displays a characteristic of a single curve undergoing DRX. The decrease in stress is not as evident in the C-Mn-V steel. Figure 5.9b) clearly indicates that there is a subtle increase in the MFS for C-Mn-V with decrease in temperature. Unlike with the small strain schedules (I and IV), Figure 5.7 and Figure 5.8, there is

softening between passes at all roughing stages in schedules II and VI. The increase in stress observed in R2 is due to strain accumulated from the partial recrystallized microstructure following R1.

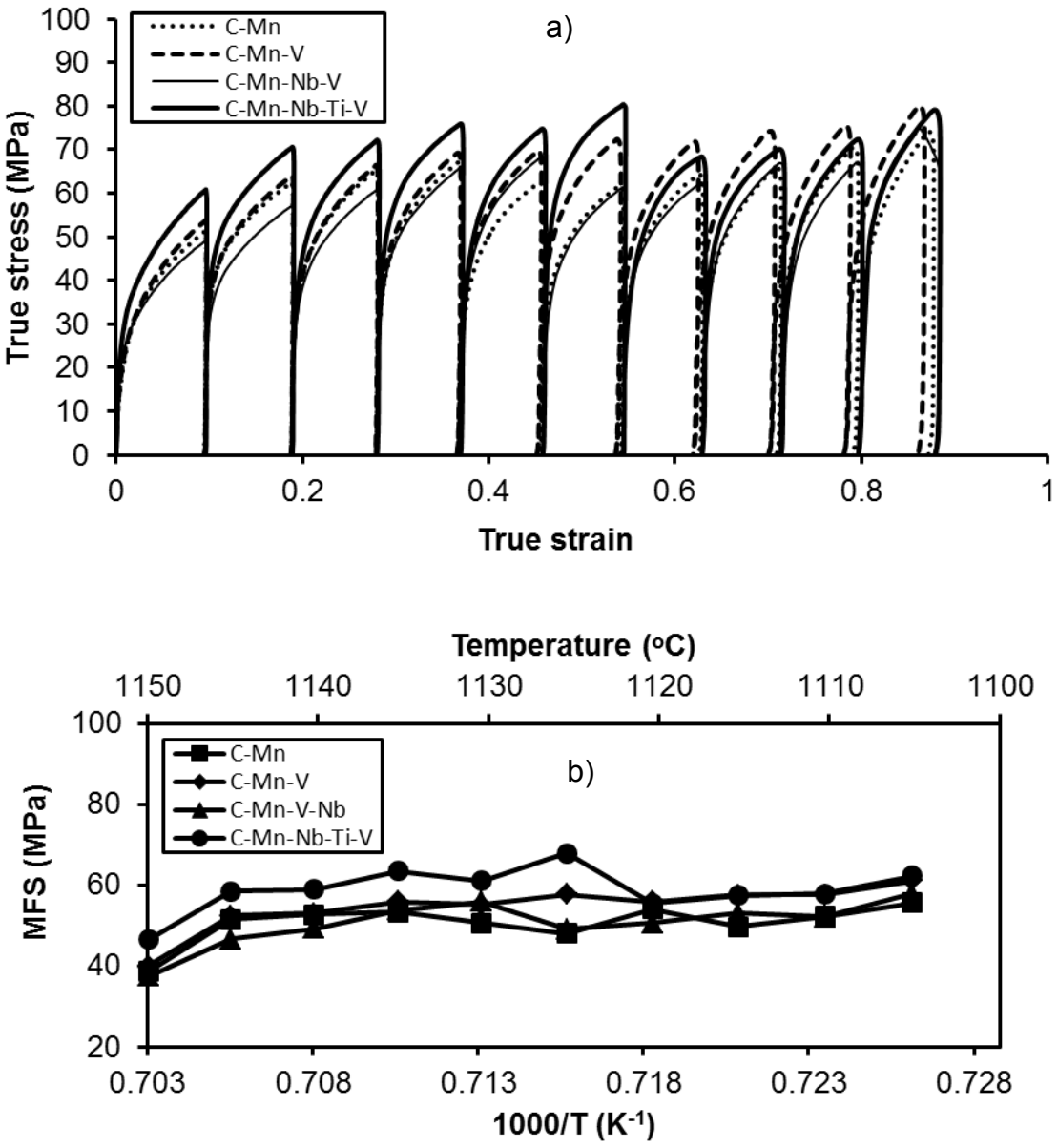

Figure 5.9.: a) True stress-strain curves for the intermediate strain sequence simulations for schedule II_0.1 ε/pass 1105 ºC exit temperature and b) the corresponding MFS for all the studied steels.

Similarly to the other schedules there is an increase in stress in R2 in schedule V due to strain accumulation. The stress then remains constant from R2 to R6 for all the steels. This displays a characteristic of a curve undergoing DRV. The 0.4 strain in the last pass

increased the stress and led to a work hardening curve for all the steels, Figure 5.10) and b.

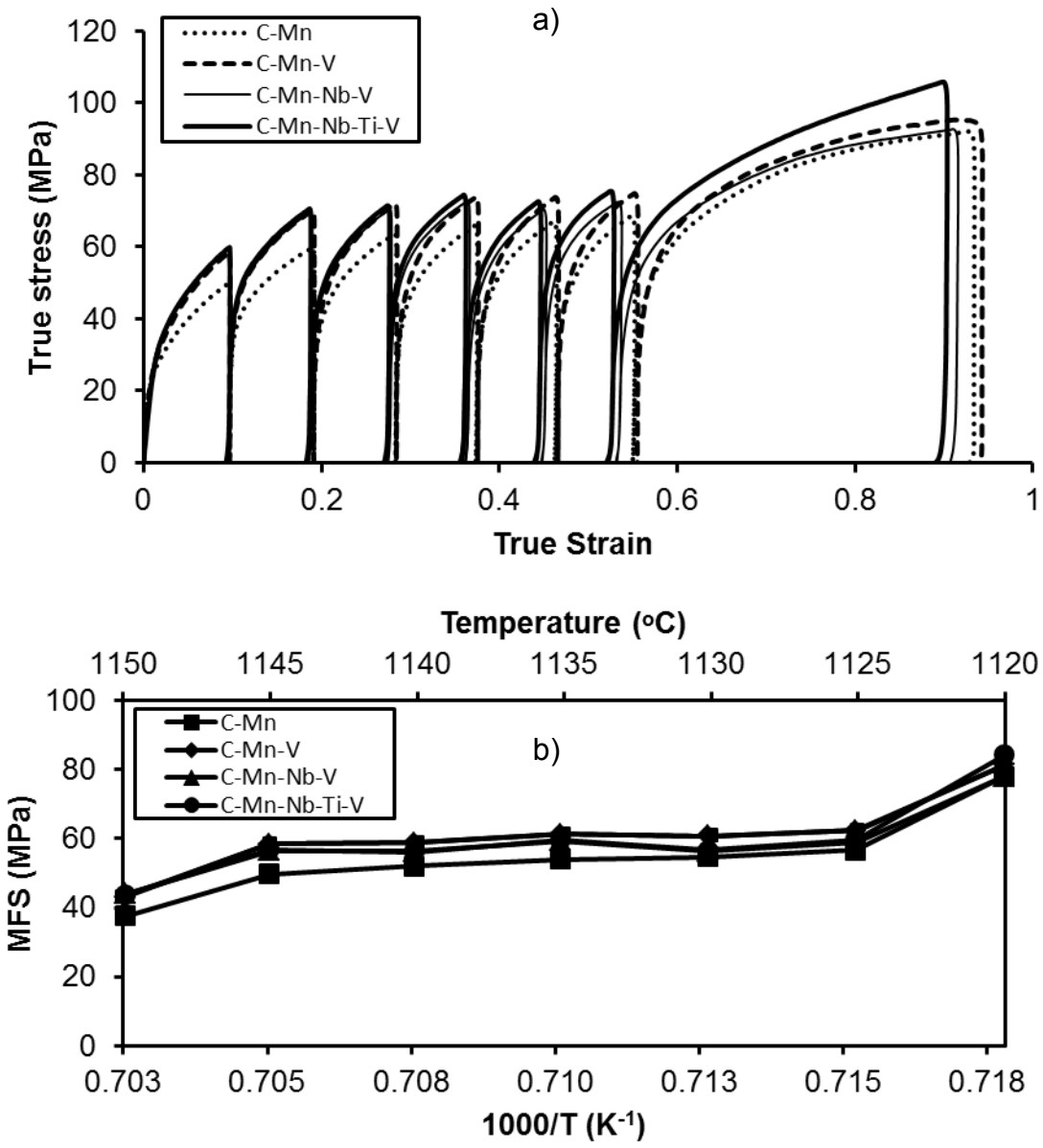

Figure 5.10.: a) True stress-strain curves for the intermediate strain sequence simulations for schedule V _0.1 ε/pass + 0.4 ε last pass 1120 ºC exit and b) the corresponding MFS for all the studied steels.

In the large strain sequence simulations, (schedule III), all the steels increased in stress between R1 and R2 as seen in other schedules, Figure 5.11a) and b). Then the stress remains constant for the microalloyed steels from R2 to R6 illustrating a characteristic of

a single curve undergoing DRV. The C-Mn steel as is the case in schedule II (Figure 5.9) shows a characteristic of a cumulative softening from R3 to R6.

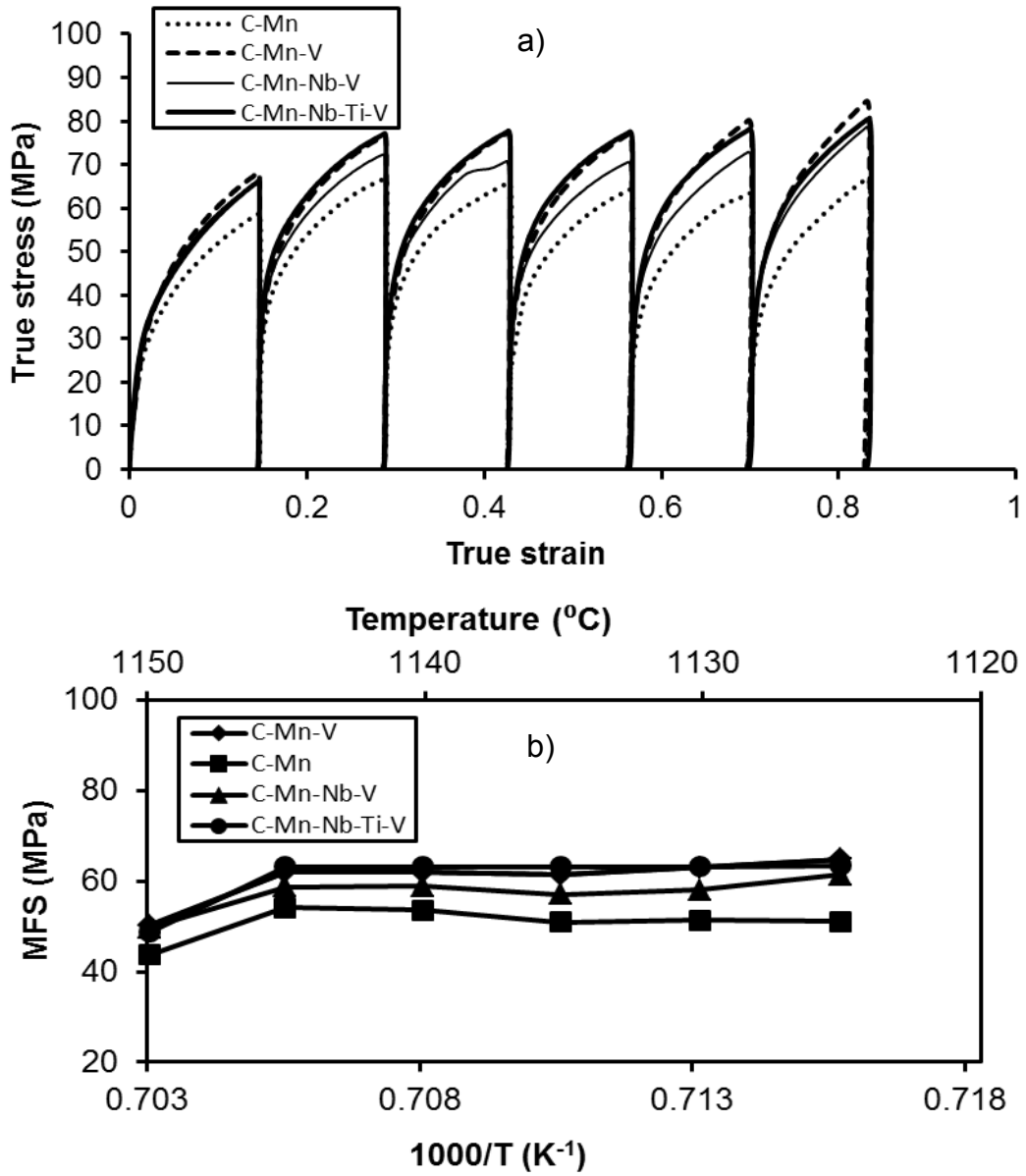

Figure 5.11.: a) True stress-strain curves for the large strain sequence simulation for a) schedule III_0.15 ε/pass 1125 ºC exit temperature and b) the corresponding MFS for all the studied steels.

In schedule VI, Figure 5.12a) and b), a similar behaviour to that of schedule III is observed in the first four passes (R1-R4) for all steels with the stress increasing from R1 to R2 and the stress remaining constant from R2 to R4. Similarly to schedules IV and V application of the 0.4 strain increased the flow stress in all steels. The C-Mn steel

displays DRV behaviour in the 0.4 strain of the last pass whilst the other steels show work hardening behaviour.

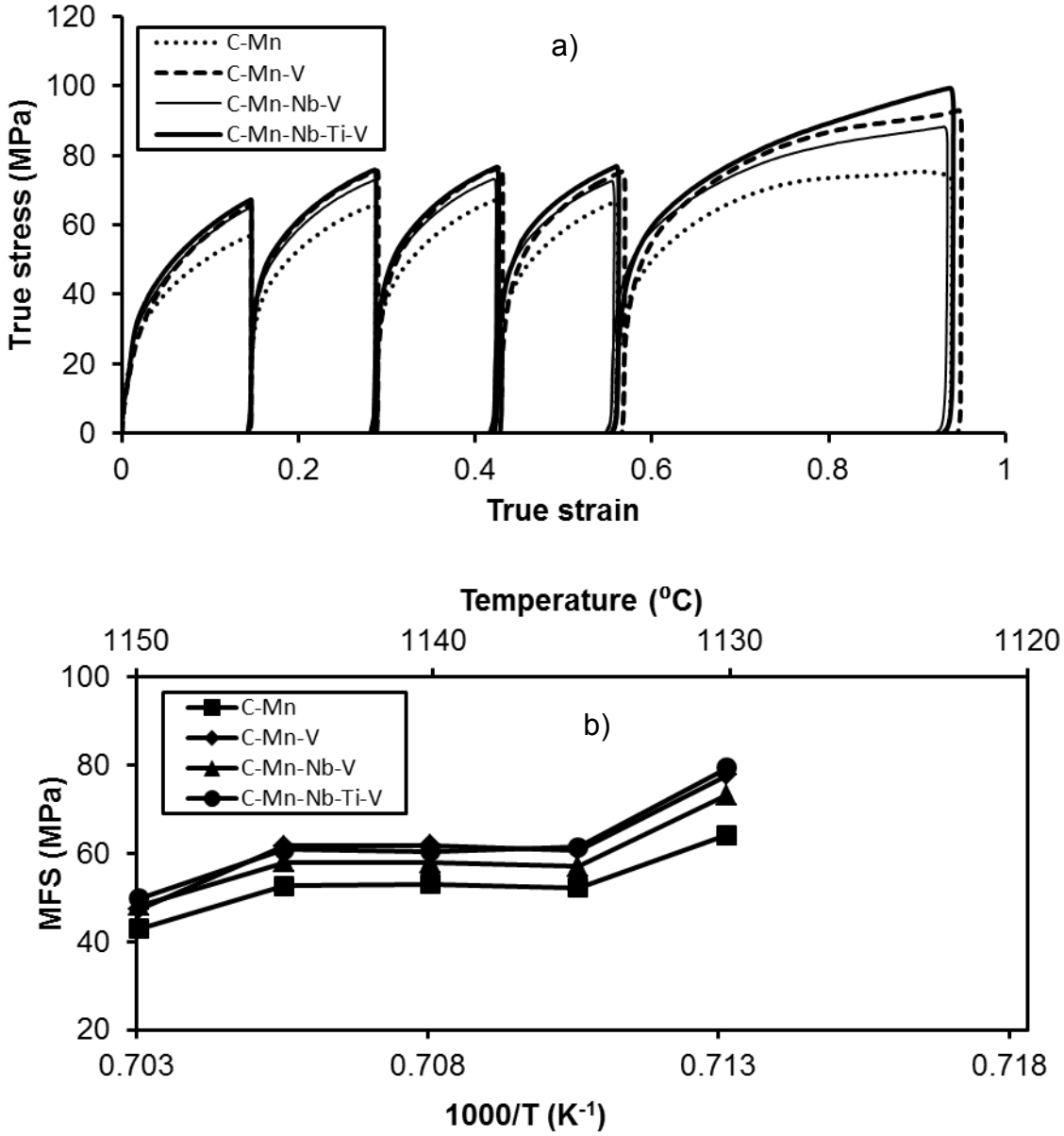

Figure 5.12.: a) True stress-strain curves for the large strain sequence simulation for a schedule VI _0.15 ε/pass + 0.4 ε last pass 1130 ºC high exit temperature and b) the corresponding MFS for all the studied steels.

5.4.2. Low Exit Roughing Temperatures

Figure 5.13 and Figure 5.14 show the true stress-strain curves and the corresponding MFS against inverse temperature plots for the intermediate strain sequence simulations

of schedule VII (0.1ε/pass) and schedule VIII (0.1ε/pass+0.4ε last pass) respectively. The true stress-strain curves for schedules IX and XII (36 seconds delay in the application of the 0.4 strain in the last pass) for the intermediate and large strain sequence respectively, are shown in Appendix C: True stress-strain curves.

Figure 5.13 a) and b) show a general steady increase with decreasing temperature for all steels in schedule VII. In contrast to the high exit temperature intermediate strain sequence (schedule III) that showed a single DRX curve behaviour, schedule VII depicts the characteristic of a single curve undergoing work hardening.

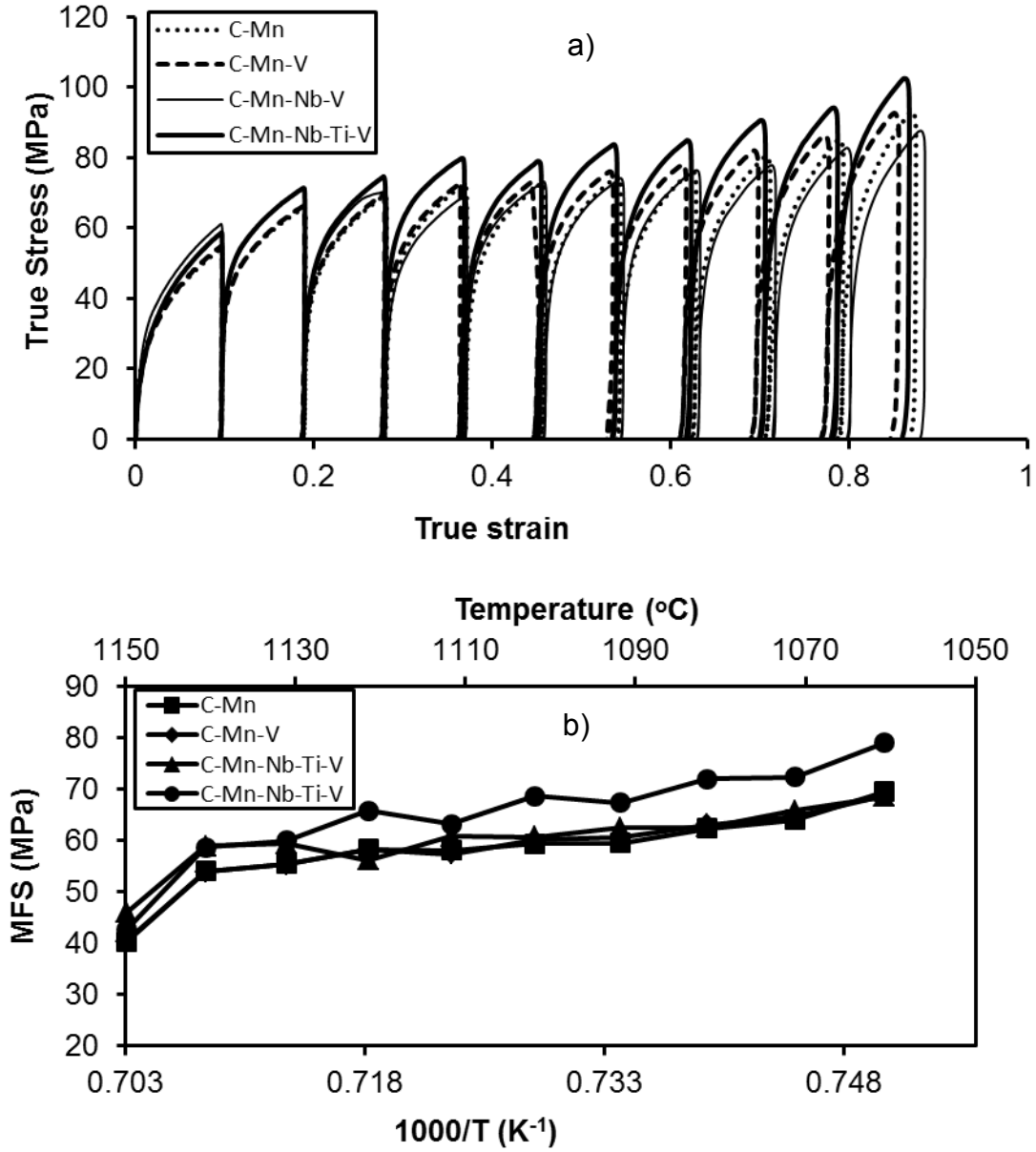

Figure 5.13.: a) True stress-strain curves for the intermediate strain sequence simulation for schedule VII_0.1 ε/pass 1060 ºC exit temperature and b) the corresponding MFS for all the studied steels.

A steady increase in stress with a decrease in temperature is also experienced in schedule VIII for all the steels Figure 5.14a) and b). The last pass of 0.4 increased the stress and led to a work hardening curve for all the steels.

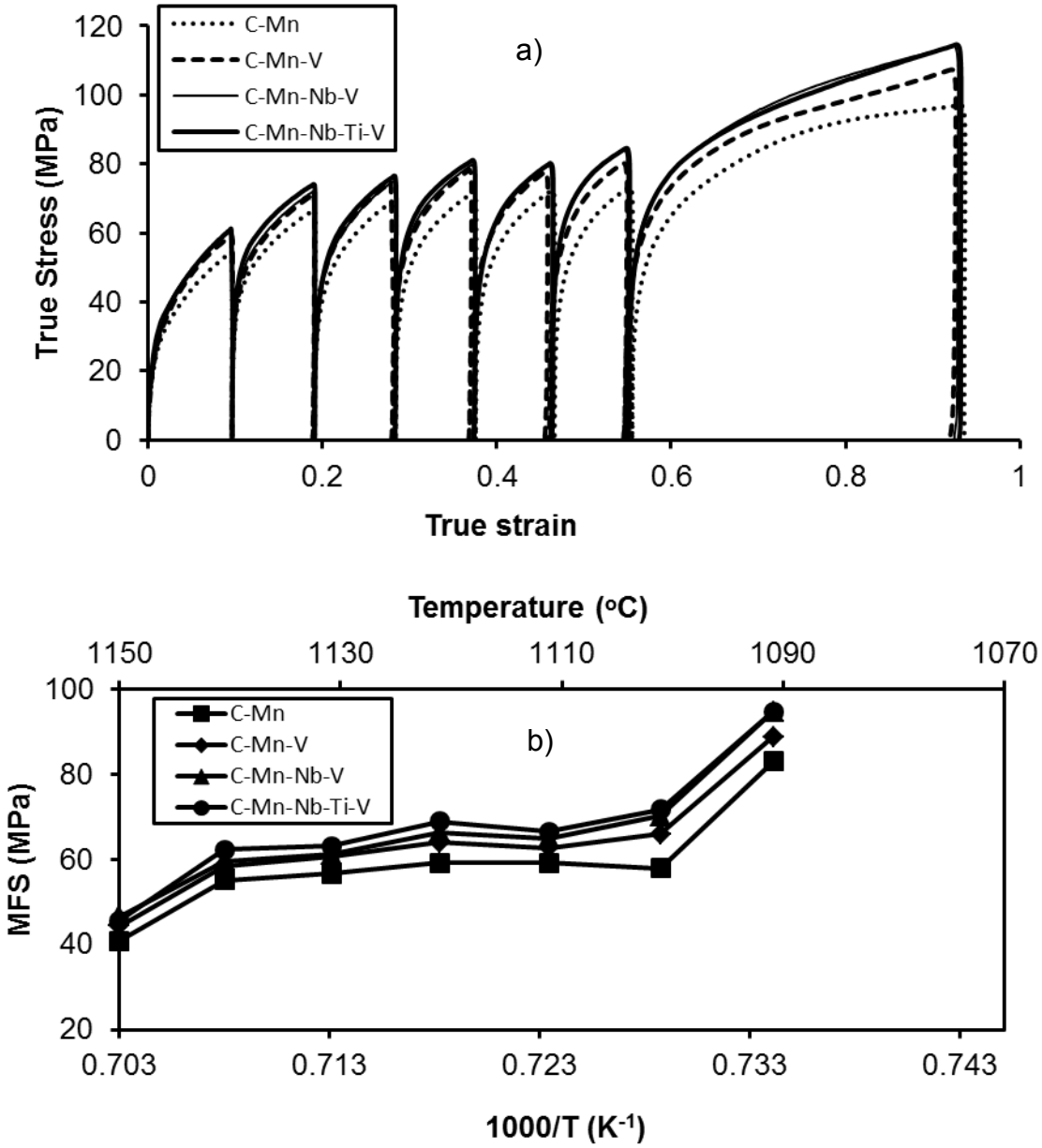

Figure 5.14.: a) True stress-strain curves for the intermediate strain sequence simulation for a) schedule VIII _0.1 ε/pass + 0.4 ε last pass 1090 ºC exit temperature and b) for all the studied steels.

Figure 5.15 and Figure 5.16 show the true stress-strain curves and the corresponding MFS against inverse temperature plots for the large strain sequence simulations of schedule X (0.15 ε/pass) and schedule XI (0.15 ε/pass + 0.4 ε last pass) respectively.

Figure 5.15a) and b) show an increase in stress with decreasing temperature for schedule X. This depicts a single work hardening curve behaviour which is in contrast to

schedule III, the high temperature exit large strain sequence, which displayed a DRV characteristic.

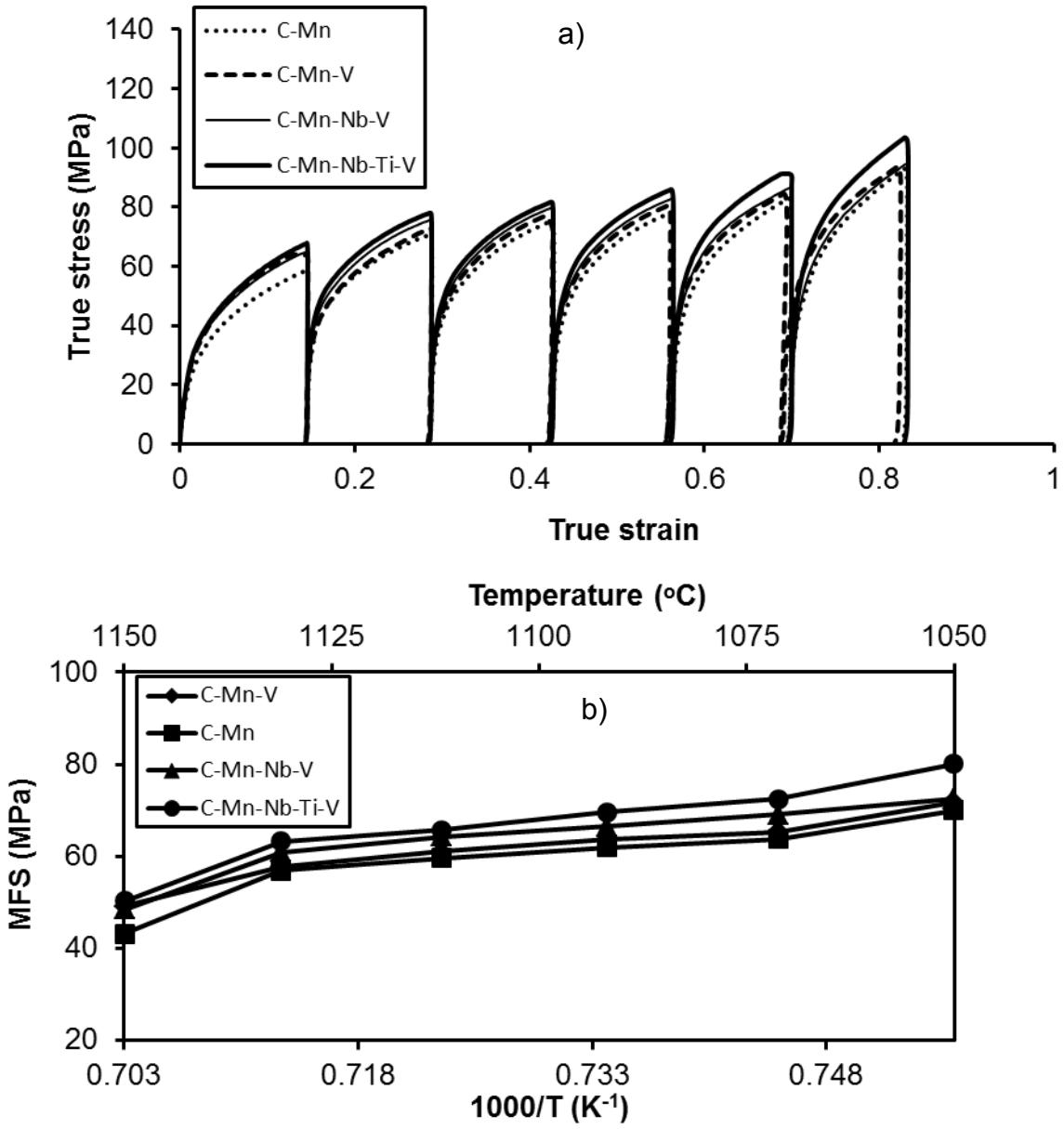

Figure 5.15.: a) True stress-strain curves for the large strain sequence simulation for schedule X_0.15 ε/pass 1050 ºC exit temperature and b) the corresponding MFS for all the studied steels.

In Figure 5.16) and b) there is a steady increase in stress as in schedule X. Application of the 0.4 strain in the last pass increased the stress and led to a DRV curve for the C-Mn steel and work hardening for all the other steels.

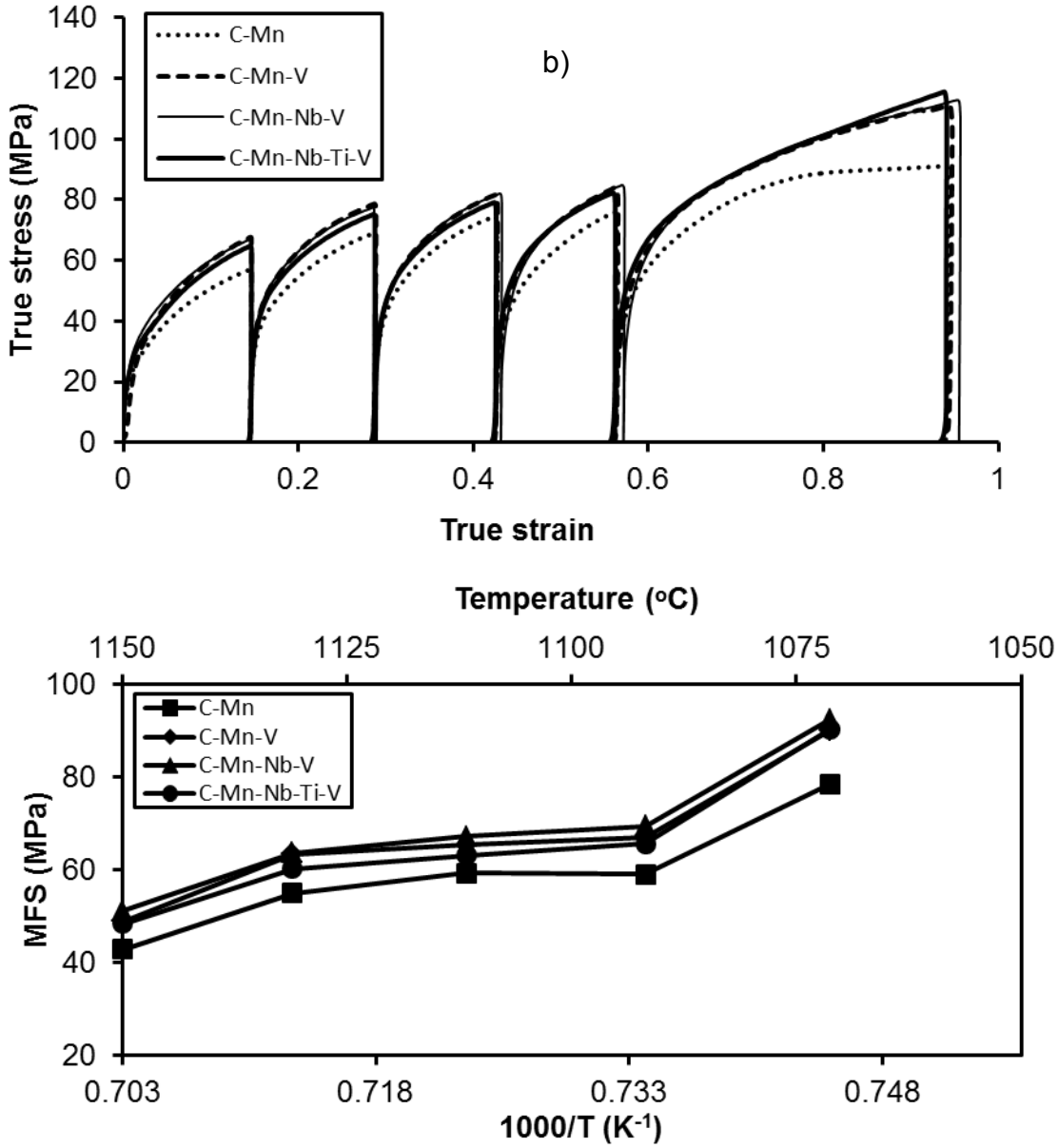

Figure 5.16.: a) True stress-strain curves for the large strain sequence simulation for schedule XI _0.15 ε/pass + 0.4 ε last pass 1070 ºC exit temperature and b) the corresponding MFS for all the studied steels.

5.4.3. Low entry temperature (1050 °C)

From both the high and low exit temperature simulations above it is evident that the C-Mn-V steel has a higher flow stress than that of the C-Mn steel and equal to the C-Mn-Nb-Ti-V steel. To better understand this, a single test was carried out where the entry temperature was reduced by 100 °C from 1150 to 1050 °C for schedule III (0.15 ε/pass). Figure 5.17 shows the true stress-strain curve for this test. In contrast to the 1150 °C

entry results above, the C-Mn-Nb-Ti-V steel has the highest flow stress than that of the C-Mn-V and the C-Mn is the lowest.

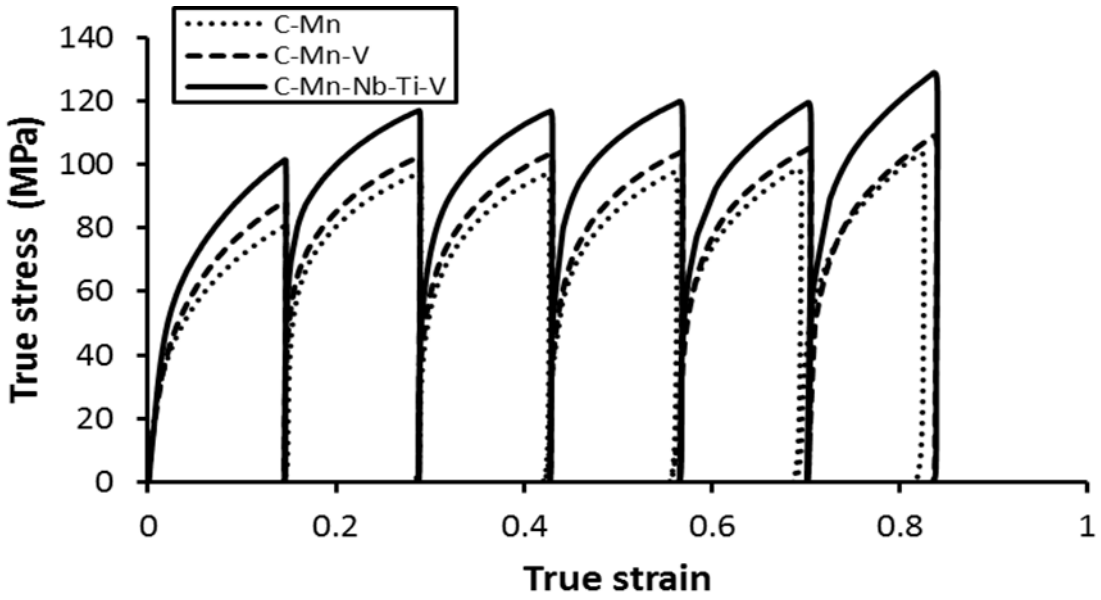

Figure 5.17.: True stress-strain curves of schedule III (0.15 ε/pass) with an entry temperature of 1050 °C and exit of 1025 °C

5.4.4. MFS Comparisons (Laboratory Vs Mill Logs)

The MFS of the industrial hot rolled steel was compared to the laboratory results. The MFS for 12 and 25 mm C-Mn-Nb-Ti-V plates were calculated from Mill Logs using Sims' equation in section 3.5 [65].

Figure 5.18 and Figure 5.19 show the comparison of the MFS for the 25 mm and 12 mm plate respectively together with the laboratory measured MFS. The laboratory determined MFS was converted to Von Mises plane strain conditions

Schedules II, IV, VII and VIII were compared to the mill data for the 25 mm plate and schedules III, VI, X and XI to the 12 mm plate. From both Figure 5.18 and Figure 5.19 it is observed that generally the hot-mill MFS is higher than the laboratory measured MFS.

The hot-mill MFS for the 25 mm plate oscillates in magnitude between temperatures of 1140 and 1090 °C, Figure 5.18. This can be due to strain accumulation arising from

variation between partial and full recrystallization in between passes. The increase in the hot-strip MFS between 1090 and 1060 °C can be due to occurrence of precipitation during hot rolling.

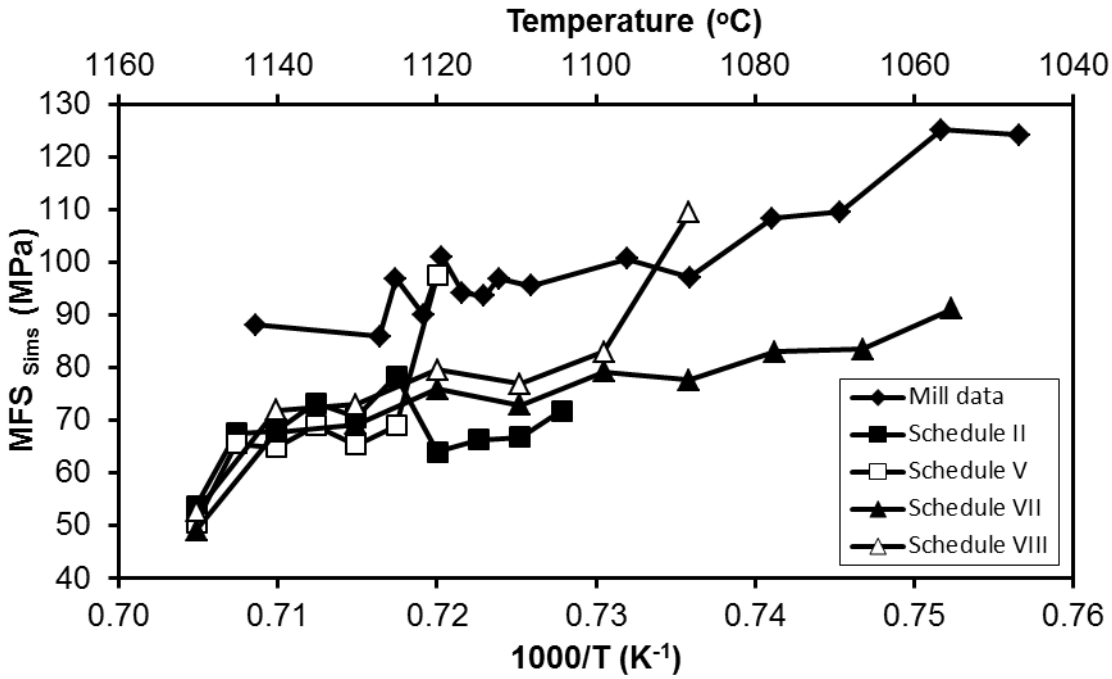

Figure 5.18.: Comparison between the 25 mm plate hot-mill MFS and the laboratory MFS for the C-Mn-Nb-Ti-V steel.

The MFS of the 12 mm plate hot-mill increases in the first three passes between 1160 and 1150 °C indicating strain accumulation. The decrease in the next two passes between 1150 and 1135 °C, may indicate that the accumulated strain led to an effective strain that led to an occurrence of DRX. The hot-mill MFS increased steadily between 1135 and 1055 °C, indicating the dependence of stress on temperature, then increases sharply between 1055 and1045 °C. This increase may be due to other strengthening mechanisms like precipitation, Figure 5.19.

The application of the last pass' 0.4 strain in the laboratory led to MFS values that are s not more than those of the hot-strip MFS for both the 12 and 25 mm plates. The safe work load for this particular mill is about 3500 tons which is about a MFS of 510 MPa if the 0.4 reduction is from a slab thickness of 240 mm. This indicates that the 0.4 strain

will not compromise the force capability of the industrial mill.

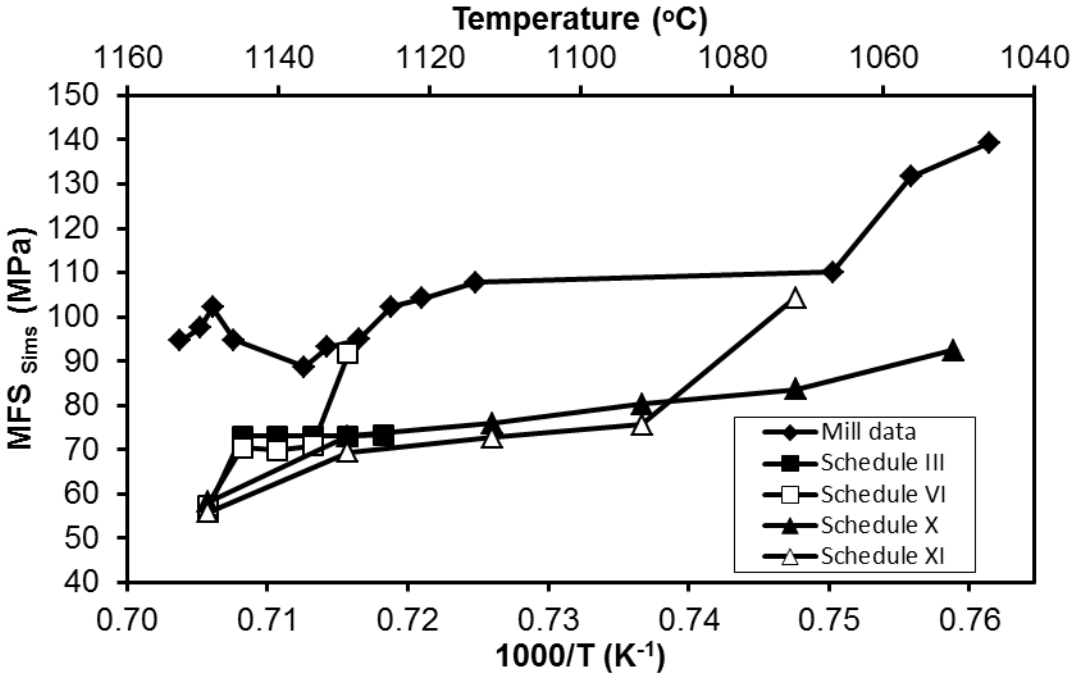

Figure 5.19.: Comparison between the 12 mm plate hot-mill MFS and the laboratory MFS for the C-Mn-Nb-Ti-V steel.

5.4.5. Critical Strain Results

Figure 5.20 shows true stress-strain curves for the studied steels after a single hit deformation of 0.8 true strain at 1100 °C and strain rate of 0.1 s^{-1}. As expected the C-Mn steel has the lowest flow stress and peaks earlier than the microalloyed counterparts. Critical strains were determined from similar curves like the one in Figure 5.20 at various temperatures and strain rate using the Ghazhani *et al*. [117] approach as discussed in section 4.7.

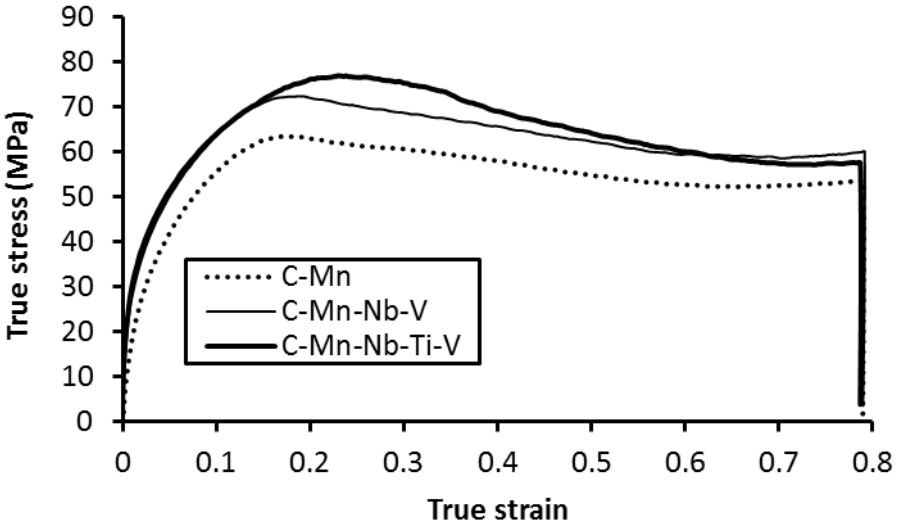

Figure 5.20.: Single hit deformation curves for the studied steels at 1100 °C and strain rate of 0.1 s^{-1}.

Figure 5.21 & Figure 5.22 show the measured critical strains and peak strains respectively for the C-Mn and C-Mn-Nb-Ti-V steels at strain rates of 0.1 and 1 s^{-1}. The critical and peak strain increases with decreasing temperature and increasing strain rate. There is no significant difference between the critical strain of the C-Mn and the C-Mn-Nb-Ti-V steel. This may indicate that most of the Nb is in solution and solute drag is not influencing the ease of softening.

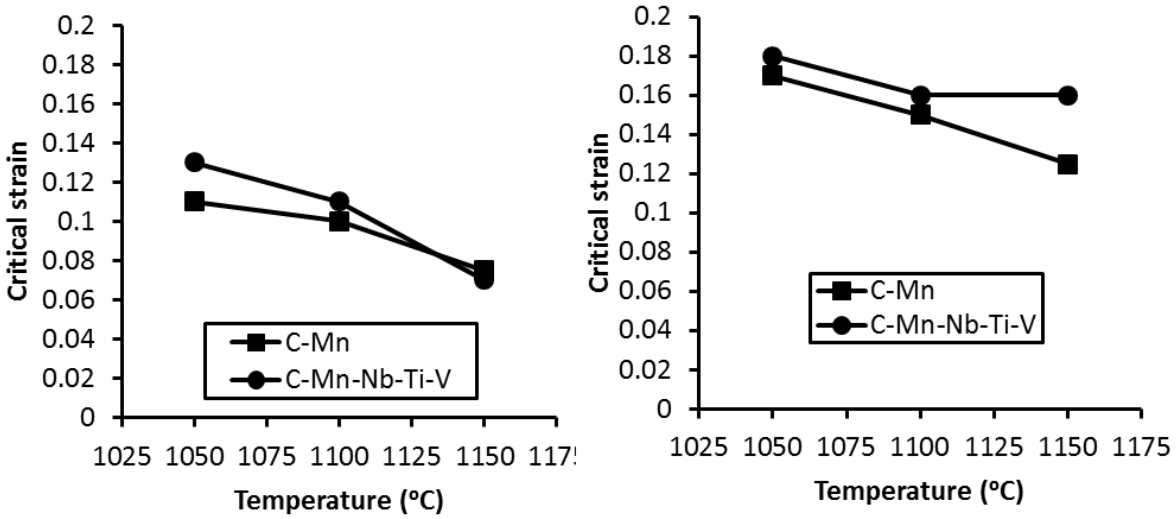

Figure 5.21.: Measured critical strain as function of deformation temperature at a strain rate of a) 0.1 s^{-1} and b)1 s^{-1} for C-Mn and C-Mn-Nb-Ti-V steels.

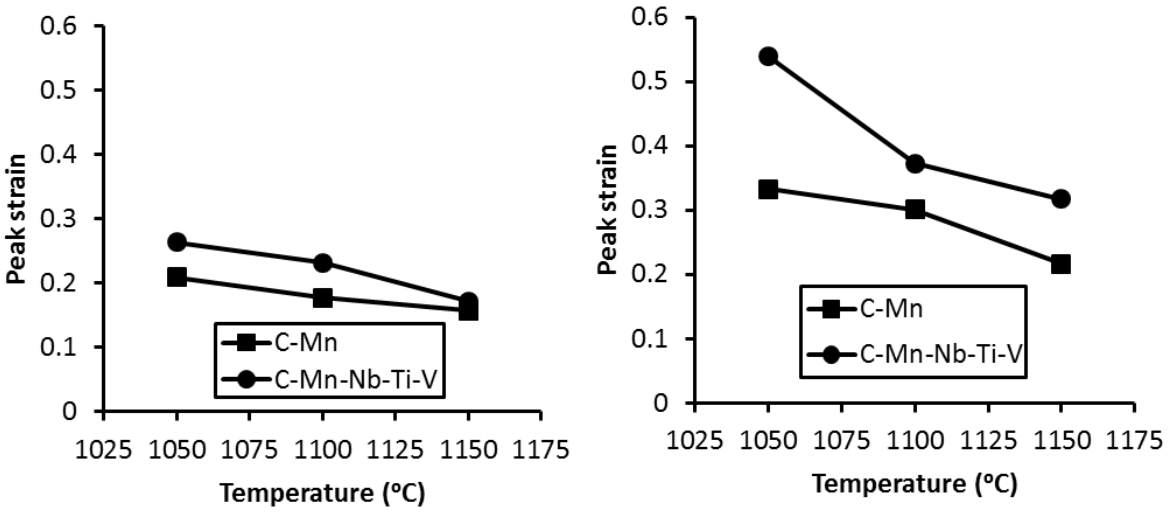

Figure 5.22.: Measured peak strain as function of deformation temperature at a strain rate of a) 0.1s^{-1} and b) 1 s^{-1} for C-Mn and C-Mn-Nb-Ti-V steels.

5.5. Results on the Recrystallized Volume Fraction

This section portrays the recrystallization behaviour of the studied steels under different rolling schedules.

5.5.1. High Exit Roughing Temperatures

Figure 5.23 and Figure 5.24 depict the recrystallized volume fraction (X) as a function of the pass number for the studied steels for the small strain sequence (schedules I and IV) and large strain sequence (schedule III and VI) simulations for high exit roughing temperatures respectively. The recrystallized volume fraction for the intermediate strain sequence, schedules II and V are shown in Appendix D: Volume recrystallized fraction.

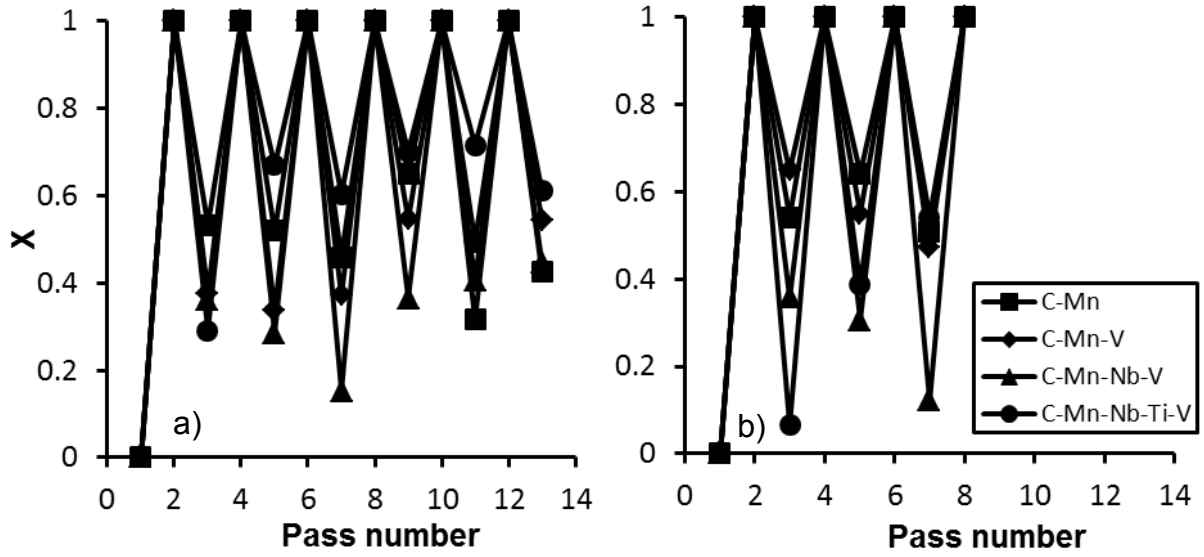

Figure 5.23.: Recrystallization behaviour of the studied steels for the small strain sequence simulation for a) schedule I_0.07 ε/pass 1085 ºC exit temperature and b) schedule IV_0.07 ε/pass + 0.4 ε last pass 1110 ºC exit temperature.

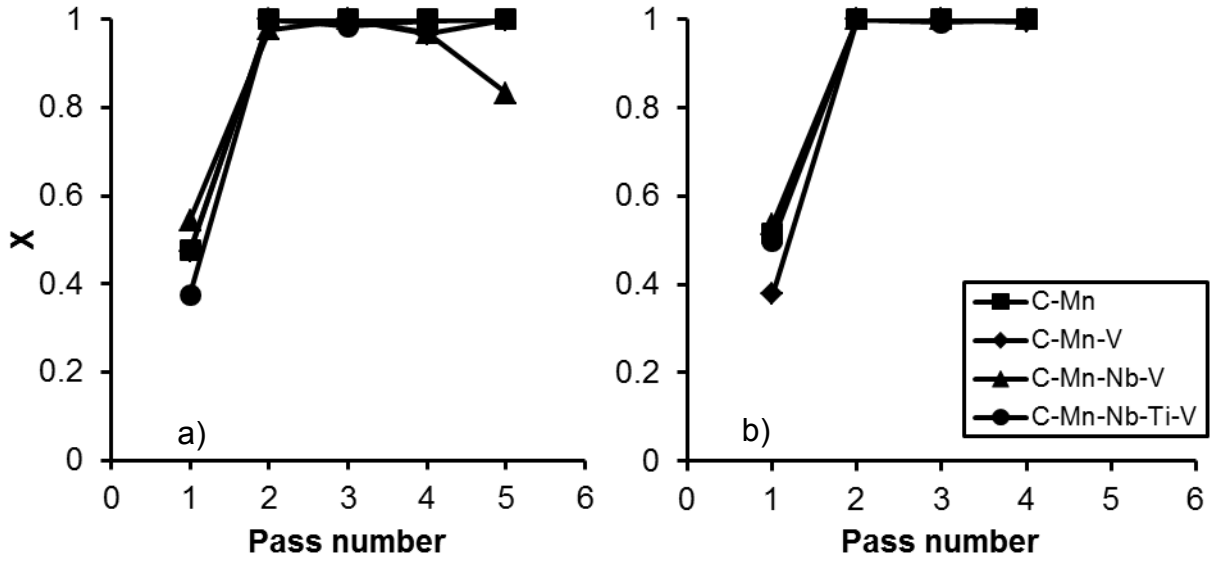

Figure 5.24.: Recrystallization behaviour of the studied steels for the large strain sequence simulation for a) schedule III_0.15ε/pass 1125 ºC exit temperature and b) schedule IV _0.15 ε/pass + 0.4 ε last pass 1130 ºC exit temperature.

Figure 5.23 shows that the small strain sequence's X varies between full and partial recrystallization due to insufficient driving force to promote softening in a single pass. The strain is retained and accumulated in the next pass. Only then is the effective strain sufficient for complete recrystallization. Application of 0.15 strain per pass produced full

recrystallization from the second pass onwards, as shown in Figure 5.24. The intermediate strain sequence's X (Appendix D: Volume recrystallized fraction) was also varying between full and partial recrystallization but the magnitude of the partial volume recrystallized fraction was higher than that of small strain sequences.

Table 5.4 maps the recrystallization behaviour of the C-Mn and C-Mn-Nb-Ti-V steels for the high exit temperature simulations as a complement to the graphical representation in Figure 5.23 and Figure 5.24 above. Full recrystallization (i.e. X ≥ 0.95) is shaded and partial recrystallization is not shaded. It is also clear as the graphical representation showed that only when the pass strain is 0.15 that full recrystallization is attained from the second pass onwards whereas for 0.07 and 0.1 pass strains X oscillates between partial and full recrystallization. There is no significant difference in X between the C-Mn and C-Mn-Nb-Ti-V steel at strains of 0.07 and 0.15. However the partially recrystallized X in the C-Mn-Nb-Ti-V steel at strains of 0.1 is lower than the C-Mn steel. This suggests that recrystallization is delayed by the solute drag of Nb.

Table 5.4.: The influence of strain per pass on the recrystallized volume fraction (X) behaviour of C-Mn and C-Mn-Nb-Ti-V steels for high exit simulations

Recrystallized volume fraction (X)						
	C-Mn			C-Mn-Nb-Ti-V		
ε/pass	**0.07**	**0.10**	**0.15**	**0.07**	**0.10**	**0.15**
1150 °C	0.00	0.13	0.48	0.00	0.26	0.38
1145 °C	1.00	1.00	1.00	1.00	1.00	1.00
1140 °C	0.53	0.87	1.00	0.29	0.67	0.98
1135 °C	1.00	1.00	1.00	1.00	1.00	1.00
1130 °C	0.52	1.00	1.00	0.67	0.51	1.00
1125 °C	1.00	0.91		1.00	1.00	
1120 °C	0.46	1.00		0.60	0.76	
1115 °C	1.00	0.82		1.00	1.00	
1110 °C	0.65	1.00		0.70	0.70	
1105 °C	1.00			1.00		
1100 °C	0.32			0.71		
1095 °C	1.00			1.00		
1090 °C	0.43			0.61		

5.5.2. Low Exit Roughing Temperatures

Figure 5.25 and Figure 5.26 depict the volume recrystallized fraction (X) as a function of the pass number for the intermediate strain sequence and large strain sequence simulations for low exit roughing temperatures, respectively. Similar to the high exit roughing temperature results, there is a higher driving force for the 0.15 strain per pass to promote recrystallization. A strain of 0.1 per pass did not have sufficient driving force and led to an oscillating pattern of full and partial recrystallization. Similar results were found for the 36 s delay schedules and are portrayed in Appendix D: Volume recrystallized fraction. As it was found with the high exit simulation at strains of 0.1, Figure 5.25, the partially volume recrystallized fraction magnitude is lower in the C-Mn-Nb-V and C-Mn-Nb-Ti-V steels compared to that in the C-Mn and C-Mn-V steels. This may indicate that recrystallization is retarded by solute drag of Nb in the Nb-containing microalloyed steels.

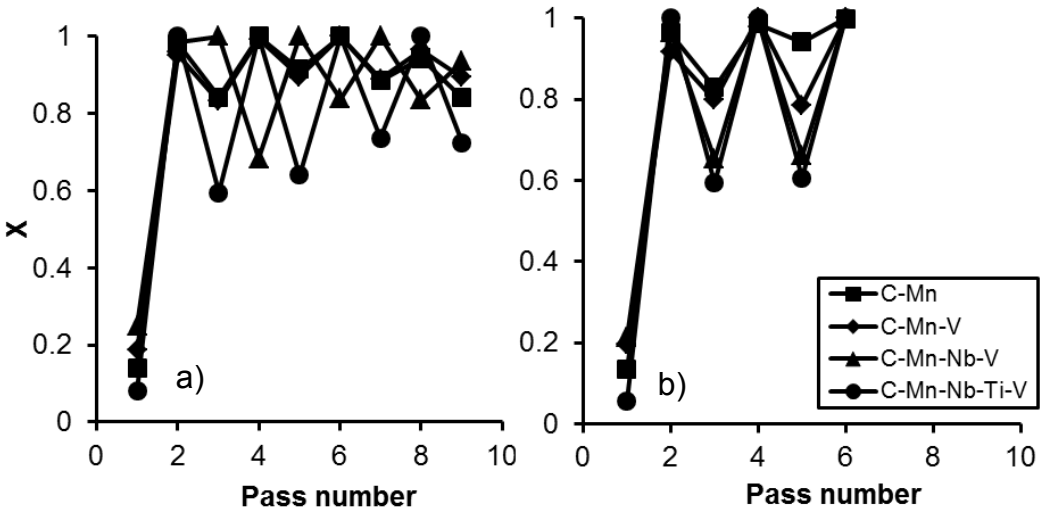

Figure 5.25.: Recrystallization behaviour of the studied steels for the intermediate strain sequence simulation for a) schedule VII_0.1 ε/pass 1060 ºC exit temperature and b) schedule VIII _0.1 ε/pass + 0.4 ε last pass 1090 ºC exit temperature.

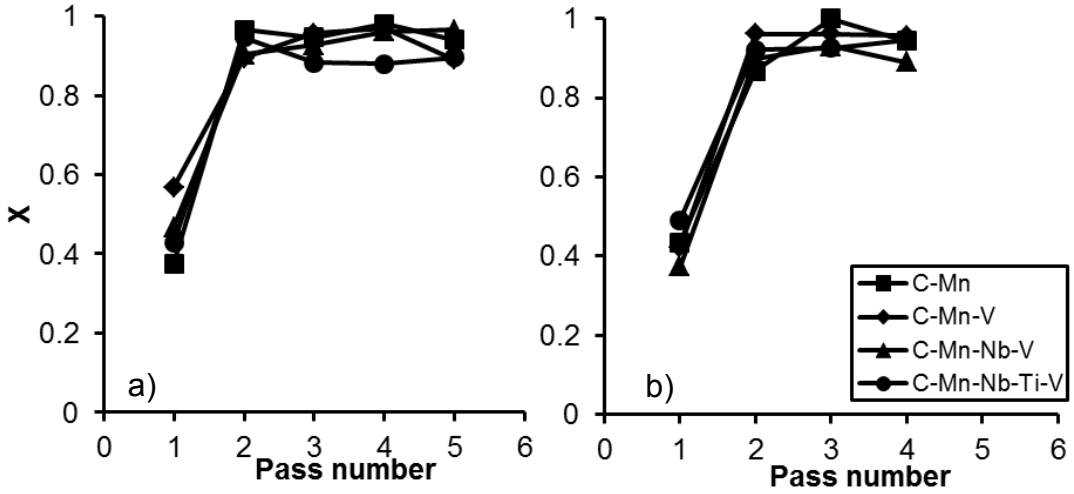

Figure 5.26.: Recrystallization behaviour of the studied steels for the large strain sequence simulation for a) schedule X_0.15 ε/pass 1050 ºC exit temperature and b) schedule XI _0.15 ε/pass + 0.4 ε last pass 1070 ºC exit temperature.

5.6. Austenite Microstructures from Post Hot Rolling Simulation

The influence of rolling schedule on the austenite microstructure after roughing is depicted in this section and is significant for this study. The C-Mn-V steel results are not shown due to etching difficulties.

5.6.1. High Exit Roughing Temperatures

Figure 5.27 and Figure 5.28 show the austenite microstructures and the corresponding grain size distribution for the C-Mn, C-Mn-Nb-V and C-Mn-Nb-Ti-V steels for the small strain sequence simulation, schedule I (0.07 ε/pass) and schedule IV (0.07 ε/pass + 0.4 ε last pass) respectively. The C-Mn steel has a coarser austenite grain size and a wider grain size distribution as compared to the C-Mn-Nb-V and C-Mn-Nb-Ti-V steels in schedule I. A bimodal grain size distribution is observed in the C-Mn steel and a uni-modal distribution that is skewed to the right is evident in both the microalloyed steels, Figure 5.27. In schedule IV, Figure 5.28, the application of a 0.4 strain in the last pass led to a much finer and uniform grain size as compared to schedule I for all the steels. This is more pronounced in the C-Mn steel, showing 64% difference in grain size between schedule I and IV as compared to 47% in the C-Mn-Nb-V steel.

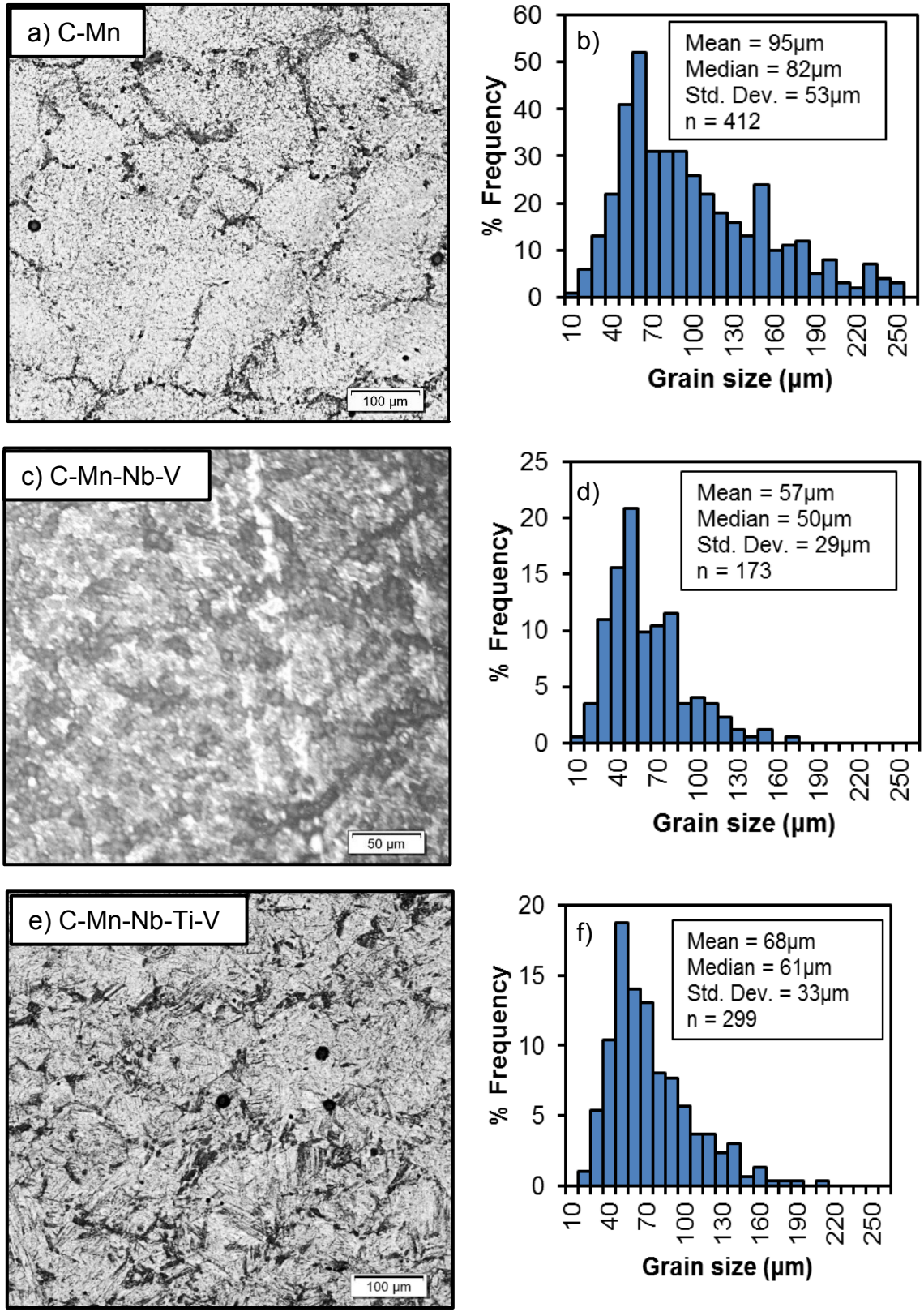

Figure 5.27.: Austenite microstructures and the corresponding grain size distribution for a)- b) C-Mn, c)-d) C-Mn-Nb-V and e)-f) C-Mn-Nb-Ti-V after small strain simulation, schedule I: 0.07 ε/pass 1085 °C exit temperature.

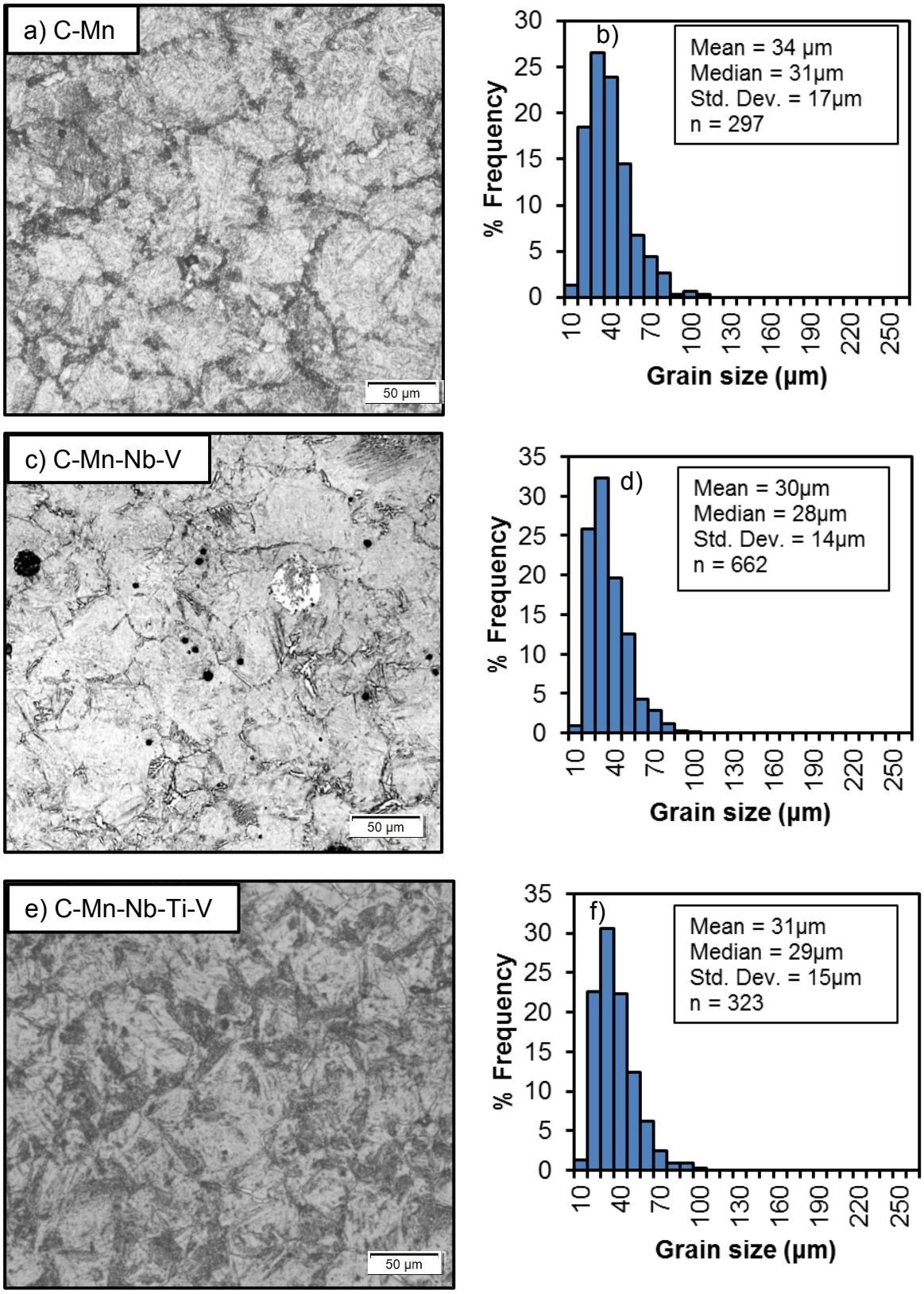

Figure 5.28.: Austenite microstructures and the corresponding grain size distribution for a)- b) C-Mn, c)-d) C-Mn-Nb-V and e)-f) C-Mn-Nb-Ti-V after small strain simulation, schedule IV: 0.07 ε/pass + 0.4 ε last pass 1085 °C exit temperature.

Figure 5.29 and Figure 5.30 show the austenite microstructures and the corresponding grain size distribution for the C-Mn, C-Mn-Nb-V and C-Mn-Nb-Ti-V steels for the large strain sequence simulation, schedule III (0.15ε/pass) and schedule VI (0.15ε/pass + 0.4ε last pass) respectively.

Figure 5.29 shows that the C-Mn steel is coarser and has a wider grain size distribution than the C-Mn-Nb-V and C-Mn-Nb-Ti-V steels. The 0.15 strain per pass led to finer grain sizes than the 0.07 strain per pass (schedule I) in Figure 5.27 for all the steels. Unlike schedule IV (0.07ε/pass + 0.4ε last pass) in Figure 5.28, the application of a 0.4 strain in the last pass led to a more refined grain size and a narrower distribution for the C-Mn-Nb-Ti-V steel only, Figure 5.30.

There is no difference in grain size and distribution for the C-Mn-Nb-V steel between schedule III (0.15ε/pass) and schedule VI (0.15ε/pass + 0.4ε last pass). The additional 0.4 strain in the last pass led to a small reduction in grain size for the C-Mn steel. This indicates that possibly a saturation point is reached where no further refinement can occur for these steels.

The austenite grain size results for all the high exit temperature roughing pass simulations are summarized in Table 5.5 and are also shown graphically in Figure 5.31. Table 5.5 and Figure 5.31 show that the austenite grain sizes decrease with an increase in applied strain per pass and is more pronounced in the C-Mn steel. Application of the 0.4 strain in the last pass generally neutralizes the grain size difference caused by the different chemistries in these steels.

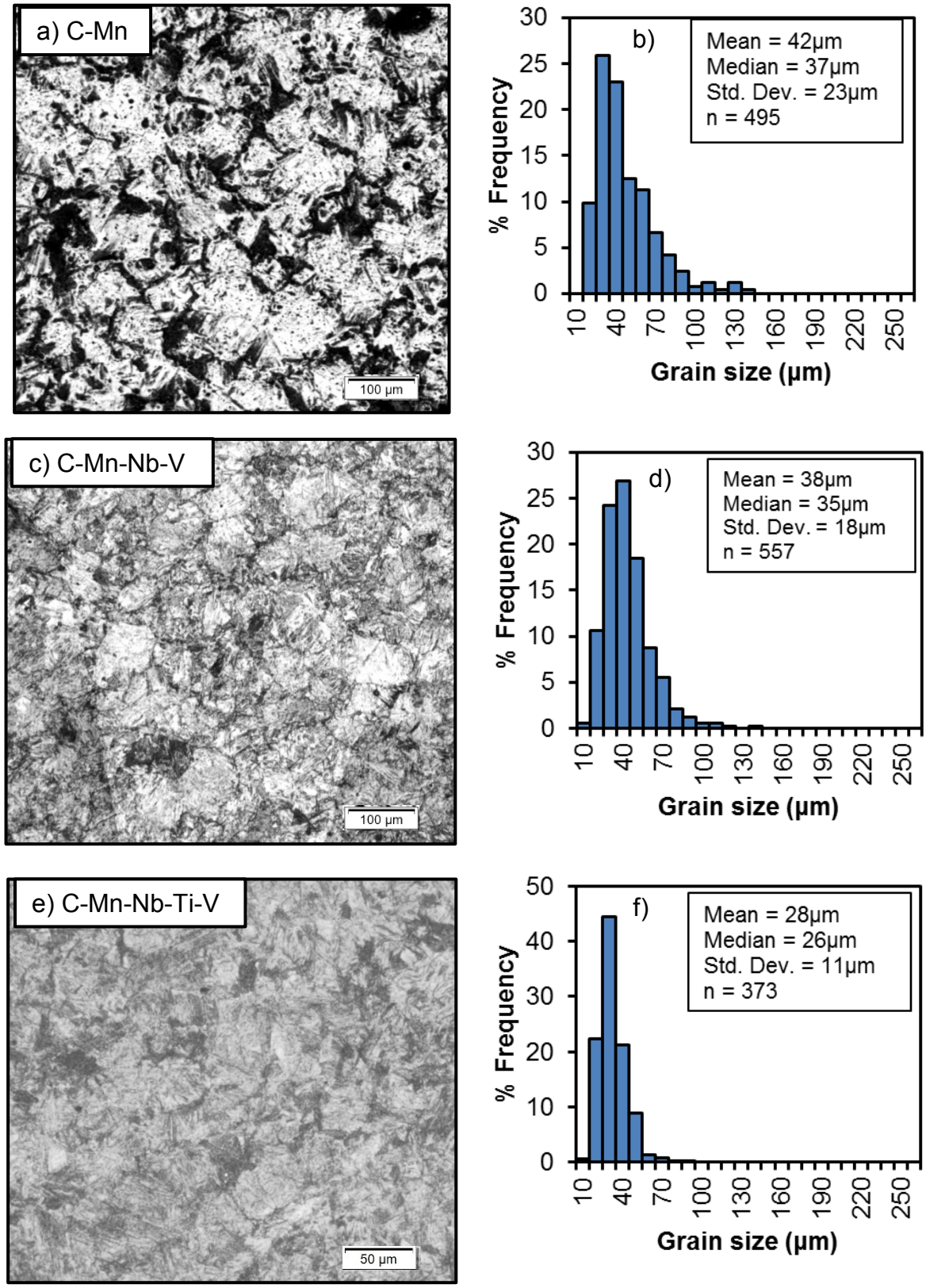

Figure 5.29.: Austenite microstructures and the corresponding grain size distribution for a)- b) C-Mn, c)-d) C-Mn-Nb-V and e)-f) C-Mn-Nb-Ti-V after large strain simulation, schedule III: 0.15 ε/pass 1125 °C exit temperature.

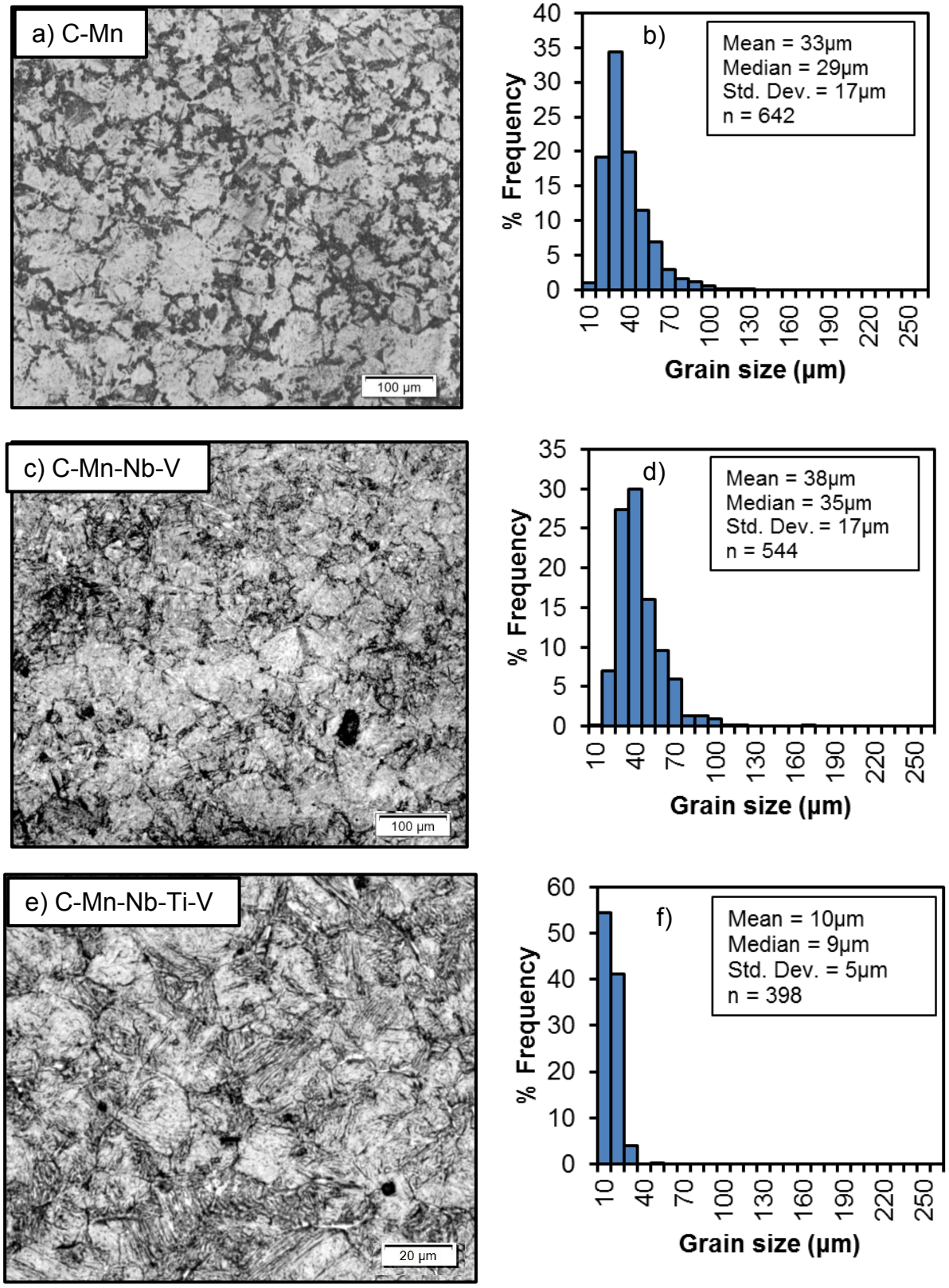

Figure 5.30.: Austenite microstructures and the corresponding grain size distribution for a)- b) C-Mn, c)-d) C-Mn-Nb-V and e)-f) C-Mn-Nb-Ti-V after large strain simulation, schedule VI: 0.15 ε/pass + 0.4 ε last pass, 1130 °C exit temperature.

Table 5.5.: Measured austenite grain sizes of the studied steels after hot rolling schedules I to VI.

Schedule	Exit temperature (°C)	Austenite grain size (µm)		
		C-Mn	C-Mn-Nb-V	C-Mn-Nb-Ti-V
I (0.07ε/pass)	1085	95	57	68
II (0.1ε/pass)	1105	57	42	-
III (0.15ε/pass)	1125	42	38	28
IV (0.07ε/pass + 0.4ε last pass)	1110	34	30	31
V (0.1ε/pass + 0.4ε last pass)	1120	29	26	-
VI ((0ε/pass + 0.4ε last pass)	1130	33	38	10

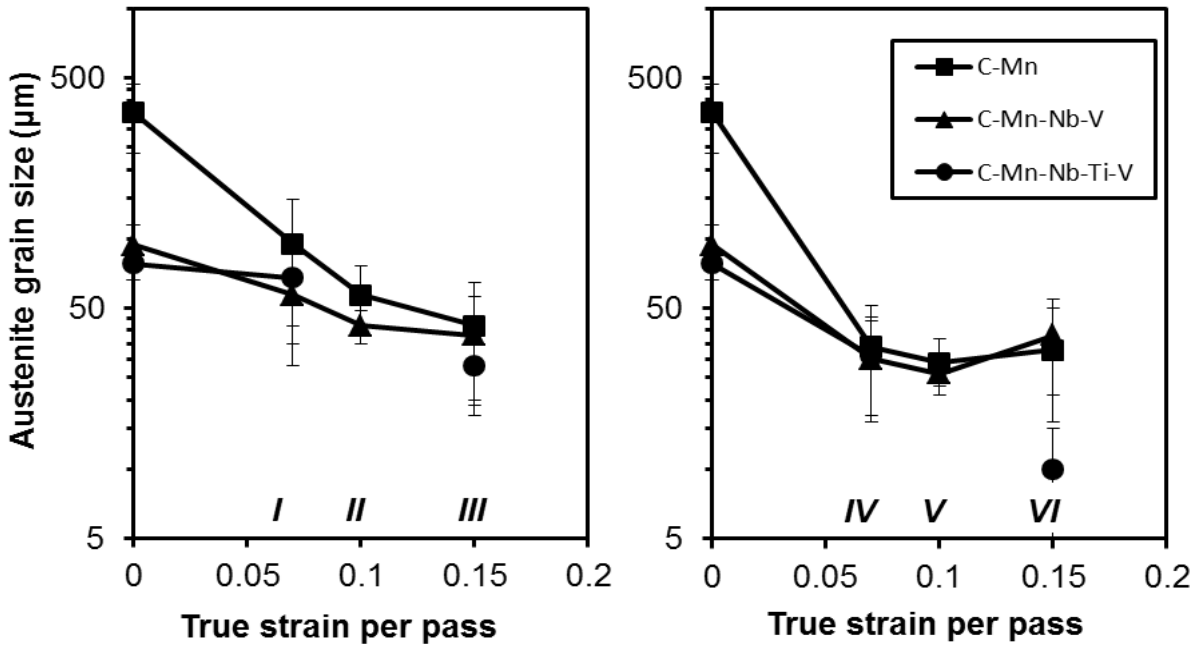

Figure 5.31.: The measured average austenite grain size as a function of applied true strain per pass for a) constant strain per pass, schedules I-III and b) application of 0.4 strain in the last pass, schedules IV-VI for the studied steels.

5.6.2. Low Exit Temperatures

Figure 5.32 shows the austenite microstructures and the corresponding grain size distributions of the C-Mn steel after the intermediate strain sequence simulations, schedule VII (0.1ε/pass) and schedule VIII (0.1ε/pass+0.4ε last pass). The application of a 0.4 strain in the last pass refined the coarse microstructure of 0.1 strain only per pass and led to a narrower grain size distribution.

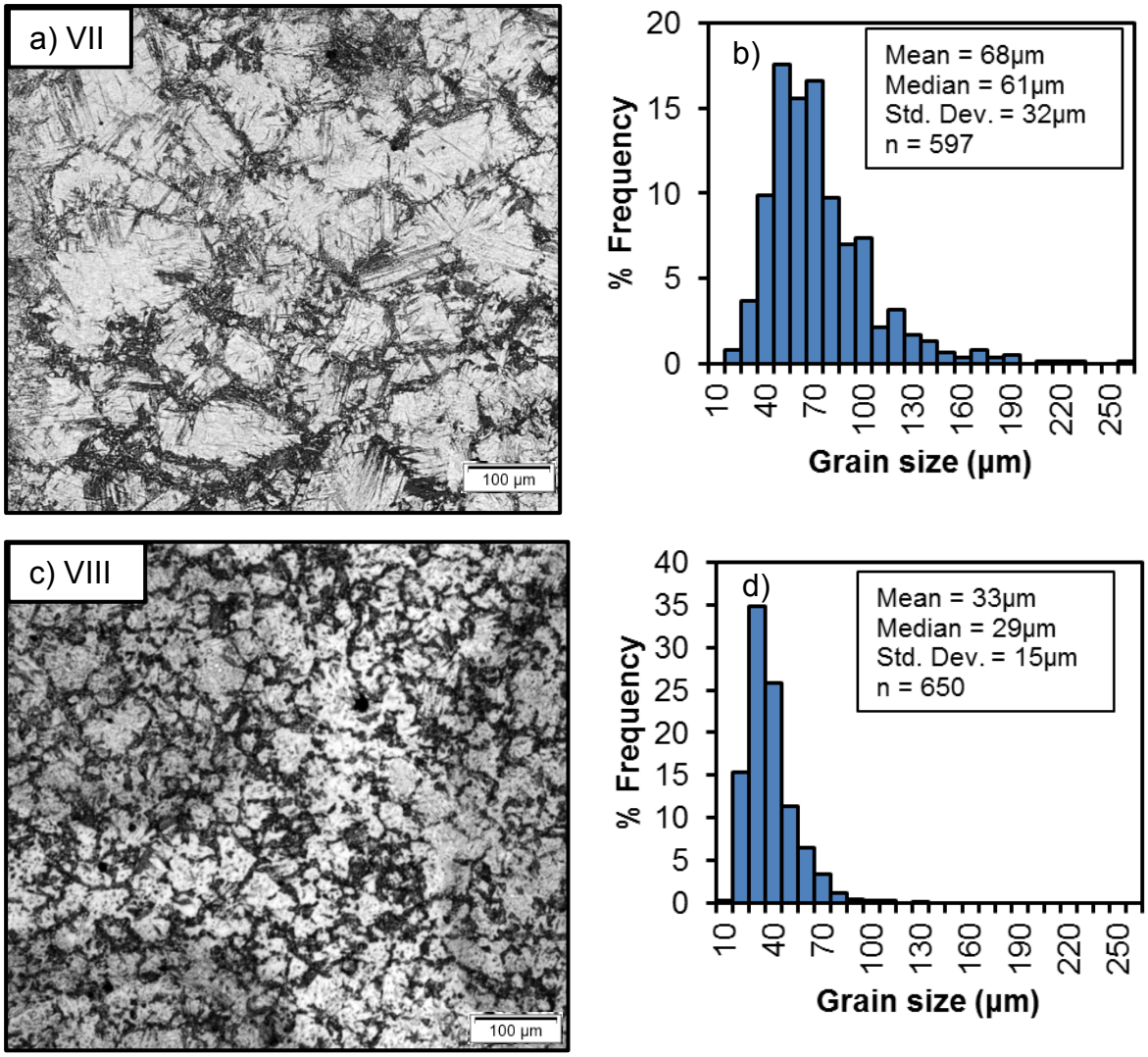

Figure 5.32.: Austenite microstructures and the corresponding grain size distribution of the C-Mn steel for the intermediate strain sequence a)-b) schedule VII (0.1 ε/pass, 1060 °C exit temperature) and c)-d) schedule VIII (0.1 ε/pass + 0.4 ε last pass, 1090 °C exit temperature).

Figure 5.33 and Figure 5.34 show the microstructures and their respective grain size distributions for the large strain sequence simulations, schedule X (0.15ε/pass) and schedule XI (0.15ε/pass + 0.4ε last pass) respectively for the C-Mn, C-Mn-Nb-V and C-Mn-Nb-Ti-V steels.

The C-Mn-Nb-Ti-V is finer and has a narrower grain size distribution than both the C-Mn and C-Mn-Nb-V steels. All the grain size distributions show a uni-modal behaviour, Figure 5.33. The additional 0.4 strain in the last pass refined the grain size for the C-Mn and C-Mn-Nb-V steels but no grain refinement is observed for the C-Mn-Nb-Ti-V steel, Figure 5.34. This may indicate a saturation point is reached.

The austenite grain sizes are shown for the lower exit roughing temperature schedules VII to XII in Table 5.6 and also portrayed in a graph in Figure 5.35. Similarly to the high exit roughing temperatures, there is grain refinement with an increase in strain per pass with the coarse C-Mn steel showing the most grain refinement.

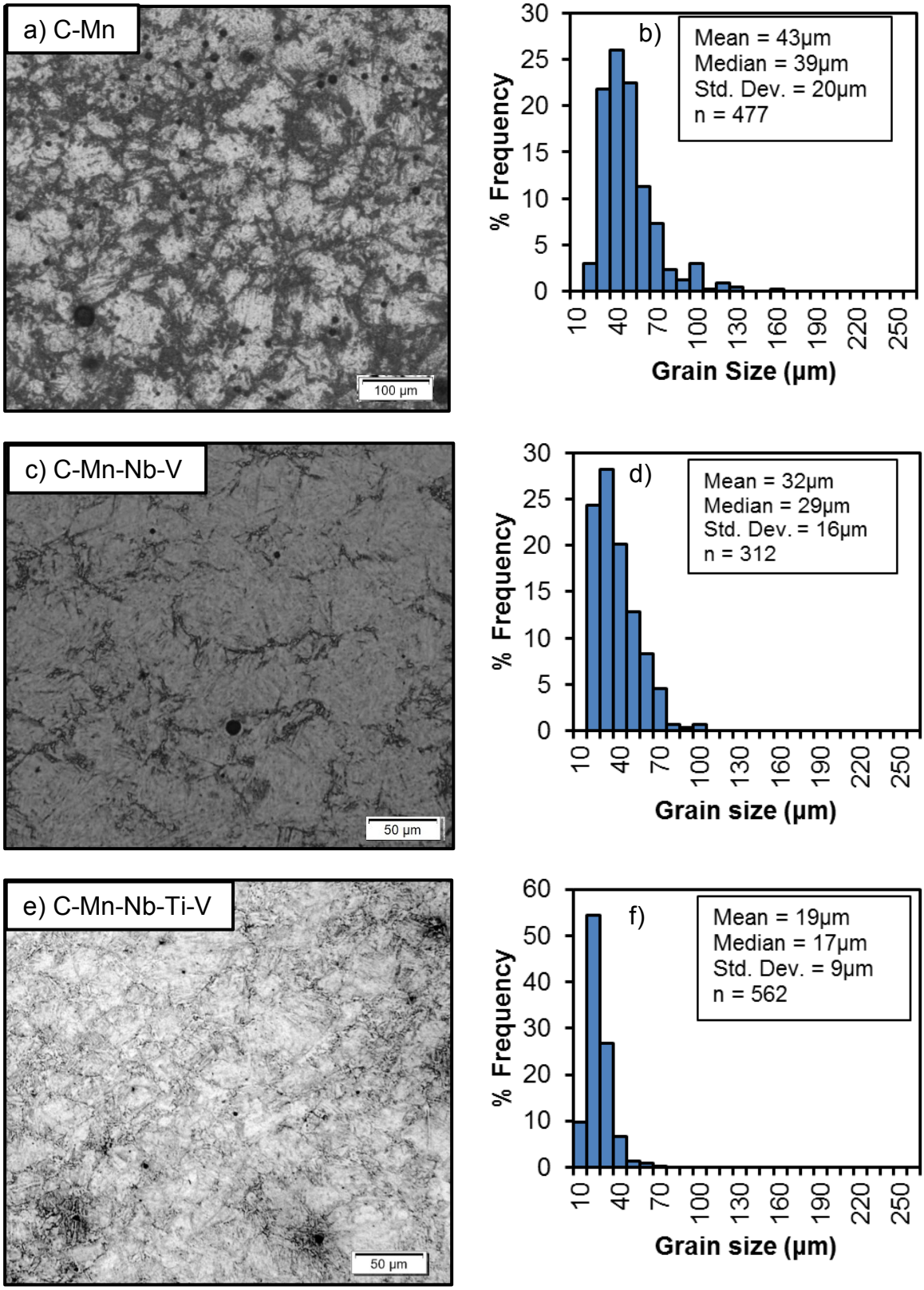

Figure 5.33.: Austenite microstructures and the corresponding grain size distribution for a)- b) C-Mn, c)-d) C-Mn-Nb-V and e)-f) C-Mn-Nb-Ti-V after large strain sequence simulation, schedule X_0.15ε/pass, 1050 °C exit temperature.

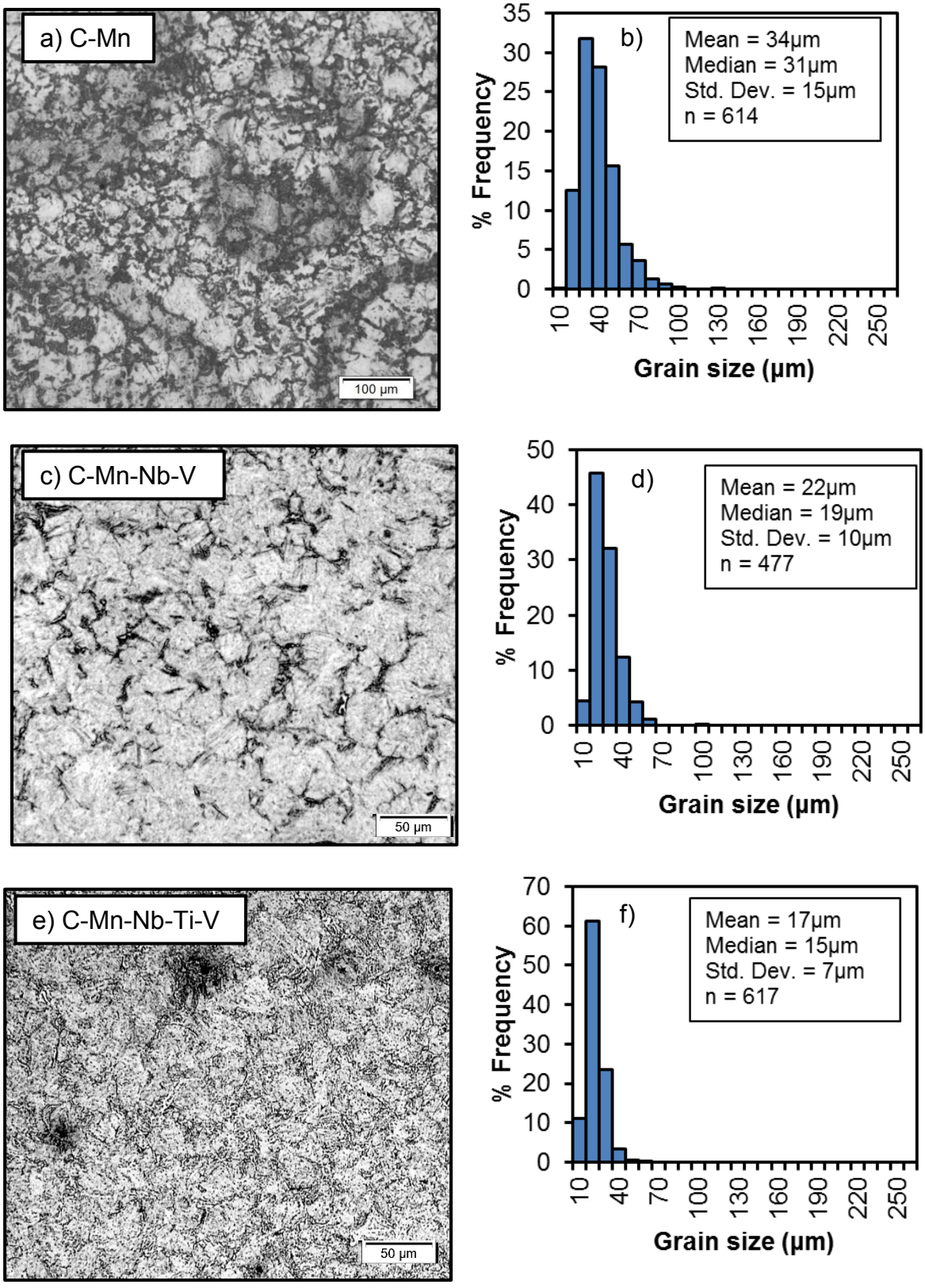

Figure 5.34.: Austenite microstructures and the corresponding grain size distribution for a)- b) C-Mn, c)-d) C-Mn-Nb-V and e)-f) C-Mn-Nb-Ti-V after large strain sequence simulation, schedule XI_0.15ε/pass+0.4ε last pass, 1070 °C exit temperature.

Table 5.6.: Measured austenite grain sizes of the studied steels after hot rolling schedules VII to XII.

Schedule	Exit temperature (°C)	Austenite grain size (μm)		
		C-Mn	C-Mn-Nb-V	C-Mn-Nb-Ti-V
VII (0.1ε/pass)	1060	68	-	38
VIII (0.1ε/pass + 0.4ε last pass)	1090	33	35	29
IX (0.1ε/pass + delayed 0.4ε last pass)	1060	33	-	-
X (0.15ε/pass)	1050	43	32	19
XI (0.15ε/pass + 0.4ε last pass)	1070	36	22	17
XII (0.15ε/pass + delayed 0.4ε last pass)	1050	34	28	-

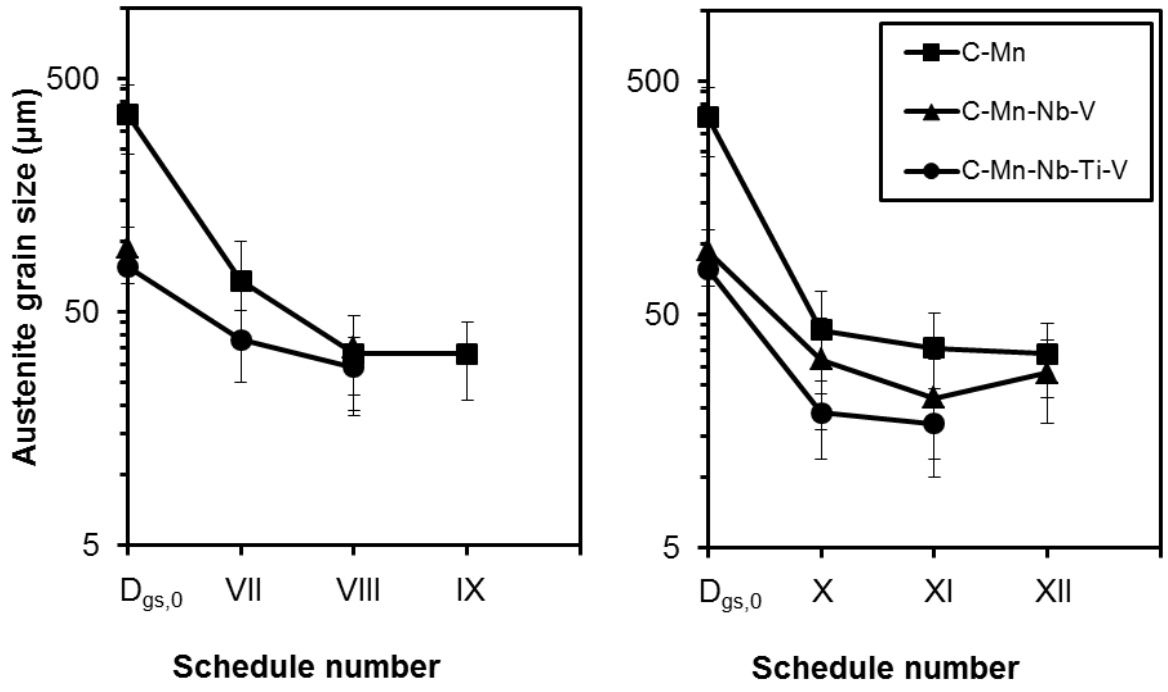

Figure 5.35.: The measured average austenite grain size as a function of the schedule number for the a) intermediate strain sequence simulations and b) large strain sequence simulations for the studied steels.

5.7. FEM Through Strain Distribution

In this section FEM simulated rolling schedules for both the compression test and flat rolling are portrayed with emphasis given to the strain distribution across the specimen thickness. The FEM simulations were carried out by Van Rensburg [97], with the constants and required inputs for the model based on the stress-strain curve results found in this study.

5.7.1. Axisymmetrical Compression Simulation

Figure 5.36 shows a single hit deformation FEM simulation on an axisymmetrical sample of 10 mm long and 5 mm diameter for a strain of 0.15 and a strain rate of 1.5 s^{-1}. Figure 5.36a) shows a schematic of a half-section of an axisymmetric compressed sample and Figure 5.36b) portrays the strain distribution along different paths of the deformed sample, i.e. along the mid-plane, axial and diagonal paths. Due to symmetry around the axis, only one quarter of the deformed sample is shown. Results for axi-symmetrical strains of 0.07, 0.1, 0.2, and 0.4 are shown in Appendix E: FEM results, and all have the same behaviour, the only difference is the magnitude of the equivalent plastic strain.

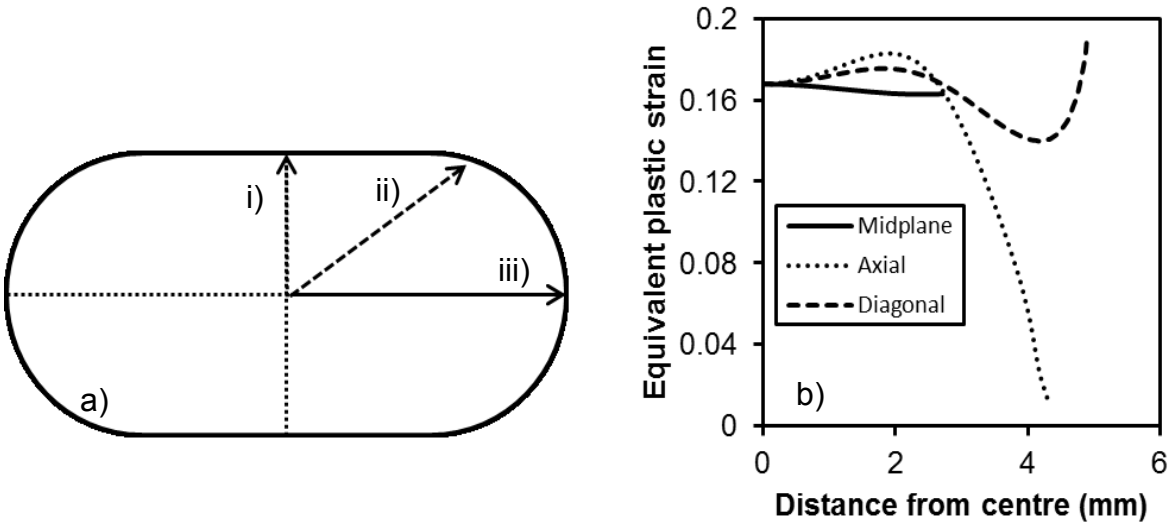

Figure 5.36.: a) A schematic sketch of a deformed axisymmetrical sample showing a quarter section and the paths at which the strain distributions were recorded i) Axial, ii) Diagonal and iii) Mid-plane b) Strain distribution along different paths of a single hit FEM simulated deformed axisymmetrical sample with an applied true strain of 0.15 and a strain rate of 1.5 s^{-1}.

Figure 5.36b) can be explained as follows; moving along the mid plane path from the centre to the edge of the deformed sample there is a slight decrease of the effective strain from a high deformation zone to a moderate zone. Moving along the axial axis there is a significant decrease of the effective strain showing that the path is from a high deformation zone to a dead zone. Traversing along the diagonal path from the high deformation zone at the centre, there is a slight drop of the effective strain and a significant increase onwards up to the edge of the specimen.

Figure 5.37 shows the relationship between the applied nominal true strain and the equivalent plastic strain (EQPL) at the centre of an axisymmetrically deformed sample. It can be seen that the amount of EQPL at the centre increases with increasing applied nominal strain.

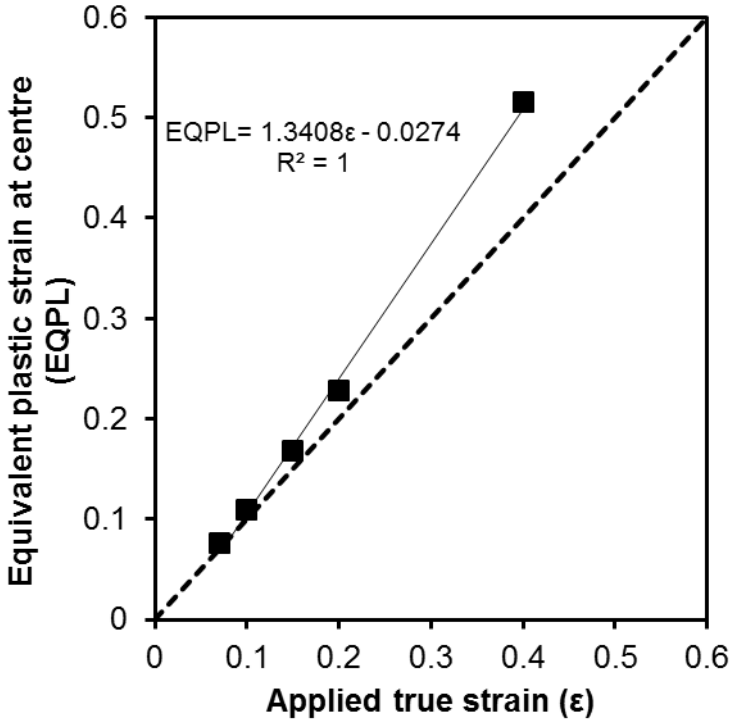

Figure 5.37.: The relationship between the localized EQPL at the centre of the axisymmetrically deformed sample with the bulk applied nominal true strain, showing a linear relationship with some deviation from the one-to-one relationship at higher strains.

5.7.2. Flat Rolling Simulation

Figure 5.38depicts a schematic diagram of half of a 240 mm plate subjected to a single pass FEM simulation with true strains of 0.07, 0.1, 0.15 and 0.2 and the corresponding equivalent plastic strains from centre to the surface of the plate. The simulation is at a temperature of 1100 °C with a roll diameter of 950 mm and a roll peripheral speed of 1.5 m/s. A friction coefficient of 0.4 was used.

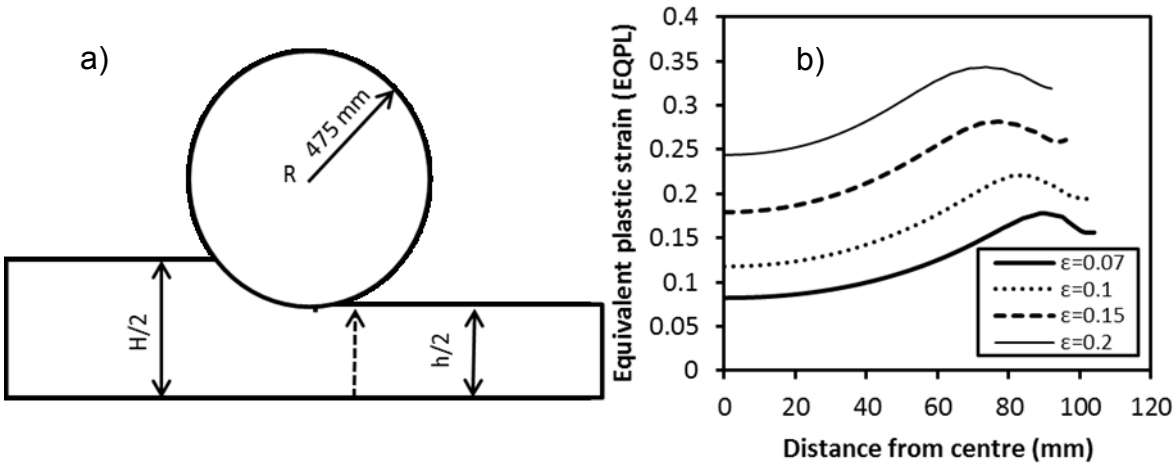

Figure 5.38.: a) Schematic half section of a FEM simulated hot rolled plate, the dotted arrow shows the path followed to plot b) the corresponding EQPL distribution from centre to the surface.

Contrary to the axisymmetrical compression simulations, Figure 5.38 shows that the EQPL in flat rolling increases from the centre to the surface of the hot rolled plate. The increased EQPL on the surface is due to the redundant strain that is caused by the friction between the work roll and the plate's surface as discussed in section 3.3.2. The EQPL increases with the applied strain but maintains the same behaviour.

Figure 5.39 shows the relationship between the EQPL at the centre, quarter and surface of the hot rolled plate and the applied bulk true strain. The relationship is linear as with the axi-symmetrical compression simulation and then deviates from the one-to-one relationship with increasing applied true strain. The deviation from one-to-one relationship is also evident with increasing distance from the centre with the surface showing the most deviation.

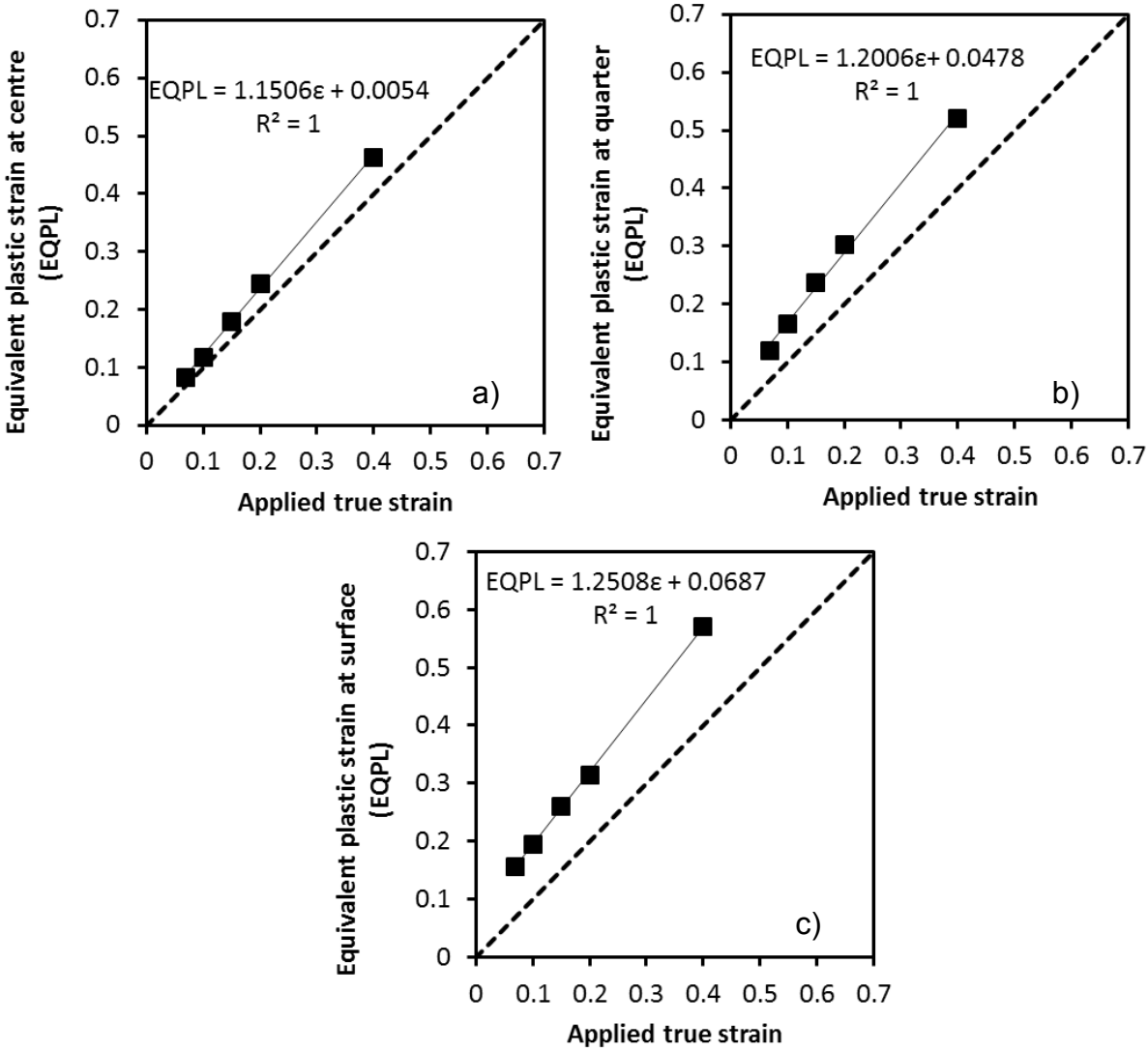

Figure 5.39.: The relationship between the localized EQPL and the bulk applied nominal true strain at the a) centre, b) quarter and c) surface of a hot rolled 240 mm plate. A linear relationship that deviates from one-to-one relationship with increasing strain and distance from centre is obtained.

Chapter 6. Discussion Of Results

6.1. Influence Of Pass Strain On Recrystallization And Grain Size

6.1.1. Recrystallization Kinetics

The driving force per unit volume for recrystallization is given by equation 3.36 as discussed in section 3.6.2.

$$\Delta G(t) = \frac{1}{2}\rho\beta\vec{b}^2 \quad \text{.....(6.1)}$$

The effective interfacial area per unit volume (S_v), which expresses the interfacial area of the deformed grain boundaries and the deformation band density (preferential nucleation sites for recrystallized grains), can be used to determine the nucleation site area for the recrystallized grains and is expressed as follows [118]:

$$S_v = \{1.67(\varepsilon - 0.1) + 1\}\left(\frac{2}{D_{gs,0}}\right) + 63(\varepsilon - 0.3) \quad \text{.....(6.2)}$$

Equations 6.1 and 6.2 show that an increase in applied strain increases the dislocation density which will increase both the driving force for recrystallization and the available nucleation site area. To gauge the extent of these effects eqn. 6.2 was used to calculate the available nucleation site area for the studied steels in the first pass where the $D_{gs,0}$ is the reheat grain size; Table 6.1 shows the S_v results, but the C-Mn results are not shown since the equation falls short when the $D_{gs,0}$ is greater than 135 μm and gives negative values. Table 6.1 shows that, as eqn. 6.2 illustrates, S_v increases with a decrease in $D_{gs,0}$ and an increase in applied strain. For a given chemistry (or grain size) a strain of 0.15 has the highest S_v and that of 0.07 has the lowest.

Table 6.1.: The effective interfacial area per unit volume (S_V) for the studied steels at various applied strains in R1.

		S_v (mm^{-1})		
Schedule	**Applied strain**	**C-Mn-V (111 µm)**	**C-Mn-Nb-V (94 µm)**	**C-Mn-Nb-Ti-V (78 µm)**
I	0.07	3	6	10
II	0.1	5	9	13
III	0.15	10	14	18

Although it is not quantified how much $\Delta G(t)$ and S_v is required for full recrystallization, the combination of increased driving force and nucleation sites with the 0.15 strain per pass therefore accounts for the complete recrystallization in between passes. The partial recrystallization in the first pass for the 0.15 strain simulations across the studied steels can be due to the relatively coarse $D_{gs,0}$ entering the first pass and thus low S_v for nucleation of the recrystallized grains.

The recrystallized fractions strain per pass schedules of 0.07 and 0.1 oscillated between partial and full. This is due to the retained strain from the previous partially recrystallized pass which leads to an increased effective strain that increases both $\Delta G(t)$ and S_v. To quantify, the S_v, effective interfacial area per unit volume was calculated using the effective strain in the second pass (R2) and the results are shown in Table 6.2. The $D_{gs,0}$ in eqn. 6.2 will now be the grain size exiting R1, $D_{gs,1}$. The $D_{gs,1}$ was predicted using the recrystallized grain size models of Militzer [3] for the C-Mn-V steel and Siciliano and Jonas [52] for the C-Mn-Nb-V and C-Mn-Nb-Ti-V steels. For schedule I the $D_{gs,1}$ was similar to the $D_{gs,0}$ for all steels because no recrystallization occurred in R1. Schedules II and III had a finer $D_{gs,1}$ than $D_{gs,0}$ and these results are summarized in Table 6.3.

Table 6.2 shows that the increased strain in R2 for schedule I increased the S_v by 5-6 mm^{-1} (difference between S_v in Table 6.2 and that in Table 6.1) in all the steels. The combination of increased strain and refined grain size in schedules II and III led to more than a double increase in S_v for all the steels.

Table 6.2.: The effective interfacial area per unit volume for the studied steels at various effective strains in R2.

		S_v (mm^{-1})		
Schedule	**Effective strain in R2**	**C-Mn-V**	**C-Mn-Nb-V**	**C-Mn-Nb-Ti-V**
I	0.13	8	12	16
II	0.17	19	27	32
III	0.22	33	39	44

Table 6.3.: Predicted austenite grain sizes exiting R1, $D_{gs,1}$ for the various schedules.

	Predicted $D_{gs,1}$ (μm)		
Schedule	**C-Mn-V [3]**	**C-Mn-Nb-V [52]**	**C-Mn-Nb-Ti-V [52]**
I	111	94	78
II	82	64	56
III	63	54	49

6.1.2. Post Hot Rolling Simulation Grain Sizes

In section 5.6 the evolution of austenite grain size as a function of the hot rolling schedules was presented. It was observed that as the applied strain per pass increases the grain refinement increases too. This is in good agreement with work done by Ouchi *et al*. [118] and Bakkaloğlu [119] who found that the austenite and final ferrite grain size was continuously refined with increased pass reduction of rolling respectively. Ouchi *et al.* [118] showed that the static recrystallized austenite grain size (D_{SRX}) is inversely proportional to the third root of the numbers of nucleation sites for the recrystallized grain per unit volume (S_v), the hot deformation resistance (K_m), strain and the roll pressure function, Q_R;

$$\mathrm{D_{SRX}(cm)} = \frac{0.17}{\sqrt[3]{\mathrm{S_v \varepsilon K_m Q_R}}} \quad \text{.....(6.3)}$$

where Q_R and K_m are respectively expressed as [118]

$$Q_R = \frac{\pi + \frac{3\left(\sqrt{(H-h)R_{roll}}\right)}{(H+h)}}{4} \quad \text{.....(6.4)}$$

$$K_m = A\varepsilon^w \dot{\varepsilon}^s \quad \text{.....(6.5)}$$

As the strain per pass increases so are the number of recrystallized grains and the finer the austenite grain size. Thus the 0.15 strain per pass led to a finer austenite grain size than that of 0.07 and 0.1. It is also known that increasing the strain increases the dislocation density and introduces smaller sub-grains thereby increasing the number of nucleation sites for static recrystallization which leads to finer recrystallized grains [3,35,123].

The extent of grain refinement was decreased with increasing strain per pass. The application of the 0.4 strain in the last pass significantly refined the grain size for the schedules of 0.07 and 0.1 strain per pass and had a lesser effect on the 0.15 strain per pass. This effect was also found by Ouchi *et al*. [118] who showed that with increased strain and decreased $D_{gs,0}$ the extent of grain refinement is reduced.

In order to explain the mechanism by which grain refinement occurs, the nominal and localized (EQPL) accumulated strain at the centre per schedule was plotted against deformation temperature and the critical (ε_c) and peak (ε_p) strains for DRX for high (Figure 6.1 and Figure 6.2) and low (Figure 6.3 and Figure 6.4) exit temperature simulations. The 1 s^{-1} ε_c and ε_p results were used since it is the average of the strain rates used in this study.

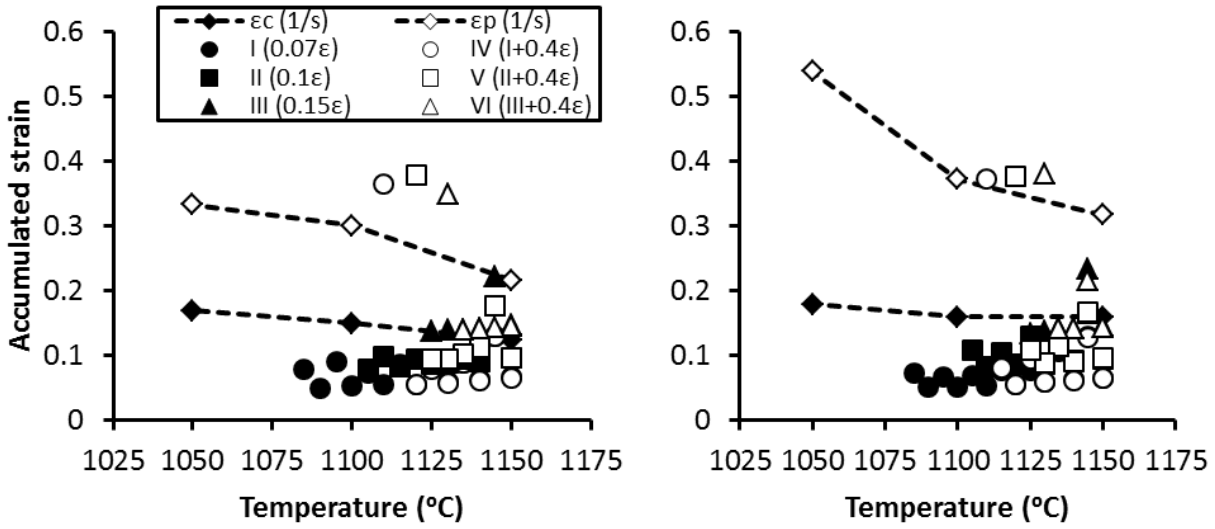

Figure 6.1.: Accumulated nominal strain for high exit temperature schedules as a function of deformation temperature and the critical and peak strain for a) C-Mn and b) C-Mn-Nb-Ti-V steels.

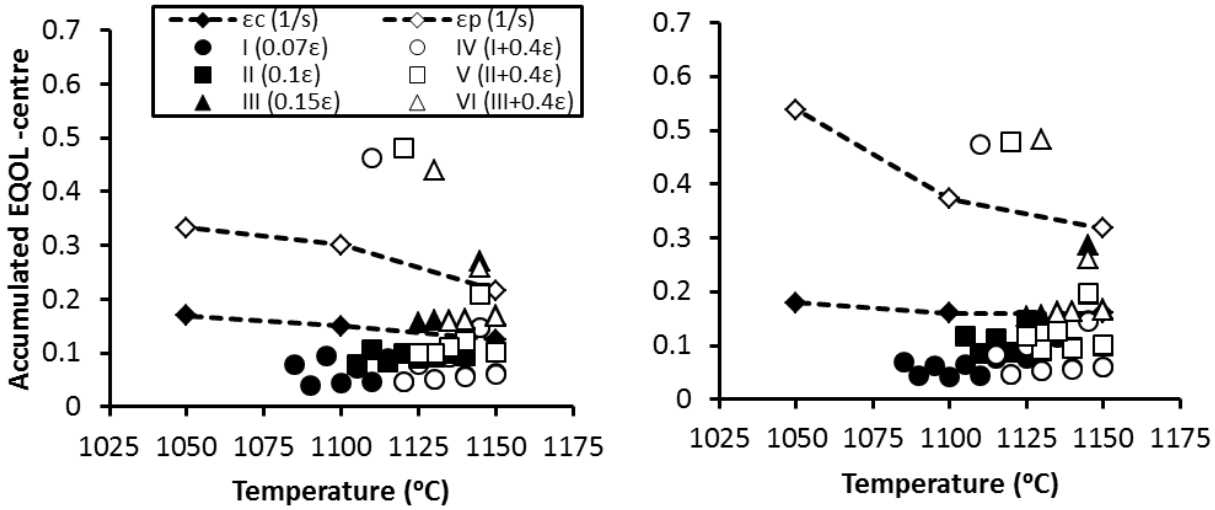

Figure 6.2.: Accumulated localized strain for high exit temperature schedules as a function of deformation temperature and the critical and peak strain for a) C-Mn and b) C-Mn-Nb-Ti-V steels.

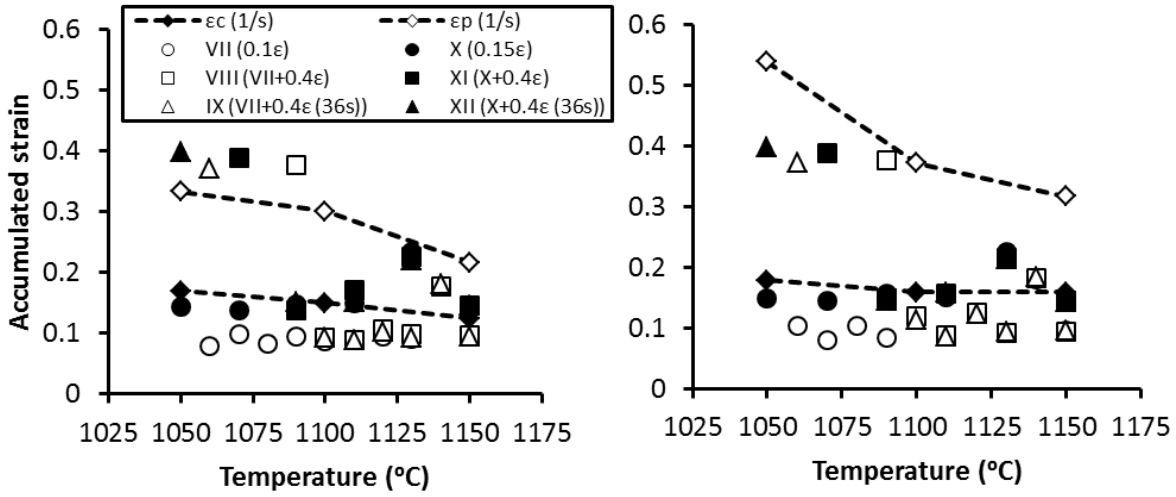

Figure 6.3.: Accumulated nominal strain for low exit temperature schedules as a function of deformation temperature and the critical and peak strain for a) C-Mn and b) C-Mn-Nb-Ti-V steels.

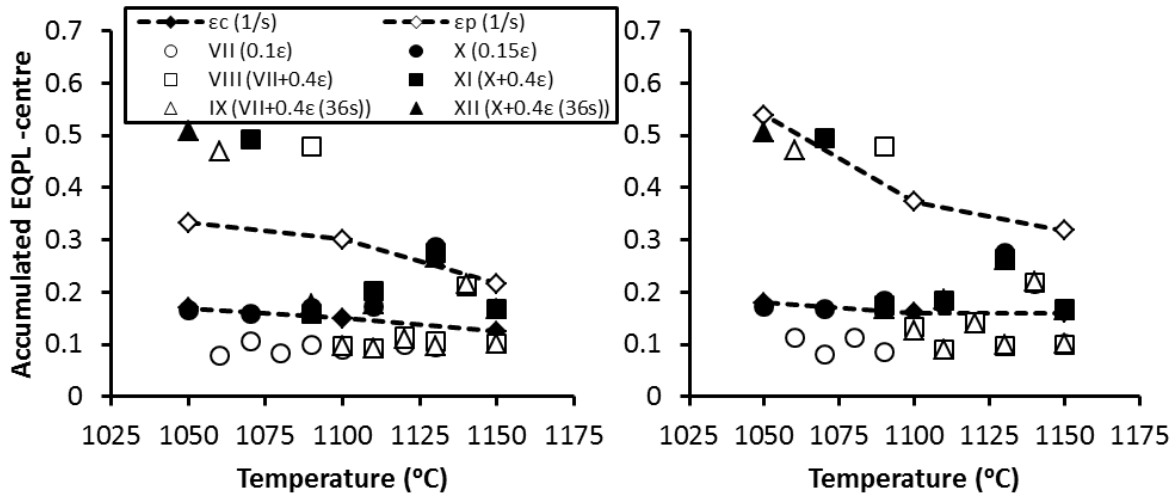

Figure 6.4. : Accumulated localized strain for low exit temperature schedules as a function of deformation temperature and the critical and peak strain for a) C-Mn and b) C-Mn-Nb-Ti-V steels.

Figure 6.1 shows that for both the C-Mn and C-Mn-Nb-Ti-V steels the bulk of the effective nominal strain for schedules I (0.07 ε/pass) and II (0.1 ε/pass) is below the critical strain for DRX. Although the effective localized strain slightly increased (Figure 6.2), the bulk strain remains below the ε_c and thus grain refinement in these schedules cannot be attributed to the occurrence of DRX. The effective nominal strain for schedule

III (0.15ε /pass) is almost equal to the critical strain for DRX for the C-Mn steel but not for the C-Mn-Nb-Ti-V steel. The effective localized strain is slightly above the ε_c for the C-Mn steel whereas it is almost equal to the ε_c in the C-Mn-Nb-Ti-V steel in schedule III. The application of the 0.4 strain in the last pass led to effective strains that are above both the ε_c and the ε_p for the C-Mn and C-Mn-Nb-Ti-V steels.

Similarly for the low exit temperature simulations, Figure 6.3 and Figure 6.4 show that the bulk of the effective nominal and localized strains for the intermediate strain simulation (0.1ε /pass) schedules VII-IX, is below the ε_c, whereas that of the large strain simulation (0.15ε /pass) schedules X-XI is on the borderline of the ε_c. The applied 0.4 nominal and localized strain is greater than both the ε_c and ε_p in the C-Mn steel. In the C-Mn-Nb-Ti-V steel the effective nominal strain is below the ε_p and the effective localized strain is above ε_p only for schedules VIII and XI.

Figure 6.1 to Figure 6.4 show a clear evidence that the effective strain is less than the ε_c in schedules I (0.07ε/pass), II (0.1ε/pass, high exit temperature) and VII (0.1ε/pass, low exit temperature) for the C-Mn steel and schedules I-III (high exit temperature) and schedule VII and X (low exit temperature) for the C-Mn-Nb-Ti-V steel. Although the effective localized strain of the large strain sequence simulation (0.15 ε/pass) is closer to the ε_c, it is still below the ε_p, and it has been shown that the first necklace formation responsible for grain refinement during DRX occurs at strains equal to ε_p [122].Therefore grain refinement for all the steels in the studied schedules cannot be attributed to DRX. For strains per pass of 0.07 to 0.1 grain refinement is mainly achieved through the repeated deformation and static recrystallization occurring during the multi-pass hot rolling simulations. Since strains of 0.15 are the threshold, both SRX and MDRX may be responsible for grain refinement in these steels. Only when a strain of 0.4 is applied in the last pass is the effective strain closer or above the ε_p and that is when grain refinement in these schedules can be attributed to occurrence of DRX. The effect of grain refinement by a static recrystallization was found by Ouchi *et al*. [118] and Bakkaloğlu [119]. Mataya *et al*. [120] found that grain refinement of alloy 718 stainless steel in the as-cast and wrought conditions was principally due to static recrystallization. Samuel *et al*. [124] showed that grain refinement of a Nb-only microlloyed steel was achieved by static recrystallization when rolling is above the T_{NR}.This concurs with the

theory of RCR (recrystallization controlled rolling), where deformation of austenite occurs above T_{NR} and grain refinement is achieved by repeated deformation and static recrystallization [37].

6.2. Comparison Across The Studied Steels

6.2.1. Reheat Austenite Grain Sizes, $D_{gs,0}$

In section 5.3 the influence of soaking time and heating rate on the $D_{gs,0}$ was shown at a reheat temperature of 1220 °C. It was found that an increase in soaking time and decrease in heating rate increased the $D_{gs,0}$ for all the studied steels. This is in agreement with the isothermal grain growth kinetics described in eqn. 2.1, showing that the grain size increases with increased soaking time and temperature. Militzer et al. [18] showed that Al-killed C-Mn steel increased in grain size with a decrease in heating rate and increase in soaking time.

In this work the C-Mn steel was the coarsest at any given heating rate and soaking time whilst the C-Mn-Nb-Ti-V steel was the finest. Thermo-Calc® results in section 5.1 showed that at 1220 °C, all the Al precipitates were in solution for the C-Mn steel which is responsible for grain refinement through AlN precipitation [18] and only about 15 % of Ti precipitates were in solution in the C-Mn-Nb-Ti-V steel. The fine grain size in the latter steel is therefore attributed to the pinning effect of the stable Ti(C,N) precipitates. This concurs with work done by Gao and Baker [30] who showed that the addition of Ti to Al-V-N steels refined the austenite grain size. Siwecki and Engberg [37] also showed that in Ti-V-N HSLA steels, TiN is a better austenite grain growth inhibitor.

The $D_{gs,0}$ of the C-Mn steel entering R1 was 353 µm and is comparable to that found by Ouchi and Okita [118] of 330 µm for a plain 0.13%C-1.15%Mn steel after soaking at 1250 °C for 20 minutes. The larger grain size in this work can be attributed to the combined effect of slow heating rate (7.5 °C/min) and relatively longer soaking time of 30 minutes.

The relatively fine grain size in the C-Mn-Nb-V steel (94 µm) before hot rolling appears to be due to the solute drag of Nb since almost 100 % of the Nb precipitates are in

solution at 1220 °C. Yu *et al*. [40] found that the grain boundary mobility in a 0.041 %C steel with 0.015 %Nb was retarded by solute drag of Nb atoms which segregates to grain boundaries and not precipitates. Ouchi *et al*. [118] showed that for a 0.031 %Nb-only microalloyed steel the grain size is 227 μm after soaking at 1250 °C for 20 minutes and Samuel *et al*. [124] also showed that a 0.028 %Nb-only steel had a grain size of 185 μm after reheating at 1250 °C and 15 minutes soaking time. The coarse austenite grain size in their work is an indication that the temperature for abnormal grain growth is exceeded. This is testament to work done by Yu *et al*. [40] who showed that the grain coarsening temperature is 1240 °C for a low C-Nb steel and Davis and Strangwood [8] showed that grain coarsening of Nb-containing steel occurred at 1225 °C.

The C-Mn-Nb-Ti-V steel had a $D_{gs,0}$ of 78 μm finer than that reported by Ouchi *et al*. [118] in a 0.019 %Ti only steel with similar base chemistry to the one in this work of 98 μm at 1250°C held for 20 minutes. The finer grain size in this work can be due to the presence of Nb. Adrian and Pickering [22] showed that in a Nb-Ti-containing steel, at soaking temperatures greater than 1050 ºC the austenite grain size decreases and the grain coarsening temperature increases with increasing (Nb + Ti) content. These authors [22] showed that with an increased Nb addition, the amount of Ti-rich carbonitrides precipitated during solidification is decreased. This was indicated by the presence of finer Nb-rich Ti carbonitrides in the higher Nb steel compared to that containing a lower Nb-content with the same amount of Ti content. These fine precipitates were responsible for effective grain boundary pinning during reheating thus a smaller austenite grain size in the higher Nb steel.

C-Mn-V austenite grain size was finer than that of the C-Mn and closer to the C-Mn-Nb-V. With a HT3 thermal cycle (7.5 °C/min heating rate from RT, 30 min. soak) the C-Mn-V grain size is 111 μm compared to 353 μm and 94 μm of the C-Mn and C-Mn-Nb-V respectively. This is not expected since Thermo-calc® showed that all the V and Al precipitates are in solution at 1220 °C and no pinning of the grain boundaries is expected. Siwecki and Engberg [37] showed that VN is not effective in austenite grain refinement most likely due to the fact that VN tends to form at lower temperatures. It is believed that V has a low solute drag coefficient compared to other microalloys [122] and thus retardation of grain boundary migration is at an absolute minimum.

However the grain size of the C-Mn-V steel is similar to that found by Gao and Baker [30] who showed that soaking a Al-V-N steel containing 43 ppm N at 1200 °C for 30 minutes led to a grain size of 120 µm although the heating rate was not specified. The smaller grain size in the current work can be due to the higher N content of 90 ppm and the same authors [30] showed that the grain size was finer in an Al-V-N steel containing 150 ppm N compared to those containing 20-49 ppm.

6.2.2. Flow Stress

In section 5.4 the true stress-strain curves along with the corresponding MFS of high and low exit temperature simulations were presented. It was found that the true stress generally increases with decrease in temperature. The C-Mn steel had the lowest flow stress across the steels and the C-Mn-Nb-Ti-V the highest. However the C-Mn-V steel had a flow stress greater than that of the C-Mn steel and equal to the C-Mn-Nb-Ti-V.
This is contrary to what most researchers find, especially at high temperatures. At high deformation temperatures it is expected that the C-Mn-V steel will behave like a plain C-Mn steel due to its low solute drag coefficient that promotes recrystallization leading to lower roll forces [121]. Militzer *et al*. [3] showed that rolling a V-only steel, full recrystallization was achieved in all the passes and the flow stress was consistently lower than the Nb-Ti steels. Hui *et al*. [99] also showed that the deformation behaviour of a V-microalloyed medium-carbon steel is similar to a plain carbon steel. However Wie *et al.* [100] also found that the flow stress of a C-Mn-V steel was higher than for the C-Mn steel at various deformation temperatures under the same conditions and they attributed this to solid solution strengthening of V. Elwazri [72] showed that a combination of V and Si in solution have a strong solute drag effect on the kinetics of static and meta-dynamic recrystallization.

Table 6.4 shows the MFS at 1100 °C and at a strain rate of 1 s^{-1} reported by Wie *et al.*[100] and Militzer *et al*. [3] compared to this work for schedule III (015ε/pass) at 1125 °C and strain rate of 1.3 s^{-1}. Although the strain was up to 0.8 and 1 for the work of Wie *et al*. [100] and Militzer *et al*. [3] respectively, the MFS was measured up to 0.15 strain for direct comparison.

Table 6.4.: MFS comparison for 0.15 strain.

	MFS (MPa)		
Author	**C-Mn**	**C-Mn-V**	**C-Mn-Nb-Ti-(V)***
Militzer [3]	-	48	51
Wie [100]	53	63	-
This work	51	65	64

*** No V in Militzer [3] steel.**

Table 6.5 compares the MFS measured up to 0.8 strain reported by Militzer *et al*. [3] and Wie *et al*.[100] to the one found in this work at 1100 °C and strain rate of 1 s^{-1}.

Table 6.5.: MFS comparasin for 0.8 strain at 1100 °C and 1 s^{-1}.

	MFS (MPa)		
Author	**C-Mn**	**C-Mn-V**	**C-Mn-Nb-Ti-(V)***
Militzer [3]	-	67	79
Wie [100]	78	86	-
This work	84	91	98

*** No V in Militzer [3] steel.**

It is clear from Table 6.4 that there is an insignificant difference in MFS between the C-Mn-V steel and the C-Mn-Nb-Ti-(V) steel for both Militzer *et al*. [3] and this work at strains of 0.15. The difference is 3 and 1 MPa respectively. The C-Mn-V MFS is 10 MPa higher than that of the C-Mn steel for Wie *et al*. [100] and 14 MPa for this work. The difference at a strain of 0.8 between the C-Mn-V and C-Mn-Nb-Ti-(V) increases, Table 6.5, and is 12 and 7 MPa for Militzer *et al*. [3] and this work respectively. The MFS difference between the C-Mn-V and C-Mn steel at a strain of 0.8 is 8 and 7 MPa for Wie et al [100] and this work respectively. The higher C content in this work (0.13 %C) and the work of Wie *et al*. [100] (0.37 %C) can be the reason for the higher MFS in the C-Mn-V steel compared to that of Militzer *et al*. [3] (0.05%C) due to solid solution strengthening. Wie at al [14] also showed that at strains of 1 s^{-1} and greater, the higher C steel of 0.37 % had a higher flow stress than that of a 0.06 % in a C-Mn-V steel at

900 and 1000 °C and this was attributed to the reduction of stacking fault energy with increased C content.

A lower entry temperature of 1050 °C, Figure 5.17 in section 5.4.3, showed that the C-Mn-Nb-Ti-V steel MFS is consistently higher than that of the C-Mn-V steel. This is due to the precipitation strengthening by Nb(C,N) as Thermo-Calc® results in section 5.1 showed that at 1050 °C only 30 % of its Nb is in solution in the C-Mn-Nb-Ti-V steel and predicts about 0.02 % of NbC precipitates (Figure 5.1 and Figure 5.2).

From the results in Figure 5.17 in section 5.4.3, Table 6.4 and Table 6.5 it is clear that the MFS of the C-Mn-Nb-Ti-(V) is only higher than that of the C-Mn-V at strains of 0.8 and not at a strain of 0.15 and at lower temperatures (≤ 1050 °C) where precipitation of NbC is enhanced. This indicates that at low strains and high temperatures the strengthening by solute Nb is minimal.

The MFS of the C-Mn-V steel is consistently higher than that of C-Mn steel irrespective of the applied strain or temperature. Although Wie *et al*. [100] attributes this to solid solution strengthening of V, in this work the Mn contents in the C-Mn and the C-Mn-V steels are 1.13 and 1.54 %Mn respectively, and it is well known that Mn is a solid solution strengthener [101]. Therefore the higher flow stress in the C-Mn-V compared to the C-Mn can be attributed to a combination of V and Mn in solution.

6.2.3. Recrystallized Volume Fraction X

Section 5.5 showed the recrystallization behaviour at different schedules and exit temperatures. The recrystallized volume X fraction for a given schedule was found to be similar in behaviour but in terms of the magnitude of X at strains of 0.1 the Nb-containing microalloyed steels (C-Mn-Nb-V and C-Mn-Nb-Ti-V) was lower than that of the C-Mn and C-Mn-V steels at partially recrystallized passes. This is most likely to be due to retardation of recrystallization by Nb solute drag. It is also known that Nb is the most effective in retarding static recrystallization through solute drag, followed by Ti and V respectively [20, 71].

6.2.4. Post Hot Rolling Austenite Grain Size D_{gs}

In section 5.6 the austenite microstructure after hot rolling was shown along with the respective grain size distributions across the steel. It was observed that for a given schedule the C-Mn had a coarser and a wider distribution of grain sizes compared to that of the C-Mn-Nb-V and C-Mn-Nb-Ti-V steels at strains of 0.07 to 0.15. The application of 0.4 strain in the last pass neutralized the difference in grain sizes, especially in the high exit roughing simulations. This can be attributed to the observation of Ouchi *et al* [118] that with increased strain there appears to be a saturation of grain refinement and that the hot rolling process conditions have the most effective influence on the recrystallized grain size rather than the chemistry of the steel. The coarser austenite grain size after roughing in the C-Mn steel is attributed to the coarse initial grain size before hot rolling as equations 6.2 and 6.3 [118] illustrate that a large initial grain size will lead to a lower S_v which will lead to a coarser recrystallized grain size. Sha *et al*. [123] also showed that the recrystallized grain size of a Nb-Ti-V steel was larger when the $D_{gs,0}$ was large and attributed this to a decreased grain boundary area in a larger $D_{gs,0}$ compared to smaller $D_{gs,0}$.

Although the D_{gs} of the C-Mn steel was relatively coarser for a given schedule it showed the greatest extent of grain refinement. To compare the extent of grain refinement after subsequent hot rolling simulations, the initial grain size, $D_{gs,0}$ was normalized by dividing it with the resultant grain size after a given schedule and plotted against the applied strain per pass, Figure 6.5. It is evident that the C-Mn steel which was the coarsest, with a $D_{gs,0}$ of 353 µm gave the greatest extent of grain refinement compared to that of the C-Mn-Nb-V and C-Mn-Nb-Ti-V steels with $D_{gs,0}$ of 94 and 78 µm respectively. This effect was found by Bai [4] for a plain C-Mn steel with two different starting grain sizes of 375 and 30 µm and given a 5 pass multi-reduction with a similar strain of 0.4 per pass and they found that the resultant grain size is similar. The same phenomenon was found by Siwecki et al. [37] for a V-N steel with two different starting grain sizes of 500 and 20 µm given a reduction of 89% in 11 passes. Mataya and Matlock [120] showed that the coarse as-cast alloy 718 stainless steel had a greater reduction ratio than that in the as-wrought condition for a given deformation strategy. This indicates that there is more grain refinement with an increasing $D_{gs,0}$. Ouchi *et al* [118] also showed that as the

strain increased and the $D_{gs,0}$ decreased a saturation is reached in the extent of grain refinement. Militzer *et al*.[3] claims that a larger $D_{gs,0}$ leads to a higher degree of grain refinement than a smaller starting grain size. This indicates that there is a limiting grain size where grain refinement saturation is reached. According to Militzer *et al*. [3] this limiting grain size is between 20 to 40 μm under industrial rolling conditions. In this work the limiting grain size ranged between 20-30 μm which lies in the range reported by Militzer *et al*. [3].

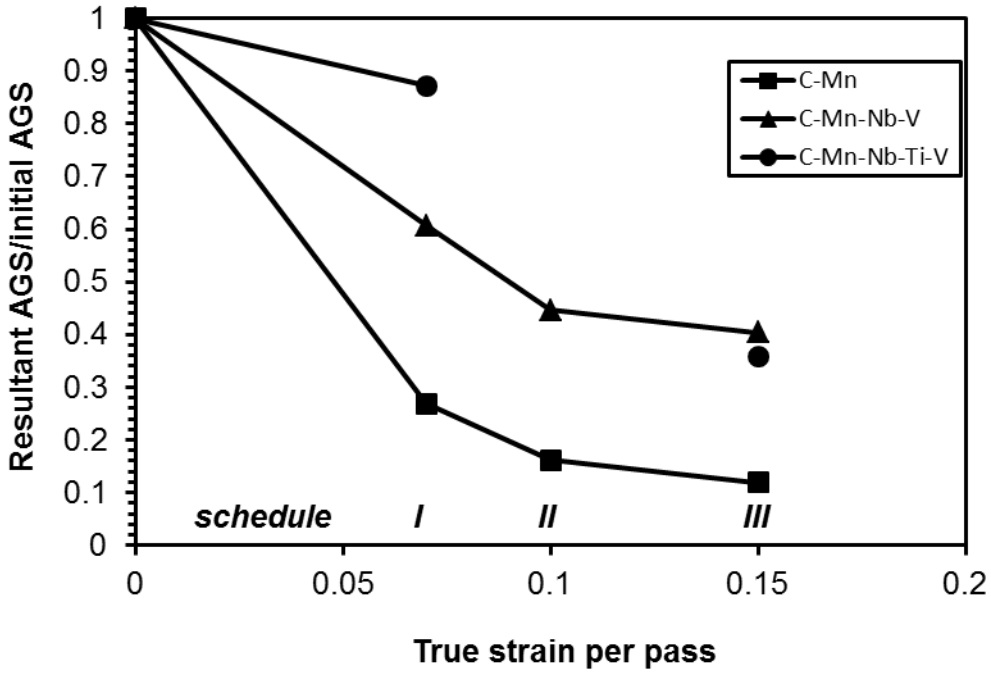

Figure 6.5.: Ratio of the resultant grain size after hot rolling simulations to that of the initial grain size as a function of applied true strain per pass for the studied steels.

6.3. Comparisons To Models In Literature

In this section the measured mean flow stress and recrystallized volume fraction after the roughing schedules are compared to models in literature. Although no modelling was done in this work, this comparison was done to check if the models can also predict laboratory results with some degree of confidence.

6.3.1. Mean Flow Stress

Figure 6.6 shows the comparison between the measured MFS for the C-Mn steel and the models in the literature discussed in section 3.5 for schedules I and III. For simplicity and clarity, only the Misaka [64] eqn. 3.25, Sicilliano [64] eqn. 3.26 and the Bruna models [69] eqn. 3.29 are depicted.

Schedule I shows that the MFS varies up and down with a decrease in temperature. The models follow the same MFS pattern as was found in this work. This is attributed to the occurrence of partial recrystallization between passes in this schedule. The retained strain from a partially recrystallized pass is carried over to the next pass and leads to an increased MFS and so on into the next passes. Table 6.6 shows the % error between the predicted MFS and to the one measured in this work for schedule I. From the second to the ninth pass the Bruna model predicts the MFS closer to the ones of the current work with 2-6% error whereas both the Misaka and Siciliano models under-predict the MFS up to 18%. The relatively high % error in the Bruna model from the 10^{th} pass onwards is due to the fact that in the present work there is cumulative softening that occurs which reduces the MFS. Thus the MFS predicted by the Bruna model continued increasing with respect to strain, strain rate and temperature. Similarly the Misaka and Siciliano models were able to predict the MFS closely to the ones measured in this work due to the cumulative softening.

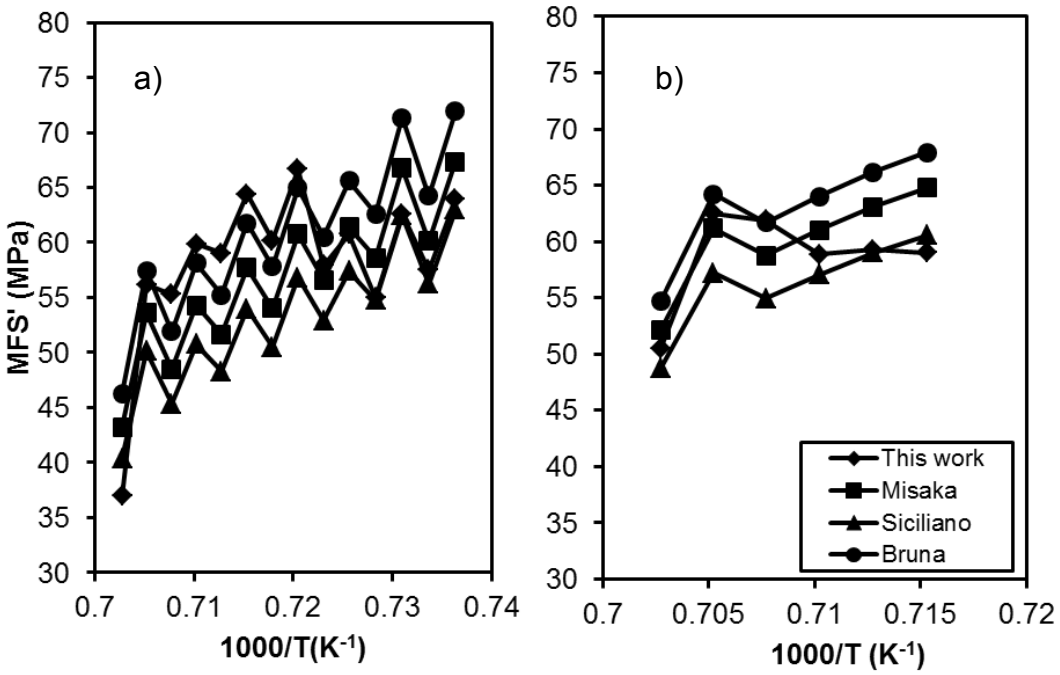

Figure 6.6.: Comparison of the measured MFS' to models in literature for the C-Mn steel for a) small strain sequence simulation, schedule I (0.07ε/pass) and b) large strain sequence simulation, schedule III (0.15ε/pass).

In schedule III the Bruna and Misaka models agree with this work for the first three passes and then continue to increase whilst the measured one decreases. The MFS of this work decreases due to the cumulative softening as shown by the true stress-true strain curves in section 5.4.1. Although accumulated strain was accounted for in calculating the MFS using the models, their predictions are based on an increase of strain and decrease of temperature. The drop in the MFS predicted by the models and found in this work in the third pass is due to a drop in the effective strain from R2 to R3. The effective strain in the pass R2 was high due to the accumulated strain from the partially recrystallized pass R1 hence, the higher MFS in R2. From the third pass onwards the predicted MFS increases linearly with decreasing temperature because full recrystallization is achieved during inter-pass times.

Table 6.7 shows the % error between the predicted MFS and the ones measured in this work for schedule III.

Table 6.6.: Accuracy of the models for the MFS of the C-Mn steel in schedule I.

	$\%error = \frac{MFS_{model} - MFS_{this\ work}}{MFS_{this\ work}} \times 100$													
Model	**R1**	**R2**	**R3**	**R4**	**R5**	**R6**	**R7**	**R8**	**R9**	**R10**	**R11**	**R12**	**R13**	**R14**
Misaka [64]	9	-11	-18	-15	-18	-16	-16	-15	-9	-6	0	0	-2	-1
Siciliano [64]	9	-11	-18	-15	-18	-16	-16	-15	-9	-6	0	0	-2	-1
Bruna [69]	25	2	-6	-3	-6	-4	-4	-3	5	8	14	14	12	13

Table 6.7.: Accuracy of the models for the MFS of the C-Mn steel in schedule III.

	$\%error = \frac{MFS_{model} - MFS_{this\ work}}{MFS_{this\ work}} \times 100$					
Model	**R1**	**R2**	**R3**	**R4**	**R5**	**R6**
Misaka [64]	3	-2	-5	4	6	10
Siciliano [64]	-3	-8	-11	-3	0	3
Bruna [69]	8	3	0	9	12	15

Figure 6.7 shows the comparison between the measured MFS for the C-Mn-Nb-Ti-V steel and the predicted MFS by the Bruna [69] eqn.3.29, Miniami [68] eqn. 3.27 and Poliak [69] eqn. 3.30 models for schedules I and III.

Similarly to the C-Mn steel, the measured MFS in schedule I varies up and down due to the partial recrystallization between passes in this schedule. After the 8th pass the measured MFS drops due to cumulative softening as in the C-Mn steel. The measured MFS in schedule III remains constant after the second pass indicating a dynamic recovery behaviour. Table 6.8 and

Table 6.9 show the % error between the predicted MFS and the measured MFS for schedules I and III respectively. Generally the Poliak model over-predicts the MFS both in schedule I and III. The Miniami and Bruna models under-predict the MFS in the first

seven passes of schedule I and lead to small % errors (6% at most) in the subsequent passes due the cumulative softening that occurs. Although all the models displayed here did not show a similar MFS behaviour to the measured MFS in schedule III, the Bruna model gave the closest prediction. The drop in the predicted MFS in R3 is due to the decreased effective strain as discussed above for the C-Mn MFS predictions.

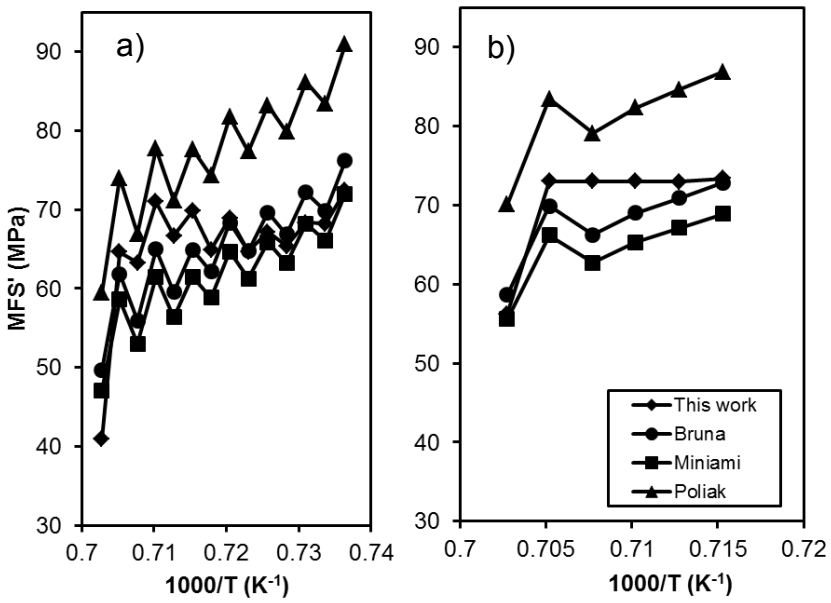

Figure 6.7.: Comparison of the measured MFS' to models in literature for the C-Mn-Nb-Ti-V steel for a) small strain sequence simulation, schedule I (0.07ε/pass) and b) large strain sequence simulation, schedule III (0.15ε/pass).

Table 6.8.: Accuracy of the models for the MFS of the C-Mn-Nb-Ti-V steel in schedule I.

	$\%error = \frac{MFS_{model} - MFS_{this\ work}}{MFS_{this\ work}} \times 100$													
Model	**R1**	**R2**	**R3**	**R4**	**R5**	**R6**	**R7**	**R8**	**R9**	**R10**	**R11**	**R12**	**R13**	**R14**
Poliak [69]	45	15	6	10	7	11	14	19	20	24	22	26	22	26
Miniami [68]	15	-9	-16	-13	-15	-12	-9	-6	-5	-2	-3	0	-3	-1
Bruna [69]	21	-4	-12	-8	-11	-7	-4	-1	0	4	2	6	2	5

Table 6.9.: Accuracy of the models for the MFS of the C-Mn-Nb-Ti-V steel in schedule III.

	$\%error = \frac{MFS_{model} - MFS_{this\ work}}{MFS_{this\ work}} \times 100$					
Model	**R1**	**R2**	**R3**	**R4**	**R5**	**R6**
Poliak [69]	25	14	8	13	16	18
Miniami [68]	-1	-9	-14	-11	-8	-6
Bruna [69]	4	-4	-9	-6	-3	-1

Figure 6.8 is the comparison of the MFS from mill data for the C-Mn-Nb-Ti-V 12 mm plate to the Miniami [68], Bruna [69] and Poliak [69] models. The Miniami and Bruna models show a good fit with the mill data whilst the one of Poliak over-predicts the MFS. Siciliano *et al*. [69] found that the Poliak and Bruna models over-predicted the MFS in the first pass of thin slab direct rolling by 21 and 17 % respectively.

It is suspected that the reason that the Poliak model (eqn. 3.30) over-predicts the MFS lies in the high coefficient of Nb of 4.51 compared to 0.51 in the Miniami model which exaggerates the Nb contribution to the MFS. To see the Nb contribution in each model the Nb content was varied from 0 to 0.1% whilst the other elements were kept constant in the C-Mn-Nb-Ti-V steel and the MFS was calculated at a temperature of 1150 °C for a strain of 0.15 and strain rate of 0.3 s^{-1}. The results are depicted in Table 6.10. It is evident that the Poliak model shows the largest sensitivity to Nb, increasing the Nb from 0 to 0.04 % increases the MFS by 15% as compared to the 2 and 7 % in the Miniami and Bruna models respectively.

Table 6.10.: The Effect of Nb content on the predicted MFS for the various models.

	MFS (MPa)			
Model	**0% Nb**	**0.02%Nb**	**0.04 %Nb**	**0.1 %Nb**
Poliak [69]	61	65	70	84
Miniami [68]	55	55	56	57
Bruna [69	55	57	59	64

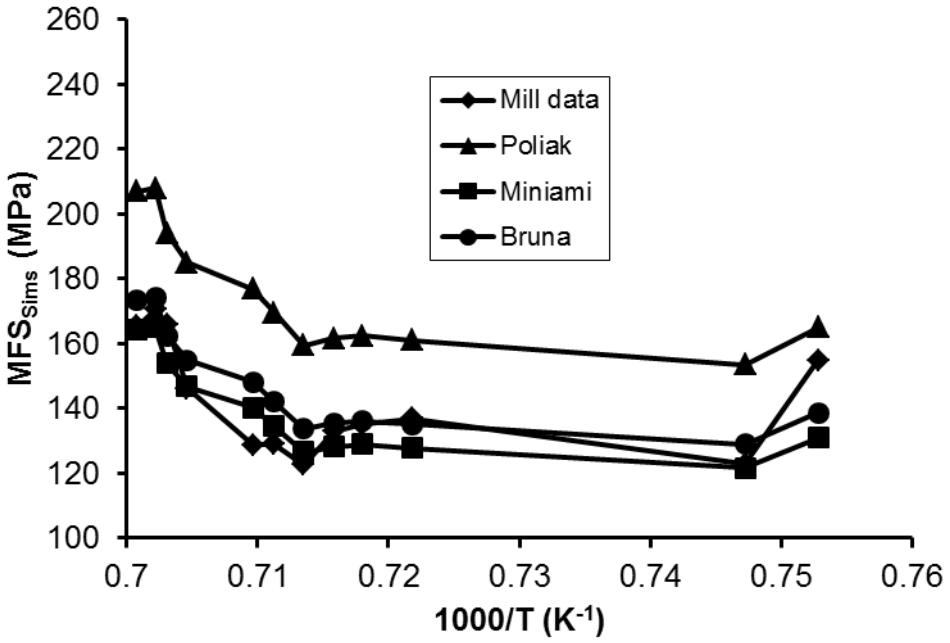

Figure 6.8.: Comparison of the determined MFS' from the mill logs of a 12 mm thick plate for the C-Mn-Nb-Ti-V steel to models in literature.

6.3.2. Recrystallized Volume Fraction

In this section, models that predict the recrystallized volume fraction as was discussed in section 3.6, are compared to measured values using the 2 % offset double stroke method. The grain growth after complete recrystallization (≥ 95 %) between passes was predicted using eqn. 3.76 and 3.82 for the C-Mn and C-Mn-Nb-Ti-V steels respectively. If there is incomplete recrystallization in a pass, the grain size entering the next pass ($D_{gs,0i+1}$) was calculated using eqn. 3.69. In the calculation a condition was set that if the $D_{rex,i}$ is greater than the $D_{gs,0i}$ then $D_{gs,0i}$ remains unchanged. Accumulated Von Mises

strain was used in the models. A Q_{def} of 300 kJ [64] was used for the C-Mn steel and for the C-Mn-Nb-Ti-V steel 380 kJ [102] was used.

Figure 6.9 shows the recrystallized volume fraction of the C-Mn steel for schedules I (0.07 ε/pass), II (0.1 ε/pass) and III (0.15 ε/pass) compared with the Siciliano and Jonas [52,64], Sellars [75,76] and Militzer *et al*. [3] models. Table 6.11 and Table 6.12 show the predictions of the initial grain size of the next pass ($D_{gs,0i+1}$) and time for 50 % recrystallization ($t_{0.5}$).

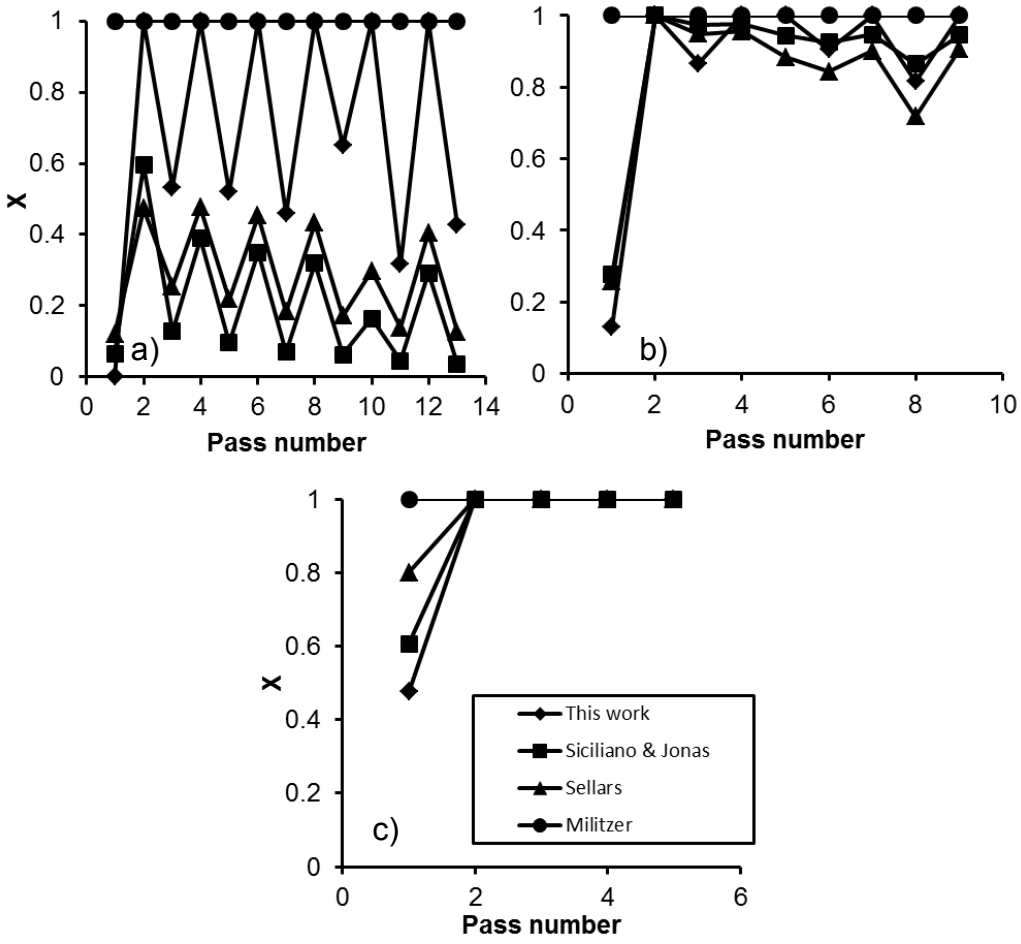

Figure 6.9.: Comparison of the measured recrystallized volume fraction to models in literature for the C-Mn steel for a) schedule I (0.07 ε/pass),b) schedule II (0.1 ε/pass) and C) schedule III (0.15 ε/pass).

Figure 6.9 shows that all the models correlate poorly at strains of 0.07 per pass. A good fit of all models is found in schedule III (0.15 ε/pass) from R2. At strains of 0.1 per pass only Siciliano's model gives the best fit, however Sellars' and Militzers's predictions are

within experimental error. At small strains (0.07-0.1) the recrystallized grain size is exaggerated since the $D_{gs,0}$ is divided by a small value which could lead to erroneous t_{05} values which again will lead to inaccurate X values. On the other hand this poor correlation can be attributed to the fact that at these small strains recrystallization is believed to occur via the SIBM mechanism which does not follow the classical nucleation theory as illustrated by these models [112].

Table 6.11.: The grain size and time for 50% recrystallization predicted by models for schedule I in the C-Mn steel.

	$D_{gs,0i+1}$ (μm)			$t_{0.5}$ (s)		
Pass No (i)	**Siciliano**	**Sellars**	**Militzer**	**Siciliano**	**Sellars**	**Militzer**
0	353			-	-	-
1	353	353	353	48.6	92.1	1.7
2	203	203	133	9.7	6.9	1.0
3	203	203	202	21.2	45.6	0.6
4	192	192	201	9.7	12.7	0.4
5	192	192	191	25.3	62.2	0.5
6	184	184	191	10.3	14.5	0.4
7	184	184	184	30.9	86.0	0.2
8	176	176	183	11.0	16.2	0.4
9	176	176	176	33.1	97.3	0.5
10	176	176	175	17.6	34.7	0.5
11	176	176	175	41.9	136.0	0.6
12	160	160	174	12.0	18.0	0.4
13	160	160	159	46.4	172.2	0.6

Table 6.12.: The grain size and time for 50% recrystallization predicted by models for schedule III in the C-Mn steel.

	$D_{gs,0i+1}$ (μm)			$t_{0.5}$ (s)		
Pass No (i)	**Siciliano**	**Sellars**	**Militzer**	**Siciliano**	**Sellars**	**Militzer**
0	353			-	-	-
1	194	194	144	6.7	3.9	1.0
2	92	92	89	0.8	0.4	0.3
3	86	86	88	0.6	0.4	0.2
4	90	90	87	0.6	0.4	0.2
5	93	93	85	0.7	0.4	0.2

Figure 6.10 shows the recrystallized volume fraction of the C-Mn-Nb-Ti-V steel for schedules I (0.07 ε/pass), II (0.1ε/pass) and III (0.15 ε/pass) compared to the Siciliano & Jonas model [52], Militzer *et al*. model [3] and Uranga *et al*. model [73,80]. Table 6.13 and Table 6.14 show the predictions of $D_{gs,0i+1}$ and $t_{0.5}$. Poor correlation between measured and predicted X for strains of 0.07 and 0.1 per pass is found for all the models. Militzer and Siciliano models gave the best fit at strains of 0.15 per pass although they over-predict X in the first pass whilst Uranga's model predicts X closely in the first two passes but it falls short from the third pass onwards.

As discussed above for the C-Mn steel, the poor correlation at small strains can be due to the over-prediction of the recrystallized grain size hence the lack of change in D_{gs0i+1} from pass 2 onwards in Table 6.13 and Table 6.14. This is since a condition of keeping the D_{gs0i} the same if $D_{rex,i}$ is greater than $D_{gs,i0}$ was set as mentioned above. The other reason may be that the recrystallization is by the SIBM process and not the classical nucleation theory. For the microalloyed steels the other factor can be due to the fact that it is expected that solute Nb will delay recrystallization as the Siciliano [52] and Uranga [73,80] models illustrate, this may however be over-emphasised especially at small strains. The combination accounts for solute Nb and Ti in the Uranga *et al*. model may have led to a lower X prediction than both Siciliano and Militzer models. This can also account for its poor prediction at strains of 0.15.

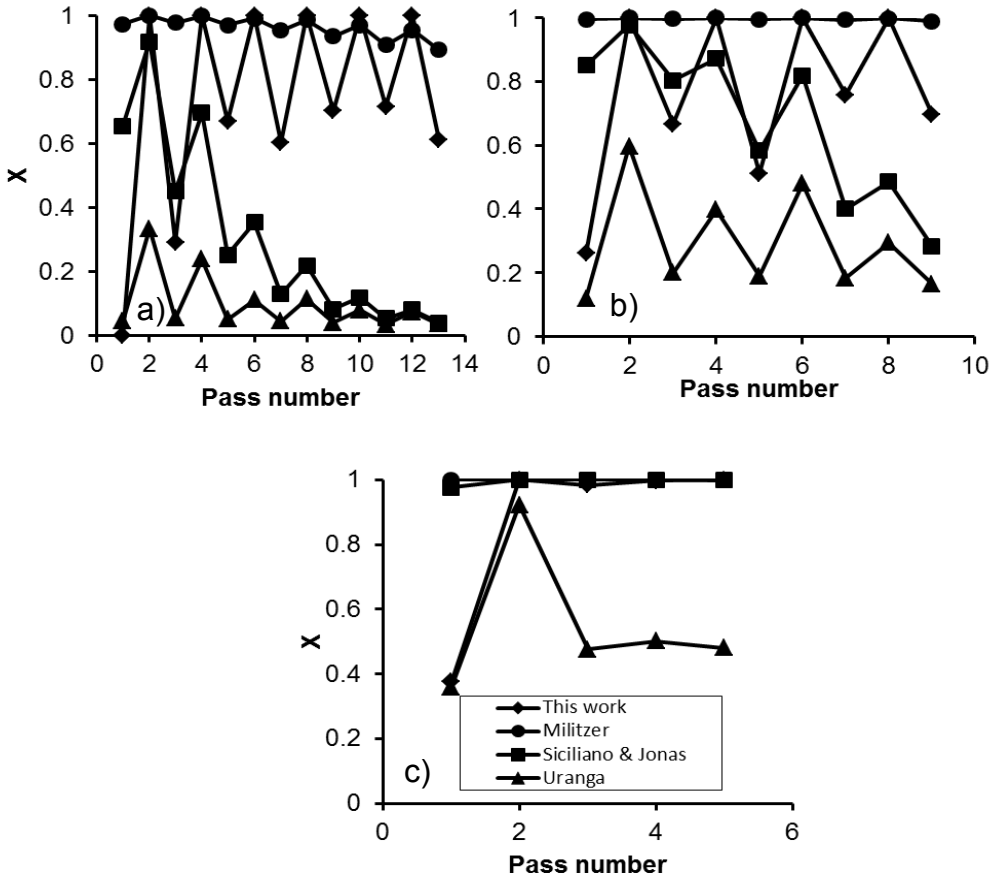

Figure 6.10.: Comparison of the measured recrystallized volume fraction to models in literature for the C-Mn-Nb-Ti-V steel for a) schedule I (0.07 ε/pass), b) schedule II (0.1 ε/pass) and C) schedule III (0.15 ε/pass).

Table 6.13.: The grain size and time for 50% recrystallization predicted by models for schedule I in the C-Mn-Nb-Ti-V steel.

	$D_{gs,0i+1}$ (μm)			$t_{0.5}$ (s)		
Pass No (i)	Siciliano	Uranga	Militzer	Siciliano	Uranga	Militzer
0	78					
1	78	78	78	5.9	139.3	1.0
2	72	72	78	2.5	15.3	0.3
3	72	72	78	15.7	111.0	1.0
4	72	72	78	7.9	23.4	0.5
5	72	72	78	38.4	115.9	1.3
6	72	72	78	25.6	53	1.0
7	72	72	78	88.4	131.8	1.6
8	72	72	78	49.6	51.2	1.1
9	72	72	78	153.9	143.8	2.0
10	72	72	78	103.2	73.3	1.5
11	72	72	78	251.6	168.2	2.4
12	72	72	78	162.5	79.6	1.7
13	72	72	78	350.8	162.0	2.7

Table 6.14.: The grain size and time for 50% recrystallization predicted by models for schedule III in the C-Mn-Nb-Ti-V steel.

	$D_{gs,0i+1}$ (μm)			$t_{0.5}$ (s)		
Pass No (i)	Siciliano	Uranga	Militzer	Siciliano	Uranga	Militzer
0	78			-	-	-
1	49	56	52	1.7	14.0	0.3
2	36	39	52	0.3	2.4	0.1
3	36	39	50	0.6	9.7	0.1
4	35	39	50	0.7	9.0	0.1
5	35	39	50	0.9	9.5	0.2

Chapter 7. Contribution To Industry

7.1. Reheating

Reheating conditions do not only control the extent of the austenite grain size but also the amount of microalloys in solution at a given temperature. The higher the amount of solute microalloys in the steel is during reheating, the more beneficial it is for the steel during and after hot rolling in terms of grain size control and strength contribution. In industry there is also an economic factor to this, where it is desired to achieve the optimum conditions for a given steel at minimum costs as possible.

In this work the reheat temperature was kept constant at 1220 °C but the use of Thermo-Calc® gave valuable information. For the C-Mn-Nb-V (0.01% Nb) steel Thermo-Calc® showed that a minimum of 1100 °C is sufficient to take almost all the Nb into solution whereas for the C-Mn-Nb-Ti-V (0.04% Nb) steel a minimum of 1200 °C is required to dissolve all the Nb. To save costs of energy this work with the assistance of Thermo-calc® recommends a reheat temperature of 1150 °C as the optimum for the C-Mn, C-Mn-V, and C-Mn-Nb-V steels and 1200 °C for the C-Mn-Nb-Ti-V steels.

7.2. Roughing

7.2.1. Strain And Inter-Pass Times

The present work shows that a combination of minimum strain of 0.15 and inter-pass times of 9 s are sufficient to promote full recrystallization in between the passes for all the studied steels. This shows that under the current studied conditions, the steel's chemistry showed little effect on the recrystallization behaviour and the applied strain per pass is the main driver. Strain per pass also showed to be dominant in controlling the grain size exiting the roughing mill, with the 0.15 strain per pass leading to a finer grain size as compared to the 0.07 and 0.1 strain per pass schedules. Although a strain of 0.4 is not applicable in industry due to mill constraints (draft and force), the work showed that such strains enhanced the extent of grain refinement. FEM also showed that at average strains of 0.15 where the localized strain at the centre is at least 0.17 it

is ensured that full recrystallization is attained at the centre of the plate. For economic viability and maintaining good functionality of the mill, a strain of 0.15 per pass and an inter-pass time of 9 seconds should be considered.

7.2.2. Temperature

Roughing in the 1050-1150 °C range was sufficient to promote recrystallization in between the passes given that the strain per pass is high enough. Since high and low exit roughing temperatures yielded the same response in terms of recrystallization behaviour and grain size, it will be optimal to adopt the low exit roughing temperatures (1050 °C) to avoid long delays to reach the finishing entry temperatures, which will minimize grain growth of the recrystallized austenite grains.

7.2.3. Mill Loads

Using Sim's model to calculate the MFS showed that the lab simulated rolling conditions gave results that are below the actual MFS values of the industrial hot rolled slabs, which shows that the proposed schedule of 0.15 per pass to promote a fully recrystallized austenite microstructure coming out of roughing will not compromise the mill constraints.

Chapter 8. Conclusions

Roughing of peritectic microalloyed steels was studied in the temperature range of 1050 to 1150 °C and strain rates of 0.3-2.9 $s^{-1}$and it was found that:

1) Pass strains equal to 0.15 lead to complete recrystallization from the second pass onwards and lead to an optimum austenite microstructure with a finer grain size and a narrower grain size distribution than the 0.07 and 0.1 pass strains in all of the steels studied. This is attributed to the increased effective interfacial area per unit volume with increasing strain which increases the number of the nucleation sites for the recrystallized grains and thereby leading to a finer austenite grain size.

2) Grain refinement in all the steels was achieved through static recrystallization during inter-pass delays for strains of 0.07 and 0.1. It was shown that the bulk of the localized effective strain was below the critical strain for DRX at strains less than 0.07 to 0.1. However at pass strains equal to 0.15 lead to a threshold where both static recrystallization and metadynamic recrystallization may be responsible for the grain refinement.

3) The application of 0.4 strain in the last pass led to a further grain refinement in all steels for pass strains of 0.07 to 0.1 and to a lesser extent for a 0.15 pass strain. The 0.4 strain in the last pass also neutralized the grain size difference across the steels, especially at high exit roughing temperatures. This is may be accounted by the fact that as the strains are increased, saturation in the extent of grain refinement of the austenite grain size is reached.

4) No significant influence of exit roughing temperature was found on the recrystallization behaviour in all steels.

5) With the aid of FEM, it was found that the equivalent strain increases from the centre to the surface of a plate during flat rolling and vice versa in axi-symmetrical deformation. The relationship of applied strain to the equivalent

strain at various locations on the axisymmetrical and flat rolling simulations was found to be linear. The following relationships were found at the centre:

a. Axisymmetrical compression:

$$EQPL = 1.34\varepsilon - 0.027$$

b. Flat rolling:

$$EQPL = 1.15\varepsilon + 0.005$$

6) Recrystallization models fell short in their predictive capacity at small strains of 0.07 to 0.1 which is primarily due to the over estimation of the recrystallized grain size at small strains. Another factor may be that at these small strains recrystallization takes place via the SIBM process and does not occur via the classical nucleation theory.

Chapter 9. Suggestions For Future Work

This work showed that the optimum austenite microstructure is found when pass strains of at least 0.15 are maintained during roughing. It is well known that the ferrite grains inherit their morphology and size from the austenite microstructure after finishing. In order to have a full picture given the optimized roughing conditions a follow up study by optimizing the finishing conditions will be necessary to ensure that the ferrite microstructure after hot rolling is also improved for better mechanical properties at room temperature for the different applications of the steels.

During roughing full recrystallization is required for a homogenous austenite microstructure. It will be worthwhile to fundamentally and industrially model the amount of recrystallization during inter-pass times for given hot rolling conditions in flat rolling with the aid of FEM. This will help guide the required hot rolling conditions (temperature,ε, $\dot{\varepsilon}$, and inter-pass times) for complete recrystallization.

The extent of grain refinement was found to diminish with decreasing intial grain size. However this observaion was for different steel chemistries which brought about the grain size differences. To eliminate the differences in chemistry, a simulation where the grain size of a same steel is varied and exposing this to similar hot rolling conditions will be able to prove the consistency of this observation.

The C-Mn-V steel had mean flow stresses that were higher than that for the C-Mn steel and equal to those of the C-Mn-Nb-Ti-V steel. Further work needs to be done to understand the influence of solute drag of V on hot working behaviour and the austenite grain size at high temperatures.

Chapter 10. References

[1]. Davis, J.R. (ed.), 2001, Alloying: Understanding the Basics, *ASM International,* 193-202, viewed on 14 January 2014, from http://www.asminternational.org.html
[2]. Lechuck, S.J., 2000, 'A study of austenite grain growth in Ti-Nb HSLA steel', Master's thesis, Dept. of Metals and Materials Engineering, The University of British Columbia.
[3]. Militzer, M., Hawbolt, E.B. & Meadowcroft, T.R., 2000, 'Microstructural model for hot strip rolling of high strength low alloy steels', *Metallurgical and Materials Transactions A*, 31(A), 1247-1259.
[4]. Bai, D.Q., 1993, 'Effect of rolling parameters on the no recrystallization temperature in Nb-Bearing steels', Master's thesis, Dept. of Mining and Metallurgical Engineering, McGill University.
[5]. Lissel, L., 2006., 'Modeling the microstructural evolution during hot working of C-Mn and of Nb microalloyed steels using a Physically Based Model', PhD. thesis, Department of Material Science and Engineering, Royal institute of Technology.
[6]. Opiela, M., 2007, 'Thermo-mechanical treatment of the C-Mn steel with Nb, Ti, V and B microadditions', *Archives of Materials Science and Engineering* 28(6), 377-380.
[7]. Ebrahimi, G.R., Arabshahi, H. & Javdani, M., 2010, 'Hot deformation behaviour of Nb-V microalloyed steel', *Journal of Mechanical Research* 2(5), 92-96.
[8]. Strangwood, M. & Davis, C.L., 2013, 'Modelling grain size distribution during TMCR of Nb-microalloyed steels', *International Journal of Metallurgical Engineering* 2(2), 125-129.
[9]. Hong, S.G., Jun, H.J., Kang, K.B. & Park, C.G., 2003, 'Evolution of precipitates in the Nb-Ti-V microalloyed HSLA steels during reheating', *Scripta Materialia* 48, 1201-1206.
[10]. Hansen, S.S., Vander Sande, J.B. & Cohen, M, 1980, 'Niobium carbonitride and austenite recrystallization in hot rolled microalloyed steels', *Metallurgical Transactions A* 11A, 387-402.
[11]. Jorge, A.M. Jr., Guedes, L.H. & Balancin, O., 2012, 'Ultra grain refinement during the simulated thermomechanical-processing of low carbon steel', *Journal of Materials Research and Technology* 1(3), 141-147.
[12]. Sarkar, S. & Militzer, M., 2009, 'Microstructure evolution model for hot strip rolling of Nb-Mo microalloyed complex phase steel', *Materials Science and Technology* 25(9), 1134-1146.
[13]. Rajput, S.K., Chaudhari, G.P. & Nath, S.K, 2014, 'Physical simulation of hot deformation of low-carbon Ti-Nb microalloyed steel and microstructural studies', *Journal of Materials Engineering and Performance* 23(8), 2930-2942.
[14]. Wei, H-L., Liu, G-Q., Zhao, H-T. & Zhang, M-H., 2014, 'Effect of carbon content on hot deformation behaviors of vanadium microalloyed steels', *Materials Science and Engineering A* 596, 112-120.
[15]. DeArdo, A.J., 2003, 'Niobium in modern steels', *International Materials Reviews* 48(6), 371-402.
[16]. Wang, K., 2003, 'A study of HSLA steels microalloyed with vanadium and titanium during simulated controlled rolling cycles', PhD. Thesis, Department of Mechanical Engineering, University of Canterbury.
[17]. Kundu, A., Davis, C. & Strangwood, M., 2011, 'Grain size distributions after single hit deformation of segregated, commercial Nb-containing steel: Prediction and experiment', *Metallurgical and Materials Transactions A*, 24A, 2794-2806.
[18]. Militzer, M., Giumelli, A., Hawbolt, E.B., & Meadowcroft, T.R., 1996, 'Austenite grain growth kinetics in Al-killed plain carbon steels', *Metallurgical and Materials Transactions A*, 27(A), 3399-3409.
[19]. Medina, S.F., Vega, M.I., Gómez, M. & Gómez, P.P., 2005, 'Influence of the size and volume fraction of TiN particles on hot strength and dynamic recrystallization in structural steels', *ISIJ International* 45(9), 1307-1315.
[20]. Maruyama, N., Uemori, R. & Sugiyama, M., 1998, 'The role of niobium in the retardation of the early stage of austenite recovery in hot-deformed steels', *Materials Science and Engineering* A250, 2-7.
[21]. Chakrabarti, D., Davis, C.L. & Strangwood, M., 2009, 'Effect of deformation and Nb segregatiom on grain size bimodality in HSLA steel', *Materials science and Technology* 25(8), 939-946.
[22]. Adrian, H. & Pickering, F.B., 1991, 'Effect of titanium additions on austenite grain growth kinetics of medium carbon V-Nb steels containing 0.008-0.018%N', *Materials Science and Technology* 7, 176-182.
[23]. Priadi, D., Napitupulu, R.A.M. & Siradj, E.S., 2011, 'Austenite grain growth calculation of 0.028% Nb steel', *Journal of Mining and Metallurgy* 47(2) B, 199-209.
[24]. Kvackaj, T., Nemethova, L, Misicko, R., Pokorny, I. & Molnarova, M., 2011, 'Influence of reheating conditions on austenite grain growth', *High Temperature Material Processing* 30, 535-538.
[25]. Miao, C.L., Shang, C.J., Zhang, G.D. & Subramanian S.V., 2010, 'Recrystallization and strain accumulation behaviours of high Nb-bearing line pipe steel in plate and steel rolling', *Materials Science and Engineering A* 527, 4985-4992

[26]. Pande, C.S., 1987, 'On a stochastic theory of grain growth', *Acta Metallurgica* 35(11), 2671-2678.
[27]. Zhao, Y-L., Shi, J., Cao, W-Q., Wang, M-Q. & Xie, G., 2011, 'Kinetics of austenite grain growth in medium-carbon niobium bearing steel', *Journal of Zhejiang University-Science A (Applied Physics & Engineering)* 12(3), 171-176.
[28]. Flores, O. & Martinez, L., 1997, 'Abnormal grain growth of austenite in a V-Nb microalloyed steel', *Journal of Materials Science* 32, 5985-5991.
[29]. Hillert, M., 1965, 'On the theory of normal and abnormal grain growth', *Acta Metallurgica* 13, 227-238.
[30]. Gao, N. & Baker, T.N., 1998, 'Austenite grain growth of microalloyed Al-V-N and Al-V-N-Ti steels', *ISIJ International* 38, 744-751.
[31]. Banerjee, K., Militzer, M., Perez, M. & Wang, X., 2010, 'Nonisothermal austenite grain growth kinetics in a microalloyed X80 linepipe steel', *Metallurgical and Materials Transactions A* 41A, 3161-3172.
[32]. Cuddy, L.J. & Raley, J.C., 1983, 'Austenite coarsening in microalloyed steels', *Metallurgical Transactions A* 14A, 1989-1995.
[33]. Staśko, R., Adrian, H. & Adrian, A., 2006, 'Effect of nitrogen and vanadium on austenite grain growth kinetics of a low alloy steel', *Materials Characterization* 56, 340-347.
[34]. Wang, H.R. & Wang, W. 2008, 'Simple model for austenite grain growth in microalloyed steels', *Materials Science and Technology* 24(2), 228-232.
[35]. Subramanian, S.V., Rehman, M.K., Zurob, H. & Gray, J.M., 2013, 'Process modeling of niobium microalloyed line pipe steels', *International Journal of Metallurgical Engineering* 2(1), 18-26.
[36]. Dutta, B., Palmiere, E.J. & Sellars C.M., 2001, 'Modelling the kinetics of strain induced precipitation in Nb microalloyed steels', *Acta Materialia* 49, 784-794.
[37]. Siwecki, T. & Engberg, G., 1997, 'Recrystallization controlled rolling of steels', '*Thermomechanical Processing in Theory, Modelling and Practice',* 121-143.
[38]. Subramanian, S.V., Zurob, H.S. & Zhu, G., n.d., 'Recrystallization control to obtain uniform fine grain size in hot rolling of HTP steel'. Department of Materials Science and Engineering, McMaster University, USA.
[39]. Maalekian, M., Radis, R., Militzer, M., Moreau, A. & Poole, W.J., 2012, 'In situ measurement and modelling of austenite grain growth in a Ti/Nb microalloyed steel', *Acta Materialia* 60, 1015-1026.
[40]. Yu, Q. & Sun, Y., 2006, 'Abnormal growth of austenite grain of low-carbon steel', *Materials and Engineering A* 420, 34-38.
[41]. Stanislaw, Z., Siwecki, T., Hutchinson, B. & Attlegård, M., 1991, 'Recrystallization controlled rolling and accelerated cooling for high strength and toughness in V-Ti-N steels', *Metallurgical Transactions A* 22A, 2681-2694.
[42]. Alogab, K.A., Matlock, D.K., Speer, J.G. & Kleebe, H.J., 2007, 'The influence of niobium microalloying on austenite grain coarsening behaviour of Ti-modified SAE 8620 steel', *ISIJ International* 47(2), 307-316.
[43]. Zurob, H.S., Hutchinson, C.R., Brechet, Y. & Purdy, G., 2002, 'Modeling recrystallization of microalloyed austenite: effect of coupling recovery, precipitation and recrystallization', *Acta Materialia* 50, 3075-3092.
[44]. Zurob, H.S., Brechet, Y. & Purdy, G., 2001, 'A model for the competition of precipitation and recrystallization in deformed austenite', *Acta Materialia* 49, 4183-4190.
[45]. Gong, P., Palmiere, E.J. & Rainforth, W.M., 2015, 'Dissolution and precipitation behaviour in steels microalloyed with niobium during thermomechanical processing', *Acta Materialia* 97, 392-403.
[46]. Kliber, J., Fabík, R. & Drozd, K., 2010, 'Hot forming recrystallization kinetics in steel', *Metalurgija* 49(1), 67-71.
[47]. Vervynckt, S., Verbeken, K., Thibaux, P. & Houbaert, Y., 2011, 'Evaluation of the austenite recrystallization by multideformation and double deformation tests', *Steel Research international* 82(4), 369-378.
[48]. Sanchez-Mourino, N., Petrov, J-H., Kim, K. & Kestens, L.A.I., 2011, 'Microstructural changes after control rolling and interrupted accelerated cooling simulations in pipeline steel', '*Steel Research international* 82(4), 352-360.
[49]. Pietrzyk, M., 2002, 'Through-process modelling of microstructure evolution in hot forming of steels', *Journal of Materials Processing Technology* 125-126, 53-62.
[50]. Zhou, S.X., 2003, 'An integrated model for hot rolling of steel strips', *Journal of Materials Processing Technology* 134, 338-351.
[51]. Biglou, J. & Lenard, J.G., 1996, 'A study of dynamic recrystallization during hot rolling of microalloyed steels', *Annals of the CIRP* 45(1), 227-230.

[52]. Siciliano, F. Jr. & Jonas, J., 2000, 'Mathematical modelling of the hot strip rolling of microalloyed Nb, multiply alloyed Cr-Mo, and plain C-Mn steels', *Metallurgical and Materials Transactions A* 31A, 511-530.
[53]. Pussegoda, L.N. & Jonas, J.J., 1991, 'Comparison of dynamic recrystallization and conventional controlled rolling schedules by laboratory simulation', *ISIJ International* 31(3), 278-288.
[54]. Siwecki, T., 1992, 'Modelling microstructure evolution during recrystallization controlled rolling' *ISIJ International* 32(3), 368-376.
[55]. Zaky, A.I., 2005, 'Determinations of the non-recrystallizationtemperature for X52 steel produced by compact slab process combined with direct hot rolling', *Journal of Materials Engineering and Performance* 15(6), 651-655.
[56]. Homsher, C.N., 2007, 'Determination of the non-recrystallization temperature (TNR) in multiple microalloyed steels', Master's thesis, Dept. Metallurgical and Materials Engineering, Colorado School of Mines.
[57]. Muntin, A. & Zinyagin, A., 2014, 'FEM modeling and experimental research of through-thickness strain distribution during hot plate rolling', *in Metal 2014 conference* proceedings, Brno, Czech Republic. May 21-23, 2014.
[58]. Pereda, B., Uranga, P., Rodriguez-Ibabe, Stalheim, D., Barbosa, R. & Rebellato, M.A., 2015, 'Through-thickness homogenization in thin slab direct rolling of Nb microalloyed steels' *in HSLA Steels 2015, Microalloying 2015 & Offshore engineering steels 2015 conference proceedings*, Hangzhou, China, November 11-13, 2015, pp. 309-315.
[59]. Szeliga, D., Kuziak, R., Kopp, R., Smyk, G. & Pietrzyk, M. 2015, 'Accounting for the inhomogeneity of deformation and identifications of microstructure evolution model', *Archives of Metallurgy and Materials* 60(4), 3087-3094.
[60]. Kusiak, J., Kawalla, R., Pietryzyk, M. & Pircher, H., 1996, 'Inverse analysis applied to the evaluation of material parameters in the history dependent flow stress equation in hot forming of metals', *Journal of Materials Processing Technology* 60, 455-461.
[61]. Pietrzyk, M., Lenard, J.G. & Kedzierski, Z., 1997, 'Inverse analysis applied to the evaluation of material parameters in microstructure evolution models for steels', in T. Chandra & T. Sakai (eds.), *Thermec '97 International Conference on Thermomechanical Processing of steels and other Materials, Volume II proceedings*. University of Wollongong, Australia, July 7-11, 1997, pp. 2077-2084.
[62]. Sztangret, M. & Pietrzyk, M., 2013, 'Applications of plane strain compression tests for identification of flow stress models of materials and for physical simulation of metal forming processes', *Vestnick of Nosov Magnitogorsk State Technical University* 2013(5), 16-23.
[63]. Lin, Y.C., Chen, M. & Zhong, J., 2008, 'Numerical simulation for stress/strain distribution and microstructural evolution in 42CrMo steel during hot upsetting process', *Computational Materials Science* 43, 1117-1122.
[64]. Siciliano, F. Jr., Miniami, K., Maccagno, T.M. & Jonas, J.J., 1996, 'Mathematical modeling of the mean flow stress, fractional softening and grain size during the hot strip rolling of C-Mn steels', *ISIJ International* 36(12), 1500-1506.
[65]. Mukhopadhyay, A., Howard, I.C. & Sellars C.M., 2005, 'Finite element modeling of effects of roll gap geometry in hot rolling', *Materials Science and Technology* 21(8), 901-911.
[66]. Richardson, G.J., Hawkins, D.N. & Sellars, C.M., 1985, *Worked examples in metalworking*, The Institute of Metals, London.
[67]. Stumpf. W., 2003, 'Grain size modelling of low carbon strip steel during hot rolling in a CSP plant using the hot charge route', *The Journal of the South African Institute of Mining and Metallurgy*, 617-632.
[68]. Minami, K., Siciliano, F. Jr., Maccagno, T.M. & Jonas, J.J., 1996, 'Mathematical modeling of mean flow stress during hot strip rolling of Nb steels', *ISIJ International* 36(12), 1507-1515.
[69]. Siciliano, F., Leduc, L.L. & Hensger, K., 2005, 'The effect of chemical composition and on the hot-deformation resistance during processing of microalloyed steels in thin slab casting/direct rolling process', *in International HSLA 2005 & ISUGS 2005 conference proceedings*, November , 2005, pp. 1-5.
[70]. Dimatteo, A., Vannucci, M. & Colla, V., 2013, 'Prediction of hot resitance during processing of microalloyed steels in plate rolling process' *International Journal of Advanced Manufacturing Technology* 66, 1511-1521.
[71]. Andrade, H.L., Akben, M.G. & Jonas J.J., 1983, 'Effect of molybdenum, niobium and vanadium on static recovery and recrystallization and on solute strengthening in microalloyed steels', *Metallurgical Transactions A* 14A, 1967-1977.
[72]. Elwazri, A.M., Essadiqi, E. & Yue, S., 2004, 'Kinetics of metadynamic recrystallization in micoalloyed hypereutectoid steels' *ISIJ International* 44(4), 744-752

[73]. Uranga, P., Fernández, A.I., López, B. & Rodriguez-Ibabe, J.M., 2004, 'Modeling of austenite grain size distribution in Nb microalloyed steels processed by thin slab casting and direct rolling (TSDR) route', *ISIJ International* 44(8), 1416-1425.
[74]. Kim, S.-I., Youngseog, L., Duk-Lak, L. & Yeon-Chul Y., 2003, 'Modelling of AGS and recrystallized fraction of microalloyed medium carbon steel during hot deformation', *Materials Science and Engineering* A355, 384-393.
[75]. Sellars, C.M., 1990, 'Modelling microstructural development during hot rolling', *Materials Science and Technology* 6, 1072-1081.
[76]. Sellars, C.M., 1985, 'The kinetics of softening processes during hot working of austenite', *Czechoslovak Journal of Physics* B35, 239-248.
[77]. Opiela, M., & Ozgowicz, W., 2012, 'Effects of Nb, Ti and V on recrystallization kinetics of austenite in microalloyed steels', *Journal of Achievements in Materials and Manufacturing Engineering* 55(2), 759-771.
[78]. Hodgson P.D. & Gibbs R.K., 1992, 'A mathematical model to predict the mechanical properties of hot rolled C-Mn and microalloyed steels', *ISIJ International* 32(12), 1329-1338.
[79]. Karjalainen, L.P., Maccagano, T.M. & Jonas, J.J., 1995, 'Softening and flow stress behaviour of Nb microalloyed steels during hot rolling simulation', *ISIJ International* 35(12), 1523-1531.
[80]. Uranga, P., Fernández, A.I., López, B. & Rodriguez-Ibabe, J.M., 2003, 'Transition between static and metadynamic recrystallization in coarse Nb microalloyed austenite', *Materials Science and Engineering* A345, 319-327.
[81]. Sha, Q.Y., Sun, Z.Q. & Li, L.F., 2015, 'Refinement of coarse grained austenite in Nb-V-Ti microalloyed steel during roughing rolling', *Ironmaking and Steelmaking* 42(1), 74-80.
[82]. Fernández, A.I., Uranga, P., López, B. & Rodriguez-Ibabe, J.M., 2003, 'Dynamic recrystallization behaviour covering a wide austenite grain size range in Nb and Nb-Ti microalloyed steels', *Materials Science and Engineering* A361, 367-376.
[83], Roucoules, C., Yue, S. & Jonas, J.J., 1995, 'Effect of alloying elements on the metadynamic recrystallization in HSLA steels', *Metallurgical and Materials Transactions A* 26(A), 181-190.
[84]. White, M.J. & Owen, W.S., 1980, 'Effects of vanadium and nitrogen on recovery and recrystallization during and after hot-working some HSLA steels', *Metallurgical Transactions A* 11A, 597-604.
[85]. Medina, S.F., 1997, 'Determination of precipitation-time-temperature (PTT) diagrams for Nb, Ti, V microalloyed steels', *Journal of Materials Science* 32, 1487-1492.
[86]. Quispe, A., Medina, S.F., Gómez, M. & Chaves, J.J., 2007, 'Influence of austenite grain size on recrystallization-precipitation interaction in a V-microalloyed steel' *Materials Science and Engineering A* 447, 11-18.
[87]. Gómez, M., Medina, S.F., Quispe, A. & Valles, P., 2002, 'Static recrystallization and induced precipitation in a low Nb microalloyed steel', *ISIJ International* 42(4), 423-431.
[88]. Wang, W., 2009, 'Precipitation of complex carbonitrides in a Nb-Ti microalloyed plate steel', *Journal of Materials Science* 44, 591-600.
[89]. Herman, J.C., Donnay, B. & Leroy, V., 1992, 'Precipitation kinetics of microalloying additions during hot rolling of HSLA steels', *ISIJ International* 32(6), 779-785.
[90]. Dyja, H. & Korczak, P., 1999, 'The thermal-mechanical and microstructural model for the FEM simulation of hot plate rolling', *Journal of Materials Processing Technology* 92-93, 463-467.
[91]. Dutta, B. & Sellars C.M., 1987, 'Effect of composition and process variables on Nb(C,N) precipitation in niobium microalloyed austenite', *Materials Science and Technology* 3, 197-206.
[92]. Gómez, M., Rancel, R., Fernández, B.J. & Medina, S.F., 2009, 'Evolution of austenite static recrystallization and grain size during hot rolling of a V-microalloyed steel', *Materials Science & Engineering A* 501, 188-195.
[93]. Yoshie, A., Fujioka, M., Watanabe, Y., Nishioka, K. & Morikawa, H., 1992, 'Modelling of microstructural and mechanical properties of steel plates produced by thermomechanical control process', *ISIJ International* 32(3), 395-404.
[94]. FEMLAB® automatic Control Manual, n.d., *Chapter 2: Reheat furnace in the steel industry*, viewd on 10 October 2014, from http://www.comsol.com.
[95]. Jonsson, M., 2006, 'An investigation of of different strategies for thermo-mechanical rolling of structural steel heavy plates', *ISIJ International* 46(8), 1192-1199.
[96]. Jin, S., Chen, Q. & Bratberg, J., 2015, 'Thermodynamic calculations and precipitation simulations of HSLA steels', *in HSLA Steels 2015, Microalloying 2015 & Offshore engineering steels 2015 conference proceedings,* Hangzhou, China, November 11-13, 2015, pp. 173-177
[97]. Jansen Van Rensburg, G.J., 2016, 'Development and implementation of state variable based user materials in computational plasticity', PhD thesis, Dept. of Mechanical & Aeronautical Engineering, University of Pretoria.

[98]. Pussegoda, L.N., Yue, S. & Jonas, J.J., 1990, 'Laboratory simulation of seamless tube piercing and rolling using dynamic recrystallization schedules' *Metallurgical Transactions A* 21A, pp. 153-164.
[99]. Hui, W-J., Chen, S-L., Shao, C-W., Zhang, Y-J. & Dong, H., 2015, 'Hot deformation behavior of vanadium-microalloyed medium-carbon steel for fracture splitting connecting rod', *Journal of Iron and Steel Research* 22(7), 615-621.
[100]. Wei, H., Liu, G. & Zhang, M, 2014, 'Physically based constitutive analysis to predict flow stress of medium carbon and vanadium microalloyed steels', *Materials Science and Engineering A* 602, 127-133.
[101].Thelning, K-E., 1984, *Steel and its heat treatment*, 2nd edn., Butterworth & Co., London.
[102]. Opiela, M. & Grajcar, A., 2012, 'Influence of plastic deformation conditions on recrystallization kinetics of Nb-Ti-V microalloyed steel', *in Metal 2012 conference proceedings,* Brno, Czech Republic May 23-25, 2012.
[103]. Schwartz, R., 2011, 'Study on the continuous casting of peritectic steel grades by a mesoscopic damage approach', PhD. Thesis, Dept. of Architecture, Geology, Environment and Construction, University of Liege.
[104] Meroni, U., Ruzza, D.W. & Carboni, A., 1997, *Method for the continuous casting of peritectic steels,* US Patent 5 592 988.
[105]. Moon, S-K., 2015, 'The peritectic transition and continuous casting practice', PhD. Thesis, Faculty of Engineering and Information Sciences, University of Wollongong.
[106]. Nassar, H., 2009, 'On peritectic reactions and transformations and hot forming of cast structures', PhD. Thesis, Department of Material Science and Engineering, Royal Institute of Technology.
[107]. Li, Y., Onodera, E. & Chiba, A., 2010, 'Friction coefficient in hot compression of cylindrical sample', *Materials Transactions* 51(10), 1210-1215.
[108]. Banerjee, J.K., 1985, 'Barreling of solid cylinders under axial compression', *Journal of Materials and Technology* 107, 138-144.
[109]. Dieter, G.E., Kuhn, H.A. & Semiatin, S.L. (eds.), 2003, *Handbook of workability and process design*, www.knovel.com, viewed 14 June 2016, from https://app.knovel.com/web/toc.v/cid:kpHWPD0001/viewerType:toc/root_slug:handbook-of-workability.
[110]. Ebrahimi, R. & Najafizadeh, A., 2004, 'A new method for evaluation of frictioin in bulk metal forming', *Journal of Materials Processing Technology*, 136-143.
[111]. Tan, X., 2002, 'Comparisons of friction models in bulk metal forming', *Tribology International* 35, 385-393.
[112]. Humphreys, F.J. & Hatherly, M., 2004, *Recrystallization and annealing related phenomena,* 2nd edn., Elsevier, Oxford.
[113]. Humphreys, F.J., 2004, 'Nucleation in recrystallization', *Materials Science Forum* 467-470, 107-116.
[114]. Rehman, M.K. & Zurob, H.S., 2013, 'A novel approach to model statistic recrystallization of austenite during hot rolling of Nb microalloyed steel Part I: Precipitate-free case', *Metallurgical and Materials Transactions A* 44A, 1862-1871.
[115]. Rios, P.R., Siciliano, F. Jr., Sandim, H.R.Z., Plaut, R.L. & Padilha, A.F., 2005. Nucleation and growth during recrystallization, *Materials Research* 8(3), 225-235.
[116]. Paggi, A., Angella, G. & Donnini, R., 2015, 'Strain induced grain boundary migration effects on grain growth of an austenitic stainless steel during static and metadynamic recrystallization', *Materials Characterization* 107, 174-181.
[117]. Ghazani, M.S., Vajd, A. & Mosadeg, B., 2015, 'Prediction of critical stress and strain for the onset of dynamic recrystallization in plain carbon steels', *Iranian Journal of Materials Science & Engineering* 12(1), 52-58.
[118]. Ouchi, C., & Okita, T., 1984, 'Austenitic grain refinement through static recrystallization immediately after hot rolling', *Transactions ISIJ* 24, 726-733.
[119]. Bakkaloğlu, A., 2002, 'Effect of processing parameters on the microstructure and properties of an Nb microalloyed steel', *Materials Letters* 56, 263-272.
[120]. Mataya, M.C. & Matlock, D.K., 1989, 'Effects of multiple reductions on grain refinement during hot working of alloy 718', *The Minerals Metals & Materials Society*, 155-178.
[121]. Glodowski, R.J., 2005, 'A review of vanadium microalloying in hot rolled steel sheet products' *International Seminar 2005 on Application technologies of Vanadium in flat-rolled steels*, pp. 43-51.
[122]. Ponge, D. & Gottstein, G., 1998, 'Necklace formation during dynamic recrystallization: Mechanisms and impact flow behavior', *Acta Materiala* 46(1), 69-80.
[123]. Sha, Q., Li, Q. & Li, D., 2013, 'Static recrystallized grain size of coarse-grained austenite in an API-X70 pipeline steel', *Journal of Materials Engineering and Performance* 22(12), 3626-3630.
[124]. Samuel, F.H., Yue, S., Jonas, J.J. & Barnes, K.R., 1990, 'Effect of dynamic recrystallization on microstructural evolution during strip rolling', *ISIJ international* 30(3), 216-225.

Chapter 11. Appendices

11.1. Appendix A

Table 11.1 is the constants to all the models pertaining to SRX as discussed in section 3.6.2.1.

Table 11.1.: Static recrystallization parameters

Steel type	*n*	*A* (s)	*δ*	*p*	*q*	*r*	*s*	*u*	Q_{SRX} (kJ/mol)	Q_{gx} (kJ/mol)	Ref.
C-Mn	1	$2.3x10^{-15}$	343	2	-2.5	-	0.4	-0.5	230	45	[52,64]
		$5x10^{-21}$		2	-4	-			330		[60]
	-	$2.5x10^{-19}$	0.5	2	-4	-	0.67	-1	300	-	[75,76]
	2	$4.35x10^{-13}$	100	1	-0.68	-1/3	1/3	-0.37	248	28	[3]
C-Mn-V	0.5	$4.29x10^{-15}$	100	1	-2	-1/3	1/3	-0.37	262	28	[3]
	-	$(0.4[V+Si]+1.1)x10^{-17}$	-	2	-2	-0.4	-	-	290	-	[3]
C-Mn-V-Ti	1.02	$8.04x10^{-7}$	-	1	-0.65	-1.24	-	-	98	-	[74]
		$6.77x10^{-10}$		1	-2	-0.46			166		[77]
	1.7	$5x10^{-18}x(\varepsilon-0.085)^{-3.5}$	-	2	-			-	280	-	[46,54]

Steel type	n	A (s)	δ	p	q	r	s	u	Q_{SRX} (kJ/mol)	Q_{gx} (kJ/mol)	Ref.
	1			1	-2.5				230		[78]
C-Mn-Nb-Ti	1	$(-5.24+550\ [Nb])\times10^{-18}$	1.1	2	-4+77[Nb]	-	0.67	-0.67	330	-	[52,68,77,79]
	-	2.1×10^{-16}		2	-3.1	-0.43			264		
	0.5	4.1×10^{-17}	1.36×10^{4}	1	-2	-1/3	1/3	-0.79	338	88	[3]
	0.77	1.52×10^{-14}	1.36×10^{4}	1	-2	-1/3	1/3	-0.79	275	88	[3]
	1	$9.92\times10^{-11}\exp[(275\times10^{3}/T-185)([Nb]+0.374[Ti])]$	1.4	1	-5.6	-0.53	0.56	-1	180	-	[73,80]
C-Mn-Nb-Ti-V	-	1.57×10^{-14}	1.1	2	-2.9	-	0.67	-0.67	271	-	[52]
		$1.46\times10^{-12}\exp[(275\times10^{3}/T-185)([Nb]+0.374[Ti]+0.00585[V])$	0.88	1	$-5.6xd_0^{-0.15}$	-0.53	0.59	-0.98	227		[81]

Steel type	*n*	*A* (s)	*δ*	*p*	*q*	*r*	*s*	*u*	Q_{SRX} (kJ/mol)	Q_{gx} (kJ/mol)	Ref.
		$2.52x10^{-10}$		2	-4	0			325		[77]

Table 11.2 is the constants to all the models pertaining to MDRX as discussed in section 0.

Table 11.2.: Metadynamic recrystallization (MDRX) parameters.

Steel type	*n*	*A* (s)	*δ*	*a*	*b*	*c*	e	*f*	Q_{app} kJ/mol	Q_{MDRX} (kJ/mol)	Q_{def} (kJ/mol)	Ref.
C-Mn	1.5	1.1	$2.6x10^{4}$	-0.8	-	-	-	-0.23	-	230	300	[64,78]
	-	$1.06x10^{-5}$	$1.8x10^{3}$	-0.6	-	-	-	-0.15	-	300	312	[75,76]
		0.4	$2.6x10^{4}$	-0.8	-	-	-	-0.23	-	240	300	[52]
C-Mn-V	1.2	$(1.5([Si]+[V])+2.8)x10^{-8}$	-	-	-0.6	-	-	-	170	380	350	[72]
C-Mn-V-Ti	1.06	$6.3x10^{-4}$	$1.9x10^{2}$	-	-	0.4	-0.4	-0.034	-	67	295.5	[74]
C-Mn-Nb-Ti	-	$4.42x10^{-7}$	1400		-0.59	-	-	-0.13	153		375	[52,68,83,79]
	1	$1.77x10^{-6}$	1370		-0.62			-0.13	153		375	[73,80]
C-Mn-Nb-Ti-V	-	1,84	-	-0.86	-	-	-	-	-	271	330	[52]

11.2. Appendix B: Reheat austenite microstructures

Figure 1.1 shows the austenite microstructures of the C-Mn, C-Mn-Nb-V and the C-Mn-Nb-Ti-V steels after reheating at 1220 °C for 30 minutes.

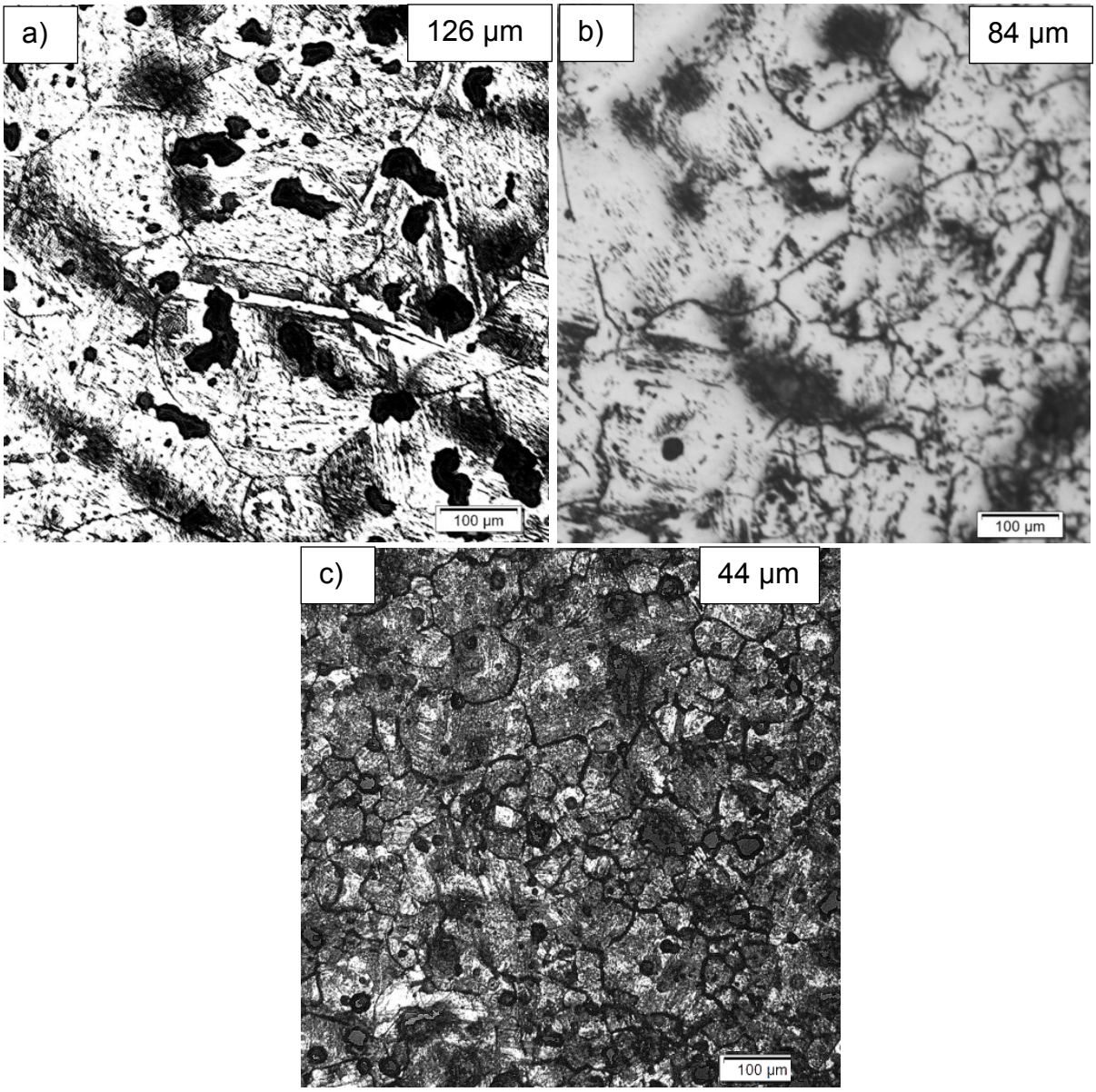

Figure 11.1.: The austenite microstructure of the a) C-Mn b) C-Mn-Nb-V and c) C-Mn-Nb-Ti-V steels at 1220 °C and soaked for 30 minutes.

Figure 11.2 shows the austenite microstructures of the C-Mn, C-Mn-V and the C-Mn-Nb-V steels after reheating at 1220 °C for 60 minutes.

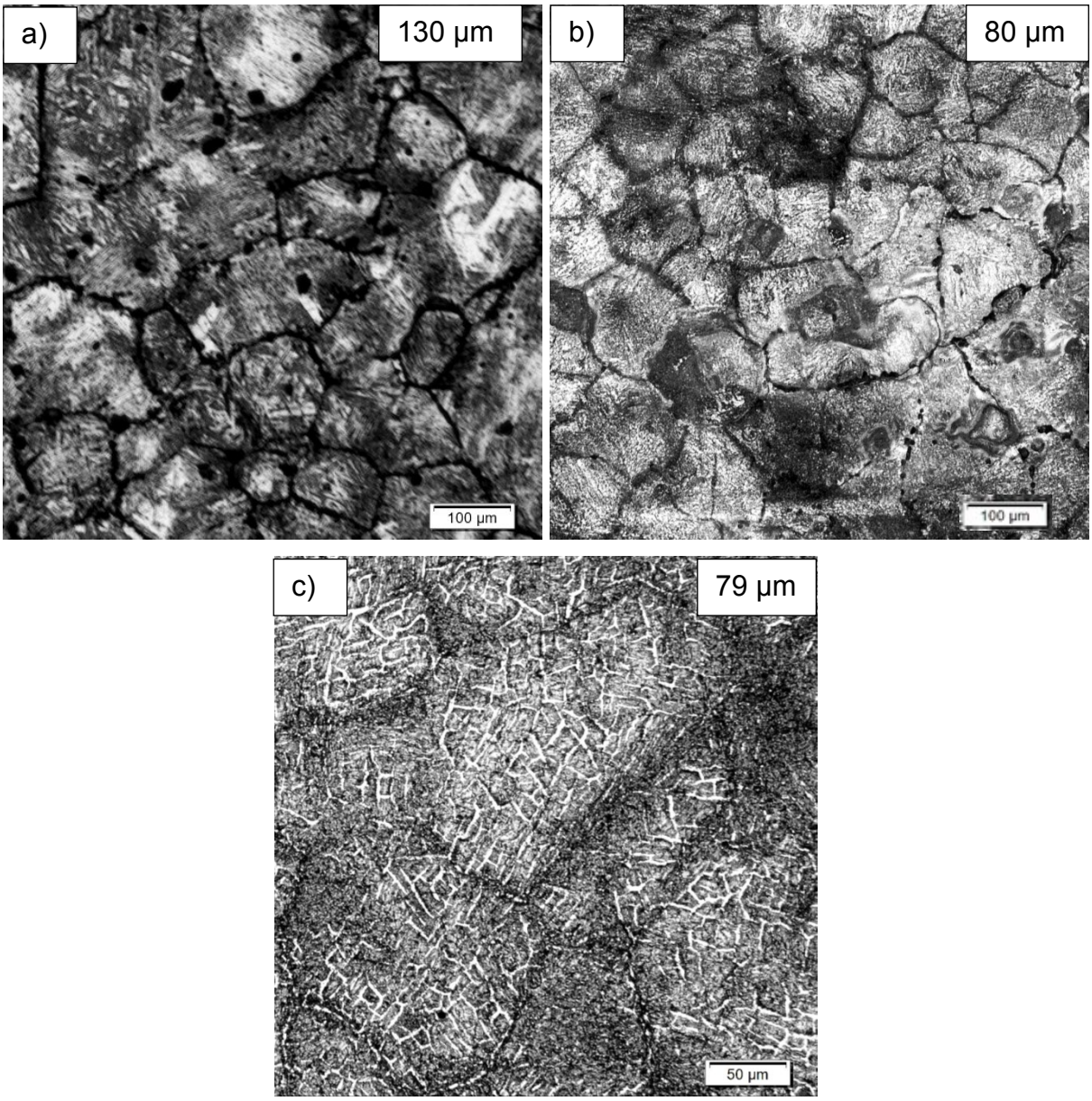

Figure 11.2.: The austenite microstructure of the a) C-Mn b) C-Mn-V and c) C-Mn-Nb-V steels after soaking at 1220 °C for 60 minutes.

Figure 11.3 depicts the austenite microstructures of the C-Mn, C-Mn-Nb-V and C-Mn-Nb-Ti-V steels after the HT2 thermal cycle (7.5 °C/min from 690 °C).

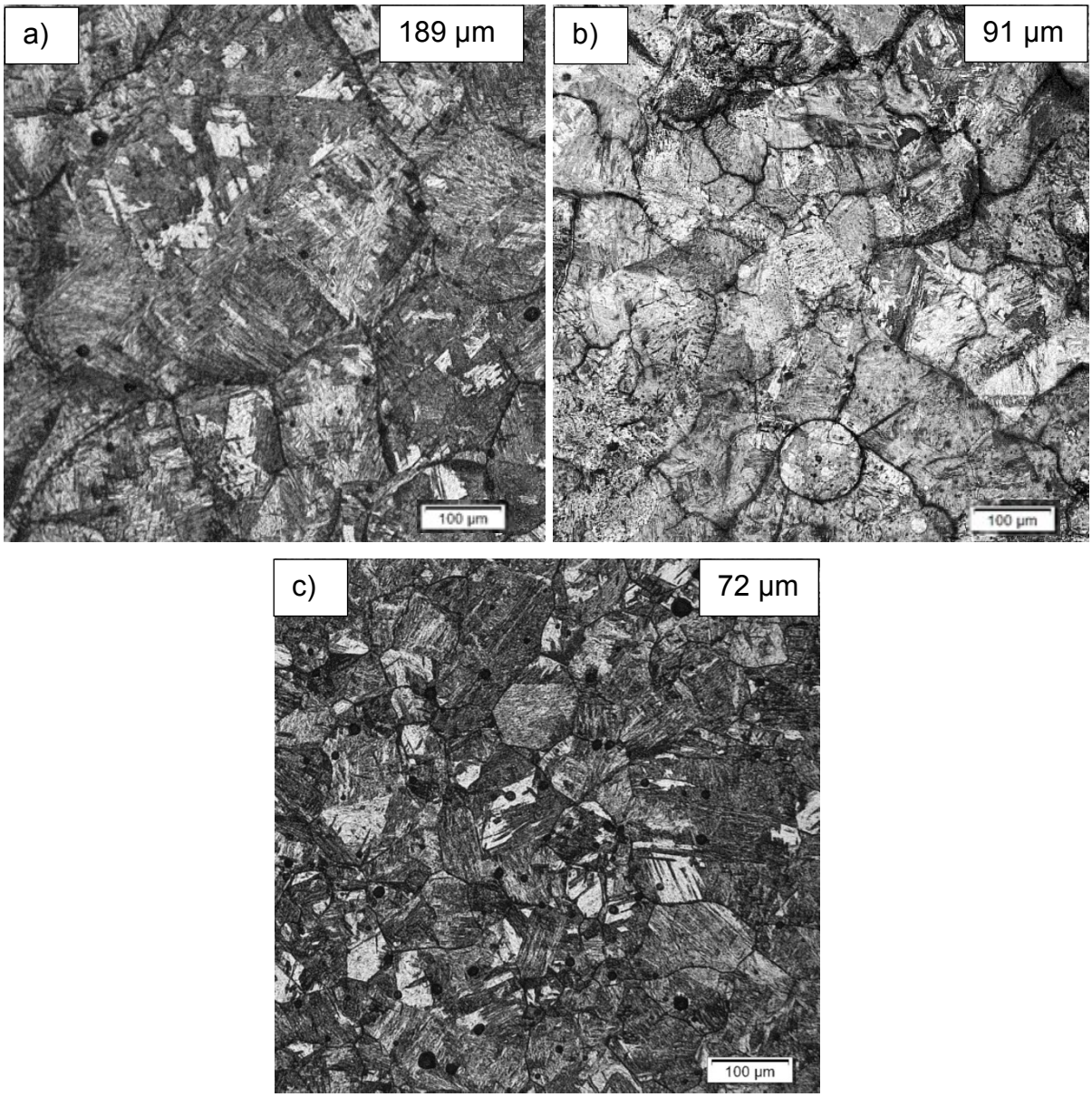

Figure 11.3.: The austenite microstructure of the a) C-Mn b) C-Mn-Nb-V and c) C-Mn-Nb-Ti-V steels after the HT2 thermal cycle.

11.3. Appendix C: True stress-strain curves

Figure 11.4 shows the true stress-strain curves for the low exit temperatures for the intermediate and large strain sequence schedules where there was a 36s delay before the application of the 0.4 strain in the last pass.

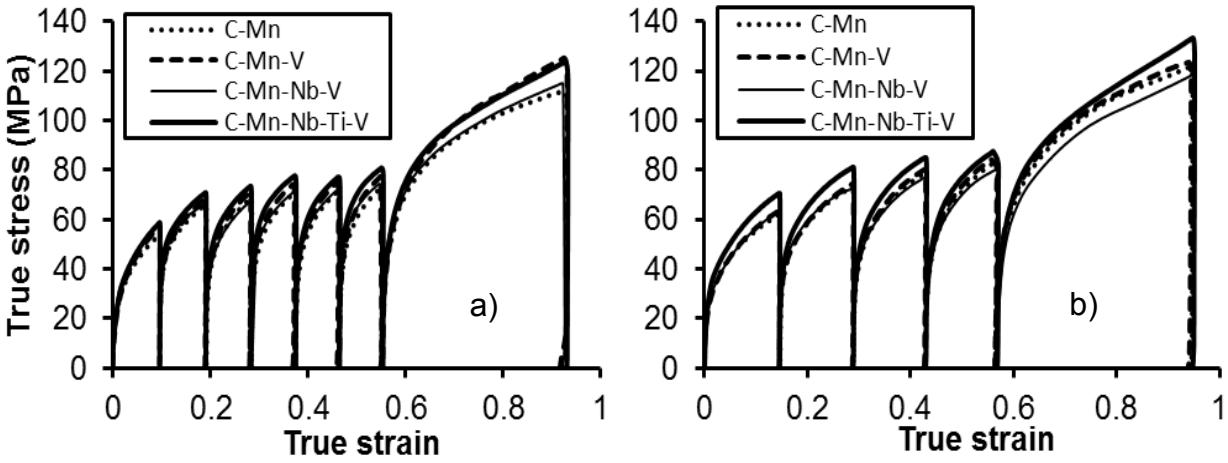

Figure 11.4.: The true stress-strain curves for the low exit roughing temperatures for the a) intermediate strain sequence schedule IX (0.1ε/pass + 0.4ε last pass_36s delay) and b) large strain sequence schedule XII (0.15ε/pass + 0.4ε last pass_36s delay)

11.4. Appendix D: Volume recrystallized fraction

Figure 11.5 shows the volume recrystallized fraction of the high exit roughing simulations for the intermediate strain sequence, schedules II and IV and Figure 11.6 is the volume recrystallized fraction of the low exit roughing simulations for schedule IX and XII for all the steels.

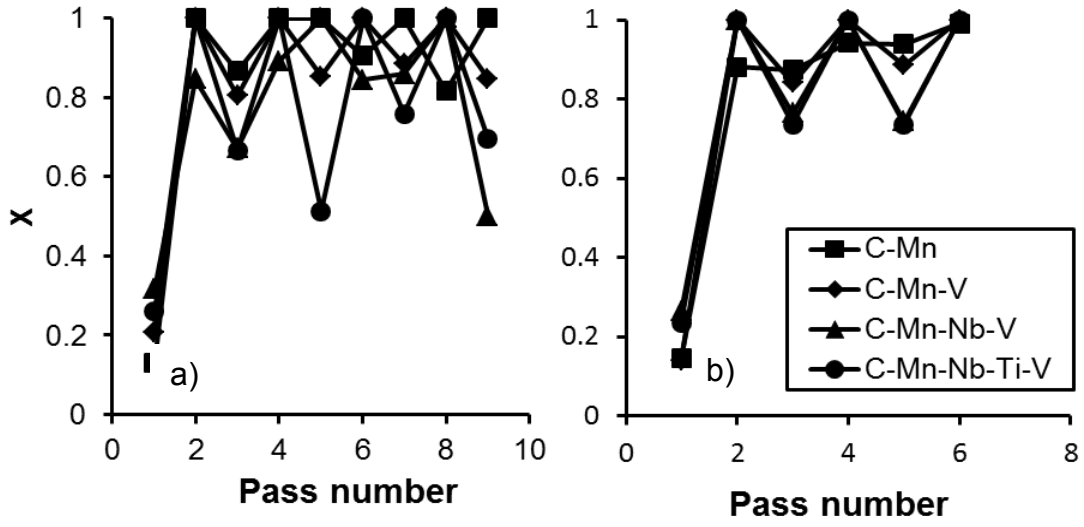

Figure 11.5.: Recrystallization behaviour of the studied steels for the intermediate strain sequence simulation for a) schedule II_0.1ε/pass 1105 ºC exit temperature and b) schedule V _0.1ε/pass+0.4ε last pass 1120 ºC exit temperature.

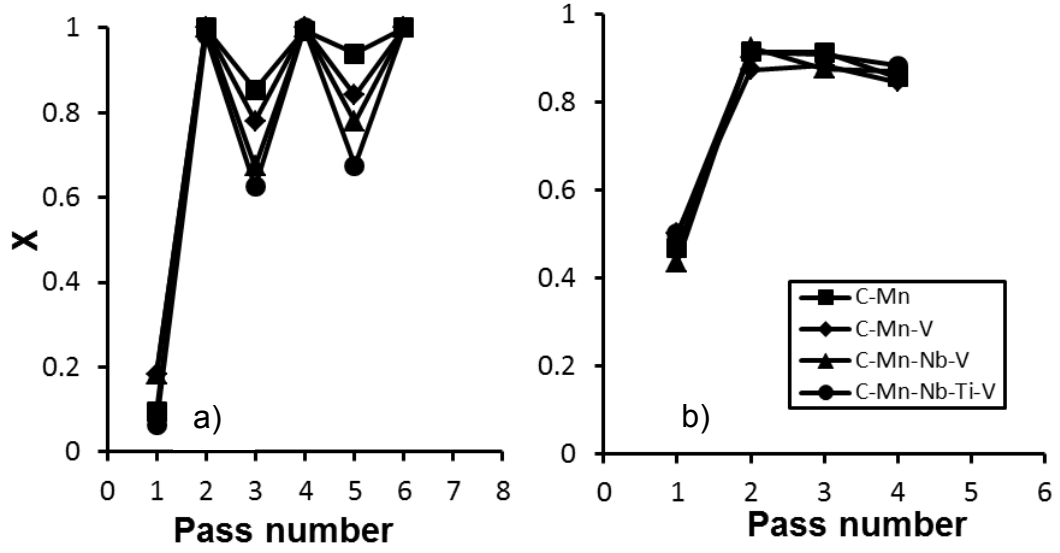

Figure 11.6. : Recrystallization behaviour of the studied steels for 36s delay schedules for a) intermediate strain sequence (IX: 0.1ε/pass) 1060 °C exit temperature and b) large strain sequence (XII: 0.1ε/pass) 1050 °C exit temperature

11.5. Appendix E: FEM results

Figure 11.7 is the strain distribution in an axisymmetric compressed sample, given different strains at 1100 °C at a strain rate of 1.5 s^{-1}.

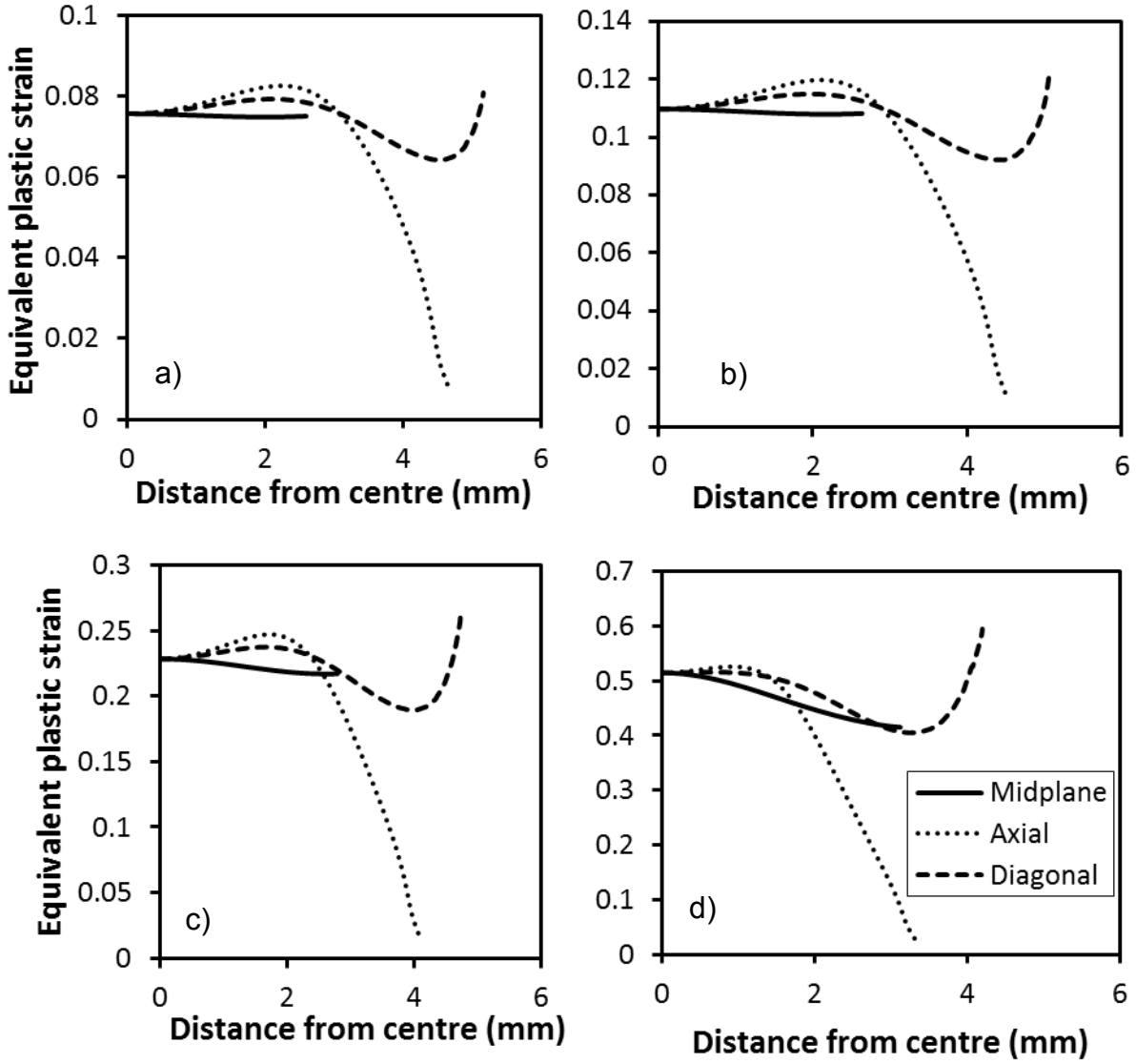

Figure 11.7. Strain distribution along different paths of a single hit FEM simulated deformed axisymmetrical sample with applied true strains of a) 0.07 b) 0.1 c) 0.2 and d) 0.4